

Edited by

Sylwia **BAJKACZ**

Ziemowit **OSTROWSKI**

# RECENT ADVANCES IN COMPUTATIONAL ONCOLOGY AND PERSONALIZED MEDICINE

Volume 1

Here and Now!



Computational Oncology  
and Personalized Medicine

PRIORITY RESEARCH AREAS SILESIAIAN UNIVERSITY OF TECHNOLOGY



MONOGRAPH  
WYDAWNICTWO POLITECHNIKI ŚLĄSKIEJ  
GLIWICE 2021  
UIW 48600



**Edited by**  
**Sylvia BAJKACZ, Ziemowit OSTROWSKI**

**RECENT ADVANCES IN COMPUTATIONAL  
ONCOLOGY AND PERSONALIZED MEDICINE**

**Volume 1**  
**HERE AND NOW!**

**WYDAWNICTWO POLITECHNIKI ŚLĄSKIEJ**  
**GLIWICE 2021**  
**UIW 48600**

***Review***

Prof. n. techn. dr hab. n. fiz. inż. lek. Halina PODBIELSKA  
Prof. dr hab. inż. Wiesław SZEJA

***Editorial Board***

EDITOR-IN-CHIEF – Dr hab. inż. Barbara KULESZ, prof. PŚ  
SECTION EDITOR – Dr hab. inż. Janusz SZEWCZENKO, prof. PŚ  
EDITORIAL OFFICE SECRETARY – Mgr Jolanta NIDERLA-WITKOWSKA

**Published with the approval of the Rector  
of the Silesian University of Technology**

***Publication supported by the Silesian University of Technology Rector's  
pro-quality programme grant No. 04/10/RGM21/1028***

***Cover design***

Maciej MUTWIL

ISBN 978-83-7880-800-8

© Copyright by  
Wydawnictwo Politechniki Śląskiej  
Gliwice 2021

**Editors:**

Sylvia Bajkacz

Department of Inorganic Chemistry, Analytical Chemistry and Electrochemistry  
Silesian University of Technology, Gliwice, Poland

Ziemowit Ostrowski

Department of Thermal Technology, Silesian University of Technology,  
Gliwice, Poland

**Series Editor:**

Joanna Polańska

Department of Data Science and Engineering, Silesian University of Technology,  
Gliwice, Poland

The series *Recent Advances in Computational Oncology and Personalized Medicine* contains publications on research, theory, applications, and design in the field of computational oncology, personalized medicine, biomaterials and medical biotechnology, imaging informatics and telemedicine, biomechanics, analysis and drug design and public health.

The series is published within *The Excellence Initiative – Research University programme* that is implemented to increase scientific excellence and the international importance of the activities of Polish universities. As one of ten Polish universities, *the Silesian University of Technology* obtained the status of a *research university* and commenced the implementation of the programme aimed at increasing its scientific excellence and international significance.

The main objectives of the programme at *The Silesian University of Technology* are:

- Increasing recognition and visibility of the SUT, building the prestige of the University in the group of world-class universities and improving the position in renowned international rankings,
- Conducting high-quality scientific research and implementation of innovations to improve the living and health conditions of people as well as economic development.
- Ensuring high-quality education at the undergraduate and masters levels and the doctoral school, based on research and innovation.
- Supporting the scientific development of employees and PhD students.
- Increasing internationalization of science and education.



## LIST OF CHAPTERS

<b>Chapter 1.</b> NUMERICAL MODELING OF THE LIESEGANG PRECIPITATION PATTERNS WITH LINEAR AND RADIAL GEOMETRIES .....	11
<i>Jarosław Bobek, Andrzej Polański</i>	
<b>Chapter 2.</b> APPLICATION SUPPORTING COGNITIVE FUNCTIONS DIAGNOSTICS AND REHABILITATION OF PATIENTS AFFECTED BY AFTER-STROKE HEMISPATIAL NEGLECT SYNDROME .....	24
<i>Justyna Twardzik, Karolina Molik, Mariola Dylong, Magdalena Hoefmann, Aleksandra Szema, Julia Salinger, Piotr Wodarski, Joanna Bartnicka, Iga Garbowska, Jacek Jurkojć</i>	
<b>Chapter 3.</b> MODELING OF ONCOLOGICAL HYPERTHERMIA USING DUAL-PHASE LAG EQUATIONS .....	37
<i>Mikołaj Stryczyński, Ewa Majchrzak</i>	
<b>Chapter 4.</b> SEGMENTATION AND THREE-DIMENSIONAL VISUALIZATION OF CHONDROMALACIA LESIONS OF THE FEMORAL HEAD .....	46
<i>Weronika Żak</i>	
<b>Chapter 5.</b> APPLICATION OF FUZZY FINITE DIFFERENCE METHOD IN HEAT AND MASS TRANSFER DURING CRYOPRESERVATION PROCESS .....	56
<i>Anna Skorupa, Alicja Piasecka-Belkhat</i>	
<b>Chapter 6.</b> OPTIMIZING SIGNATURE SELECTION SCHEME FOR K-MER COUNTING PROBLEM .....	67
<i>Marek Kokot, Sebastian Deorowicz</i>	
<b>Chapter 7.</b> REMOVING COMPRESSION ARTIFACTS ON WHOLE SLIDE HE-STAINED HISTOPATHOLOGICAL IMAGES .....	79
<i>Piotr Józwik-Wabik, Bartłomiej Gładys, Marek Hermansa, Dawid Macha, Seweryn Kalisz, Tomasz Strzoda, Paweł Foszner, Adam Popowicz, Michał Marczyk</i>	
<b>Chapter 8.</b> GENOME VARIANT CALLING IN CONTEXT OF SEQUENCING READS CORRECTION .....	89
<i>Maciej Długosz</i>	

<b>Chapter 9.</b> UMAP-BASED GRAPHIC REPRESENTATION OF POLCOVID CHEST X-RAY DATA SET HETEROGENEITY .....	100
<i>Marek Socha, Aleksandra Suwalska, Wojciech Prazuch, Michał Marczyk, Joanna Polanska, and POLCOVID Study Group</i>	
<b>Chapter 10.</b> TUMOR DETECTION ON HE-STAINED HISTOPATHOLOGICAL IMAGES USING DEEP LEARNING METHODS: CHALLENGES AND SOLUTIONS .....	115
<i>Tomasz Strzoda, Seweryn Kalisz, Piotr Józwik-Wabik, Dawid Macha, Marek Hermansa, Bartłomiej Gładys, Adam Popowicz, Paweł Foszner, Michał Marczyk</i>	
<b>Chapter 11.</b> MALDI-MSI MOLECULAR IMAGING DATA CLASSIFICATION SYSTEM .....	126
<i>Paweł Pendzialek, Joanna Polańska</i>	
<b>Chapter 12.</b> TUMOR SUBCLONAL RECONSTRUCTION PIPELINES – COMPARISON OF RESULTS .....	137
<i>Paweł Kuś, Roman Jaksik, Marek Kimmel</i>	
<b>Chapter 13.</b> PROJEKTNEURO – A STEP TOWARDS EFFECTIVE PERSONALIZED THERAPY OF NEUROLOGICAL PATIENTS ..	149
<i>Karolina Łopata, Iga Zdanowska, Magdalena Latos, Tomasz Jastrząb, Jagoda Różycka, Agnieszka Gorzkowska</i>	
<b>Chapter 14.</b> MEASUREMENT STATION FOR APD DIAGNOSTICS AND THERAPY CREATED AS PART OF THE "ASSIST MED SPORT SILESIA" PROJECT .....	161
<i>Michał Kręcichwost, Natalia Moćko, Agata Sage</i>	
<b>Chapter 15.</b> AUTOMATIC BLOOD VESSEL SEGMENTATION ALGORITHM IN ULTRAWIDE-FIELD FLUORESCEIN ANGIOGRAPHY .....	172
<i>Sławomir Siwek, Wojciech Więclawek</i>	
<b>Chapter 16.</b> IMPACT OF THE MULTI-WALL MWCNT CARBON NANOTUBES ON THE BIOCOMPATIBILITY OF MICRO AND NANOFIBERS OF COMPOSITE POLYCAPROLACTONE MATRIX .....	183
<i>Kornelia Jankowska, Marek J. Łos, Andrzej Hudecki, Jolanta Hybiak</i>	

## SPIS TREŚCI

<b>Rozdział 1: MODELOWANIE NUMERYCZNE STRĄCENIOWYCH WZORCÓW LIESEGANGA DLA GEOMETRII LINIOWEJ I RADIALNEJ.....</b>	<b>11</b>
<i>Jarosław Bobek, Andrzej Polański</i>	
<b>Rozdział 2: APLIKACJA WSPOMAGAJĄCA DIAGNOSTYKĘ I REHABILITACJĘ FUNKCJI POZNAWCZYCH OSÓB PO UDARACH Z ZESPOŁEM ZANIEDBYWANIA POŁOWICZEGO .....</b>	<b>24</b>
<i>Justyna Twardzik, Karolina Molik, Mariola Dylong, Magdalena Hoefmann, Aleksandra Szema, Julia Salinger, Piotr Wodarski, Joanna Bartnicka, Iga Garbowska, Jacek Jurkojć</i>	
<b>Rozdział 3: MODELOWANIE HIPERTERMII ONKOLOGICZNEJ Z ZASTOSOWANIEM RÓWNAŃ Z DWOMA CZASAMI OPÓŹNIENÍ .....</b>	<b>37</b>
<i>Mikołaj Stryczyński, Ewa Majchrzak</i>	
<b>Rozdział 4: SEGMENTACJA I TRÓJWYMIAROWA WIZUALIZACJA ZMIAN CHONDROMALACJI W NASADZIE GŁÓWKI KOŚCI UDOWEJ....</b>	<b>46</b>
<i>Weronika Żak</i>	
<b>Rozdział 5: ZASTOSOWANIE ROZMYTEJ METODY RÓŻNIC SKOŃCZONYCH W PROCESIE TRANSFERU MASY I CIEPŁA PODCZAS KRIOKONSERWACJI .....</b>	<b>56</b>
<i>Anna Skorupa, Alicja Piasecka-Belkhat</i>	
<b>Rozdział 6: OPTIMALIZACJA SCHEMATU DOBORU SYGNATUR W PROBLEMIE ZLICZANIA K-MERÓW .....</b>	<b>67</b>
<i>Marek Kokot, Sebastian Deorowicz</i>	
<b>Rozdział 7: USUWANIE ARTEFAKTÓW KOMPRESJI HISTOPATOLOGICZNYCH OBRAZÓW HE CAŁYCH TKANEK ...</b>	<b>79</b>
<i>Piotr Józwik-Wabik, Bartłomiej Gładys, Marek Hermansa, Dawid Macha, Seweryn Kalisz, Tomasz Strzoda, Paweł Foszner, Adam Popowicz, Michał Marczyk</i>	
<b>Rozdział 8: DETEKcja WARIANTÓW GENOMÓW W KONTEKŚCIE KOREKCJI ODCZYTÓW SEKWENCJONOWANIA.....</b>	<b>89</b>
<i>Maciej Długosz</i>	



<b>Rozdział 9: GRAFICZNA REPREZENTACJA HETEROGENICZNOŚCI ZBIORU RADIOGRAMÓW Z BAZY POLCOVID ZA POMOCĄ TECHNIKI UMAP .....</b>	<b>100</b>
<i>Marek Socha, Aleksandra Suwalska, Wojciech Prazuch, Michał Marczyk, Joanna Polanska, and POLCOVID Study Group</i>	
<b>Rozdział 10: WYKRYWANIE TKANKI NOWOTWOROWEJ NA OBRAZACH HISTOPATOLOGICZNYCH BARWIONYCH HE PRZY UŻYCIU METOD GŁĘBOKIEGO UCZENIA .....</b>	<b>115</b>
<i>Tomasz Strzoda, Seweryn Kalisz, Piotr Józwik-Wabik, Dawid Macha, Marek Hermansa, Bartłomiej Gładys, Adam Popowicz, Paweł Foszner, Michał Marczyk</i>	
<b>Rozdział 11: SYSTEM KLASYFIKACJI DANYCH OBRAZOWANIA MOLEKULARNEGO MALDI-MSI.....</b>	<b>126</b>
<i>Paweł Pendzialek, Joanna Polańska</i>	
<b>Rozdział 12: ANALIZA STRUKTURY KLONALNEJ NOWOTWORÓW – PORÓWNANIE WYNIKÓW RÓŻNYCH KOMBINACJI METOD</b>	<b>137</b>
<i>Paweł Kuś, Roman Jaksik, Marek Kimmel</i>	
<b>Rozdział 13: PROJEKTNEURO – KROK W KIERUNKU SKUTECZNEJ SPERSONALIZOWANEJ TERAPII PACJENTÓW NEUROLOGICZNYCH .....</b>	<b>149</b>
<i>Karolina Łopata, Iga Zdanowska, Magdalena Latos, Tomasz Jastrząb, Jagoda Różycka, Agnieszka Gorzkowska</i>	
<b>Rozdział 14: STANOWISKO POMIAROWE DO DIAGNOZY I TERAPII APD POWSTAJĄCE W RAMACH PROJEKTU „ASSIST MED SPORT SILESIA” .....</b>	<b>161</b>
<i>Michał Kręcichwost, Natalia Moćko, Agata Sage</i>	
<b>Rozdział 15: ALGORYTM AUTOMATYCZNEJ SEGMENTACJI NACZYŃ KRWIONOŚNYCH Z OBRAZÓW SZEROKOKĄTNEJ ANGIOGRAFII FLUORESCYJNEJ .....</b>	<b>172</b>
<i>Sławomir Siwek, Wojciech Więclawek</i>	
<b>Rozdział 16: WPŁYW DODATKU WIELOŚCIENNYCH NANORUREK WĘGLOWYCH MWCNT NA BIOKOMPATYBILNOŚĆ MIKRO I NANOWŁÓKIEN KOMPOZYTOWYCH O OSNOWIE POLIKAPROLAKTONU .....</b>	<b>183</b>
<i>Kornelia Jankowska, Marek J. Łos, Andrzej Hudecki, Jolanta Hybiak</i>	
<b>Streszczenie.....</b>	<b>193</b>

## PREFACE

The book covers the recent research and applied solutions in the area of computational oncology and personalized medicine, being the topic of the *Priority Research Area #1* (POB1) of the *Silesian University of Technology*. The chapters are the result of the research conducted by the staff of the Silesian University of Technology and cooperating partners of the socio-economic environment. It aims to present research results and interests and to exchange information on scientific activities related to the topics of POB1.

The idea behind the monograph is to promote the paradigm change from delayed reactive medical services to evidence-based Predictive, Preventive & Personalised Medicine (3PM / PPPM; [www.epmanet.eu](http://www.epmanet.eu)). We hope that this publication will help to spread the conducted research with the external scientific community.

The chapters of this book cover topics that are the response of the scientific community to the needs raised by clinical partners, including such up-to-date and critical research like solutions helping to fight against the COVID-19 pandemic. The presented research can be grouped in several frames:

**Medical image processing** (removing compression artefacts and tumour detection in histopathological images) and **segmentation** (angiography blood vessel segmentation; chondromalacia lesions of the femoral head).

**Bioinformatics** applications (genome sequencing; counting all substrings of specific length occurring in the set of input sequences; tumour subclonal reconstruction pipelines).

**Modelling in biomedicine:** bioheat transfer (in oncological hyperthermia and tissue cryopreservation) as well as modelling of reaction – diffusion – precipitation reactions.

**Classification systems** (head and neck cancer biopsy) and **visualization of the large datasets** (in chest X-ray imaging, in COVID-19 patients, that allows differentiating the covid patients).

**Personalized medicine** (effective personalized therapy in neurological patients) and **novel software** applied in rehabilitation (hemispatial neglect syndrome; measurement/diagnostic station for auditory processing disorders diagnosis and therapy).

The book ends with a chapter on **biomaterials research** (polymeric materials in regenerative medicine).

The publication of the book is one of the activities carried out by the *Silesian University of Technology*. It is published, among others, as a result of *The Excellence Initiative - Research University programme*. As one of ten Polish universities, *The Silesian University of Technology* obtained the status of a *research university* and commenced the implementation of the programme aimed at increasing its scientific excellence and international significance.

Editors would like to express their gratitude to the authors who have submitted their original research chapters as well as all the reviewers for their valuable comments. Your effort has contributed to the high quality of the book that we pass on to the readers.

We also hope that the book can also help to ignite a new, joint, interdisciplinary and challenging research and will lead to the implementation of novel diagnostic tools, drugs, therapies, etc. that could lead to an increase in life quality.

Sylwia Bajkacz  
Ziemowit Ostrowski  
Gliwice, September 2021

Jarosław BOBEK\*<sup>1</sup>, Andrzej POLAŃSKI<sup>1</sup>

## **Chapter 1. NUMERICAL MODELING OF THE LIESEGANG PRECIPITATION PATTERNS WITH LINEAR AND RADIAL GEOMETRIES**

### **1.1. Introduction**

Liesegang patterns are stripes, bands or rings [1] formed by moving fronts of chemical reactions. Processes involved in formation of Liesegang patterns are diffusion, reaction and precipitation. Liesegang patterns occur in many reactions/processes and can be seen in all types of media, hard substances, gels, liquids or gases. Due to variety of possible media and processes/scenarios Liesegang patterns are reported and researched in many systems in chemistry, geology, biology [2]. Occurrence of the Liesegang phenomenon requires at least two chemical reactants, called inner and outer electrolytes. Outer electrolyte, of higher concentration diffuses into the medium and reaction with inner electrolyte takes place. Under certain conditions precipitation of the reaction product then occurs leading to formation of layers of separate precipitates.

Formation of precipitation patterns [1, 3] in reaction – diffusion systems have always gained a lot of interest of researches, motivated both by challenges of experimental and modeling problems and wide range of potential applications. A very interesting and motivating recent application of precipitation phenomena is designing reaction – diffusion – precipitation processes for oscillatory drug release systems [4]. It can involve different chemical reagents and different geometries. Developing such systems poses several challenges. The first challenge is developing reliable mathematical/computational models of reaction – diffusion – precipitation reactions. The second one is using the developed model as a control system that allows obtaining desired

---

\* Corresponding author: jaroslaw.bobek@polsl.pl, Akademicka 16, 44-100 Gliwice, PL.

<sup>1</sup> Department of Computer Graphics, Vision and Digital Systems, Silesian University of Technology.

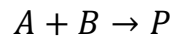
parameters of time and space distributions of concentrations. Finally, the third one is experimental validation.

In this paper we present a mathematical and computational model of reaction – diffusion – precipitation systems with linear and radial geometries. Our mathematical and computational system allows validations of reaction – diffusion – precipitation reactions modeling assumptions and fitting model parameters to data. In order to verify our modeling environment we use experimental data on formation of Liesegang patterns [5], [6-8]. We solve partial differential equations of reaction-difusion-precipitation processes by using discretization based on suitable 1D or 2D meshes. We confront computational predictions of percipitation patterns with experimental measurements by evaluating Matalon-Packter laws, i.e., laws concerning precipitation bands spacing, their time occurence and their widths.

In contrast to the literature, where only 1D Liesegang patterns are studied numerically, our research has led to creating a stable computational environment allowing predicting outcomes of both 1D and 2D diffusion – precipitation chemical reactions.

#### Chemical and mathematical model

Liesegang patterns are based on reaction process of two diffusing substances. The effect of reaction is stationary product which precipitate periodically in time. Basic reaction could be represented as



where:

A, B – inner/outer electrolyte

P – reaction product.

The inner electrolyte can be understood as substance equally distributed in the whole reaction system and the outer electrolyte as substance delivered from outside of reaction system.

So, the whole chemical process can be divided in three mainly operations [9]:

1. Diffusion of outer electrolyte into and inner electrolyte inside reaction system [10].
2. Precipitation of reaction product.
3. Agglomeration of diffusing substances on precipitated product.

The first one point is substance diffusion. In accordance to second Fick's law the diffusion equation for chemical system can be described as

$$\frac{\partial c}{\partial t} = D * \nabla^2 c$$

Simultaneously when substances concentration ratio exceeds critical value the precipitation process occurs. Important information is that whole product doesn't appear in same time. That process is stationary and can be described as

$$\frac{\partial c}{\partial t} = k_p * ([A] * [B] - K_{SO}) * \theta([A] * [B] - K_{SO})$$

where:

[A], [B] – concentration of substrates

$k_p$  – reaction rate constant

$K_{SO}$  – product solubility constant

$\theta(x)$  – Heaviside step function

The second point references to supersaturation theory [11] which is simplest method to describe precipitation of Liesegang rings. When substrates concentration ratio exceeds critical value the precipitation process occurs. That is one-way reaction – product doesn't dissolve into substrates.

To complete mathematical description of diffusion-precipitation-agglomeration system we need to provide agglomeration equation. First of all, the crystal product is needed because surrounding ions agglomerate on precipitated crystals. When substrates accumulate on crystal surfaces precipitation process still occurs so agglomeration process can be described as

$$\frac{\partial c}{\partial t} = \lambda * [A] * [B] * [P]$$

where:

[A], [B], [P] – concentration of substrates and product

$\lambda$  – aggregation rate

Summarizing all of equations (2), (3) and (4) whole model can be described as

$$\frac{\partial a}{\partial t} = D_a \nabla^2 a - k_p * (a * b - K_{SO}) * \theta(a * b - K_{SO}) - \lambda * a * b * p$$

$$\frac{\partial b}{\partial t} = D_a \nabla^2 b - k_p * (a * b - K_{SO}) * \theta(a * b - K_{SO}) - \lambda * a * b * p$$

$$\frac{\partial p}{\partial t} = k_p * (a * b - K_{SO}) * \theta(a * b - K_{SO}) + \lambda * a * b * p$$

which includes diffusion of inner and outer electrolyte, product precipitation and agglomeration (reducing concentration of substrates and increasing concentration of product) and product stationarity [12, 13].

Initial condition of substances concentration in system should be assumed as

$$\begin{aligned} a(x, 0) &= a_0 * \theta(x > 0 \& x < L) \quad \text{or} \quad a(x, 0) = a_0 * \theta(x < R) \\ b(x, 0) &= b_0 * \theta(x \leq 0 | x \geq L) \quad \text{or} \quad b(x, 0) = b_0 * \theta(x \geq R) \\ p(x, 0) &= 0 \end{aligned}$$

At the beginning there's no product, the inner electrolyte (a) is equally distributed in whole system and the outer electrolyte (b) is only outside of system.

Next point is to define boundary conditions. The outer electrolyte has to be continuously delivered into system. The product should never exit whole reaction environment such as inner electrolyte, but boundary condition for inner electrolyte is little more difficult. When product appears, it's behavior should be as boundary for inner electrolyte. It can be defined as high agglomeration rate but also high reaction rate constant [12, 14]. The general boundaries can be defined as

$$\begin{aligned} a(x == 0 | x == L, t) &= a_0 \\ \frac{\partial b(x == 0 | x == L)}{\partial x} &= 0 \\ \frac{\partial p(x == 0 | x == L)}{\partial x} &= 0 \end{aligned}$$

but also, important boundary named "moving boundary condition" [9, 12] which represents precipitating product at position  $x_n$  and at time  $t_n$  behaving as limit of system

$$b(x == x_n, t > t_n) = 0$$

where:

$x_n$  – appearing band position

$t_n$  – appearing band time

### *Geometry*

In experiments we tested one- (1D) and two-dimensional (2D) geometry [15]. In 1D system the assumption that length is much greater than width is needed. Hence, we can interpret the diffusion process as depending only on one coordinate. The concentration of inner electrolyte was equally distributed along reaction environment and outer electrolyte was delivered at both ends. For 2D geometry to minimize dependencies the circle geometry with same assumption of electrolytes distribution was prepared. 1D geometry was prepared with length parameter of the reaction area equal to 200 mm and 2D geometry was prepared with radius equal to 10 mm.

### *Mesh generation*

For generating 2D mesh was used Matlab implementation of the Delaunay triangulation algorithm with maximal edge length set to 0.25. Algorithm is based on linear geometric order. For 1D geometry reaction area length was divided into 0.1 mm fragments [15].

### *Computational method*

Calculations were made using Matlab R2020b software and more specifically using Partial Differential Equation (PDE) toolbox. The first step was to implement equations (5). PDE toolbox interpret equation as

$$m \frac{\partial^2 u}{\partial t^2} + d \frac{\partial u}{\partial t} - \nabla * (c \nabla u) + au = f$$

so, we can write (5) system as

$$\begin{aligned} 0 \frac{\partial^2 a}{\partial t^2} + 1 \frac{\partial a}{\partial t} - \nabla * (D_a \nabla u) + 0 * a \\ &= -k_p * (a * b - K_{SO}) * \theta(a * b - K_{SO}) - \lambda * a * b * p \\ 0 \frac{\partial^2 b}{\partial t^2} + 1 \frac{\partial b}{\partial t} - \nabla * (D_b \nabla u) + 0 * b \\ &= -k_p * (a * b - K_{SO}) * \theta(a * b - K_{SO}) - \lambda * a * b * p \\ 0 \frac{\partial^2 b}{\partial t^2} + 1 \frac{\partial b}{\partial t} - \nabla * (0 * \nabla u) + 0 * p \\ &= k_p * (a * b - K_{SO}) * \theta(a * b - K_{SO}) + \lambda * a * b * p \end{aligned}$$

In both geometries system of equation coefficients m, d, c, a and f are matrixes. For our setup the m parameter is equal 0, d is identity matrix, c is diagonal matrix of diffusion coefficients, a is equal 0 and f is no derivate dependent part.

### *Experimental model*

Experimental parameters were idealized to point precipitation of product in result of reaction-diffusion process. Initial value of substrates concentration was: 0.5 mol/dm<sup>3</sup> for outer electrolyte and 0.05 (0.1) mol/dm<sup>3</sup> for inner electrolyte in 1D system (2D) [15]. Boundary conditions were implemented as equations (7) and (8). 1D and 2D parameters are presented in Table 1.1. [5-8].



Table 1.1

## Experimental models' parameters

	1D model	2D model
Inner electrolyte diffusion coefficient	$1 * 10^{-3} [mm^2 * s^{-1}]$	$0.8 * 10^{-3} [mm^2 * s^{-1}]$
Outer electrolyte diffusion coefficient	$1 * 10^{-3} [mm^2 * s^{-1}]$	$1.2 * 10^{-3} [mm^2 * s^{-1}]$
Solubility constant	$3.5 * 10^{-5} [mol^2 * dm^{-6}]$	$3.5 * 10^{-3} [mol^2 * dm^{-6}]$
Reaction rate constant	$1 * 10^1 [dm^3 * mol^{-1} * s^{-1}]$	$1 * 10^1 [dm^3 * mol^{-1} * s^{-1}]$
Aggregation rate constant	$1 * 10^1 [dm^6 * mol^{-2} * s^{-1}]$	$1 * 10^1 [dm^6 * mol^{-2} * s^{-1}]$
Experiment time	$2 * 10^6 [s]$	86400 [s] (24 h)

*Results and discussion*

Using parameters described in Table 1.1., two models (1D and 2D) was tested and verified against Matalon-Packter law (spacing law), width law and time law. Both models are suitable to be good description of diffusion-precipitation-agglomeration system.

*1D model*

One dimensional model was predicated using described geometry and parameters to predict creation of rings. However, problem is only described on one coordinate, rings aren't noticeable – only where product precipitate.

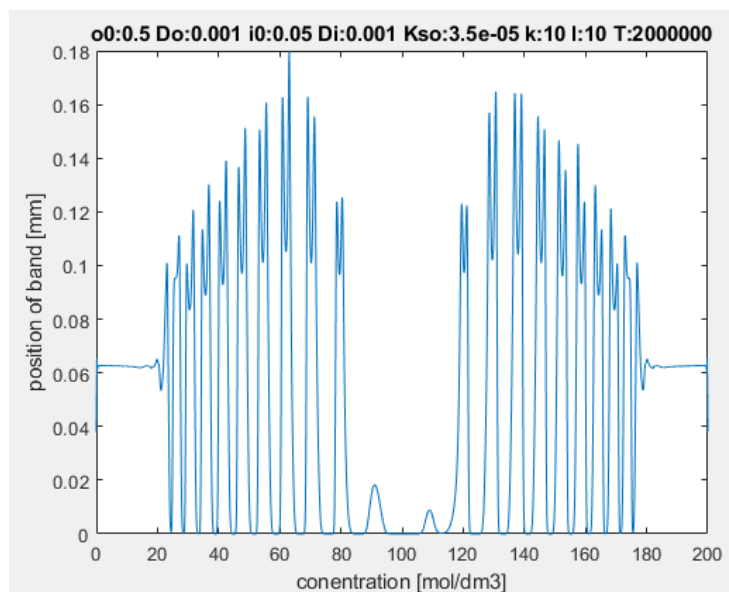


Fig. 1.1. Predicated bands with 1D model

Rys. 1.1. Wzorce przewidziane modelem 1D

Table 1.2

## Predicted bands in 1D model

band no.	position $X_n$ [mm]	width [mm]	time $T_n$ [s]
1	26.5	4.1	150000
2	30.8	4.8	200000
3	36.1	4.9	280000
4	41.8	4.9	360000
5	48.2	5.5	470000
6	55.1	5.7	610000
7	62.7	5.8	800000
8	71.1	6.1	1000000
9	80.7	6.3	1260000

Table 1.2 contains bands description seen on Fig. 1.1. That data was used to prove that model explain Liesegang rings, precipitating bands should fulfill spacing, time and width law (Matalon-Packter law). The time law is presented in Fig. 1.2 as linear dependency position of precipitating band against root precipitation time. The width law is presented in Fig. 1.3 as linear dependency position of precipitating band against width of this band. The spacing law can be simplest presented as linear dependency of band position difference against band position what is shown in Fig. 1.4.

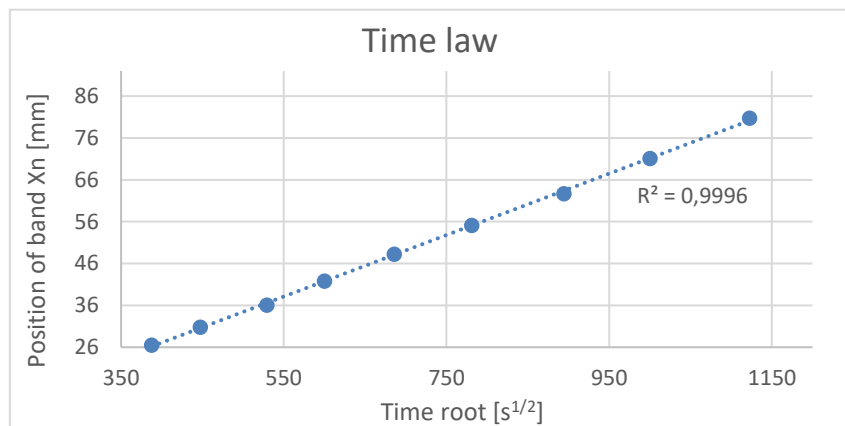


Fig. 1.2. Time law verification for 1D model

Rys. 1.2. Weryfikacja zależności odstępów czasowych dla modelu 1D

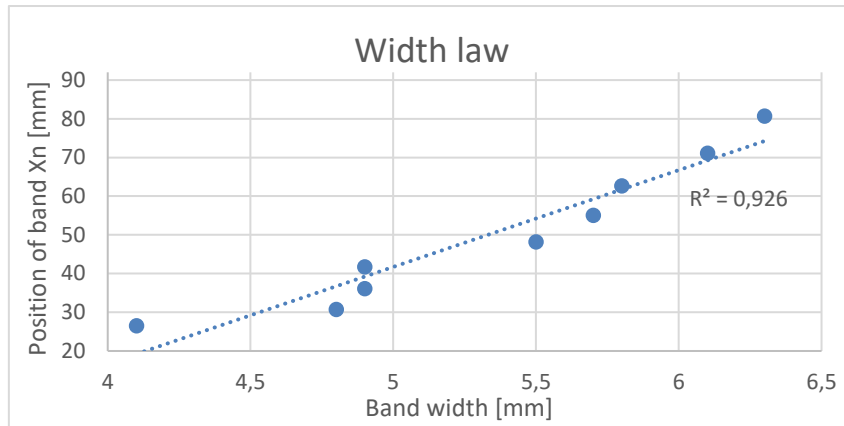


Fig. 1.3. Width law verification for 1D model

Rys. 1.3. Weryfikacja zależności grubości wzorców dla modelu 1D

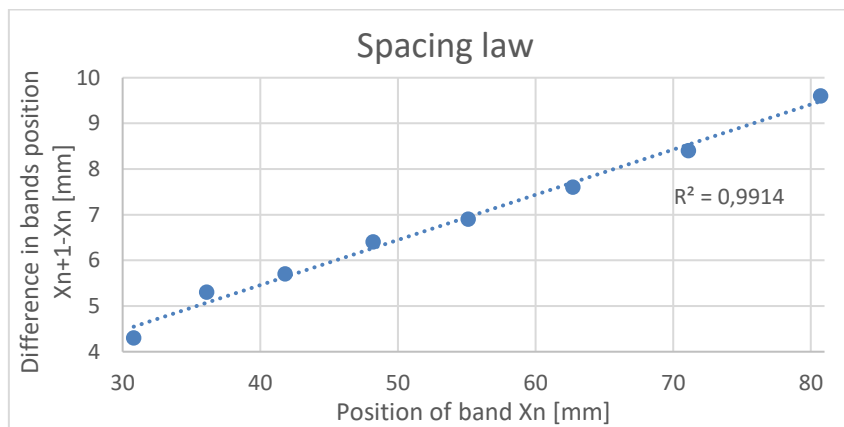


Fig. 1.4. Spacing law verification for 1D model

Rys. 1.4. Weryfikacja zależności odstępów między wzorcami dla modelu 1D

All three figures contains linear dependency. The R-square parameter informs about good data fir to linear function. Model can be interpreted as good description of precipitation Liesegang rings in one dimension.

### 2D model

Two dimensional model was analyzed by using described geometry and parameters to predict creation of rings. Diffusion process occurs in both x and y coordinates which makes whole prediction faster. It was needed to shorten experiment time. The used solubility rate constant is greater than in 1D model cause of higher initial concentration of substrates and to avoid local supersaturation. The diffusion coefficients have to differ from each other to avoid continously precipitation of product caused by process happening in both dimensions.

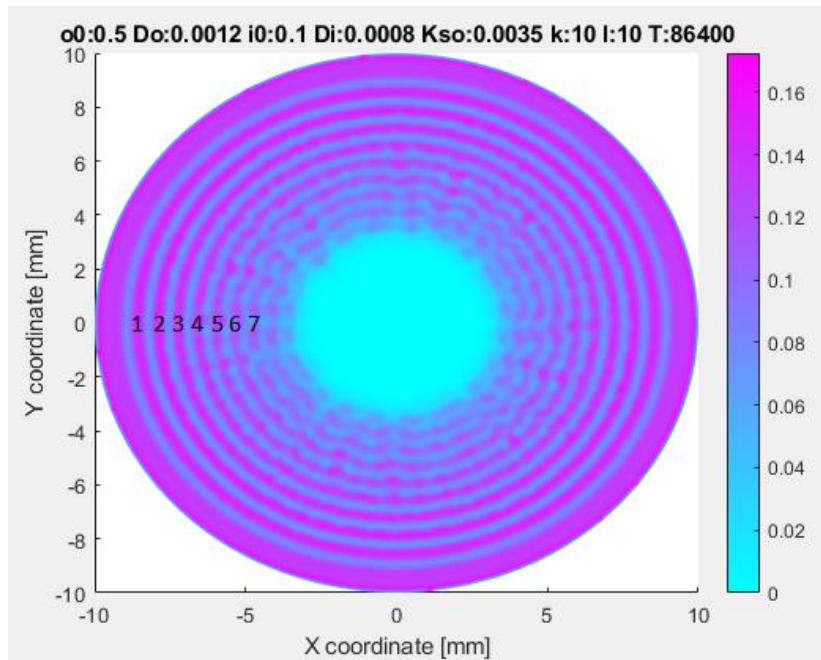


Fig. 1.5. Predicted bands in 2D model

Rys. 1.5. Wzorce przewidziane modelem 2D

Fig. 1.5 contains predicted rings in two dimensional circular geometry. The bands which can be interpreted as good precipitated product were marked. Outside precipitated product cannot be interpreted as ring because of high initial concentration of electrolytes. The seventh ring is not completely continuous but still can be interpreted as a ring since it is well visible. The inner bands cannot be interpreted as Liesegang ring because the concentration of product is low (may be not noticeable). In Table 1.3 parameters of precipitated bands with precipitation time are presented.

Table 1.3

Predicted bands in 2D model

band no.	position R [mm]	width [mm]	time [s]
1	8.54	0.4	840
2	7.87	0.4	1380
3	7.2	0.38	1980
4	6.58	0.35	2700
5	5.99	0.32	3540
6	5.43	0.31	4440
7	4.84	0.31	5520

Model was verified against time law (Fig. 1.6), width law (Fig. 1.7) and spacing law (Fig. 1.8). The model well describes the two-dimensional diffusion process – all laws verifications fits to linear dependency. Analogously to 1D model, values of R-square parameter were shown on figures.

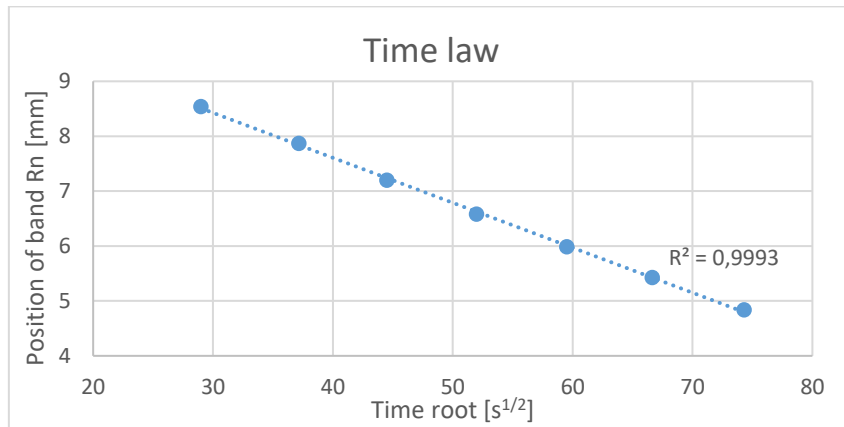


Fig. 1.6. Time law verification for 2D model

Rys. 1.6. Weryfikacja zależności odstępów czasowych dla modelu 2D

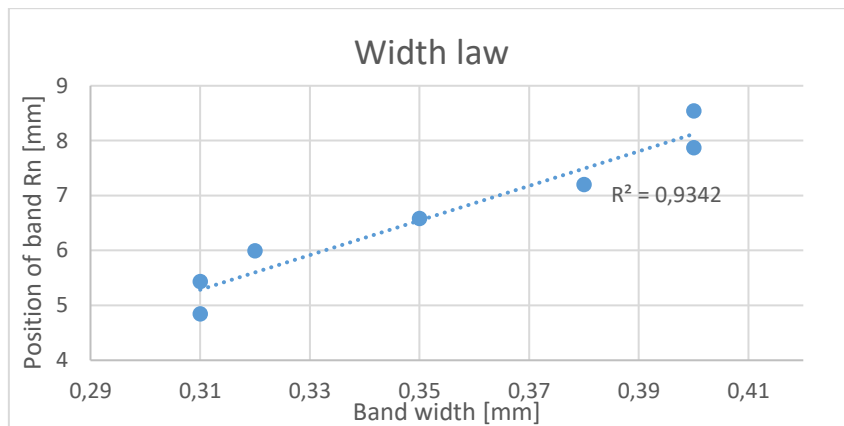


Fig. 1.7. Width law verification for 2D model

Rys. 1.7. Weryfikacja zależności grubości wzorców dla modelu 2D

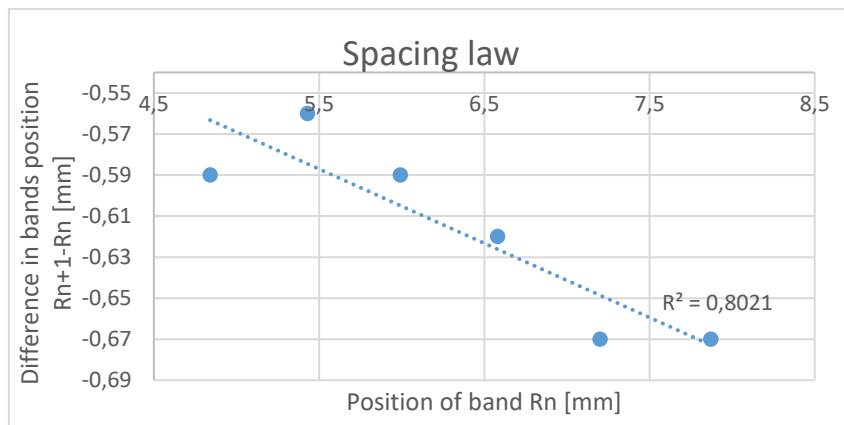


Fig. 1.8. Spacing law verification for 2D model

Rys. 1.8. Weryfikacja zależności odstępów między wzorcami dla modelu 2D

## 1.2. Conclusion

We have validated our diffusion – precipitation modeling procedures by predicting values of parameters of precipitation patterns, bands spacing, time occurrence of precipitation strips or rings and sizes of their widths. Parameters of the reactions obtained from the literature [5-8] were listed in Table 1.1 Predicted values versus experimental measurements are shown in Figures 1.2, 1.3, and 1.4 for 1D geometry and in Figures 1.6, 1.7 and 1.8 for 2D geometry of the reaction. One can see good correlation between predicted and measured values.

Our system is ready for further development concerning controlling times and shapes of precipitation patterns by boundary conditions.

## Bibliography

1. M.I.I.L. Hideki Nabika, „Pattern Formation in Precipitation Reactions: The”, Langmuir, tom 36, pp. 481-497, 2020.
2. E. Ramírez-Álvarez, F. Montoya, T. Buhse, W. Rios-Herrera, J. Torres-Guzmán, M. Rivera, G. Martínez-Mekler, M.F. Müller, „On the dynamics of Liesegang-type pattern formation in a gaseous system”, Scientific Reports, tom 6, nr 23402, 2016.
3. K.S. Jinxing Jiang, „Formation of Ultrathin Liesegang Patterns”, Langmuir, tom 32, pp. 9126-9134, 2016.
4. H. Ni, M. Pan, K. Shi, „Preparation of isometric Liesegang patterns and application in multi-pulsed drug release system”, J Sol-Gel Sci Technol, nr 91, pp. 216-224, 2019.
5. D. Granjon, O. Bonny, A. Edwards, „Coupling between phosphate and calcium homeostasis: a mathematical model”, Renal Physiology, nr 313, pp. F1181-F1199, 2017.
6. S.C.A. Das, „Tracer diffusion studies in the system phosphoric acid-disodium hydrogen phosphate-water by a radioactive method”, Radiation Physics and Chemistry, nr 45, pp. 773-778, 1995.
7. H.S. Harne, H.W. Parker, „The Diffusion Coefficient of Calcium Chloride in Dilute and Moderately Dilute Solutions at 25°”, Journal of the American Chemical Society, nr 77, pp. 265-266, 1955.

8. S. Recillas, V.R. Lugo, M.L. Montero, S. Viquez, „Studies on the precipitation behavior of calcium phosphate solutions”, *Journal of Ceramic Processing Research*, nr 13, pp. 5-10, 2012.
9. J. George, I. Paul, P.A. Varughese, G. Varghese, „Rhythmic pattern formations in gels and Matalon–Packter law: A fresh perspective”, *Pramana*, nr 60, p. 1259-1271, 2003.
10. J. Crank, *The Mathematics of diffusion*, Oxford: Oxford university press, 1975.
11. H.W. Morse, G.W. Pierce, „Diffusion and Supersaturation in Gelatine”, *Physical Review (Series I)*, nr 17, p. 129, 1903.
12. T. Antal, M. Drozd, J. Magnin, Z. Rácz, M. Zrinyi, „Derivation of the Matalon–Packter law for Liesegang patterns”, *The Journal of Chemical Physics*, nr 109, p. 9479, 1998.
13. A. Büki, É. Kárpáti-Smidróczki, K. Meiszel, M. Zrínyi, „Experimental and theoretical investigation of static and dynamic chemical pattern formations in gels”, *Gels. Progress in Colloid & Polymer Science*, nr 102, pp. 110-117, 1996.
14. M. Al-Ghoul, R. Sultan, „Front Propagation in Patterned Precipitation. 1. Simulation of a Migrating  $\text{Co}(\text{OH})_2$  Liesegang Pattern”, *The Journal of Chemical Physics*, nr 105, pp. 8053-8058, 2001.
15. H. Zhang, K. Zhan, Y. Chen, G. Chen, X. Zhou, J. Liu, M. Wu, H. Ni, „Three dimension Liesegang rings of calcium hydrophosphate in gelatin”, *Journal of Sol-Gel Science and Technology*, nr 71, pp. 597-605, 2014.

## **NUMERICAL MODELING OF THE LIESEGANG PRECIPITATION PATTERNS WITH LINEAR AND RADIAL GEOMETRIES**

### **Abstract**

We present a computational study of reaction – diffusion – precipitation systems for two types of geometries, linear and radial. The elaborated numerical procedures allow validations of reaction – diffusion – precipitation reactions modeling assumptions and fitting model parameters to data. We used results of our study for comparing computational predictions of the obtained precipitation patterns with experimental measurements. The main contribution of our research is creating a stable computational environment allowing predicting outcomes of both 1D and 2D diffusion – precipitation chemical reactions. One area of application of the elaborated computational

environment designing personalized, controlled drug release systems, where predicting/controlling shapes and positions of reaction fronts is of high importance.

**Keywords:** Reaction – diffusion systems, precipitation, Liesegang patterns, Drug release, Numerical modeling.



Justyna TWARDZIK<sup>1</sup>, Karolina MOLIK<sup>1</sup>, Mariola DYLONG<sup>1</sup>,  
Magdalena HOEFTMANN<sup>2</sup>, Aleksandra SZEMA<sup>1</sup>, Julia SALINGER<sup>1</sup>,  
Piotr WODARSKI<sup>1</sup>, Joanna BARTNICKA<sup>2</sup>, Iga GARBOWSKA<sup>3</sup>, Jacek JURKOJC<sup>1</sup>

## **Chapter 2. APPLICATION SUPPORTING COGNITIVE FUNCTIONS DIAGNOSTICS AND REHABILITATION OF PATIENTS AFFECTED BY AFTER-STROKE HEMISPATIAL NEGLECT SYNDROME**

### **2.1. Introduction**

The *hemineglect syndrome*, also known as *unilateral neglect* or *hemispatial neglect*, is a complication following an ischemic stroke or a disorder observed in the course of a brain tumor. Damage to the brain's structures contributes to the development of the disorder, but the exact cause of the disease is yet not fully understood.

The essence of this disorder is incorrect processing of information about the personal and extracorporeal space concerning the side opposite to the damaged hemisphere. Hemispatial neglect occurs most often, but not always, after damage to the right part of the brain, which means that a patient after a stroke of the right hemisphere ignores the existence of the left side of the body or the environment, and does not respond to stimuli acting on this side [1, 3, 7, 17]. Patients are not necessarily aware of their limitations in functioning and it significantly deteriorates their quality of life, making it very difficult to perform daily activities. Some of the symptoms of hemineglect syndrome (HS) are: one-sided unawareness or altered sensation of one's body - the patients may find their limbs unnecessary or ignore one side of the body during daily activities. This disorder manifests itself for example when the patient puts on only one sleeve, one shoe or shaves only half of the face. Other symptoms are: neglecting one side of the surrounding space

---

<sup>1</sup> Department of Biomedical Engineering, Silesian University of Technology.

<sup>2</sup> Department of Organization and Management, Silesian University of Technology.

<sup>3</sup> Department of Physiotherapy, Jerzy Kukuczka Academy of Physical Education in Katowice.

(e.g. seeing people in the field of view only on the right side), ignoring stimuli on the neglected side or unilateral akinesia, i.e. patient's failure to use the limbs on the left side despite the lack of paresis [8, 17].

### **2.1.1. The hemineglect syndrome diagnostics**

Isolated motor symptoms rarely constitute the basis for a diagnosis of unilateral neglect. The dynamics of symptoms has the greatest impact on the correct diagnosis of the disorder. Contact with the patient and analysis of their behavior are also important. A number of neuropsychological studies allow to obtain a complete picture of the disorder and link motor and perceptual abnormalities with the patient's imagination. That allows therapists to understand the way patients perceive their own body and environment [7, 17].

In the clinical picture of the disease, attention is paid to disturbances in the reproduction of visual or auditory sensations, as well as to the orientation towards external stimuli coming from the neglected side. The most frequently used diagnostic tool is the BIT, i.e. the Behavioral Inattention Test [16], or more precisely a shortened version of the BITC (Conventional Subtests of the Behavioral Inattention Test). This test consists of paper-and-pencil tasks of varying difficulty. The method includes tests of drawing, dividing lines, copying drawings or drawing from memory [15]. As a part of the copying test, the patient is asked to redraw a simple picture consisting of individual, smaller elements. A symptom that allows for presuming hemispacial neglect in a patient is redrawing only a part of the picture (Fig. 2.1). The search (cross-out) test (Fig. 2.2), in turn, consists of searching for stars of a given size by the person. Figure 2.2 shows an example of how this type of test was performed by a person with unilateral neglect syndrome. The principle of performing each of the above-mentioned tests is very similar. The patient visually searches for given symbols or objects on the board or marks their centers (as in the case of the line dividing test). Selected methods of diagnosing the hemispacial neglect syndrome are presented below [17].

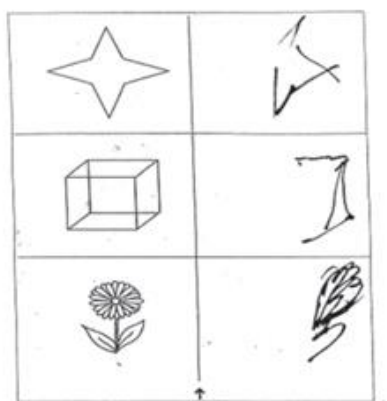


Fig. 2.1. Copy test [17]  
Rys. 2.1. Test kopiowania

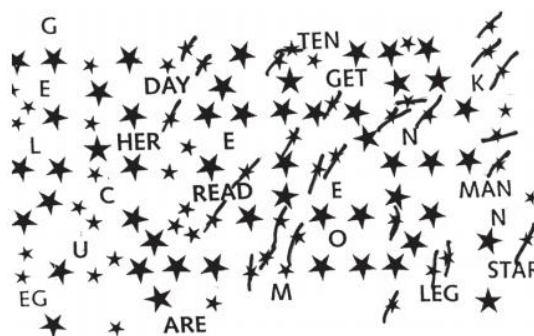


Fig. 2.2. Star search test [17]  
Rys. 2.2. Test wyszukiwania gwiazdek

### 2.1.2. Conventional rehabilitation of the hemineglect syndrome

The rehabilitation of people after strokes should be multidisciplinary. It is important that the rehabilitation team consists of people with different specializations, including a doctor, physiotherapist, orthopedist, neuropsychologist, speech therapist and a nurse. Rehabilitation of patients diagnosed with unilateral neglect should be started as soon as possible. The aim of rehabilitation is to restore total or partial efficiency, as well as to prevent the effects of long-term immobilization and reduce the risk of abnormal (pathological) motor patterns [2, 4, 10, 14]. The therapy of people with spatial hemineglect should make the patient aware of the existing attention deficit, as greater awareness of the disease increases the patient's motivation [11]. In the treatment of people with hemineglect syndrome, in addition to the principles used in traditional post-stroke rehabilitation, emphasis is placed on the use of visual and acoustic stimuli, stimulating and encouraging the use of limbs on the neglected side - symmetrical activation of the limbs, as well as exteroceptive stimulation, i.e. providing tactile stimuli, massages and muscle stimulation with low-frequency currents (FES). An important aspect in rehabilitation is also the use of Kabat proprioceptive priming and Bobath stimulation, the use of sensory modulation techniques, vestibular stimulation, reference to remembered motor experiences and the use of psychological compensation techniques, including: lateral signaling, rehabilitation of attention disorders and visual coordination - computer-assisted movement or visual-spatial searching training [11-13]. In addition, general methods used in post-stroke rehabilitation, such as the method of forced movement (CIMT) and the same methods as in diagnostics, are used in the

rehabilitation of people with hemineglect syndrome, e.g. copying patterns, reading texts, arranging puzzles or finding differences in pictures [17].

### **2.1.3. Rehabilitation of the hemineglect syndrome using VR technology**

Due to computer technology development and the possibilities offered by VR technology, the use of virtual reality in rehabilitation of people with hemispatial neglect syndrome has become the subject of many studies. Numerous applications use multisensory stimulation, which is extremely beneficial in the rehabilitation of the disorder. Additionally, all solutions use an uncomplicated, low-detail VR environment that does not distract the patient. Most often, in VR rehabilitation games, we can find pointing to or searching for specific elements on a virtual stage, as well as additionally moving them to specific places. One of the most popular solutions used in the rehabilitation of side skipping is the use of the urban environment, where the patient's task is to cross the road to the other side of the road [5, 6, 9]. The difficulty of the task is the movement of cars and, in some cases, pedestrians. Depending on the application, the difficulty level is adjustable, and the games use various tips in the form of car headlights or a horn. However, there are few applications with highly realistic graphics that increase patient involvement in therapy and translate into improved outcomes. In addition, not all scenarios are similar to everyday activities - some of them are quite abstract, which can make it difficult for the patient to understand the rules of the game and reduce his involvement.

The use of virtual reality in the treatment of HS can be beneficial in many respects. Unlike conventional diagnostic methods, VR methods allow therapists to monitor the patient's behavior in dynamic activities involving many senses at the same time. An example would be a simulation of driving a car or walking in a park. The advantage of VR methods is also the possibility of recording the movement of the eyeballs, limbs and head, as well as recording and analyzing the patient's reaction to stimuli. This can significantly facilitate rehabilitation, as it is then possible to adapt the VR application to the patient and to the degree of his disability.

### *Rehabilitation of motor functions*

Rehabilitation of motor functions with the use of virtual reality takes place by introducing an avatar figure into an artificially generated image, which the patient can control through gestures and movement of the whole body. Performing activities in the virtual world translates into the improvement of optimal movement patterns in everyday life, as well as the performance of movements similar to natural ones during exercise. The scenarios which are present during the rehabilitation session would not be possible in the real world. The advantage of rehabilitation with the use of VR is the variety of activities, as well as repeatability, which does not significantly affect the patient's fatigue. Depending on the severity of the disease, the therapist individually selects the intensity and type of training, and can also adjust other game parameters, such as location of the stimulating element depending on the position of the head. The patient's results along with the relevant examination parameters are recorded in a numerical manner, which allows the progress of rehabilitation to be monitored. A patient who has a problem with moving a limb, seeing it artificially generated in virtual reality, is activating the mirror neurons, which stimulate the mechanisms of neuroplasticity. Thanks to this process, it is possible to rebuild the damaged structures of the pyramidal system in the brain

### *Rehabilitation of cognitive functions*

Virtual reality allows stimulating everyday life situations and it helps to exercise cognitive functions. The patient obtains real-time feedback, with no physical consequences of the made mistakes. The advantage of this training is simplicity and intuitiveness, which is necessary due to the limited acquisition of new skills by patients.

#### **2.1.4. Examples of existing VR solutions dedicated to the unilateral neglect rehabilitation**

There are currently many devices on the market that support the rehabilitation of patients using virtual reality technology. Among them are those that help to recover stroke patients, as well as people with hemiplegia. An example of such a system can be NIRVANA [19]. It is a virtual reality based medical device, specially designed to support physical and cognitive rehabilitation in patients with neuromotor and neurological disorders such as stroke, cerebral palsy, Parkinson's disease or autism. This

system creates projections of the environment on a flat surface, wall or floor, allowing the patient to completely immerse himself in the virtual world. Importantly, this device does not require the use of additional elements on the patient's body, such as HMD goggles or markers. Another example is MYRO [18], in which, as in NIRVANA, there is no need for any auxiliary devices. Myra, the therapeutic panel was created with the aim of computer-assisted, motor and cognitive therapy of the upper limb. The device is used in typical occupational therapy and physiotherapy. The movements of the upper limb, repeated in the available exercises, provide internal and external stimulation and strengthen the neuroplasticity that modifies the central nervous system to restore lost functions. Another example of a system used during rehabilitation is Rewellio [20], a device based on a combination of virtual reality technologies (using HMD goggles) and a hand tracking system to stimulate the rehabilitated areas of the brain. Rewellio supports the therapy with a variety of engaging VR games. However, despite the wide selection of technological solutions designed for rehabilitation, it can be easily seen that most of them are dedicated to physiotherapy centers. However, there are no solutions that would be available to a wide audience, enable systematic rehabilitation at home and promote exercises under the supervision of a qualified physiotherapist. This gap in the market could be filled by an application that is affordable and technologically intuitive to use and has clear instructions, tailored to the needs of older patients.

The analysis of market and scientific works covering similar themes, it has been found that there is a need for further research into the use of VR in the rehabilitation of hemispatial neglect. The aim of the study is to develop indications for the diagnosis and rehabilitation of cognitive functions of people affected by hemispatial neglect using virtual reality technology and to prepare a VR application that would allow verification and correction of the adopted indications.

## **2.2. Methodology**

The correct implementation of the therapeutic application requires a proper indication of the patient's needs. As the hemispatial neglect syndrome most often accompanies injuries occurring in the right hemisphere of the brain, dysfunction is observed in the area of its action in patients with HS. Table 2.1 shows the specific tasks performed by both hemispheres of the brain.

It is common that damage to the right hemisphere is accompanied by paresis of the left side of the body, which makes recovery difficult. In addition, people with unilateral skipping syndrome require rehabilitation tailored to their needs, which takes into account the inability to perform the task with functions controlled by the healthy hemisphere. As a result of damage to the center responsible for abstract thinking and creativity, patients are focused on performing tasks and precise thinking, which means that messages and instructions must be formulated in a simple and intuitive way, and should take into account the specificity of the reception of information by the undamaged hemisphere and brain centers. In the rehabilitation of HS, it is extremely important to maximize the stimulation of the side neglected, i.e. the use of more stimuli acting on the side opposite to the damage.

Table 2.1

Tasks performed by different hemispheres of the brain	
Left hemisphere	Right hemisphere
proves the right side of the body	shows the left side of the body
remembers information given verbally, digitally	remembers information provided vividly
analysis	synthesis
works sequentially	operates globally
solves tasks	produces dreams
remembers facts, grammar, spelling	differentiates between colors
	understands metaphors

This stimulation can occur through the use of a blinking light source, moving elements or objects changing color. Importantly, the delivered stimuli must be strong and unexpected in order to attract the patient's attention. An example of such a stimulus may be putting the rehabilitated person in a virtual threat situation coming from the neglected side of the body. However, it should be noted that the excess of sounds used in the program will distract the patient. Applications used as part of rehabilitation should be adapted, as far as possible, to the rehabilitated person in terms of gender, age or interests. The formulated tasks should also be similar to the daily activities or related to the

patient's profession, which arouses the patient's motivation and interest in the therapy. In addition, an important aspect when designing such systems is influencing the feelings and emotions of people with HS, for example by using the images of relatives or using a reward system other than points.

### **2.2.1. Indications for the VR application**

In response to the presented needs of people struggling with hemineglect syndrome, indications were formulated, on the basis of which the designed application was created. According to them, the designed rehabilitation system should use immersive reality, allowing for a high level of player's immersion in the virtual world, and thus deepening his involvement in rehabilitation. Motivating goals and challenges, emotional impact, tasks similar to daily activities, and a realistic scene are also factors that increase the patient's enthusiasm for exercise. The use of familiar environments, behaviors and tasks reduces stress for the patients as well as prevents their discouragement in the initial stages of exercise. Due to special requirements of people with damaged one hemisphere of the brain, usually the right one, tasks and messages must be clearly formulated, preferably step by step. Moreover, it is worth to use multisensory cues, sound and visual effects in the application, which allow patients to perform tasks or draw their attention to a given element of the game, especially on the neglected side. What is important, the rehabilitation of neglected side should be performed as frequently as possible to bring the desired effect. An important aspect is also a feedback, that is informing the patient about correctly or badly performed tasks and progress in recovery. When creating a VR application for the rehabilitation of HS, it should be remembered that this rehabilitation should also include the features of conventional post-stroke therapy. So, an important aspect is the involvement of the body limbs, which can improve motor skills and increase patient's awareness of the body parts affected by the disorder, which also contributes to the effectiveness of rehabilitation. The last two important factors when designing an application that potentially would be widely accessible to individuals struggling with varying degrees of cerebral impairment and facing multiple disabilities, are personalization, as well as accessibility and ease of use. Personalization of the application will allow the therapist or the patient who exercises at home to adjust the parameters of the game, e. g. the frequency of generated stimuli, to their capabilities and desired pace. The use of personalized tasks may also allow using the application in both,



initial and final phase of the exercises. Thanks to the use of virtual reality it is possible to personalize the application according to the age and condition of the patient. The simple interface and uncomplicated operating system will allow the game to be used by patients of any age.

### **2.2.2. Description of the created application**

As part of the work, two applications were created using the Visual Studio environment and the Unity environment.

As part of the first application, the workshop scenery was prepared for men (Fig. 2.3). The scenery shows the actual conditions in the room, but with less detail. In front of the player there is a table with tools and shelves above it. The second application contains a scenery depicting a room equipped with a dressing table with various women's items such as lipstick or a brush (Fig. 2.4). It is dedicated to women and created in such a way that it resembles everyday life as much as possible.

The patient's task is to find the appropriate items and place them on the shelf according to clearly defined voice instructions. Both scenes in the applications have been selected in such a way that they are as close as possible to typical interests depending on gender. Thanks to the use of tasks similar to everyday activities, patients may feel more sense in carrying them out, because they are aware that they are doing something useful. A particle emitter is used to increase attention to the object and where it is to be placed. Thanks to this, the patient, apart from the voice message, receives an additional hint that allows him to notice objects on the omitted side. The places where the patient is to place the item have been deliberately placed in such a way that the patient has to make greater ranges of movement, which promotes his convalescence. The tasks proposed as part of rehabilitation were performed in such a way as to stimulate the neglected side to the maximum. In line with the previously mentioned assumptions, the player uses VR goggles to experience the feeling of being immersed in the virtual world as much as possible. The game also uses tasks similar to everyday activities, matched in terms of gender to the patient, and the entire scenery reflects the realism of the rooms on which it is modeled. The whole thing is accessible to patients from a different age group and easy to use.



Fig. 2.3. Scenery for men – a garage

Rys. 2.3. Sceneria dla mężczyzn – garaż



Fig. 2.4. Scenery for women – a dressing table

Rys. 2.4. Sceneria dla kobiet – toaletka

During the entire examination, the location of objects and the patient's head are recorded, as well as the time of performing the tasks. Thanks to this, it is possible to determine the speed of executing commands and the trajectory of movement of the head and hands. The obtained parameters make it possible to compare and evaluate the progress of rehabilitation.

### 2.3. Summary

Hemineglect syndrome is a neurological disorder which is a complication of brain stroke, significantly worsening the quality of patients' daily life. This disorder significantly affects the performance of even the simplest everyday activities, which is why it is so important to undertake appropriate rehabilitation.

There is a wide range of VR applications for people who have suffered ischemic strokes, but very few of them are intended directly for the rehabilitation of hemineglect syndrome. Moreover, the existing systems are dominated by the commercial aspect and are not sufficiently adapted to the needs of patients. There is a noticeable need to develop new rehabilitation methods, including those using VR technology - the advantages of such a solution include its mobility and the possibility of using it at home. When creating an application which supports the rehabilitation of HS, it is necessary to recognize the nature of the problem thoroughly. The specific symptoms of unilateral neglect require careful development of the app concept as well as its adaptation to patients' needs. Numerous research steps should also be undertaken. The application designed in this work can be further developed, and the next step will be to conduct measurements of upper limb kinematics and trunk as well as head orientation of healthy subjects. These examinations will be aimed at determining movement patterns so as to expand the possibilities of using the application towards supporting diagnostics of patients. Expanding the functionality of the software may also be positively influenced by increasing possibility of personalization, as well as extending it with new tasks and introducing a diagnostic element.

### **Acknowledgements**

The research reported in this paper was co-financed by the European Union from the European Social Fund in the framework of the project "Silesian University of Technology as a Center of Modern Education based on research and innovation" POWR.03.05.00-00-Z098/17

### **Bibliography**

1. Domańska Ł.: Zespół pomijania stronnego. [W:] Herzyk A., Kądziaława D. (red.): Zaburzenia w funkcjonowaniu człowieka z perspektywy neuropsychologii klinicznej. UMCS, Lublin 1996, s. 151-174.
2. Gleinert M.: Terapia wymuszonego ruchu - historia, główne założenia i perspektywa na przyszłość, *Ann. Acad. Med. Gedan.*, 2016, 46, s. 75-80.
3. Heilman K.M., Bowers D., Valenstein E., Watson R.T.: Hemispace and hemispatial neglect. [W:] M. Jeannerod (red.): *Neurophysiological and neuropsychological aspects of spatial neglect*, Amsterdam: Elsevier, 1987, p. 115-144.

4. Jaracz K., Kozubski W. (red.): *Pielęgniarstwo neurologiczne. Podręcznik dla studiów medycznych*. Wydawnictwo Lekarskie PZWL, Warszawa 2008.
5. Katz N., Ring H., Naveh Y., Kizony R., Feintuch U., Weiss P. L.: Interactive virtual environment training for safe street crossing of right hemisphere stroke patients with unilateral spatial neglect, *Disability and Rehabilitation*, 2005, 27(20), p. 1235-43.
6. Kim J., Kim K., Kim D.Y., Chang W.H., Park C.I., Ohn S.H., Han K., Ku J., Nam S.W., Kim I.Y., Kim S.I.: Virtual environment training system for rehabilitation of stroke patients with unilateral neglect: crossing the virtual street, *Cyberpsychol Behav*, 2007,10(1), p. 7-15.
7. Kułakowska A., Halicka D., Kapica-Topczewska K., Drozdowski W.: Percepcyjny wariant zespołu zaniedbywania jednostronnego w następstwie udaru niedokrwienego mózgu – opis przypadku, *Aktualn Neurol*, 2006, 6 (3), s. 175-180.
8. Mesulam M.-M.: The multiplicity of neglect phenomena. *Neuropsychological Rehabilitation*, 4, 1994, p. 173-176.
9. Navarro MD., Lloréns R., Noé E., Ferri J., Alcañiz M.: Validation of a low-cost virtual reality system for training street-crossing. A comparative study in healthy, neglected and non-neglected stroke individuals, *Neuropsychol Rehabil*, 2013, 23(4), p. 597-618.
10. Opara J.: Nowoczesna rehabilitacja poudarowa – co to znaczy, s. 29-42.
11. Polanowska K., Seniów J.: W poszukiwaniu metod rehabilitacji chorych z zespołem zaniedbywania – przegląd zagadnień. *Rehabil. Med.*, 2005; 9(4), s. 14-23.
12. Robertson I.H., Hogg K., McMillan T.M.: Rehabilitation of unilateral neglect: Improving function by contralesional limb activation. *Neuropsychol. Rehab.*, 1998, 8(1), p. 19-29.
13. Seniów J., Polanowska K.: Motoryczny wariant zespołu zaniedbywania jednostronnego w następstwie uszkodzenia mózgu. *Neurol. Neurochir. Pol.*, 2005; 39(2), s. 141-149.
14. Siwik P., Osowska A., Przepióra-Rusak I.: Wpływ występowania Zespołu Zaniedbywania Jednostronnego na wczesną rehabilitację pacjentów po udarze mózgu, *Pol. Ann. Med.*, 2008, 15(1), s. 43-50.
15. Wieczorek D., Jodzio K.: Propozycja kompleksowej diagnozy objawów pomijania stronnego u osób z uszkodzeniem mózgu, *Studia Psychologiczne*, 2002, 40(4), s. 151-171.
16. Wilson B., Cockburn J., Halligan P.: Development of a behavioural test of visuo-spatial neglect, *Archives of Physical Medicine*, 1987, 68, p. 98-102.

17. Wojtan A., Wojtan S.: Charakterystyka zespołu zaniedbywania połowiczego; specyfika opieki pielęgniarstwa, Problemy pielęgniarstwa, 2009, s. 132-138.
18. <https://technomex.pl/nowoczesna-neurorehabilitacja-rehabilitacja-neurologiczna/tyromotion/myro> [date of access: 20.11.2020].
19. <https://www.btsbioengineering.com/nirvana/discover-nirvana/> [date of access: 17.12.20].
20. <https://rewellio.com/> [date of access: 17.12.2020].

## **APPLICATION SUPPORTING COGNITIVE FUNCTIONS DIAGNOSTICS AND REHABILITATION OF PATIENTS AFFECTED BY AFTER-STROKE HEMISPATIAL NEGLECT SYNDROME**

### **Abstract**

The hemineglect syndrome is a neurological disorder that affects mostly post-stroke patients. As a result of damage to the right brain hemisphere, the patient's perception of own body and environment on the left side becomes disturbed. It is especially important to introduce a multidisciplinary rehabilitation as soon as possible. Developing virtual technology may be helpful since it is able to provide a highly realistic scenery that will engage the patient to participate in therapy. The created application meets indications that have been carefully formulated, based on detailed literature data analysis.

**Keywords:** hemispacial neglect, virtual reality, rehabilitation, unilateral neglect, ischemic stroke.

Mikołaj STRYCYŃSKI\*<sup>1</sup>, Ewa MAJCHRZAK<sup>1</sup>

## **Chapter 3. MODELING OF ONCOLOGICAL HYPERTHERMIA USING DUAL-PHASE LAG EQUATIONS**

### **3.1. Introduction**

Oncological hyperthermia is a method of complementary treatment of neoplastic diseases which consists in the targeted application of thermal energy in the treatment of cancer. It is a method supporting chemotherapy and radiotherapy [1-4]. Modeling of hyperthermia allows one, among others, to determine the power density of external heating and the duration of the procedure, which will ensure the destruction of cancerous tissues.

In this work, a single blood vessel and surrounding biological tissue with a tumor region is considered. The temperature distribution is described by the system of dual-phase lag equations (DPL) [5-8] supplemented by the boundary and initial conditions. The effect of the heating technique (e.g. ultrasound, microwave, etc.) is taken into account by introducing the source function  $Q_{ext}$  into the equation describing the temperature distribution in the tumor region [9]. When the heating time  $t_{ext}$  is achieved, the source function  $Q_{ext}$  is equal to zero. The absorbed total energy density  $Q_{ext} t_{ext}$  is kept constant, but different heating schemes (heating power density  $Q_{ext}$  and heating duration) are considered. The formulated problem is solved using the implicit scheme of the finite difference method. To estimate degree of the tumor destruction the Arrhenius integral is used [10-13].

---

\* Corresponding author: mikolaj.stryczynski@polsl.pl, ul. Konarskiego 18a, 44-100 Gliwice, Poland.

<sup>1</sup> Faculty of Mechanical Engineering, Silesian University of Technology.

### 3.2. Mathematical model

A single blood vessel and surrounding biological tissue with a tumor region, as shown in Figure 3.1, is considered (axisymmetric problem).

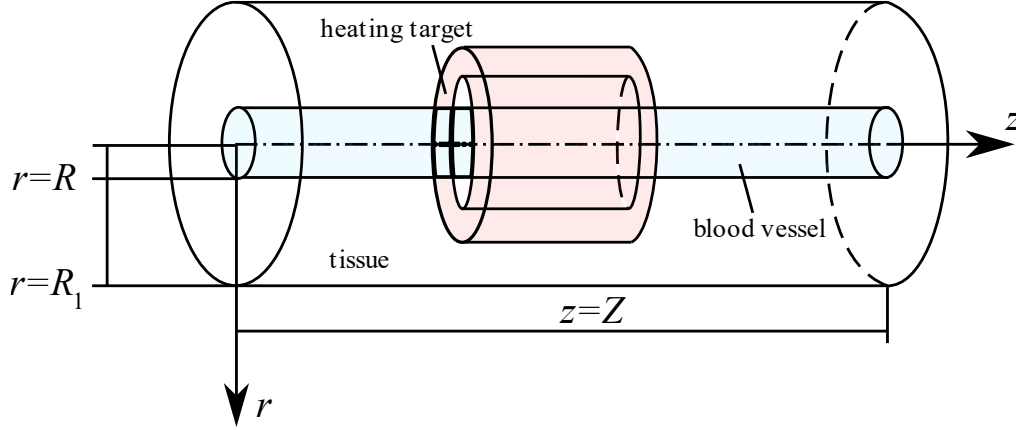


Fig. 3.1. Domain considered  
Rys. 3.1. Rozpatrywany obszar

Blood temperature is described by the equation [5]

$$(r, z) \in \Omega_1: \quad c_b \rho_b \left( \frac{\partial T_b}{\partial t} + v \frac{\partial T_b}{\partial z} + \tau_{qb} \frac{\partial^2 T_b}{\partial t^2} + \tau_{qb} v \frac{\partial^2 T_b}{\partial t \partial z} \right) = \lambda_b \nabla^2 T_b + \tau_{Tb} \lambda_b \frac{\partial (\nabla^2 T_b)}{\partial t} + Q_{metb} + \tau_{qb} \frac{\partial Q_{metb}}{\partial t} \quad (1)$$

where

$$\nabla^2 T_b = \frac{1}{r} \frac{\partial}{\partial r} \left( r \frac{\partial T_b}{\partial r} \right) + \frac{\partial^2 T_b}{\partial z^2} = \frac{1}{r} \frac{\partial T_b}{\partial r} + \frac{\partial^2 T_b}{\partial r^2} + \frac{\partial^2 T_b}{\partial z^2} \quad (2)$$

and  $c_b$  is the specific heat of blood,  $\rho_b$  is the mass density of blood,  $\lambda_b$  is the thermal conductivity of blood,  $v$  is the blood flow velocity in the axial direction,  $\tau_{Tb}$  is the thermalization time,  $Q_{metb}$  is the metabolic heat source, while  $T_b = T_b(r, z, t)$  is the blood temperature,  $r, z$  are the spatial coordinates and  $t$  denotes the time.

Temperature field in the tissue with a tumor is described by equation

$$(r, z) \in \Omega_2 \cup \Omega_3: \quad c_p \left( \frac{\partial T}{\partial t} + \tau_q \frac{\partial^2 T}{\partial t^2} \right) = \lambda \nabla^2 T + \lambda \tau_T \frac{\partial (\nabla^2 T)}{\partial t} + Q + \tau_q \frac{\partial Q}{\partial t} + Q_{ext} + \tau_q \frac{\partial Q_{ext}}{\partial t} \quad (3)$$

where

$$Q = w_b c_b (T_a - T) + Q_{met} \quad (4)$$

and  $c$  is the specific heat,  $\rho$  is the mass density,  $\lambda$  is the thermal conductivity,  $\tau_q$  is the relaxation time,  $\tau_T$  is the thermalization time,  $w_b$  is the blood perfusion rate,  $T_a$  is the arterial blood temperature,  $Q_{met}$  is the metabolic heat source,  $Q_{ext}$  is the source function associated with the external heating (heating power density) and  $T = T(r, z, t)$  is the tissue temperature. It should be noted that the same values of thermophysical parameters for tumor region and healthy tissue are assumed here.

Only the tumor sub-domain is heated, hence

$$(r, z) \in \Omega_3 : Q_{ext} = Q_{ext}(r, z, t) = \begin{cases} Q_0, & t \leq t_{ext} \\ 0, & t > t_{ext} \end{cases} \quad (5)$$

where  $t_{ext}$  is the exposure time, while  $Q_0$  is a constant value.

On the contact surface between blood vessel and biological tissue the continuity condition of temperature and heat flux is assumed

$$(r, z) \in \Gamma_c : \begin{cases} T_b = T \\ q_b = q \end{cases} \quad (6)$$

On the outer surface of the tissue the constant temperature (body core temperature) is accepted. For  $z = 0, z = Z$  the no-flux conditions are assumed.

The initial conditions are also known [5]

$$t = 0 : T_b = T = T_p$$

$$\left. \frac{\partial T_b}{\partial t} \right|_{t=0} = \frac{Q_{metb}}{c_b \rho_b}, \quad \left. \frac{\partial T}{\partial t} \right|_{t=0} = \frac{w_b c_b (T_a - T_p) + Q_{met}}{c \rho} \quad (7)$$

Tissue damage can be estimated on the basis of the so-called Arrhenius integral [13]

$$A(r, z, t^F) = P \int_0^{t^F} \exp\left(-\frac{E}{RT(r, z, t)}\right) dt \quad (8)$$

where  $P$  is the pre-exponential factor,  $E$  is the activation energy,  $R$  is the universal gas constant ( $R = 8.314472$ ),  $T$  is the temperature in Kelvin and  $t^F$  is the end time of analysis. A value of damage integral  $A(r, z, t^F) = 1$  corresponds to a 63% probability of cell death at a specific point  $(r, z)$ , while  $A(r, z, t^F) = 4.6$  corresponds to a 99% probability of cell death at this point.

The problem formulated is solved using the implicit scheme of the finite difference method. The details are presented in [5-7].



### 3.3. Results of computations

The thermally significant blood vessel of dimensions  $R = 0.001$  m,  $Z = 0.02$  m is considered. The blood flow velocity is equal to  $v = 0.2$  m/s. The heating target volume is specified as  $0.0015$  m  $\leq r \leq 0.0025$  m and  $0.005 \leq z \leq 0.015$ . The following values of thermophysical parameters are assumed: thermal conductivities  $\lambda_b = 0.488$  W/(mK),  $\lambda = 0.5$  W/(mK), specific heats  $c_b = 3770$  J/(kgK),  $c = 4000$  J/(kgK), mass densities  $\rho_b = 1060$  kg/m<sup>3</sup>,  $\rho = 1000$  kg/m<sup>3</sup>, metabolic heat sources  $Q_{met\ b} = Q_{met} = 245$  W/m<sup>3</sup>, blood perfusion rate  $w_b = 0.5$  kg/(m<sup>3</sup>s), arterial blood temperature  $T_a = 37^\circ\text{C}$  [5], relaxation times  $\tau_{qb} = \tau_q = 3$  s and thermalization times  $\tau_{Tb} = \tau_T = 1$  s [8]. The initial temperature of tissue and blood is equal to  $T_p = 37^\circ\text{C}$ , on the outer surface of the tissue the boundary temperature equals  $37^\circ\text{C}$ . The following parameters in the Arrhenius integral (8) are assumed:  $P = 3.1 \cdot 10^{98}$  1/s,  $E = 6.28 \cdot 10^5$  J/mol [9].

The absorbed total energy density  $Q_{ext} t_{ext}$  is kept constant as  $240 \cdot 10^6$  J/m<sup>3</sup>, but different heating schemes are taken into account:  $Q_{ext} = 120$  MW/m<sup>3</sup>,  $t_{ext} = 2$  s;  $Q_{ext} = 60$  MW/m<sup>3</sup>,  $t_{ext} = 4$  s;  $Q_{ext} = 30$  MW/m<sup>3</sup>,  $t_{ext} = 8$  s and  $Q_{ext} = 20$  MW/m<sup>3</sup>,  $t_{ext} = 12$  s). The computations were performed until  $t^F = 20$  s.

#### 3.3.1. Temperature distribution

In Figures 3.2–3.5 the temperature distribution after 20 s is shown. As can be seen, the method of heating the tumor affects the temperature distribution in the tissue.

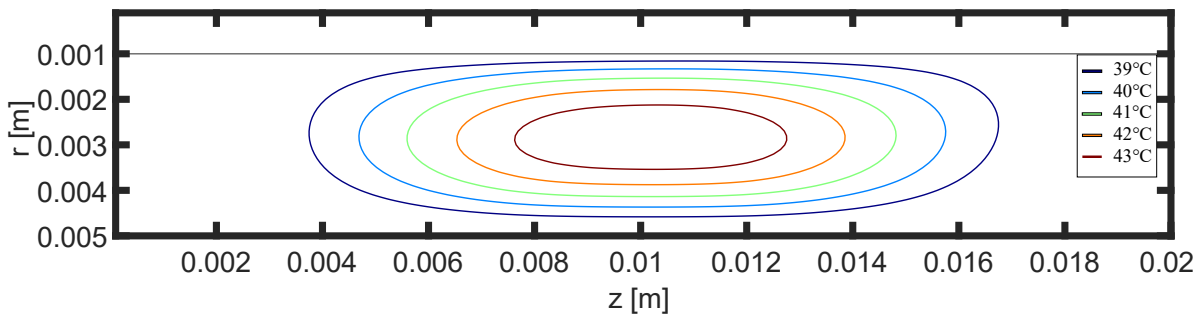


Fig. 3.2. Temperature distribution after 20 s ( $Q_{ext} = 120$  MW/m<sup>3</sup>,  $t_{ext} = 2$  s)

Rys. 3.2. Rozkład temperatury po 20 sekundach ( $Q_{ext} = 120$  MW/m<sup>3</sup>,  $t_{ext} = 2$  s)

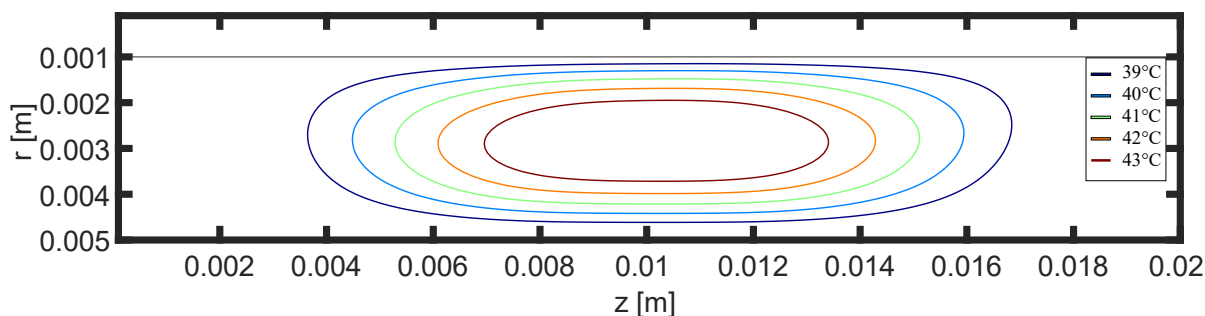


Fig. 3.3. Temperature distribution after 20 s ( $Q_{ext} = 60 \text{ MW/m}^3$ ,  $t_{ext} = 4 \text{ s}$ )

Rys. 3.3. Rozkład temperatury po 20 sekundach ( $Q_{ext} = 60 \text{ MW/m}^3$ ,  $t_{ext} = 4 \text{ s}$ )

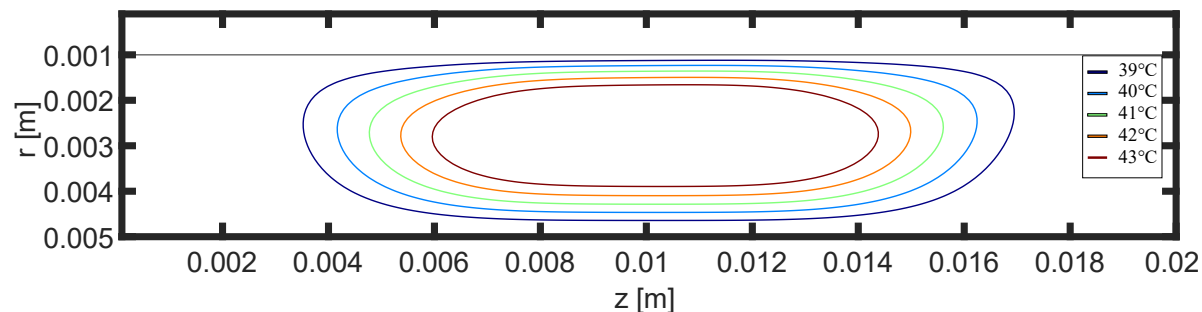


Fig. 3.4. Temperature distribution after 20 s ( $Q_{ext} = 30 \text{ MW/m}^3$ ,  $t_{ext} = 8 \text{ s}$ )

Rys. 3.4. Rozkład temperatury po 20 sekundach ( $Q_{ext} = 30 \text{ MW/m}^3$ ,  $t_{ext} = 8 \text{ s}$ )

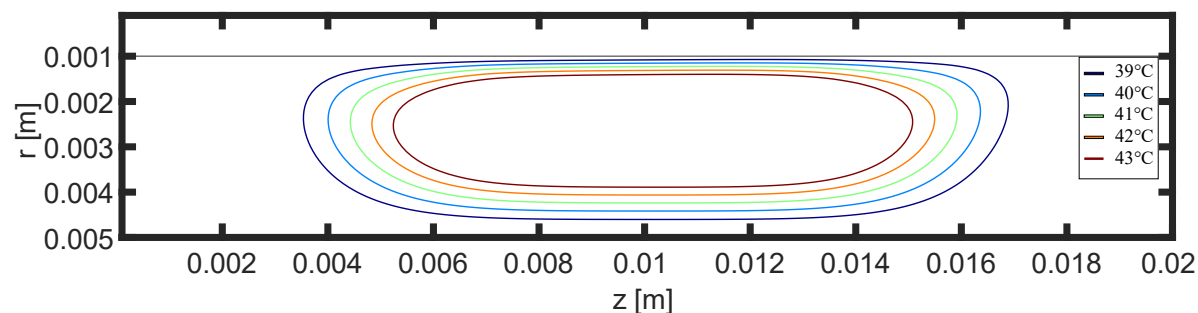


Fig. 3.5. Temperature distribution after 20 s ( $Q_{ext} = 20 \text{ MW/m}^3$ ,  $t_{ext} = 12 \text{ s}$ )

Rys. 3.5. Rozkład temperatury po 20 sekundach ( $Q_{ext} = 20 \text{ MW/m}^3$ ,  $t_{ext} = 12 \text{ s}$ )

In Figure 3.6 the temperature courses at the central point of tumor are presented. In the case of short heating duration the temperature rises faster and reaches higher values compared to the longer heating time.

### 3.3.2. Arrhenius integral

Figures 3.7–3.10 illustrate the distribution of Arrhenius integral after 20 seconds for various heating schemes. Dashed lines correspond to the tumor region. Sub-domain between 1 and 4.6 corresponds to the [66% – 99%] probability of tissue destruction, while sub-domain where Arrhenius integral is greater than or equal to 4.6 corresponds to the 99% probability of tissue destruction.

As can be seen, for heating scheme:  $Q_{ext} = 20 \text{ MW/m}^3$ ,  $t_{ext} = 12 \text{ s}$  (Figure 3.9) the cancerous tissue is not destroyed. The most effective heating scheme is:  $Q_{ext} = 120 \text{ MW/m}^3$  and  $t_{ext} = 2 \text{ s}$  (Figure 3.7).

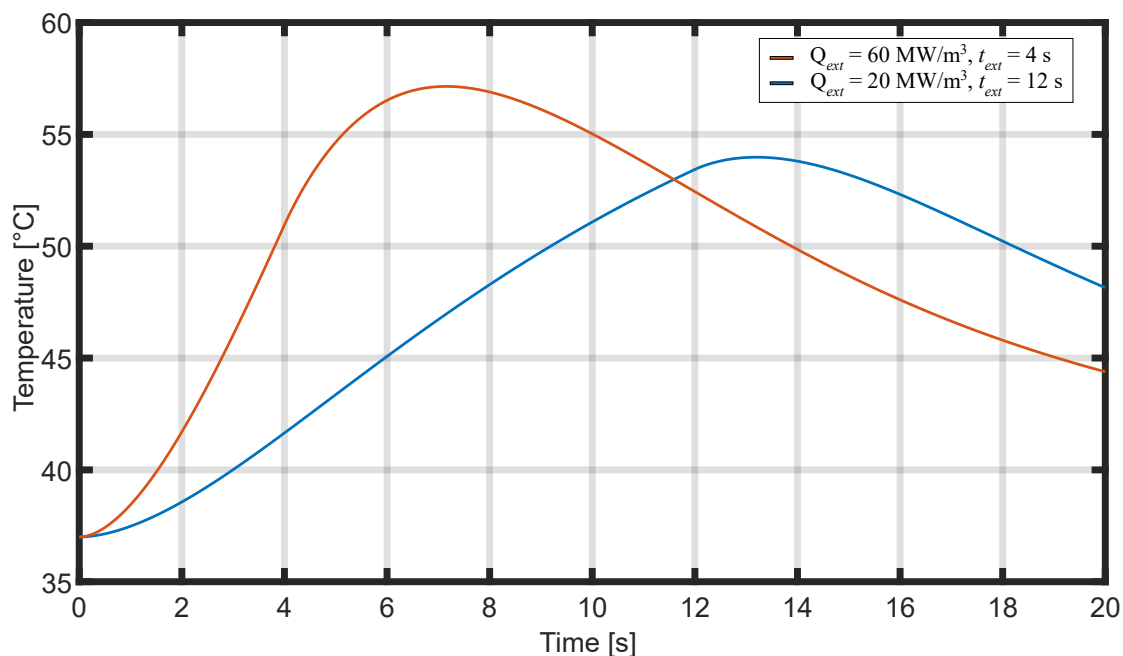


Fig. 3.6. Temperature history at the central point of tumor

Rys. 3.6. Przebieg temperatury w centralnym punkcie nowotworu

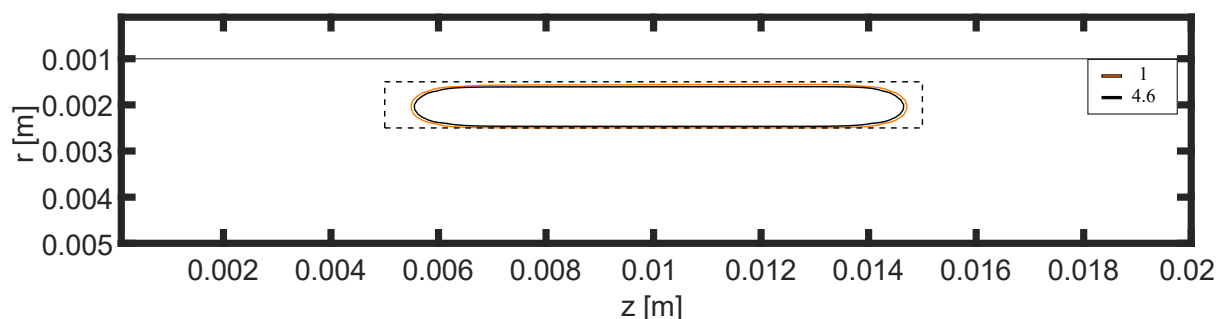


Fig. 3.7. Arrhenius integral distribution after 20 s ( $Q_{ext} = 120 \text{ MW/m}^3$ ,  $t_{ext} = 2 \text{ s}$ )

Rys. 3.7. Rozkład całki Arrheniusa po 20 sekundach ( $Q_{ext} = 120 \text{ MW/m}^3$ ,  $t_{ext} = 2 \text{ s}$ )

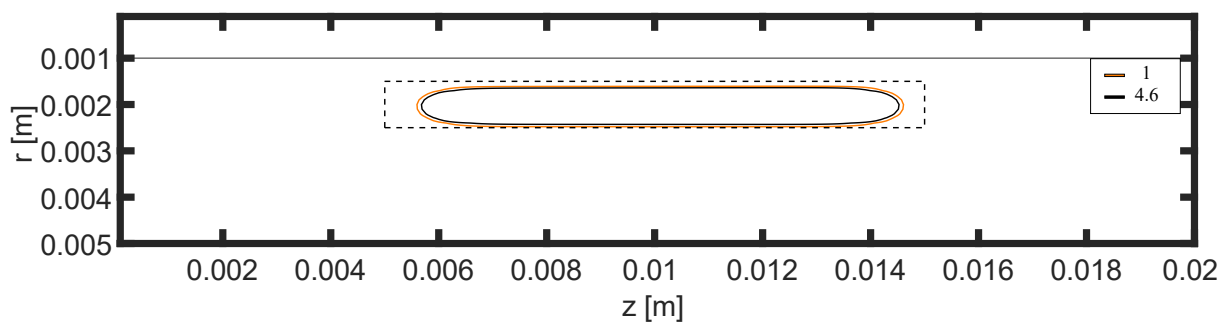


Fig. 3.8. Arrhenius integral distribution after 20 s ( $Q_{ext} = 60 \text{ MW/m}^3$ ,  $t_{ext} = 4 \text{ s}$ )

Rys. 3.8. Rozkład całki Arrheniusa po 20 sekundach ( $Q_{ext} = 60 \text{ MW/m}^3$ ,  $t_{ext} = 4 \text{ s}$ )

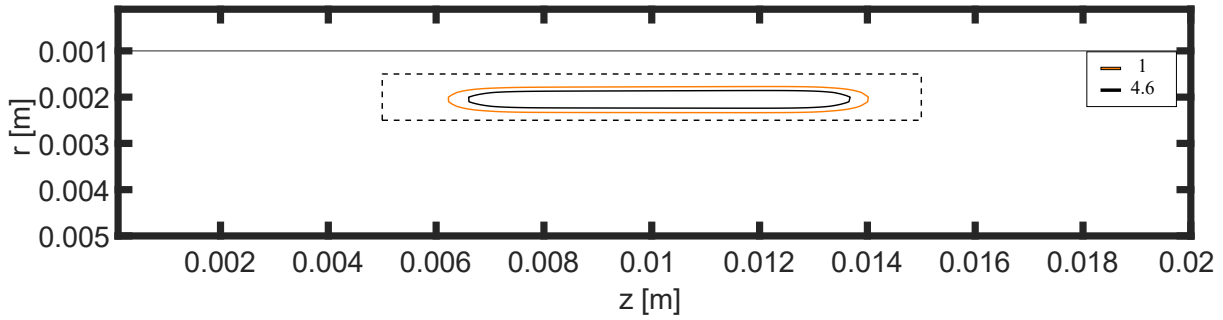


Fig. 3.9. Arrhenius integral distribution after 20 s ( $Q_{ext} = 30 \text{ MW/m}^3$ ,  $t_{ext} = 8 \text{ s}$ )  
 Rys. 3.9. Rozkład całki Arrheniusa po 20 sekundach ( $Q_{ext} = 30 \text{ MW/m}^3$ ,  $t_{ext} = 8 \text{ s}$ )

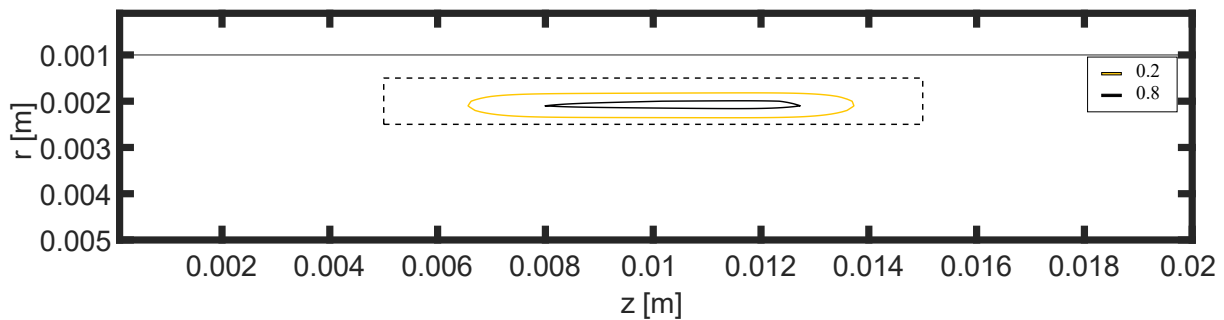


Fig. 3.10. Arrhenius integral distribution after 20 s ( $Q_{ext} = 20 \text{ MW/m}^3$ ,  $t_{ext} = 12 \text{ s}$ )  
 Rys. 3.10. Rozkład całki Arrheniusa po 20 sekundach ( $Q_{ext} = 20 \text{ MW/m}^3$ ,  $t_{ext} = 12 \text{ s}$ )

### 3.4. Conclusions

The single blood vessel surrounded by the biological tissue with a tumor has been considered. Different heating schemes of tumor, it means heating power density  $Q_{ext}$  and heating duration  $t_{ext}$ , under the assumption that the total energy density  $Q_{ext} t_{ext}$  is constant, have been taken into account. The blood and tissue temperature fields have been described by the dual-phase lag equations supplemented by appropriate boundary and initial conditions. The problem has been solved by implicit scheme of finite difference method.

The calculations carried out showed that a short heating time and high heating power density guarantee successful tumor destruction.

### Acknowledgements

The research is financed from financial resources from the statutory subsidy of the Faculty of Mechanical Engineering, Silesian University of Technology in 2021.

## Bibliography

1. M. Franckena et al., Long-term improvement in treatment outcome after radiotherapy and hyperthermia in locoregionally advanced cervix cancer: an update of the Dutch Deep Hyperthermia Trial, *International Journal of Radiation Oncology, Biology and Physics* (2018) **70**: 1176-1182.
2. E. Kosari, K. Vafai, Thermal tissue damage analysis for magnetothermal neuromodulation and lesion size minimization. *Brain Multiphysics* (2020) **1**.
3. C.J. Diederich, Thermal ablation on high-temperature thermal therapy: overview of technology and clinical implementation. *International Journal of Hyperthermia* (2005) **21**: 745-753.
4. K.Ch. Liu, Y.S. Chen. Analysis of heat transfer and burn damage in a laser irradiated living tissue with the generalized dual-phase-lag model. *International Journal of Thermal Sciences* (2016) **103**: 1-9.
5. E. Majchrzak, M. Stryczyński, Dual-phase lag model of heat transfer between blood vessel and biological tissue, *Mathematical Biosciences and Engineering* (2021) **18**: 1573-1589.
6. E. Majchrzak, B. Mochnacki, Dual-phase lag model of thermal processes in a multi-layered microdomain subjected to a strong laser pulse using the implicit scheme of FDM. *International Journal of Thermal Sciences* (2018) **133**: 240-251
7. B. Mochnacki, E. Majchrzak. Numerical model of thermal interactions between cylindrical cryoprobe and biological tissue using dual-phase lag equation. *International Journal of Heat and Mass Transfer* (2017) **108**:1-10.
8. Y. Zhang. Generalized dual-phase lag bioheat equations based on nonequilibrium heat transfer in living biological tissues. *International Journal of Heat and Mass Transfer* (2009) **52**: 4829-4834.
9. T.C. Shih, H.L. Liu, T.L. Horng. Cooling effect of thermally significant blood vessels in perfused tumor tissue during thermal therapy. *International Communications in Heat and Mass Transfer* (2006) **33**: 135-141.
10. M. Paruch. Identification of the degree of tumor destruction on the basis of the Arrhenius integral using the evolutionary algorithm. *International Journal of Thermal Sciences* (2018) **130**: 507-517.
11. A. Babbar, V. Jain, D. Gupta, D. Agrawal, Finite element simulation and integration of CEM43 °C and Arrhenius Models for ultrasonic-assisted skull bone grinding: A thermal dose model. *Medical Engineering and Physics* (2021) **90**: 9-22.

12. S. Schuster, H. Stark, What can we learn from Einstein and Arrhenius about the optimal flow of our blood? *Biochimica et Biophysica Acta* (2014) **1840**: 271-276.
13. M.H. Niemz, Laser-tissue interaction: fundamentals and applications. Springer, Berlin (2007).

## MODELING OF ONCOLOGICAL HYPERTHERMIA USING DUAL-PHASE LAG EQUATIONS

### Abstract

In the paper a single blood vessel and surrounding biological tissue with a tumor region is considered. The blood and tissue temperature fields are described by the dual-phase lag equations supplemented by appropriate boundary and initial conditions. The degree of destruction of tumor was estimated on the basis of the so-called Arrhenius integrals. The problem was solved using the implicit scheme of the finite difference method. The main purpose of the work is to analyze various heating schemes (power density and heating duration  $t_{ext}$ ) and to investigate which of the schemes is more effective in order to destroy the tumor tissue: short heating time and high power density, or long heating time and low power density. It turned out that the first of these options is more effective.

**Keywords:** oncological hyperthermia, dual-phase lag equation, finite difference method, Arrhenius integral.

Weronika ŻAK<sup>1</sup>

## **Chapter 4. SEGMENTATION AND THREE-DIMENSIONAL VISUALIZATION OF CHONDROMALACIA LESIONS OF THE FEMORAL HEAD**

### **4.1. Introduction**

The knee joint is the largest joint in the human body, in addition, it has a very complex structure and it is most vulnerable, immediately after the ankle joint, to the transmission of huge loads and forces in the human body. The structure is based on the articular surfaces of three bones: femur, tibia and knee cap. The joint is also reinforced with two crescent fibrous cartilage, called articular meniscus (*lat. menisci articulares*). It is further strengthened by external ligaments (collateral and joint bag) and cruciate ligaments (anterior and posterior). It is a hinged joint that allows bending and straightening movements, besides, with a bent joint, rotational movements are possible [3].

Articular cartilage occurs on the surface of the bone in all joints. It is mainly made up of protein molecules (collagen), proteoglycans, and water [4]. It is designed to carry heavyweight, thanks to the fact that it can change its shape under the influence of acting loads, which results in an even distribution of forces. When moving, it absorbs the friction between bones against each other, so that the joint can move smoothly [5].

Chondromalacia is a condition that occurs mainly within cartilaginous tissue. It can occur on the surface of the cap of all bones but is most often diagnosed within the knee joint. This is a condition that is characterized by softening, fraying of a large number of fibers on the surface of the articular cartilage, or in extreme cases its rupture. These pathological changes lead to its uneven thickness or local defect, causing the bones to rub against each other and, as a result, impair their proper movement. The reasons for

---

<sup>1</sup> Department of Biomedical Engineering, Silesian University of Technology.

this condition can be many, in addition to physiological changes in the structure or diseases such as rheumatoid inflammation of the joints or degenerative diseases, one can also mention biomechanical causes, which include: injuries, excessive use of the knee joint, flat feet, obesity.

The most commonly used non-invasive methods of imaging cartilage lesions include MRI (*Magnetic Resonance Imaging*) and Ultrasonography. Studies such as X-rays and CT (*Computer Tomography*) do not achieve sufficiently satisfactory cartilage visualization effects and are included in invasive studies due to the use of ionizing radiation. Exploratory arthroscopy stands out among the invasive imaging methods that provide the most information. Imaging diagnostics are aimed at showing the actual condition, the extent of pathological changes and precise visual information about cartilage, which can allow to plan treatment individually under the patient. Due to the need to classify the changes, according to their extent, depth, and reference of each of the tested cases to the existing guidelines, a four grades scale of Outerbridge chondromalacia was created (Table 4.1) [1]. In publication [2] the authors rely on the diagnosis of chondromalacia (and grade agency) based on MR images.

Table 4.1

Outerbridge grading of chondromalacia

Grade	Description
I	signal intensity alterations with an intact surface of the articular cartilage compared with the surrounding normal cartilage
II	partial thickness defect of the cartilage
III	fissuring of the cartilage to the level of the subchondral bone
IV	deep cartilage defects, exposed subchondral bone

## 4.2. Methodology

The procedure (Figure 4.1) begins with selecting the plane in which you want to segment. In the case of a front plane on the analyzed imaging series, the procedure slightly differs, this is due to the presence of imaging artifacts and the starting point must be selected depending on the cross-section up to three times, and then all images after segmentation are combined into one final one. After segmentation of the structure



in this plane, the procedure is already the same in all planes. When the image is loaded, a parameter is selected for the maximum intensity difference between pixels, which allows only pixels of the bone area to be segmented from the image, elements in the image with an intensity greater than or less than the set tolerance are not attached to the bone pixels. The starting point in the bone area is then selected, the intensity of which is the base value on which the procedure for integrating or not a pixel into the bone area is based. Attach pixels to the starting point using the region growing method. Once properly segmented, the next step is to save this structure as a .jpeg file so that it can be used to create a three-dimensional model from all images in a given plane. Based on this segmented structure, functionalities such as calculating the normalized surface area, finding a centroid, and calculating the dice factor value are also possible. In each plane, a photo vector was created from the .jpeg structures, which was the input for the function that creates the three-dimensional model.

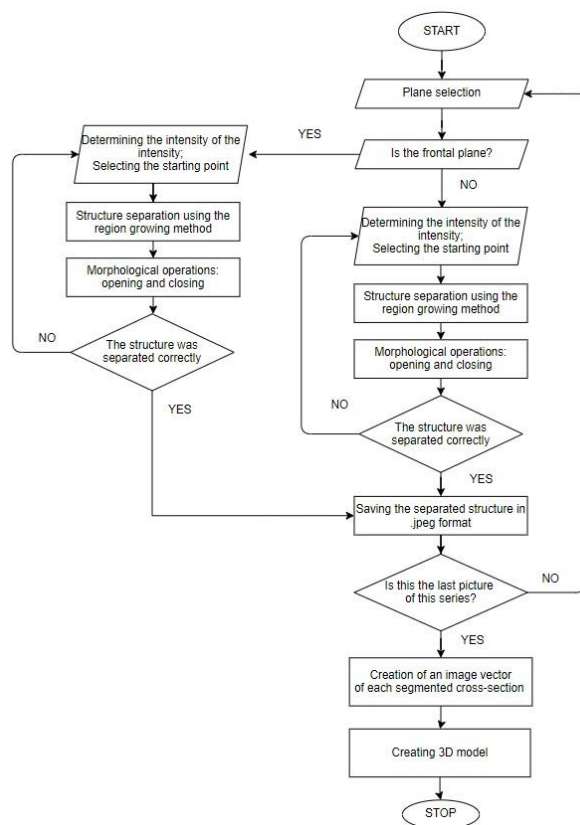


Fig. 4.1. Block diagram  
Rys. 4.1. Schemat blokowy

Segmentation is the basic stage of image analysis that allows it to be divided into disjointed areas in terms of a given feature (e.g. Pixels Intensity). Through segmentation, it is possible to extract structures and analyze and interpret them later without

information redundancy. The segmentation method used in this work was the region growing method, which is based on the selection of the starting point and the value in mentioned earlier – the maximum difference in intensity. Then, in each iteration of the method, the analyzed pixel is analyzed by comparing its pixels in the neighborhood. Typically, it is a type of 4-neighborhood or 8-neighborhood. Both types are shown in Figure 4.2. The neighborhood type is nothing more than a topology of the position of the pixels surrounding the currently analyzed pixel in terms of intensity. If the inclusion criterion is met, the analyzed pixel is incorporated into the area with the starting point. Each pixel is subjected to this procedure. By combining all pixels, homogeneous areas are created in terms of the accepted criterion, which consequently leads to the segmentation of the selected structure [6].

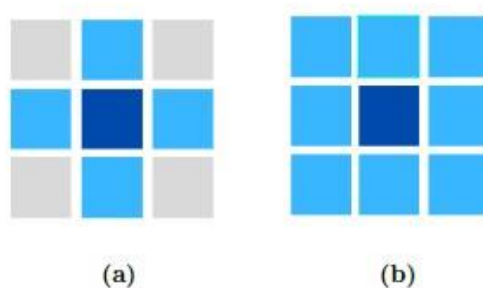


Fig. 4.2. Types of neighborhood: (a) 4-neighborhood, (b) 8-neighborhood  
Rys. 4.2. Typy sąsiedztwa: (a) 4-sąsiedztwo, (b) 8-sąsiedztwo

For better results (Jagged Edge Alignments, Small Hole Fills), mathematical morphology operations are used, based mainly on dilatation and erosion operations on the currently analyzed pixel. The basic concept of mathematical morphology is the structural element. It is a set of pixels, most often in the form of a matrix of any shape, which in the case of binary images can take the value of 0 or 1. Examples of structural elements are shown in Figure 4.3. Each structural element has its own coordinate system, where the selected pixel is the reference point. This point is called a seed point. One of the two main operations is dilatation, which consists of the extension of the set of elements. In applying this operation, a structural element is applied to each pixel being analyzed, and if at least one of the pixels of the analyzed binary image is covered with a logical value of 1 in the structured element, the analyzed pixel is added to the resulting image. The image is characterized by the growth of the area. This operation is used when you need to smooth the edges, fill small holes, but it can also bring with it side effects such as assuming two small objects together. The operation in some way inverse to the one described above is erosion. Each pixel is also analyzed in this

operation, but the resulting value of 1 is determined only by that pixel when all pixels within the structural elements are non-zero. The final image after applying this operation is an image with some defects relative to the original image, with cavities dependent on the size of the structural element.

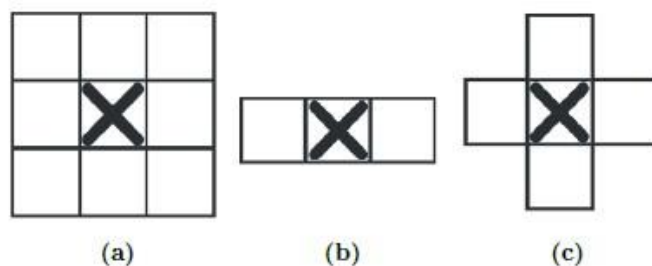


Fig. 4.3. Examples of structural elements  
Rys. 4.3. Przykładowe elementy strukturalne

Combining these two operations after each other is called an opening or closing operation using the same structured element, depending on the order in which those operations are performed. If you perform an erosion operation and then a dilatation operation, we are talking about an opening that is designed to remove small details, small objects and separate two or more structures in the image from the analyzed image. Performing a dilatation and then erosion operation is called closing an image. This causes small holes to be filled in the image. The filling of these holes depends on the size of the structural element. Both operations are used to remove distortion from the image, so for better results, both of these operations can be performed sequentially after each other. The order in which the operation is performed does not significantly affect the final effect.

In order to assess the similarity of the segmented structure to the expert outline, the Dice coefficient was used. It is an indicator that allows you to determine spatial overlapping of two analyzed binary images. It is calculated according to equation 1. Values in the range  $\langle 0;1 \rangle$  mean: 0 – total absence of similarity, no spatial overlap between the analyzed images. Value 1 – indicates the total overlap of images. Values between 0 and 1 indicate overlapping images to some extent, in part [7]. In segmentation, the expected value was expected to achieve results at  $DSC \geq 0.8$ .

$$DSC = \frac{2(A \cap B)}{A+B} \quad (1)$$

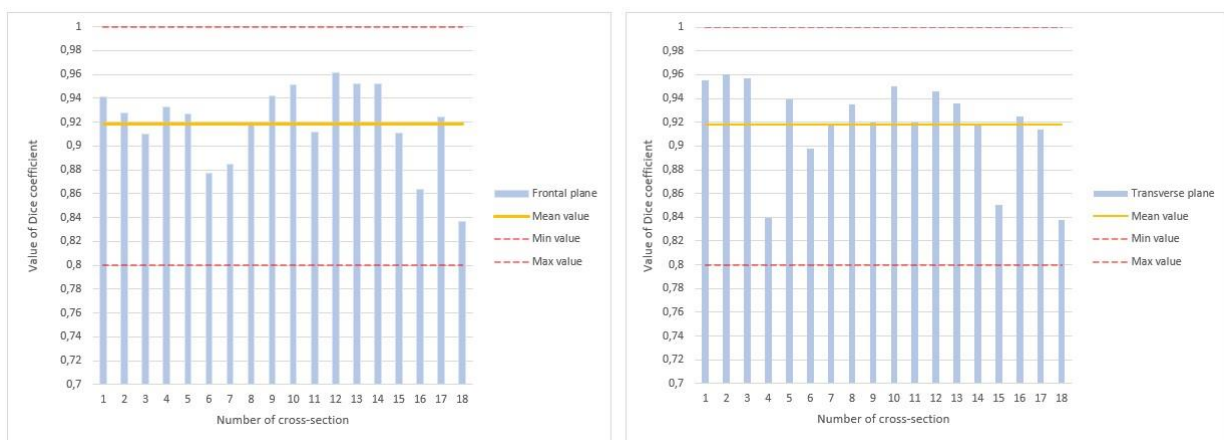
### 4.3. Discussion and Results

#### 4.3.1. Materials

Segmentation of the femoral head took place in images of the T1-weighted series of magnetic resonance imaging of the knee joint in the frontal plane and in images of the T2-weighted series of magnetic resonance imaging of the knee joint in the sagittal and transverse plane. The picture series in each plane counted:

- sagittal plane: 112 cross-sections, but only those on which bone structures were visible were used for segmentation, 72 cross-sections were used;
- frontal plane: 19 cross-sections, of which 18 were segmented femur;
- transverse: the series consisted of 18 cross-sections, each of which was segmented.

On each of the cross-sections is moved possible to segment an interesting structure. The Dice coefficient has been calculated to confirm the correctness of this segmentation. All results are presented in Figure 4.4 and Figure 4.5. The highest value of the coefficient has been achieved in the sagittal plane in cross-section 77 (Figure 4.6) and the smallest in the transverse plane in cross-section 4 (Figure 4.7). Green and magenta colors have been used for differences between superimposed structures and white for overlapping images. This value, in the case of the result with the highest value of coefficients, may be due to clear bone outlines, which in the image resulted in a large difference in intensity levels between pixels, which allowing for satisfactory results in the case of the area growth method. In cases coefficient value being lower, it may be watch that the segmented structure was larger than the expert stroke made. This could be due to a poor fit of the structural element for the mathematical morphology operation.



(a)

(b)

Fig. 4.4. Visualization of the results (a) in Frontal plane, (b) in Transverse plane

Rys. 4.4. Wizualizacja wyników (a) w płaszczyźnie czołowej, (b) w płaszczyźnie poprzecznej

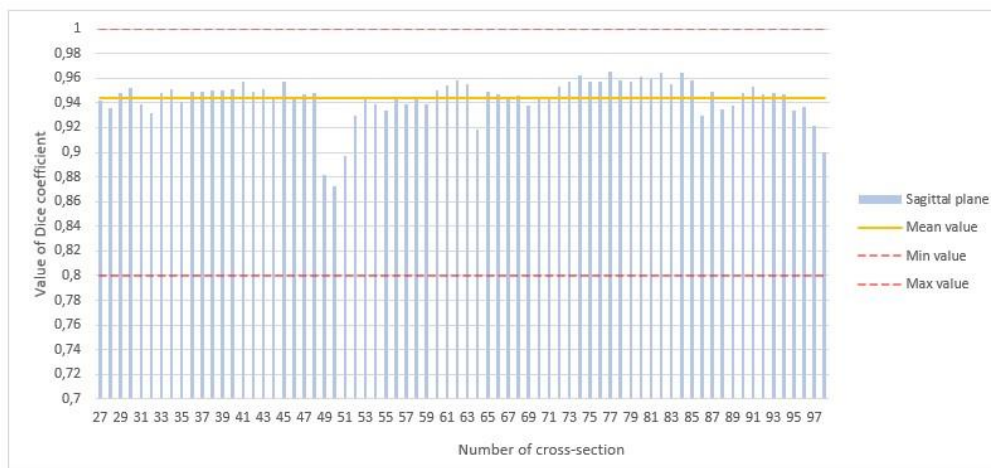


Fig. 4.5. Visualization of the results in Sagittal plane

Rys. 4.5. Wizualizacja wyników w płaszczyźnie strzałkowej

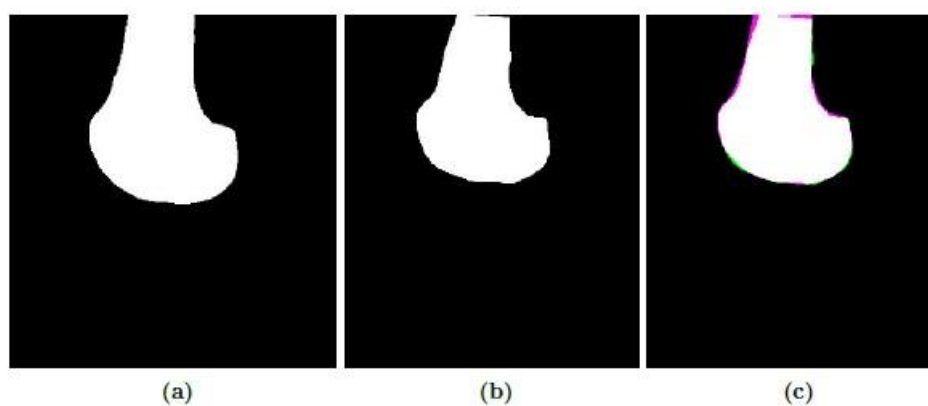


Fig. 4.6. Visualization of the highest coefficient value: (a) segmented structure, (b) expert outline, (c) overlay of both structures

Rys. 4.6. Wizualizacja największej wartości współczynnika: (a) wysegmentowana struktura, (b) obrys ekspercki, (c) nałożenie obu struktur

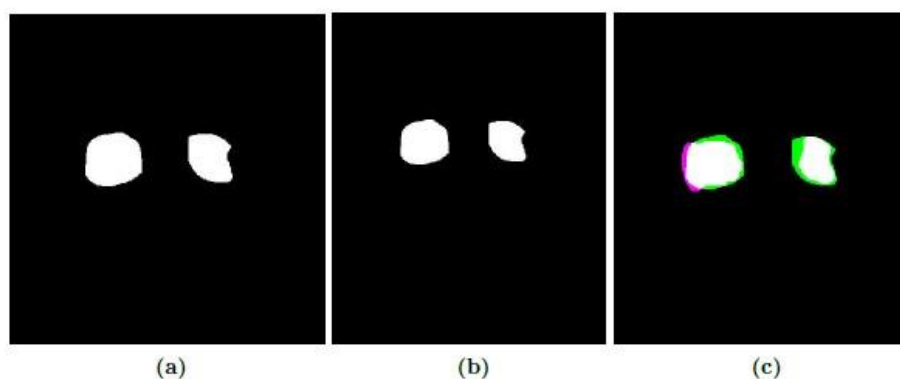


Fig. 4.7. Visualization of the smallest coefficient value: (a) segmented structure, (b) expert outline, (c) overlay of both structures

Rys. 4.7. Wizualizacja najmniejszej wartości współczynnika: (a) wysegmentowana struktura, (b) obrys ekspercki, (c) nałożenie obu struktur

For each plane, a three-dimensional model of the femoral head was created, which reflects the bone to a better or worse degree (Figure 4.8). The best model is the model in the sagittal plane, no doubt because it was in this plane that there were as many as 72 cross-sections, and the gap between them was small. Models in the transverse and frontal plane are created from fewer sections, which reduces their accuracy in model mapping. Additionally, the changes are best seen in the sagittal plane.

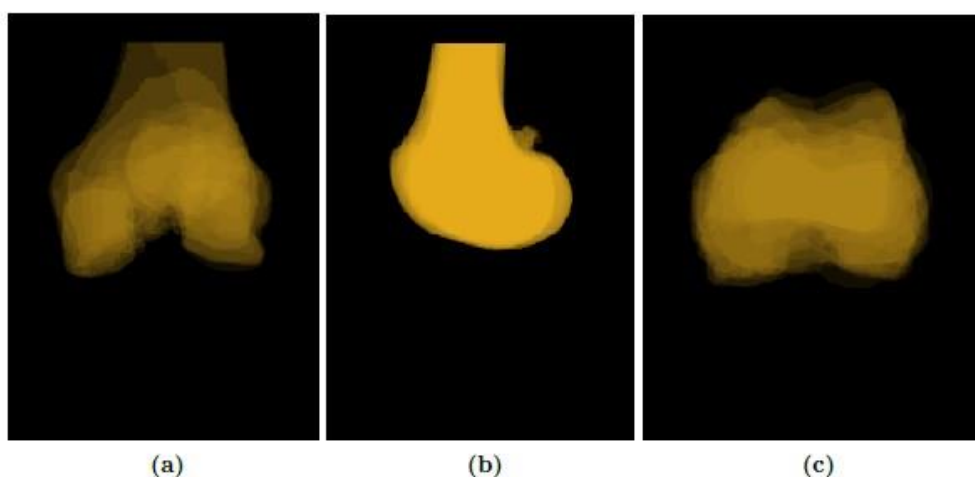


Fig. 4.8. Visualization in plane: (a) frontal, (b) sagittal, (c) transverse

Rys. 4.8. Wizualizacja w płaszczyźnie: (a) czołowej, (b) strzałkowej, (c) poprzecznej

With the increase in the degree of diagnosed chondromalacia, it becomes increasingly difficult to assess the extent of its pathological changes in magnetic resonance imaging. This model can provide doctors with information that can help them plan for further personalized treatment.

Bone segmentation with such changes is very demanding, mainly due to the size of the change and the slight differences in the intensity levels of the pixels that make up the femur. It is difficult to select the maximum intensity difference parameter because too little value causes the entire structure not to be segmented, while too much causes additional structures to be included in the bone area. In the imaging series for which segmentation has been performed, these changes are best seen in the sagittal plane in the T2-weighted MR series.

Segmentation based on thresholding methods is the oldest and fastest, but the disadvantage of this group of methods is low accuracy compared to other methods [8]. In the discussed article, the authors recommend the method of active contours as a better method of segmentation based on the obtained results, which give much better results. Other methods that give good segmentation results recommended by the authors are

graph-based segmentation, atlas-based method, model-based image segmentation and Machine Learning based methods.

In the future, the development plan is to try this method on changes in chondromalacia on other imaging studies that include other degrees of the Outerbridge scale.

## **Bibliography**

1. C. Slattery, C.Y. Kweon, Classifications in Brief: Outerbridge Classification of Chondral Lesions, Clin Orthop Related Res., (2018).
2. B. Kilic, A. Zekiglu, A. Serdar Yücel, Arthroscopic Microfracture Method Results in Chondromalacia Patellae and Our Cases, Journal of Applied Environmental and Biological Sciences, (2015).
3. S. Głowiński, Modelowanie dynamiki stawu kolanowego Technika transportu szynowego, (2013).
4. Open Medica, Chondromalacja rzepki, <https://openmedical.pl/chondromalacja-rzepki-objawy-leczenie-i-rehabilitacja/>.
5. Harvard University, Chondromalacia, [https://www.health.harvard.edu/a\\_to\\_z/chondromalacia-a-to-z](https://www.health.harvard.edu/a_to_z/chondromalacia-a-to-z).
6. R. Tadeusiewicz, Komputerowa analiza i przetwarzanie urazów, Wydawnictwo fundacji i Postępu Telekomunikacji, Kraków, (1997).
7. K.H. Zou, S.K. Warfiels, A. Bharatha, C. Tenpany, M.R. Kaus, S.J. Haker, W.M. Wells, F.A. Jolesz, R. Kikinis, Statistical Validation of Image Segmentation Quality Based on a Spatial Overlap Index, Academic radiology, vol 11, (2004).
8. Khokhar, Ridhma and Kaur, Manvjeet and Sofat, Sanjeev and Chouhan, Devendra, Review of automated segmentation approaches for knee images, IET Image Processing, (12.2020).

## SEGMENTATION AND THREE-DIMENSIONAL VISUALIZATION OF CHONDROMALACIA LESIONS OF THE FEMORAL HEAD

### Abstract

The purpose of this paper is to present the results of the segmentation of the femoral head with changes in chondromalacia in the base of the medial bone load zone of the second degree of the femur from MR images. The article shows the manual segmentation method based on the region growing method and the steps involved in applying mathematical morphology to improve the segmented structure. Segmentation was performed in pictures in three planes: transverse, sagittal and frontal. From the segmented sections, a three-dimensional models were created to illustrate the appearance of the bones. All steps have been implemented in the MATLAB environment using the Image Processing toolbox. To confirm the correctness of the segmentation, a Dice coefficient was used, the values of which were in the range of 0.839 to 0.965.

**Keywords:** chondromalacia, segmentation, 3D vizualization, computer aided treatment.



Anna SKORUPA<sup>\*1</sup>, Alicja PIASECKA-BELKHAYAT<sup>1</sup>

## **Chapter 5. APPLICATION OF FUZZY FINITE DIFFERENCE METHOD IN HEAT AND MASS TRANSFER DURING CRYOPRESERVATION PROCESS**

### **5.1. Introduction**

Cryopreservation is a process in which organs, cells, tissues or other biological constructs are preserved by cooling samples to a very low temperature (between  $-80^{\circ}\text{C}$  to  $-196^{\circ}\text{C}$ ). During cryopreservation, the biological activity of the tissues is reduced or completely stopped and then the physiological temperature is restored again. Successful cryopreservation does not significantly affect the basic functions of cryopreserved biological tissues or cells, such as their mechanical properties [1,2]. Cryopreservation has many practical applications, including medicine. The process is used to preserve stem cells (tissue engineering research) or to cryobank transported organs (in transplantology) [3].

In recent years, the success of cryopreservation of cells and tissues has gradually increased, thanks to the use of cryoprotectants and temperature control equipment. It is important to choose, depending on the cell type, the right cooling rate, heating rate and the CPA, which is used to reduce the amount of ice formed at a given temperature. A cryoprotectant that is commonly used during an articular cartilage cryopreservation is dimethyl sulfoxide (DMSO). In order to avoid the formation of ice regardless of the cooling and heating rates, the liquidus tracking method is used. In the LT process, the temperature decreases/increases gradually during addition/removal of cryoprotectant, and the thermophysical state of the articular cartilage sample remains on or above the liquidus line so that no ice is formed, independently of the cooling/warming rate [4, 5].

---

\* Corresponding author: anna.skorupa@polsl.pl, Konarskiego 18A, 44-100 Gliwice, PL.

<sup>1</sup> Department of Computational Mechanics and Engineering, Faculty of Mechanical Engineering, Silesian University of Technology.

In the present study, the numerical analysis of the articular cartilage sample cryopreservation process including heat and mass transfer proceeding is presented. In the model, the liquidus-tracking protocol for the cryopreserved articular cartilage sample is simulated. Additionally, in the mathematical model, thermophysical parameters such as thermal conductivity and volumetric specific heat are given as fuzzy numbers because they cannot be determined in a deterministic way and their values are approximated in an experimental way. The problem discussed has been solved using the fuzzy finite difference method algorithm using  $\alpha$ -cuts and the rules of directed interval arithmetic [6, 7]. The application of  $\alpha$ -cuts allows one to simplify mathematical operations in the fuzzy number set. In the research, the thermal proceeding is modelled using the fuzzy Fourier equation, whereas the cryoprotectant transport through extracellular matrix are described by fuzzy mass transfer equation.

## 5.2. Fuzzy governing equations

Thermal processes proceeding in the axially symmetrical heterogeneous articular cartilage sample can be described by the fuzzy energy equation [5,8]

$$\tilde{c} \frac{\partial \tilde{T}(r, z, t)}{\partial t} = \left[ \frac{1}{r} \frac{\partial}{\partial r} \left( \tilde{\lambda} r \frac{\partial \tilde{T}(r, z, t)}{\partial r} \right) + \frac{\partial}{\partial z} \left( \tilde{\lambda} \frac{\partial \tilde{T}(r, z, t)}{\partial z} \right) \right] \quad (1)$$

where  $\tilde{\lambda}$  is the fuzzy thermal conductivity,  $\tilde{c}$  is the fuzzy volumetric specific heat,  $\tilde{T}$  is the fuzzy temperature,  $t$  is the time,  $r$  and  $z$  denote the cylindrical coordinates.

The considered equation (1) is supplemented by the boundary conditions of the 2<sup>nd</sup> or 3<sup>rd</sup> type (see Fig. 5.1) and initial condition

$$\left\{ \begin{array}{l} r = 0, \quad 0 \leq z \leq \frac{H}{2}: \quad \tilde{\lambda} \frac{\partial \tilde{T}(r, z, t)}{\partial r} = \tilde{0} \\ 0 \leq r \leq R, \quad z = \frac{H}{2}: \quad -\tilde{\lambda} \frac{\partial \tilde{T}(r, z, t)}{\partial z} = \tilde{0} \\ r = R, \quad 0 \leq z \leq \frac{H}{2}: \quad -\tilde{\lambda} \frac{\partial \tilde{T}(r, z, t)}{\partial r} = \gamma(\tilde{T} - T_{\text{bulk}}) \\ 0 \leq r \leq R, \quad z = 0: \quad \tilde{\lambda} \frac{\partial \tilde{T}(r, z, t)}{\partial z} = \gamma(\tilde{T} - T_{\text{bulk}}) \\ t = 0: \quad \tilde{T}(r, z, 0) = T_0 \end{array} \right. \quad (2)$$

where  $T_{\text{bulk}}$  is the temperature of the bathing solution,  $T_0$  is the initial temperature and  $\gamma$  is the natural convection heat transfer coefficient [5,8].

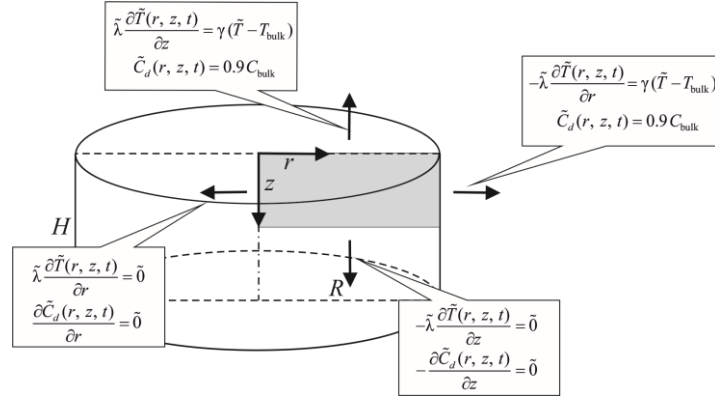


Fig. 5.1. Domain considered and boundary conditions

Rys. 5.1. Schemat rozpatrywanego obszaru oraz warunki brzegowe

The modelling of the cryoprotectant transport through the extracellular matrix can be written as follows

$$\frac{\partial \tilde{C}_d(r, z, t)}{\partial t} = \left[ \frac{1}{r} \frac{\partial}{\partial r} \left( \tilde{D}_d r \frac{\partial \tilde{C}_d(r, z, t)}{\partial r} \right) + \frac{\partial}{\partial z} \left( \tilde{D}_d \frac{\partial \tilde{C}_d(r, z, t)}{\partial z} \right) \right] \quad (3)$$

where  $\tilde{C}_d$  is the fuzzy cryoprotectant concentration in the extracellular matrix, while  $\tilde{D}_d$  is the fuzzy diffusion coefficient of the cryoprotectant in the extracellular matrix estimated by the Einstein-Stokes equation [8, 9]

$$\tilde{D}_d = \frac{k_B \tilde{T}}{6\pi\eta r_s} \quad (4)$$

where  $k_B$  is the Boltzmann constant,  $r_s$  is the radius of the spherical particle molecule and  $\eta$  is the dynamic viscosity.

The mathematical model (see equation (3)) should be supplemented by the boundary-initial conditions (see Fig. 5.1)

$$\left\{ \begin{array}{l} r = 0, \quad 0 \leq z \leq \frac{H}{2}: \quad \frac{\partial \tilde{C}_d(r, z, t)}{\partial r} = \tilde{0} \\ 0 \leq r \leq R, \quad z = \frac{H}{2}: \quad -\frac{\partial \tilde{C}_d(r, z, t)}{\partial z} = \tilde{0} \\ r = R, \quad 0 \leq z \leq \frac{H}{2}: \quad \tilde{C}_d(r, z, t) = 0.9 C_{\text{bulk}} \\ 0 \leq r \leq R, \quad z = 0: \quad \tilde{C}_d(r, z, t) = 0.9 C_{\text{bulk}} \\ t = 0: \quad \tilde{C}_d(r, z, 0) = C_0 \end{array} \right. \quad (5)$$

where  $C_{\text{bulk}}$  is the cryoprotectant concentration in the bathing solution (the coefficient 0.9 relates to the real mass exchange between the sample and the bathing solution) and  $C_0$  is the initial cryoprotectant concentration [5, 8].

The presented mathematical model does not include the phenomenon of phase changes. This is due to the fact that the LT method is used to model heat and mass transfer. The LT protocol regulates the temperature and concentration in such a way that the temperature of the sample is above or on the liquidus line, which eliminates the probability of ice crystallization in cells – see the calculated eutectic temperatures and the melting points of tissue in [4].

### 5.3. Fuzzy finite difference method

Numerical model of thermal processes and mass transfer proceeding in domain of tissue is based on the fuzzy finite difference method in the version presented in [6, 10]. At the beginning, a time grid with a constant step  $\Delta t$  and a geometrical mesh are introduced. The boundary nodes are located at the distance  $0.5 h$  or  $0.5 k$  with respect to the real boundary ( $h, k$  are the steps of regular mesh in directions  $r$  and  $z$ ), respectively.

The approximate form of the interval energy equation (1) for the internal nodes ( $i, j$ ) and the transition  $t^{f-1} \rightarrow t^f$  is the following

$$\begin{aligned} \tilde{c}_{i,j}^{f-1} \frac{\tilde{T}_{i,j}^f - \tilde{T}_{i,j}^{f-1}}{\Delta t} = & \frac{\Phi_{i,j-1}}{\tilde{R}_{i,j-1}^{f-1}} (\tilde{T}_{i,j-1}^{f-1} - \tilde{T}_{i,j}^{f-1}) + \frac{\Phi_{i,j+1}}{\tilde{R}_{i,j+1}^{f-1}} (\tilde{T}_{i,j+1}^{f-1} - \tilde{T}_{i,j}^{f-1}) + \\ & \frac{\Phi_{i-1,j}}{\tilde{R}_{i-1,j}^{f-1}} (\tilde{T}_{i-1,j}^{f-1} - \tilde{T}_{i,j}^{f-1}) + \frac{\Phi_{i+1,j}}{\tilde{R}_{i+1,j}^{f-1}} (\tilde{T}_{i+1,j}^{f-1} - \tilde{T}_{i,j}^{f-1}) \end{aligned} \quad (6)$$

where

$$\Phi_{i,j-1} = \frac{r_{i,j} - 0.5h}{r_{i,j} h} \quad \Phi_{i,j+1} = \frac{r_{i,j} + 0.5h}{r_{i,j} h} \quad \Phi_{i-1,j} = \Phi_{i+1,j} = \frac{1}{k} \quad (7)$$

are the shape functions of differential mesh, while the fuzzy thermal resistances are defined as follows:

$$\begin{aligned}
\tilde{R}_{i,j+1}^{f-1} &= \frac{0.5h}{\tilde{\lambda}_{i,j}^{f-1}} + \frac{0.5h}{\tilde{\lambda}_{i,j+1}^{f-1}} & \tilde{R}_{i,j-1}^{f-1} &= \frac{0.5h}{\tilde{\lambda}_{i,j}^{f-1}} + \frac{0.5h}{\tilde{\lambda}_{i,j-1}^{f-1}} \\
\tilde{R}_{i+1,j}^{f-1} &= \frac{0.5k}{\tilde{\lambda}_{i,j}^{f-1}} + \frac{0.5k}{\tilde{\lambda}_{i+1,j}^{f-1}} & \tilde{R}_{i-1,j}^{f-1} &= \frac{0.5k}{\tilde{\lambda}_{i,j}^{f-1}} + \frac{0.5k}{\tilde{\lambda}_{i-1,j}^{f-1}}
\end{aligned} \tag{8}$$

The final approximate form of the interval mass equation (3) for the internal nodes  $(i, j)$  and the transition  $t^{f-1} \rightarrow t^f$  is the following

$$\begin{aligned}
\frac{(\tilde{C}_d)_{i,j}^f - (\tilde{C}_d)_{i,j}^{f-1}}{\Delta t} &= \frac{\Phi_{i,j-1}}{\tilde{W}_{i,j-1}^{f-1}} \left[ (\tilde{C}_d)_{i,j-1}^{f-1} - (\tilde{C}_d)_{i,j}^{f-1} \right] + \frac{\Phi_{i,j+1}}{\tilde{W}_{i,j+1}^{f-1}} \left[ (\tilde{C}_d)_{i,j+1}^{f-1} - (\tilde{C}_d)_{i,j}^{f-1} \right] \\
&+ \frac{\Phi_{i-1,j}}{\tilde{W}_{i-1,j}^{f-1}} \left[ (\tilde{C}_d)_{i-1,j}^{f-1} - (\tilde{C}_d)_{i,j}^{f-1} \right] + \frac{\Phi_{i+1,j}}{\tilde{W}_{i+1,j}^{f-1}} \left[ (\tilde{C}_d)_{i+1,j}^{f-1} - (\tilde{C}_d)_{i,j}^{f-1} \right]
\end{aligned} \tag{9}$$

where the fuzzy diffusion resistances between the central node and the adjoining ones are the following:

$$\begin{aligned}
\tilde{W}_{i,j+1}^{f-1} &= \frac{0.5h}{(\tilde{D}_d)_{i,j}^{f-1}} + \frac{0.5h}{(\tilde{D}_d)_{i,j+1}^{f-1}} & \tilde{W}_{i,j-1}^{f-1} &= \frac{0.5h}{(\tilde{D}_d)_{i,j}^{f-1}} + \frac{0.5h}{(\tilde{D}_d)_{i,j-1}^{f-1}} \\
\tilde{W}_{i+1,j}^{f-1} &= \frac{0.5k}{(\tilde{D}_d)_{i,j}^{f-1}} + \frac{0.5k}{(\tilde{D}_d)_{i+1,j}^{f-1}} & \tilde{W}_{i-1,j}^{f-1} &= \frac{0.5k}{(\tilde{D}_d)_{i,j}^{f-1}} + \frac{0.5k}{(\tilde{D}_d)_{i-1,j}^{f-1}}
\end{aligned} \tag{10}$$

The system of equations (6) and (9) has been solved using the assumption of the stability condition for explicit differential scheme [10]. The method of attaching boundary conditions is discussed in detail in [8].

More information about the fuzzy finite difference method and fuzzy trapezoidal numbers used in the next part of the paper can be found in [6, 7].

#### 5.4. Results of computations

As a numerical example, the heat and mass transport in the homogenous cylindrical articular cartilage sample of dimensions  $H = 1$  mm and  $R = 3$  mm has been analysed. The following thermophysical parameters as fuzzy trapezoidal numbers have been introduced: thermal conductivity  $\tilde{\lambda} = [\lambda - 0.05\lambda, \lambda - 0.025\lambda, \lambda + 0.025\lambda, \lambda + 0.05\lambda]$  and volumetric specific heat

$\tilde{c} = [c - 0.05c, c - 0.025c, c + 0.025c, c + 0.05c]$ , where  $\lambda = 0.518 \text{ W}\cdot\text{m}^{-1}\cdot\text{K}^{-1}$  and  $c = 3.924 \cdot 10^6 \text{ J}\cdot\text{m}^{-3}\cdot\text{K}^{-1}$ . The mathematical model has also been supplemented by: initial temperature in tissue domain  $T_0 = 22^\circ\text{C}$ , initial cryoprotectant concentration  $C_0 = 0\%$  (w/w) and heat transfer coefficient  $\gamma = 525 \text{ W}\cdot\text{m}^{-2}\cdot\text{K}^{-1}$ . Additionally, to determine the diffusion coefficient, the following input data have been used: the Boltzmann constant  $k_B = 1.38 \cdot 10^{-23} \text{ J}\cdot\text{K}^{-1}$ , radius of the spherical particle molecule  $r_s = 2.541 \cdot 10^{-10} \text{ m}$  and the dynamic viscosity  $\eta = 1.996 \cdot 10^{-3} \text{ Pa}\cdot\text{s}$  [5, 8].

In this work, the LT protocol proposed by Pegg et al. [4] and improved by Yu et al. [5] was applied. It consists of seven steps in cooling and addition phase and six steps in warming and removal phase. This approach prevents ice crystal formation without causing toxicity, because temperature and concentration of bathing solution for each step are properly regulated. The values of temperature ( $T_{\text{bulk}}$ ) and concentration ( $C_{\text{bulk}}$ ) of bathing solution in respective steps, which refer to boundary conditions in numerical model, can be found in Tab. 5.1.

Table 5.1

The assumption of the LT protocol [5]

Phase	Step	Time	Temperature of bathing solution	Concentration of bathing solution
		$t$ [min]	$T_{\text{bulk}}$ [ $^\circ\text{C}$ ]	$C_{\text{bulk}}$ [% (w/w)]
Cooling and addition	1	10	22	10
	2	9.8	22	20
	3	18.2	-5	29
	4	25	-8.5	38
	5	19.8	-16	47
	6	26.4	-23	56
	7	23.8	-35	63
Warming and removal	1	23.8	-35	56
	2	26.4	-23	47
	3	19.8	-16	38
	4	25	-8.5	29
	5	18.2	-5	20
	6	29.85	22	0

The simulation has been performed using the finite difference method (FDM) with the rules based on fuzzy analysis for trapezoidal numbers with application of  $\alpha$ -cuts and the

directed interval arithmetic [7, 8]. The following assumption in numerical model was introduced: time step  $\Delta t = 0.001$  s, mesh steps  $h = 0.0001$  m and  $k = 0.00005$  m, numbers of nodes:  $10 \times 30$ .

Fig. 5.2 illustrates the history of the temperature over time for transition from  $22^\circ\text{C}$  to  $-5^\circ\text{C}$  from step 2 to step 3 in the cooling and addition phase for  $\alpha$  equal to 0 and 0.75, where two curves represent the beginning and the end of  $\alpha$ -cuts. The obtained results refer to the point with the coordinates  $r = 0.1$  mm and  $z = 0.45$  mm.

Fig. 5.3 shows the history of the concentration over time for transition from  $22^\circ\text{C}$  to  $-5^\circ\text{C}$  from step 2 to step 3 in the cooling and addition phase for the same values of parameter  $\alpha$  and in the same point. The gaps between the lines on the graphs are narrow, therefore the zoom for 19-20 s was made.

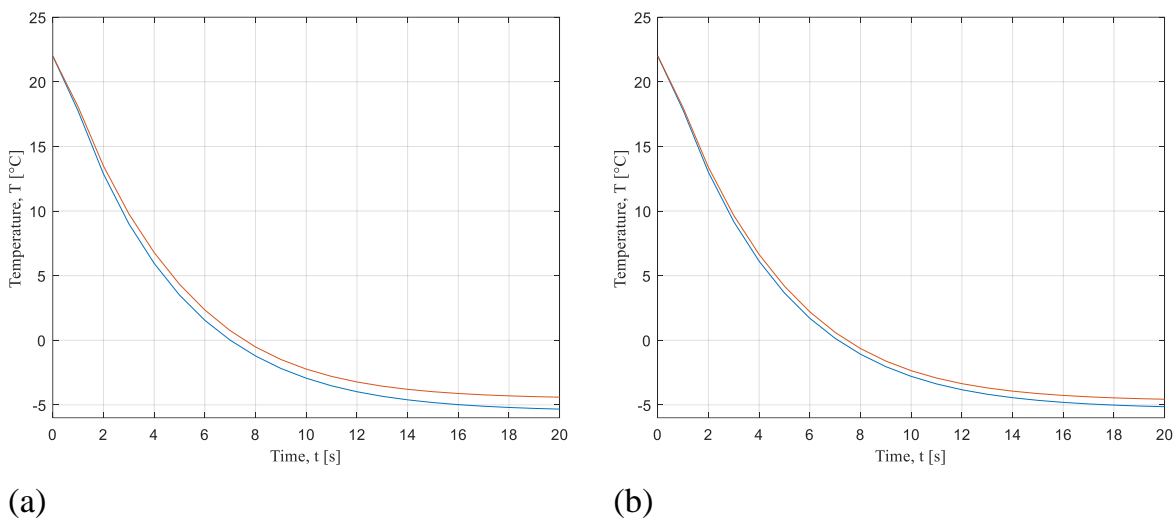


Fig. 5.2. History of temperature over time from  $22^\circ\text{C}$  to  $-5^\circ\text{C}$  for: (a)  $\alpha = 0$ ; (b)  $\alpha = 0.75$

Rys. 5.2. Wykres zależności temperatury od czasu przy przejściu z  $22^\circ\text{C}$  do  $-5^\circ\text{C}$  dla: (a)  $\alpha = 0$ ; (b)  $\alpha = 0.75$

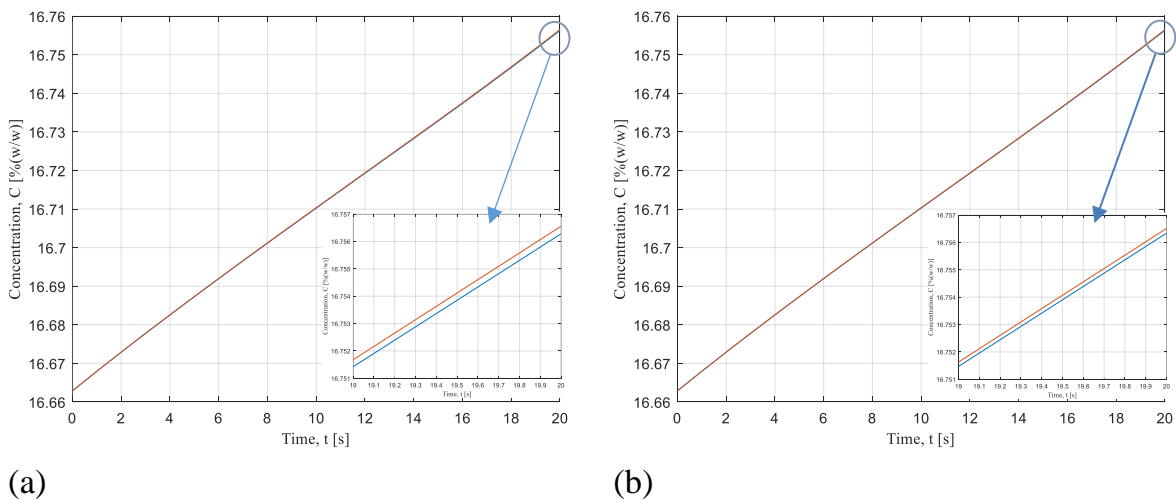


Fig. 5.3. History of concentration over time from  $22^\circ\text{C}$  to  $-5^\circ\text{C}$  for: (a)  $\alpha = 0$ ; (b)  $\alpha = 0.75$

Rys. 5.3. Wykres zależności koncentracji od czasu przy przejściu z  $22^\circ\text{C}$  do  $-5^\circ\text{C}$  dla: (a)  $\alpha = 0$ ; (b)  $\alpha = 0.75$

Table 5.2 contains a comparison of obtained temperatures and concentration with the values given by Yu et al. [5]. The computed interval temperatures coincide with the values proposed in the experiment. On the other hand, the concentrations determined in the simulation differ from the values both suggested in the experiment and studied by Yu et al. [5]. The discrepancies are visible mainly for those steps, in which higher concentration of bathing solution is assumed (e.g. step 7 in the cooling and addition phase or step 1 in the heating and removal phase).

Table 5.2

Interval values of temperature and concentration at the end of each step

Phase	Step	Temperature [°C]		Concentration [% (w/w)]				
		proposed in [5]	obtained in simulation	proposed in [5]	calculated in [5]	obtained in simulation		
			$\alpha = 0$	$\alpha = 0.75$			$\alpha = 0$	$\alpha = 0.75$
Cooling and addition	1.	22	[22.00, 22.00]	[22.00, 22.00]	10	6.80	[7.839, 7.839]	[7.839, 7.839]
	2.	22	[22.00, 22.00]	[22.00, 22.00]	20	15.73	[16.663, 16.663]	[16.663, 16.663]
	3.	-5	[-5.51, -4.54]	[-5.31, -4.70]	29	23.23	[25.837, 25.840]	[25.838, 25.840]
	4.	-8.5	[-9.37, -7.71]	[-9.03, -7.00]	38	32.22	[34.138, 34.140]	[34.139, 34.140]
	5.	-16	[-17.64, -14.51]	[-17.00, -15.05]	47	37.32	[42.096, 42.106]	[42.099, 42.104]
	6.	-23	[-25.36, -20.86]	[-24.44, -21.64]	56	44.30	[50.336, 50.342]	[50.337, 50.341]
	7.	-35	[-38.58, -31.75]	[-37.20, -32.93]	63	47.50	[56.595, 56.608]	[56.598, 56.606]
Warming and removal	1.	-35	[-38.58, -31.75]	[-37.20, -32.93]	56	-	[50.503, 50.491]	[50.501, 50.493]
	2.	-23	[-25.36, -20.86]	[-24.44, -21.64]	47	-	[42.364, 42.358]	[42.362, 42.359]
	3.	-16	[-17.64, -14.51]	[-17.00, -15.05]	38	-	[34.404, 34.394]	[34.402, 34.396]
	4.	-8.5	[-9.37, -7.71]	[-9.03, -7.00]	29	-	[26.161, 26.159]	[26.162, 26.160]
	5.	-5	[-5.51, -4.54]	[-5.31, -4.70]	20	-	[18.236, 18.233]	[18.236, 18.233]
	6.	22	[22.00, 22.00]	[22.00, 22.00]	0	-	[0.023, 0.023]	[0.023, 0.023]



Figure 5.4 presents results of calculation at the given point after 20 s of step 3 in cooling and addition phase for particular  $\alpha$ -cuts. It can be seen that the intervals between respective temperatures or concentrations are wider for lower values of parameter  $\alpha$ .

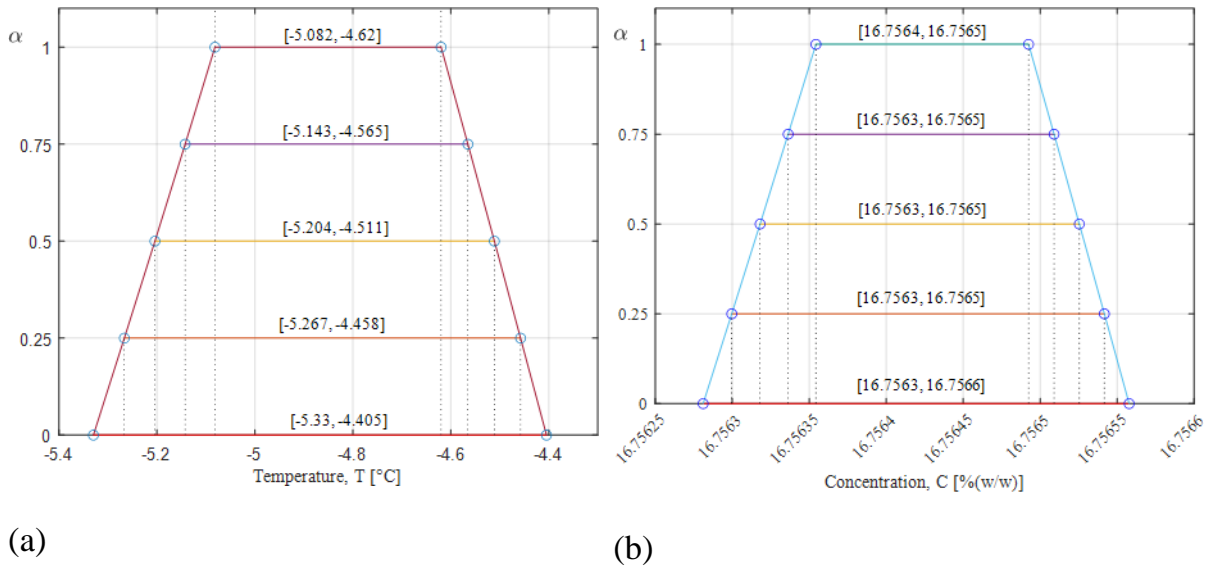


Fig. 5.4. Interval temperature (a) and interval concentration (b) at the given node after 20 s of step 3 in cooling and addition phase for chosen values of parameter  $\alpha$ .

Rys. 5.4. Przedziały temperatur (a) oraz przedziały koncentracji (b) w danym węźle po 20 s kroku 3 w fazie chłodzenia i dodawania dla wybranych wartości parametru  $\alpha$ .

## 5.5. Conclusions

In the paper, the numerical analysis of heat and mass transfer phenomena during cryopreservation is presented. The process is considered in the 2D axially symmetrical articular cartilage sample. The discussed problem has been solved using fuzzy Fourier equation and fuzzy mass diffusion equation. In the numerical simulation, the fuzzy FDM has been applied, assuming that the parameters, such as volumetric specific heat and thermal conductivity, are defined as trapezoidal fuzzy numbers.

The application of FDM gives the solutions as intervals. This type of analysis allows for a better interpretation of real phenomena, because imprecise parameters determined experimentally are entered into the model as fuzzy numbers.

Furthermore, using  $\alpha$ -cuts during numerical modelling allows to avoid complicated arithmetic because it lets one consider fuzzy numbers as directed interval values. It can be also concluded that the intervals are narrower for the higher values of parameter  $\alpha$ .

The obtained results have been compared with the results of the experiment. While the fuzzy temperatures include suggested values, the concentrations differ from the calculations presented in [5]. It can be caused by estimation of the diffusion coefficient using the Einstein–Stokes model (compared with the diffusion coefficient in [5]).

It should be noted that obtained data are not fully comparable. In the work of Yu et al [5], in addition to using a different way to calculate the diffusion coefficient, a model of mass transport across the cell membrane is also included.

In the future, it is planned to extend the presented model with the mass (cryoprotectant) transport across cell membrane.

## Bibliography

1. G. Zhao, J. Fu, Microfluidics for cryopreservation, *Biotechnol. Adv.* (2017) **35**: 323-336.
2. F. Xu, S. Moon, X. Zhang, L. Shao, Y.S. Song, U. Demirci, Multi-scale heat and mass transfer modelling of cell and tissue cryopreservation, *Philos. Trans. R. Soc. A Math. Phys. Eng. Sci.* (2010) **368**: 561-583.
3. T.H. Jang, S.C. Park, J.H. Yang, J.Y. Kim, J.H. Seok, U.S. Park, C.W. Choi, S.R. Lee, J. Han, Cryopreservation and its clinical applications, *Integr. Med. Res.* (2017) **6**: 12-18.
4. D.E. Pegg, L. Wang, D. Vaughan, Cryopreservation of articular cartilage. Part 3: The liquidus-tracking method, *Cryobiology* (2006) **52**: 360-368.
5. X. Yu, S. Zhang, G. Chen, Modeling the addition/removal of dimethyl sulfoxide into/from articular cartilage treated with the liquidus-tracking method, *Int. J. Heat Mass Transf.* (2019) **141**: 719-730.
6. A. Piasecka-Belkhat, *Interval boundary element method for imprecisely defined unsteady heat transfer problem* (in Polish), Wyd. Politechniki Śląskiej, Gliwice, 2011.
7. A. Piasecka-Belkhat, A. Korczak, Analysis of ultrashort laser pulse irradiation with 2d thin metal films using the fuzzy lattice boltzmann method, *J. Theor. Appl. Mech.* (2021) **58**: 209-219.
8. A. Skorupa, A. Piasecka-Belkhat, Numerical Modeling of Heat and Mass Transfer during Cryopreservation Using Interval Analysis, *Appl. Sci.* (2021) **11**: 302.

9. W. Liu, G. Zhao, Z. Shu, T. Wang, K. Zhu, D. Gao, High-precision approach based on microfluidic perfusion chamber for quantitative analysis of biophysical properties of cell membrane, *Int. J. Heat Mass Transf.* (2015) **86**: 869-879.
10. B. Mochnacki, J. Suchy, *Numerical methods in computations of foundry processes* (in Polish), Wydawnictwo Naukowe PWN, Kraków, 1993.

## **APPLICATION OF FUZZY FINITE DIFFERENCE METHOD IN HEAT AND MASS TRANSFER DURING CRYOPRESERVATION PROCESS**

### **Abstract**

In the paper, the numerical analysis of heat and mass transfer proceeding in the articular cartilage sample subjected to a cryopreservation process is presented. The two-dimensional, axially symmetrical model with fuzzy thermophysical parameters is considered. The base of the heat transfer model is the fuzzy Fourier equation, while the phenomenon of cryoprotectant transport through the extracellular matrix is described by the fuzzy mass transfer equation. The liquidus tracking (LT) approach was used to control the temperature and the concentration of cryoprotectant (CPA) to prevent the formation of ice regardless of the cooling or heating rate. The problem under discussion was solved using the fuzzy finite difference method using  $\alpha$ -cuts with the application of the rules of directed interval arithmetic. Additionally, the trapezoidal approximation of fuzzy articular cartilage thermophysical parameters is applied. In the final part of the paper, the results of numerical simulations are compared with the results of experiments carried out for deterministically defined thermophysical parameters.

**Keywords:** cryopreservation, heat and mass transfer, fuzzy finite difference method, fuzzy numbers, directed interval arithmetic.

Marek KOKOT\*, Sebastian DEOROWICZ

## Chapter 6. OPTIMIZING SIGNATURE SELECTION SCHEME FOR K-MER COUNTING PROBLEM

### 6.1. Motivation

#### 6.1.1. *k*-mer counting

The amount of data produced by next-generation sequencing instruments is enormous. A single experiment may result in hundreds of billions of symbols (bases) grouped in reads, each of length up to hundreds of letters. Reads are short (in comparison with the genome length) and are not error-free. To be able to obtain any knowledge from such a noisy data, it is required to have each genome base represented into multiple reads. The average number of reads in which a single base is represented, is called depth of coverage. The higher the depth of coverage, the better for quality of analyses. Managing such amounts of data is challenging and requires development of high-performance algorithms. Many bioinformatics analyses are realized in a form of a pipeline constituted of a couple of steps. Often the first step is so-called *k*-mer counting. Formally, *k*-mer (*k*-length string) counting algorithm may be defined as follows. The input of the algorithm are a set of sequences (usually reads) and the value of *k*. The output is a set of pairs, where the first element is a *k*-mer being a substring of at least one input sequence and the second element is the number of occurrences of this *k*-mer in all the sequences. The strand (forward or reverse) a read originates from is unknown. Thus, usually canonical *k*-mers are counted. A canonical *k*-mer is the lexicographically smaller of a *k*-mer and its reverse complement. A reverse complement of a *k*-mer is obtained by reversing its symbols and changing them according to the mapping: A→T, C→G, G→C, T→A. For example, a reverse complement of 5-mer **ATGCT** is **AGCAT**, and

---

\* Corresponding author: marek.kokot@polsl.pl, ul. Akademicka 16, 44-100 Gliwice, PL. Department of Algorithmics and Software, Silesian University of Technology.

as the reverse complement is lexicographically smaller, it is also a canonical  $k$ -mer. The ordering of  $k$ -mer does not need to be lexicographic, for example, DSK [1] uses  $A < C < T < G$  as an ordering of symbols.

Some examples of bioinformatics analyses where  $k$ -mer counting is used are de novo assembly [2], fast multiple sequence alignment [3], repeat detection [4], correction of sequencing reads [5]. There are also alignment-free analyses in which sets of  $k$ -mers of multiple samples are combined to get some biological knowledge. For example, in a DIAMUND [6] algorithm,  $k$ -mers of healthy parents and a child with a genetic disease are combined to find novel mutations. Alternatively, the same strategy may be applied to healthy and diseased (e.g., cancerous) tissues. Another examples of similar approaches are NIKS [7], which is also designed to find a mutation in closely related samples and GenomeTester4 [8], which allows to find group-specific  $k$ -mers to identify bacteria.

There were many approaches designed to solve  $k$ -mer counting problem presented in the literature. Very often they utilize specialized, dictionary-based data structures tuned to work well in a parallel environment. Jellyfish [12], DSK [1], Gerbil [16], MSPKmerCounter [15] use hash tables as a main data structure. In KMC 1 [17], KMC 2 [18], KMC 3 [19] sorting is used to identify identical  $k$ -mers. The khmer [9, 10], BFCOUNTER [13] and Turtle [14] are examples of algorithms utilizing Bloom filters. In a KCMBT [20] multiple tries are used. Tallymer [21] exploits suffix arrays. Some of the mentioned algorithms are so-called disk-based, which means they utilize disk space to reduce memory consumption. Those are KMC 1, KMC 2, KMC 3, DSK, Gerbil, MSPKmerCounter. The main idea of these algorithms is to split the data into many bins, in a way that allows to process each bin independently and consuming less memory than in the case of processing the whole input at once. The best in terms of memory usage and computation time are KMC 3, DSK, and Gerbil. A detailed comparison of  $k$ -mer counting software may be found in [11].

### 6.1.2. Disk-based approaches and optimization criteria

Disk-based  $k$ -mer counters are usually two-stage algorithms. In the first stage, all  $k$ -mers are extracted from the input sequences and assigned to one of  $n$  bins. Each bin is, in fact, a disk file. The  $k$ -mers are assigned to bins using some function  $f$ , so it is assured that each instance of the same  $k$ -mer in the input will be stored in the same bin. The number of bins,  $n$ , is a couple of hundred which is much less than the number of distinct  $k$ -mers,

so in one bin there are many distinct  $k$ -mers. This way each bin may be processed independently in the second stage. Concatenation of  $k$ -mers counted per each bin is a final result of the algorithm.

It is desired to keep the bins evenly distributed, more precisely to keep the biggest (in a term of the number of contained  $k$ -mers) bin as small as possible. The reason is that all  $k$ -mers from a bin must be loaded into RAM, so the number of  $k$ -mers in the largest bin determines the minimal amount of RAM required to finish computations. On the other hand, it is also desired to keep the total size of bins (in bytes this time) as small as possible. The total bins size determines disk space requirements for intermediate files. In most cases, the disk space is not an issue as it is quite cheap (especially in comparison with RAM), but the time access is much higher. For this reason, keeping the total bins size small does not only decrease disk space requirements, but also decreases running time. The main issue with storing  $k$ -mers in intermediate files is the fact that two adjacent  $k$ -mers from the input sequence share  $k - 1$  common symbols, but when assigned to the different bins, the common symbols must be stored twice. Having  $f$  increasing chances for a series of adjacent  $k$ -mers to be assigned to the same bin would help reduce the redundancy. Minimizer of a  $k$ -mer is a lexicographically smallest  $m$ -mer ( $m < k$ ) of a  $k$ -mer. It is likely for two adjacent  $k$ -mers to have the same minimizers which makes the minimizer approach a good candidate of  $f$ . If  $l$  consecutive  $k$ -mers share the same minimizer, they may be stored together occupying  $k + f - 1$  symbols in a form of super- $k$ -mer. This is much better than storing the  $k$ -mers in plain and spending  $l \times k$  symbols. The example presenting this idea is shown in Fig. 6.1.

TGTTCCATTTTTATGCTATAACATTTTGTATTATTA	TGTTCCATTTTTATGCTATAACATTTTGTATTATTA
TGTTCCATTTTTATGCTATA	TGTTCCATTTTTATGCTATAA
GTTCCATTTTTATGCTATAA	
TTCCTATTTTTATGCTATAAC	TTCCTATTTTTATGCTATAACA
TCCTATTTTTATGCTATAACA	
CCTATTTTTATGCTATAACAT	CCTATTTTTATGCTATAACATTTTGTATTATTA
CTATTTTTATGCTATAACATT	super- $k$ -mers
TATTTTTATGCTATAACATTT	
ATTTTTATGCTATAACATTTT	
TTTTATGCTATAACATTTTG	
TTTATGCTATAACATTTTGT	
TTATGCTATAACATTTTGTA	
TATGCTATAACATTTTGTAT	
ATGCTATAACATTTTGTATT	
TGCTATAACATTTTGTATTA	
GCTATAACATTTTGTATTAT	
CTATAACATTTTGTATTATT	
TATAACATTTTGTATTATTA	

Fig. 6.1. Example of minimizer-based  $k$ -mer binning. On the left side, the sequence and all its 20-mers are presented. Colors were used to mark minimizers for  $m = 5$ . All  $k$ -mers with the same minimizer may be stored as a longer sequence (right side)

Rys. 6.1. Przykład przyporządkowania  $k$ -merów do kubełków opartego na minimizerach. Po lewej stronie przedstawiono sekwencję i wszystkie zawarte w niej 20-mery. Za pomocą kolorów oznaczono minimizery dla  $m=5$ . Wszystkie  $k$ -mery z tym samym minimizerem mogą być przechowywane w postaci dłuższej sekwencji (prawa strona)

Minimizers are not perfect, for example, usually the size of the biggest bin is much larger than the size of the second biggest. Also, the total size of bins seems not as good as possible. The with minimizers were previously noticed and described in [18]. It has been shown, that some  $m$ -mers tend to produce short super- $k$ -mers (which corresponds to higher total bins size, which in turn leads to higher disk usage and slower computations) and also causes bin sizes imbalance. As a solution signatures were proposed. The idea is to treat some  $m$ -mers as disallowed, meaning they are skipped when finding the lowest  $m$ -mer in a  $k$ -mer. There is a special bin for a  $k$ -mers built with only disallowed  $m$ -mers. This approach allowed to reduce both total bins sizes and the size of the largest bin.

It may be observed that the greater  $m$  is the lower is the probability that two adjacent  $k$ -mers share the same minimizer (or signature). It leads to a higher number of super- $k$ -mers and therefore to higher disk usage. On the other hand, the higher  $m$  the better  $k$ -mers are distributed into bins. As a consequence, some compromise must be made and typically  $5 \leq m \leq 12$ . In practice, when canonical  $k$ -mers are counted, only canonical  $m$ -mers are taken into account to assure the correctness of the result. The number of possible canonical  $m$ -mers (and also the number of bins) is  $2^{2m-1}$  if  $m$  is even and  $2^{m-1}(2m+1)$  if  $m$  is odd. As it was mentioned, it is desired to keep the number of bins couple of hundreds. For this reason, in practice, some bins are merged.

In [23] the frequency-based ordering was proposed. The idea is to count all  $m$ -mers from a part of the input data and sort the pairs ( $m$ -mers and counters) in non-decreasing order of counters. The resulting order of  $m$ -mers is used instead of a lexicographic one. Although this approach decreases the size of the largest bin significantly, it does not take into account the aspect of the total number of super- $k$ -mers. In [24, 25, 26] a universal hitting set, UHS, was presented. UHS is defined for specific values of  $m$  and  $k$ . It is a set of  $m$ -mers that for each possible  $k$ -mer it is assured that at least one of its  $m$ -mers is in UHS. In the simplest case, it is a set of all possible  $m$ -mers, but the presented idea is to find minimal UHS, i.e., containing as low  $m$ -mers as possible (without violating the UHS definition). Having UHS the idea to count  $k$ -mers is to treat all  $m$ -mers  $\notin$  UHS as disallowed.

## 6.2. Methods

Our goal is to find a minimizer-based binning scheme that minimizes two criteria:

1. The total number of super- $k$ -mers and.
2. The total number of  $k$ -mers assigned to the largest bin.

Usually, these criteria are exclusive, but as it turns out to some extent they may be both optimized. All presented heuristics starts with minimizers (each canonical  $m$ -mer allowed). During optimization, some  $m$ -mer will be disabled or re-enabled. The work is focused on human sequencing data. The first approaches were performed on human chromosome 22, but the results did not generalize to sequencing data. The same effect occurred for a bigger chromosome 11. In consequence as a training set 1,500,000 reads from real human sequencing data were taken.

The starting approach was to iteratively disable  $m$ -mer related to the largest bin. Single iteration was to find such  $m$ -mer and block it. The number of iterations was set to 1,000. At each iteration, the number of super- $k$ -mers, the total number of  $k$ -mers in the largest bin, and the total number of  $k$ -mers in the bin for disabled  $m$ -mers was recorded.

The main approach was based on simulated annealing, SA, [22]. The cost function was:

$$C = w_s n_s + w_m n_m, \quad (1)$$

where  $n_s$  is a total number of super- $k$ -mers,  $n_m$  is the number of  $k$ -mers in the largest bin,  $w_s$  and  $w_m$  are weights set to  $w_s = 1$ ,  $w_m = 250$ . The starting temperature,  $t_0$ , was set to  $-0.01 C_s / \ln(P_0)$ , where  $C_s$  is the value of cost function for starting solution (all  $m$ -mers allowed),  $P_0$ , an initial probability of acceptance of a worse solution, was set to 0.5. Let us denote the current temperature by  $t$ , the number of iteration by  $N$ , terminate temperature by  $t_k$ . At the end of each iteration, the temperature is decreased to  $\alpha t$ , where  $\alpha = \sqrt[N]{t_k/t_0}$ . At each iteration, a random  $m$ -mer is chosen and its state (allowed/disallowed) is reversed. It is more likely that lexicographically smaller  $m$ -mers will be selected as minimizers, consequently, lexicographically larger  $m$ -mers will tend to have only little impact on the value of cost function. For this reason,  $m$ -mers are not selected with uniform distribution. Instead, one of three geometric distributions is used at each iteration. The probability of success of those distributions are respectively 0.005, 0.002, 0.0005.



### 6.3. Results

In the experiments, three data sets were used, each containing sequencing reads of the human genome. The first one, denoted as HS1, is of size 1.35G bases, the second one, denoted as HS2, is of size 736.4G bases. In both sets, the average read length was 101. The third set, denoted as HS1 part, was a part of HS1 data set containing 1.5M reads. Results of the simple approach based on disallowing  $m$ -mer related to the largest bin are present in Fig. 6.2.

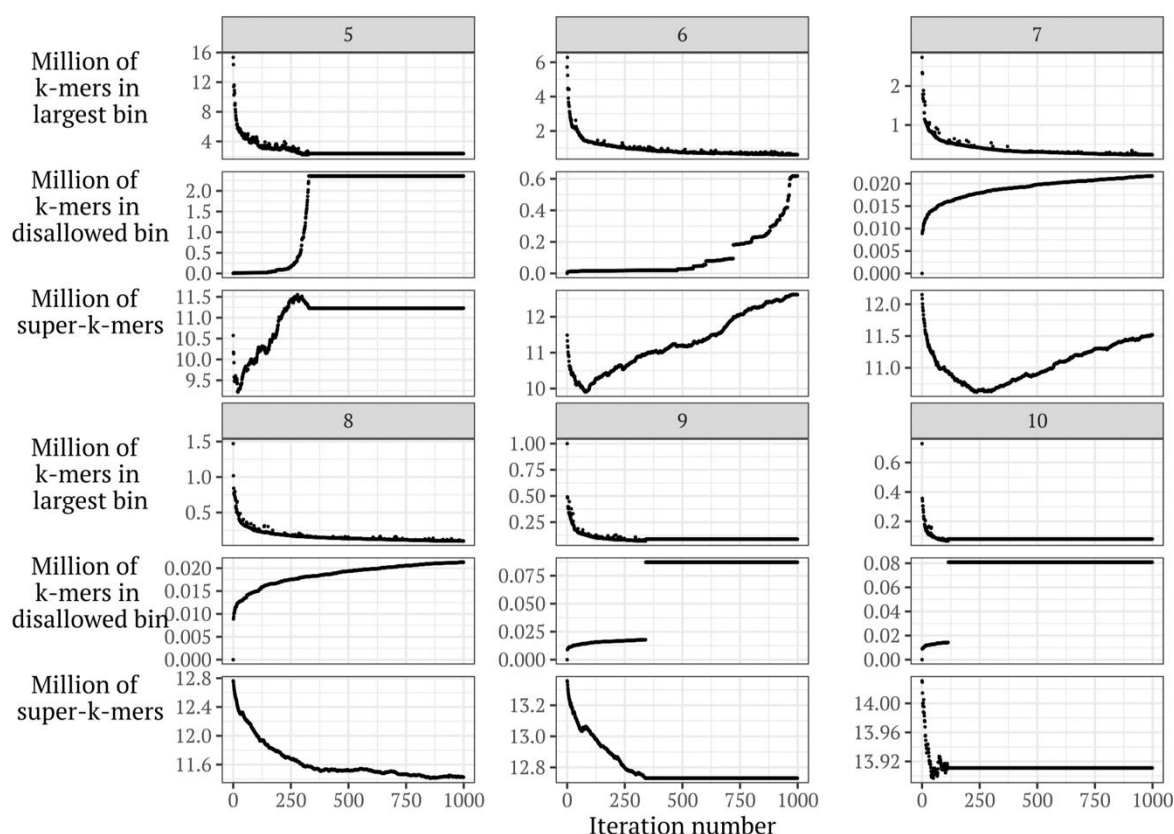


Fig. 6.2. Results of optimization based on iterative disallowing  $m$ -mer related to the largest bin,  $k = 28$ ,  $m$  is shown in the gray rectangle

Rys. 6.2. Wyniki optymalizacji bazującej na iteracyjnym blokowaniu  $m$ -mera związanego z największym kubelkiem,  $k = 28$ , w szarym prostokącie przedstawiona jest wartość  $m$

At the beginning (iteration 0; all  $m$ -mers are allowed) when  $m$  increases the number of  $k$ -mers in the largest bin decreases, and the number of super- $k$ -mers increases. It is in line with theoretical expectations. The fastest decrease of the number of  $k$ -mers in the largest bin is in the first 250 iterations. Interestingly, in this range also the number of super- $k$ -mers decreases. The decrease is especially significant for  $m < 8$ . It may be noticed that with further iterations the number of super- $k$ -mers starts to grow and for  $m \in \{5, 6\}$  it even exceeds the number of super- $k$ -mers at iteration 0. For  $m \in \{5, 9, 10\}$

there is a saturation after a relatively small number of iterations, which is because the bin for disallowed  $m$ -mers becomes the largest one. For  $m = 5$ , the total number of  $m$ -mers is low, and after a couple of hundreds of iterations a large fraction of  $m$ -mers is disabled, which leads to many  $k$ -mers containing only disallowed  $m$ -mers. The case of  $m > 8$  is more complex, the size of the largest bin is relatively small. What is interesting, the last disallowed  $m$ -mer is **TCCATTCCA** ( $m = 9$ ), **TGGAATGGAA** ( $m = 10$ ), **CCATTCCATTC** ( $m = 11$ , not presented on the plot). It may be speculated that the largest bin contains  $k$ -mers with tandem repeats.

Although this simple optimization technique allows optimizing both criteria to some point, it is not perfect. The SA and simple approach were run for HS 1 part, and resulting binning were used for evaluation on all data sets. The number of iterations in SA was set to 2 M. The evaluation was performed using a modified version of KMC, in which original binning was replaced with the new ones. For HS 1 part, the number of  $k$ -mers in the largest bin was 280.90  $k$  for  $m = 7$ , which is a minimal value from all tested heuristics, but at the same time, the total number of super- $k$ -mers was 11.53 M. It is worse than in the case of KMC (10.32 M) and only slightly better than in the case of pure minimizers (12.15 M). SA for  $m = 7$  leads to 9.84 M super- $k$ -mers which is the best value found in experiments. The number of  $k$ -mers in the largest bin was 384.25  $k$ , which is better than KMC (711.39  $k$ ). For HS 1 also simple optimization for  $m = 7$  leads to the best result in terms of the size of the largest bin (216.46 M), but again at a cost of the total number of super- $k$ -mers (10.41 G), while in case of SA it is only 8.89 G (and the size of largest bin is 348.09 M). Results of SA for  $m = 8$  are also interesting as the total number of super- $k$ -mers is 9.35 M and the number of  $k$ -mers in the largest bin is 225.84 M (which is close to the best). In the case of HS 3 the best result in terms of the largest bin are for SA for  $m = 8$  (1.19 G), the total number of super- $k$ -mers, in this case, is 51.02 G. The best result in terms of the total number of super- $k$ -mers is SA for  $m = 7$  (48.48 G), the number of  $k$ -mers in the largest bin, in this case, is 2.04. One dimensional model was predicated using described geometry and parameters to predict creation of rings. However, problem is only described on one coordinate, rings aren't noticeable – only where product precipitate.

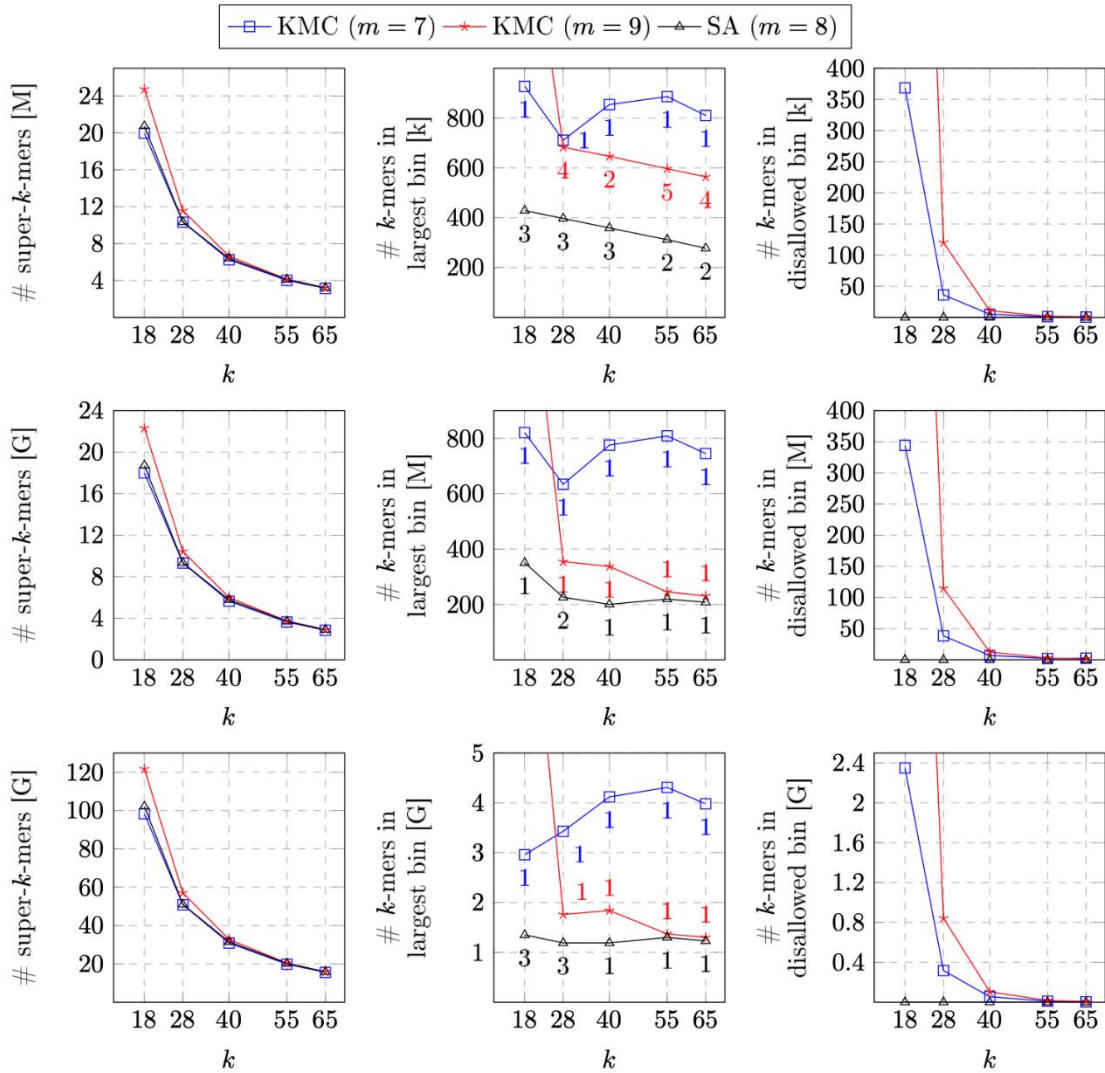


Fig. 6.3. Comparison of signature binning used in KMC and developed with simulated annealing for various  $k$  values. The first row of plots shows results for a part of HS 1 data set used as an input of simulated annealing algorithm, the second row shows the result on whole HS 1 data set, the third shows results for HS 2 data set. The first column presents the total number of super  $k$ -mers, the second one presents the total number of  $k$ -mers in the largest bin, the third one presents the total number of  $k$ -mers in the bin of disallowed  $m$ -mers. Additionally, the number of  $m$ -mers assigned to the biggest bins are shown on plots in the second column. In case of KMC ( $m=9$ ,  $k=18$ ) some values are excluded from charts to improve readability. This is caused by the fact that the disabled bin became the largest one. Its sizes were 1.78M, 1.6G, 9.83G  $k$ -mers for HS 1 part, HS 1 and HS 2 respectively

Rys. 6.3. Porównanie przyporządkowania  $k$ -merów do kubeków użytego w algorytmie KMC i opracowanego z wykorzystaniem symulowanego wyżarzania dla różnych wartości  $k$ . Pierwszy wiersz wykresów przedstawia wyniki dla wycinka zestawu HS 1, który był użyty jako wejście algorytmu symulowanego wyżarzania, drugi wiersz przedstawia wyniki dla całego zestawu HS 1, trzeci wiersz przedstawia wyniki dla zestawu HS 2. Pierwsza kolumna przedstawia całkowitą liczbę super- $k$ -merów, druga przedstawia całkowitą liczbę  $k$ -merów w największym kubku, trzecia przedstawia całkowitą liczbę  $k$ -merów w kubku zabronionych  $m$ -merów. Dodatkowo liczba  $m$ -merów przypisanych do największego kubka jest przedstawiona na wykresach w drugiej kolumnie. W przypadku KMC ( $m=9$ ,  $k=18$ ) niektóre wartości zostały usunięte z wykresów dla poprawy czytelności. Jest to spowodowane tym, że kubek zablokowanych  $m$ -merów staje się największym kubkiem. Jego rozmiary to 1,78 M, 1,6 G, 9,83 G  $k$ -merów dla zestawów wycinek HS 1, HS 1, HS 2 odpowiednio

According to these results SA with  $m = 8$  was chosen as the best and compared to original KMC  $m$ -mers binning for various values of  $k$  on all data sets. The results are presented in Fig. 6.3. For  $k = 18$ ,  $m = 9$  the largest bin is a bin of disallowed  $m$ -mers. As expected, in the case of KMC increasing  $m$  causes a reduction of the size of the largest bin and an increase of the total number of super- $k$ -mers. It may be noticed that the number of super- $k$ -mers for SA is only slightly higher than in the case of KMC with  $m = 7$ . The size of the largest bin is relevantly lower in the case of SA than in the case of KMC which compensates a slightly higher total number of super- $k$ -mers. It is also worth noting that results presented on the charts expose the number of  $k$ -mers per file and, in some cases, the largest file reflects multiple  $m$ -mers. It means that the size of the largest file could be further lowered in KMC by allowing more temporary files (in KMC the default number of intermediate files is 512).

## 6.4. Discussion

In this paper two optimization methods for  $m$ -mer binning scheme for  $k$ -mer counting problem were presented. The first method was very simple and was intended to show some properties of the minimizer-based approach in  $k$ -mer counting. The second approach, simulated annealing, was more complex and allowed to optimize both criteria (total number of super- $k$ -mers as well as the number of  $k$ -mers in the largest bin). It confirms that the parameters of this metaheuristic were suitable. The results show that a trained binning scheme leads to satisfactory results when used as a part of KMC algorithm. In future work, the impact on computational time, RAM, and disk usage should be measured.

## Bibliography

1. G. Rizk, D. Lavenier, R. Chikhi, DSK:  $k$ -mer counting with very low memory usage, *Bioinformatics* (2013) 29(5):652-653.
2. P.E.C. Compeau, P.A. Pevzner, G. Tesler, How to apply de Bruijn graphsto genome assembly, *Nature Biotechnology* (2011) 29(11):987.
3. R.C. Edgar, MUSCLE: multiple sequence alignment with high accuracy and high throughput, *Nucleic Acids Research* (2004) 32(5):1792-1797.

4. S. Kurtz, A. Narechania, J. C. Stein, D. Ware, A new method to compute K-mer frequencies and its application to annotate large repetitive plant genomes, *BMC Genomics* (2008) 9(1):517.
5. Y. Liu, J. Schroder, B. Schmidt, Musket: a multistage k-mer spectrum-based error corrector for Illumina sequence data, *Bioinformatics* (2012) 29(3):308-315.
6. S.L. Salzberg, M. Perteza, J.A. Fahrner, N. Sobreira, DIAMUND: Direct comparison of genomes to detect mutations, *Human Mutation* (2014) 35(3):283-288.
7. K.J.V. Nordstrom, M.C. Albani, G.V. James, C. Gutjahr, B. Hartwig, F. Turck, U. Paszkowski, G. Coupland, K. Schneeberger, Mutation identification by direct comparison of whole-genome sequencing data from mutant and wild-type individuals using k-mers, *Nature Biotechnology* (2013) 31(4):325.
8. L. Kaplinski, M. Lepamets, M. Remm, GenomeTester4: a toolkit for performing basic set operations-union, intersection and complement on k-mer lists, *Gigascience* (2015) 4(1):58.
9. Q. Zhang, J. Pell, R. Canino-Koning, A.C. Howe, C.T. Brown, These are not the k-mers you are looking for: efficient online k-mer counting using a probabilistic data structure, *PloS one* (2014) 9(7):e101271.
10. M.R. Crusoe, H.F. Alameldin, S. Awad, E. Boucher, A. Caldwell, R. Cartwright, A. Charbonneau, B. Constantinides, G. Edvenson, S. Fay et al., The khmer software package: enabling efficient nucleotide sequence analysis, *F1000Research* (2015) 4.
11. Manekar, Swati C., Shailesh R. Sathe, A benchmark study of k-mer counting methods for high-throughput sequencing, *GigaScience* (2018) 7.12: giy125.
12. G. Marcais, C. Kingsford, A fast, lock-free approach for efficient parallel counting of occurrences of k-mers, *Bioinformatics* (2011) 27(6):764-770.
13. P. Melsted, J. K. Pritchard, Efficient counting of k-mers in DNA sequences using a bloom filter, *BMC Bioinformatics* (2011) 12(1):333.
14. R.S. Roy, D. Bhattacharya, A. Schliep, Turtle: Identifying frequent kmers with cache-efficient algorithms, *Bioinformatics* (2014) 30(14):1950-1957.
15. Y. Li et al., MSPKmerCounter: a fast and memory efficient approach for k-mer counting, *arXiv preprint arXiv:1505.06550* (2015).
16. M. Erbert, S. Rechner, M. Muller-Hannemann, Gerbil: a fast and memoryefficient k-mer counter with GPU-support, *Algorithms for Molecular Biology* (2017) 12(1):9.

17. S. Deorowicz, A. Debudaj-Grabysz, S. Grabowski, Disk-based k-mer counting on a PC, *BMC Bioinformatics* (2013) 14(1):160.
18. S. Deorowicz, M. Kokot, S. Grabowski, A. Debudaj-Grabysz, KMC 2: fast and resource-frugal k-mer counting, *Bioinformatics* (2015) 31(10):1569-1576.
19. M. Kokot, M. Dlugosz, S. Deorowicz, KMC 3: counting and manipulating kmer statistics, *Bioinformatics* (2017) 33(17):2759-2761.
20. A.A. Mamun, S. Pal, S. Rajasekaran, KCMBT: a k-mer Counter based on Multiple Burst Trees, *Bioinformatics* (2016) 32(18):2783-2790.
21. S. Kurtz, A. Narechania, J.C. Stein, D. Ware, A new method to compute K-mer frequencies and its application to annotate large repetitive plant genomes, *BMC Genomics* (2008) 9(1):517.
22. S. Kirkpatrick, C.D. Gelatt, M.P. Vecchi et al., Optimization by simulated annealing, *Science* (1983) 220(4598):671680.
23. R. Chikhi, A. Limasset, S. Jackman, J.T. Simpson, P. Medvedev, on the representation of de Bruijn graphs, In *International conference on Research in computational molecular biology*, pages 35-55. Springer (2014).
24. G. Marcais, D. Pellow, D. Bork, Y. Renstein, R. Shamir, C. Kingsford, Improving the performance of minimizers and winnowing schemes, *Bioinformatics* (2017) 33(14):i110i117.
25. Y. Orenstein, D. Pellow, G. Marcais, R. Shamir, C. Kingsford, Compact universal k-mer hitting sets, In *International Workshop on Algorithms in Bioinformatics*, pages 257-268. Springer (2016).
26. Y. Orenstein, D. Pellow, G. Marcais, R. Shamir, C. Kingsford, Designing small universal k-mer hitting sets for improved analysis of high-throughput sequencing, *PLoS Computational Biology* (2017) 13(10):e1005777.

## **OPTIMIZING SIGNATURE SELECTION SCHEME FOR K-MER COUNTING PROBLEM**

### **Abstract**

The first step of many bioinformatic applications is counting all substrings of specific length occurring in the set of input sequences. Despite the conceptual simplicity of this task, it is far from trivial on real data sets. Therefore, there were a lot of algorithms

proposed in the literature. Some of them are disk-based, where disk space is used to reduce RAM consumption. Efficient algorithms of this group tend to split input data into multiple bins that may be further processed independently. The splitting procedure seems to be crucial in terms of disk and RAM usage. In this paper, we discuss two optimization techniques to improve the splitting procedure. The first one is simple and is used to characterize the data. The second one is more complex as it is based on a simulated annealing metaheuristic.

**Keywords:** *k*-mer counting, simulated annealing, metaheuristics.

Piotr JÓŻWIK-WABIK<sup>1</sup>, Bartłomiej GŁADYS<sup>1</sup>, Marek HERMANSA<sup>1</sup>, Dawid MACHA<sup>1</sup>, Seweryn KALISZ<sup>1</sup>, Tomasz STRZODA<sup>1</sup>, Paweł FOSZNER<sup>2</sup>, Adam POPOWICZ<sup>3</sup>, Michał MARCZYK<sup>\*4</sup>

## **Chapter 7. REMOVING COMPRESSION ARTIFACTS ON WHOLE SLIDE HE-STAINED HISTOPATHOLOGICAL IMAGES**

### **7.1. Introduction**

Histopathological tissue slides stained with hematoxylin and eosin (HE) are commonly used in medical diagnosis. The hematoxylin stains cell nuclei blue, and eosin stains the extracellular matrix and cytoplasm pink. Other structures are seen with different combinations of these colors. A single slide contains a wealth of information that can be used to monitor the mechanisms contributing to disease progression or patient survival [1]. Since whole-slide imaging (WSI) scanners were introduced, it is possible to digitize large fragment of tissue section in a cost-effective and efficient manner. One of the biggest advantages of WSI compared to conventional glass slides is that they enable the use of automatic image analysis methods. This allows to perform diagnosis-related tasks like segmentation of Region of Interest (ROI) such as tumor region detection [2], lymphocyte detection [3] and many others.

Most WSI scanners perform scanning at 20× or 40× magnification with a spatial resolution in the order of 0.50 μm/pixel and 0.25 μm/pixel, respectively [4]. WSIs are often saved as SVS files. In this format the images are stored as a pyramid structure with different resolution at each level of the pyramid. Because of the large size (highest-

---

<sup>1</sup> Faculty of Automatic Control, Electronics and Computer Science, Silesian University of Technology.

<sup>2</sup> Department of Graphics, Computer Vision and Digital Systems, Silesian University of Technology.

<sup>3</sup> Department of Electronics, Electrical Engineering and Microelectronics, Silesian University of Technology.

\* Corresponding author: [michal.marczyk@polsl.pl](mailto:michal.marczyk@polsl.pl), ul. Akademicka 16, 44-100 Gliwice, PL

<sup>4</sup> Department of Data Science and Engineering, Silesian University of Technology.



resolution images in SVS can have hundreds of thousands of pixels), the captured RGB images are compressed most commonly with JPEG or JPEG 2000 methods.

Applying JPEG compression to WSI may introduce image artifacts. When the quality parameter  $Q=30$  is used, the resulting  $8 \times 8$  pixel blocks can be visually seen. These artifacts may have a negative impact on the segmentation of small structures observed in the tissue image. In image analysis a large number of methods designed to reduce compression artifacts exist, ranging from relatively simple hand-designed filters to machine learning-based image restoration methods. Among common filtering methods, there are adaptive filtering with locally adjusted filter kernels [5], bilateral filters [6] or block-shift filtering-based algorithm [7]. Learning-based methods are built on large datasets to approximate inversion of the compression function. Some examples are multi-layer perceptron for JPEG deblocking [8], piecewise linear regression in the space of DCT [9] or maximum a posteriori (MAP) framework build upon experts scores [10]. To illustrate the problem, we applied a segmentation-based method for lymphocyte identification (LISI) [11, 12] on whole-slide HE stained tissue images with a different JPEG compression quality parameter  $Q$  (Figure 7.1). As can be seen, identifying lymphocytes (represented by blue cluster) and other tissue structures under existence of compression artifacts is problematic and the segmented regions might be improper (Figure 7.1). In this paper, we introduce an edge-preserving algorithm for removing compression artifacts. First, using dataset containing smaller fragments of uncompressed image, we presented visually the results of proposed method and evaluated its performance using several image quality measures. Then, using whole-slide image data with compressed images, we showed the impact of artifacts removal on the segmentation obtained by the LISI algorithm.

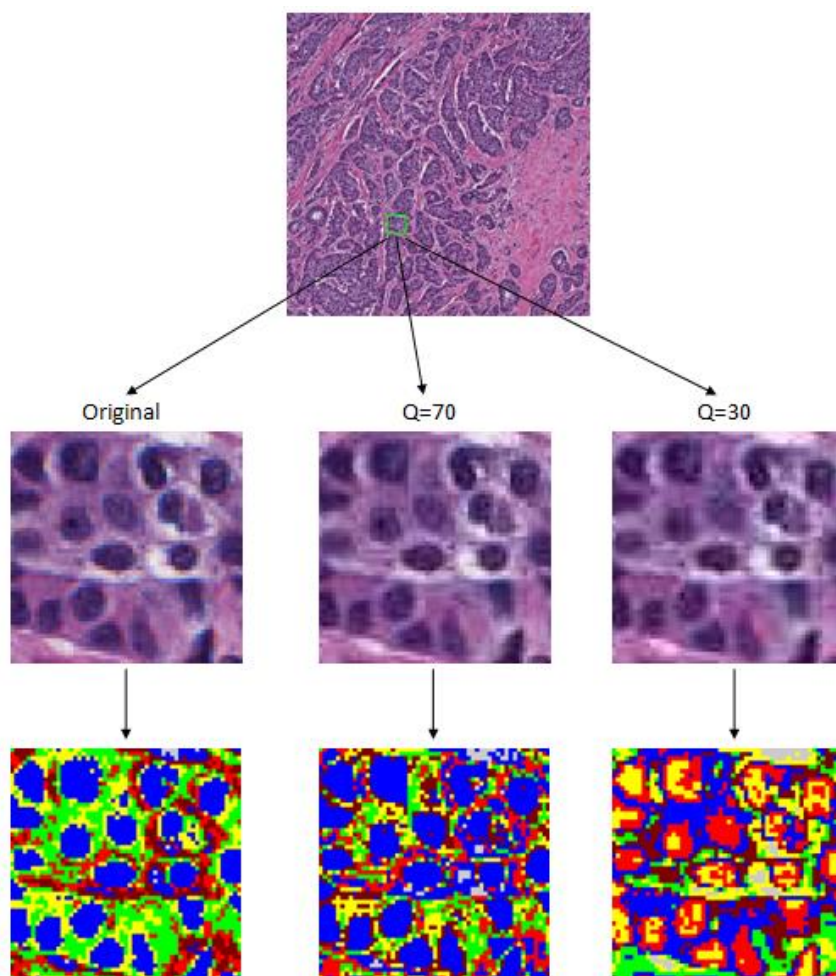


Fig. 7.1. Results of the image segmentation using LISI method on the same part of a whole-slide image with different compression quality parameter

Rys. 7.1. Wyniki segmentacji obrazu metodą LISI na tej samej części obrazu całej tkanki dla różnych wartości parametru jakości kompresji

## 7.2. Materials and methods

### 7.2.1. Data

BreCaHAD dataset contains 162 histopathological images of breast cancer divided into 17 different cases [13]. The images were obtained from archival exemplary cases of surgical pathology that were archived for educational purposes. Each image was taken with 40x magnification and saved as 1360x1024 uncompressed TIF file.

TCGA-BRCA dataset contains 1 987 whole slide images of breast cancer patients [14]. The images were scanned with usually 40x magnification and saved in SVS format using lossy JPEG compression with quality  $Q$  between 30 and 70. We randomly selected

a single image with  $Q$  equal 30 to show the results of segmentation after using proposed compression artifacts removal method.

### 7.2.2. Image quality metrics

Mean Squared Error (MSE) and Peak Signal-to-Noise Ratio (PSNR) are the most widely used metrics to evaluate the quality of reconstructed images after artifact removal. MSE is computed by averaging squared intensity differences of the distorted image and the original image. PSNR is the most versatile measure for image restoration tasks and can be represented as follows:

$$PSNR = 10 \cdot \log_{10} \left( \frac{MAX_I^2}{MSE} \right) \quad (1)$$

where  $MAX_I$  is the maximum possible pixel value of the image.

These two methods have been criticized because they do not correlate well with perceived quality measurement. To face these issues, Structural Similarity index (SSIM) has been proposed [15], which operates on the principle of comparison of local patterns of pixel intensities. Given images  $I$  and  $J$ , SSIM is defined as follows:

$$SSIM(I, J) = \frac{(2\mu_I\mu_J + C_1)(2\sigma_{IJ} + C_2)}{(\mu_I^2 + \mu_J^2 + C_1)(\sigma_I^2 + \sigma_J^2 + C_2)} \quad (2)$$

where  $\mu$  is the average and  $\sigma$  is the variance of pixel intensity.

As the last measure, we calculated spatial correlation coefficient (SCC) between the high-pass filtered original and processed images as an index of the spatial quality. This measurement is based on the fact that the most important spatial information in original image is mostly concentrated in the high frequency domain.

### 7.2.3. Compression artifacts removal method

The algorithm starts by counting gradient magnitudes for each color channel of an image  $I$  and then binarizes them using Otsu method. Next, the edge map  $M$  is created using the following assumption: if a pixel is annotated as an edge in all channels, we assign the value 0, otherwise 1. Additionally, all pixels of the compression grid get also value 1. Filtering is then performed on  $M$  to get the weight matrix  $W$ . Subsequently, each channel of  $I$  is multiplied with corresponding values of  $M$  and filtered after that. As a result, we obtain the matrix  $R$ . At the end, we divide each value of  $R$  by corresponding values of  $W$  to obtain the smoothed image  $I'$ .

Proposed algorithm is inspired by the method described in [16], however we improved it significantly to make it relevant for processing of histopathological images. In our implementation we do not filter color channels separately, but we use combined information from all channels. Moreover, we decided to use pixels annotated as real edges, but we introduced an edge map. Last difference is that for filtering we use a  $7 \times 7$  gaussian filter with standard deviation  $\sigma=1.1$ .

### 7.3. Results and discussion

We used BreCaHAD dataset that includes uncompressed images to evaluate performance of proposed compression artifacts removal method under different compression rates. We tested three JPEG compression quality values Q: 30, 70 and 100. We compared the original images with the compressed one and the one after removing artifacts using three image quality metrics described in the previous section (Figure 7.2). Calculating different metrics on 162 images revealed mutual results that can be used before deciding about running compression artifacts removal. Application of proposed algorithm increased image quality ( $p=3.45e-06$  for PSNR,  $p=2.54e-12$  for SSIM,  $p=3.44e-06$  for SCC, measured using Wilcoxon test) for slides with low compression quality (Q=30). When Q was set to 70, in most cases the quality was reduced after removing artifacts. For Q=100, it seems that compression artifacts removal is not necessary. Results obtained by SCC metric seem to be most stable, as the results on different images are similar.

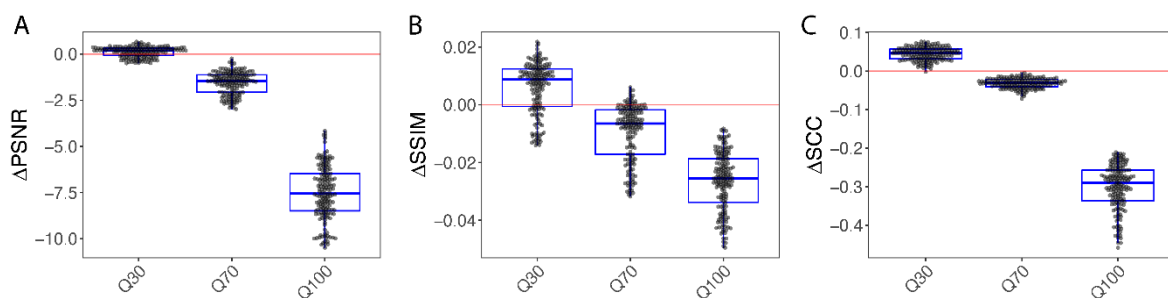


Fig. 7.2. Comparison of image quality before and after compression artifacts removal using PSNR (a), SSIM (b) and SCC (c) measures. Delta value shown in y-axis is the measure difference calculated between filtered and compressed image (the higher the value above 0, the better). X-axis shows results after compression with different quality values Q

Rys. 7.2. Porównanie jakości obrazu przed i po usunięciu artefaktów kompresji przy użyciu miar PSNR (a), SSIM (b) i SCC (c). Wartość delta pokazana na osi y to różnica miar obliczona między obrazem filtrowanym a skompresowanym (im wyższa wartość powyżej 0, tym lepiej). Oś X pokazuje wyniki po kompresji dla różnych wartości jakości Q

To visually show the effect of compression artifacts removal, we selected two images based on the image quality score values. We chose images compressed with  $Q=30$  value and plotted images with the best and the worst scores (Figure 7.3). Direct comparison of original images shows that there were probably some technical problems with staining for worst-score image, since we observe a large color variance within each individual cell nucleus (Figure 7.3 A, D). This might explain the problem of the proposed method to efficiently detect edges on this image, which led to worse result. Nevertheless, in both cases  $8 \times 8$  pixel blocks introduced during compression (Figure 7.3 B, E) are efficiently removed (Figure 7.3 C, F). Observed image blur is an effect of Gaussian smoothing. Despite the fact that two extreme examples were selected, visually it is hard to find the difference between processed images. Further research is required in order to obtain higher correlation between results after compression artifacts removal and image quality metrics outcome.

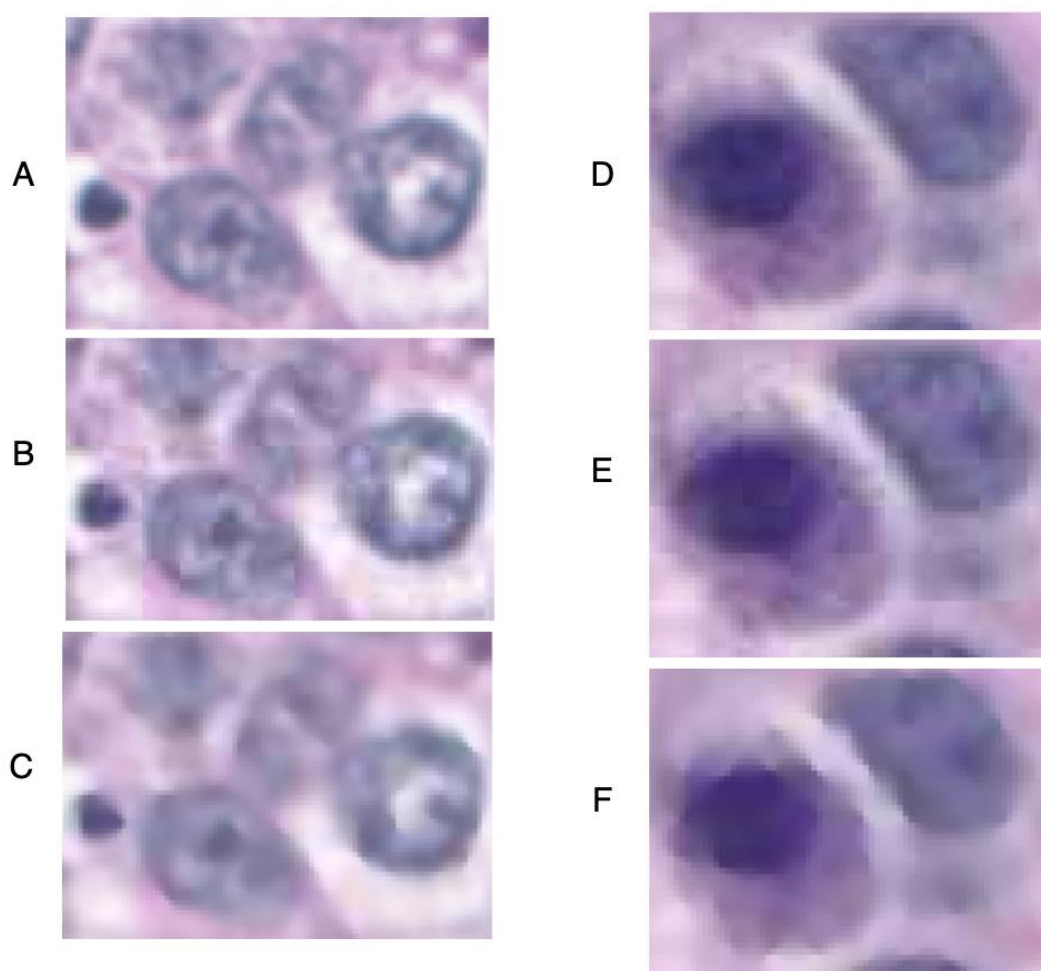


Fig. 7.3. Zoomed sections of the images with the worst (left) and the best (right) image quality scores after removing compression artifacts. Individual panels show original image (A, D), image compressed with  $Q=30$  (B, E) and image after compression artifacts removal (C, F)

Rys. 7.3. Powiększone fragmenty obrazów z najgorszą (po lewej) i najlepszą (po prawej) jakością obrazu po usunięciu artefaktów kompresji. Poszczególne panele pokazują oryginalny obraz (A, D), obraz skompresowany dla  $Q=30$  (B, E) oraz obraz po usunięciu artefaktów kompresji (C, F)

We used TCGA-BRCA dataset that includes compressed images to visually evaluate influence of the proposed compression artifacts removal method on the image segmentation using LISI algorithm. Selected image presented on Figure 7.4 was scanned with 40x magnification and saved in SVS format using lossy JPEG compression with parameter  $Q=30$ . The color coding in LISI algorithm of the most important clusters is as follows: blue for nuclei, green for stroma and yellow for cytoplasm. It can be seen that the clusters obtained after removing the compression artifacts reflect the actual biological structures much better than in case with no processing. We visually compared all other images in the TCGA-BRCA dataset. For a significant number of images, the use of the compression artifact removal algorithm had a positive effect on the segmentation results obtained with the LISI algorithm. Unfortunately, it is impossible to quantify how much the use of the described algorithm affects obtained results, since the ground truth is not known.

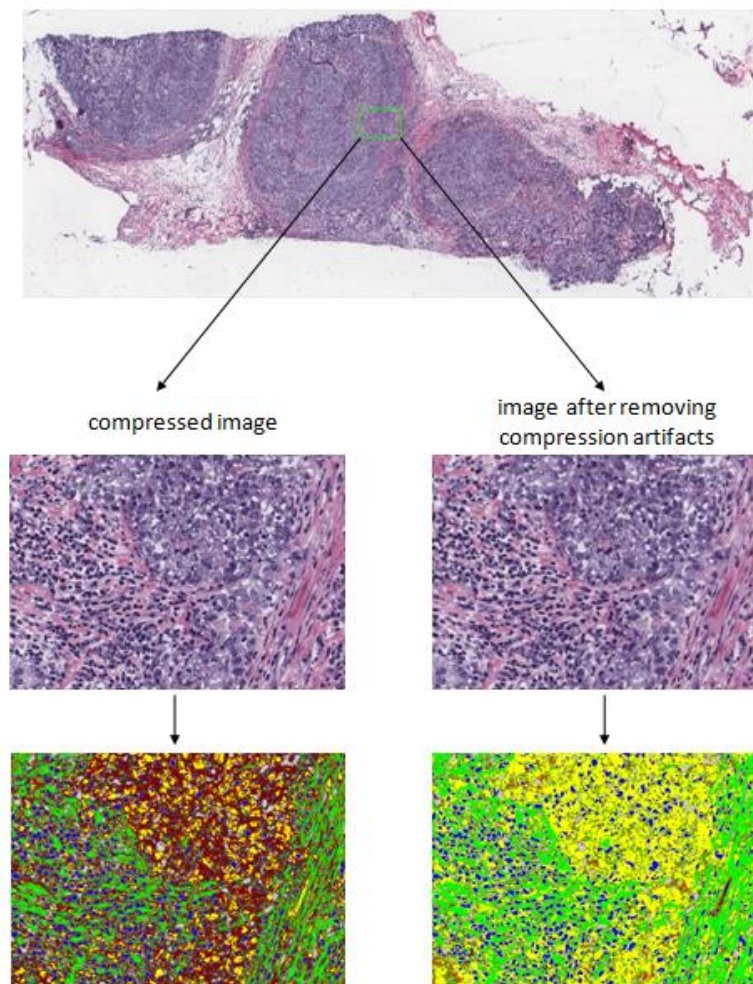


Fig. 7.4. The influence of the compression artifacts removal algorithm on the segmentation of whole-slide image using LISI method. Left side: segmentation results on original image, right side: segmentation results after removing the compression artifacts

Rys. 7.4. Wpływ algorytmu usuwania artefaktów kompresji na segmentację obrazu całej tkanki metodą LISI. Lewa strona: wyniki segmentacji na oryginalnym obrazie, prawa strona: wyniki segmentacji po usunięciu artefaktów kompresji

## 7.4. Conclusions

JPEG compression of HE-stained images is currently a standard in histopathology. Our approach to remove compression artifacts was successful, mostly for images compressed with low quality parameter Q, which is a commonly used setting. When Q value was set higher, like Q=70 in our case, performance of the proposed method was slightly worse. Nevertheless, the main goal of removing 8x8 compression grid has been achieved. We showed that existing of compression artifacts might affect image segmentation and their removal is crucial in that task. We plan to tune the algorithm to work better with images compressed with higher quality parameter, to develop an universal compression artifacts removal tool for HE stained WSI images.

## Acknowledgements

The research reported in this paper was co-financed by the European Union from the European Social Fund in the framework of the project "Silesian University of Technology as a Center of Modern Education based on research and innovation" POWR.03.05.00-00-Z098/17.

## Bibliography

1. M. Aswathy, M. Jagannath, Detection of breast cancer on digital histopathology images: Present status and future possibilities. *Informatics in Medicine Unlocked* **8**, 74-79 (2017).
2. F.A. Spanhol, L.S. Oliveira, C. Petitjean, L. Heutte, in *2016 international joint conference on neural networks (IJCNN)*. (IEEE, 2016), pp. 2560-2567.
3. J. Saltz *et al.*, Spatial Organization and Molecular Correlation of Tumor-Infiltrating Lymphocytes Using Deep Learning on Pathology Images. *Cell Reports* **23**, 181-193.e187 (2018).
4. S. Nam *et al.*, Introduction to digital pathology and computer-aided pathology. *J Pathol Transl Med* **54**, 125-134 (2020).
5. D. Tschumperlé, R. Deriche, Vector-valued image regularization with PDEs: A common framework for different applications. *IEEE transactions on pattern analysis and machine intelligence* **27**, 506-517 (2005).
6. T. Wang, G. Zhai, JPEG2000 image postprocessing with novel trilateral deringing filter. *Optical Engineering* **47**, 027005 (2008).

7. G. Zhai, W. Lin, J. Cai, X. Yang, W. Zhang, Efficient quadtree based block-shift filtering for deblocking and deringing. *Journal of Visual Communication and Image Representation* **20**, 595-607 (2009).
8. G. Qiu, MLP for adaptive postprocessing block-coded images. *IEEE transactions on circuits and systems for video technology* **10**, 1450-1454 (2000).
9. K. Lee, D.S. Kim, T. Kim, Regression-based prediction for blocking artifact reduction in JPEG-compressed images. *IEEE Transactions on Image Processing* **14**, 36-48 (2004).
10. D. Sun, W.-K. Cham, Postprocessing of low bit-rate block DCT coded images based on a fields of experts prior. *IEEE Transactions on Image Processing* **16**, 2743-2751 (2007).
11. F. Binczyk, M. Marczyk, J. Polanska, in *MAQC Society 2nd Annual Meeting*. (Shanghai, China, 2018), pp. 33.
12. F. Binczyk, M. Marczyk, J. Polanska, in *Computational Approaches in Precision Medicine*. (Vienna, Austria, 2017), pp. poster.
13. A. Aksac, D.J. Demetrick, T. Ozyer, R. Alhadjj, BreCaHAD: a dataset for breast cancer histopathological annotation and diagnosis. *BMC Research Notes* **12**, 82 (2019).
14. K. Clark *et al.*, The Cancer Imaging Archive (TCIA): Maintaining and Operating a Public Information Repository. *Journal of Digital Imaging* **26**, 1045-1057 (2013).
15. Z. Wang, A.C. Bovik, H.R. Sheikh, E.P. Simoncelli, Image quality assessment: from error visibility to structural similarity. *IEEE transactions on image processing* **13**, 600-612 (2004).
16. B. Oztan, A. Malik, Z. Fan, R. Eschbach, in *Color Imaging XII: Processing, Hardcopy, and Applications*. (International Society for Optics and Photonics, 2007), vol. 6493, pp. 649306.

## **REMOVING COMPRESSION ARTIFACTS ON WHOLE SLIDE HE-STAINED HISTOPATHOLOGICAL IMAGES**

### **Abstract**

Whole-slide imaging in histopathology produces high-resolution digital files that may take up an enormous amount of disk space, therefore a wide range of compression methods is used in practice. The most common is JPEG compression algorithm that splits an image into 8x8 pixel blocks with adjustable compression quality. In most cases,



the compression quality parameter is set to around 30, which decreases the size of a single image significantly, but also leads to the appearance of an artificial grid. The grid significantly impedes the work of segmentation algorithms that are used to explore the complex structure of the scanned tissue. In this paper, we introduced an edge-preserving algorithm for removing compression artifacts and showed how using it affects the image quality and image segmentation. We conclude that removing artifacts might be crucial, mostly in case where the compression quality parameter is low.

**Keywords:** histopathological images, HE-staining, JPEG lossy compression, artifacts removal.

Maciej DŁUGOSZ\*<sup>1</sup>

## Chapter 8. GENOME VARIANT CALLING IN CONTEXT OF SEQUENCING READS CORRECTION

### 8.1. Introduction

Illumina DNA sequencers produce a huge amount of data in lowering costs [16] Such a data has a form of short (about 100–150 bp) sequences called *reads*. A number of reads applications is long: cancer mutation discovery, genetic disorders analysis, genome *de novo* assembly, and many others. Data processing have to cope with many of technical problems, including huge data size, not uniform reads distribution within a genome, lack of reads covering (i.e. originating from) some of the genome regions, reads shorter than many of repeating fragments of a genome, and presence of sequencing errors.

The last problem is partially solved thanks to some built into algorithms strategies of errors tolerance. Besides, there was developed a group of specialized algorithms (correctors) aiming at the detection and elimination of the errors. The efficacy of those is often experimentally evaluated by simulating sequencing *in silico* or observing the impact of the correction on solving typical problems, like reads mapping. However, as the author knows, there is no thorough comparative analysis of such impact on real, full pipes of data processing. There were some tiny trials, but they were limited to two human chromosomes and generating simple statistics [1], or counting false-positive variants for simple model organism *C. elegans* [2]. More advanced experiments was presented in [3], however, the algorithm introduced therein, Coval, is a mixture of methods improving reads mapping, so it is not a correction algorithm *sensu stricto*. Moreover, the paper does not involve a comparison of other algorithms.

---

\* Corresponding author: maciej.dlugosz@polsl.pl, Akademicka 2A, 44-100 Gliwice, PL.

<sup>1</sup> Department of Algorithmics and Software, Silesian University of Technology.

As variant calling (VC) is a crucial process in clinical genetic testing [4], it is necessary to scrupulously explore all of its aspects. In this paper, the author shows experimental results of the first thorough evaluation of different correction algorithms impact on variant calling utilizing Illumina sequencing reads.

The experiments were performed with reads of two full genomes. A number of correctors were chosen to test various ideas of a correction. The corrected reads were utilized to perform the entire short VC process. Resulting variants sets were compared to a ground truth sets to measure the VC quality and, indirectly, the correction quality. Such an approach is a novel method of error correction algorithms evaluation. The obtained results give an overview on existing correctors quality and verify reasonability of correction utilization in VC application.

## **8.2. Sequencing data processing**

### **8.2.1. Error correction**

Typically, algorithms deployed to correct reads errors exploit, i.a., redundancy of the sequencing data. The redundancy level is measured with *sequencing depth*, which is defined as a ratio of the sum of all reads lengths and the genome length.

Error correction efficacy and strategies are varied. In a paper [5] correctors were categorized into three types: (i) *k-spectrum-based*, (ii) *suffix tree/array-based*, (iii) *multiple sequence alignment-based*. Also a type (iv) *hidden Markov-model-based* was proposed [6]. Moreover, some of the algorithms fulfill traits of different groups (*hybrid algorithms*), and some of them are difficult to include to any of them.

### **8.2.2. Variant calling**

The process of VC is a multi-stage task. Typically, it includes mapping of the reads to the reference genome, which is defined as aligning reads to the genome fragments, which sequences characterise high similarity to those reads, which suggests, that the reads originate from that fragments. Existing differences between reads and the genome fragment sequences can be caused by variants present in the sequenced genome or by other factors, like sequencing errors.

Reads mapping is a general task of different reads processing pipelines. In the context of VC it is followed by specialized processes responsible for proper variant determining, filtering, or annotating. In one of the simplest situations as a result two types of variants are obtained: single nucleotide variants (SNVs), which are differences of single genome bases, and short indels, which are leaks of short sequences in the proband genome or additional sequences appearing there. Evaluation of VC quality is possible with the utilization of available for some organisms *ground truth* variant sets, which represent our best knowledge about variants present in the sample.

### 8.3. Methods and data

#### 8.3.1. Experimental data

The experiments aimed at determining the impact of Illumina reads correction on the quality of variant calling results. The experiments performed on a few sets of reads. It has to be emphasised, that availability of variant ground truth sets is limited. One of such sets for human is the oft-used Genome in a Bottle [7], however, the choice of the second organism posed a problem due to a leak of publicly available sets. Finally, *Arabidopsis thaliana* was selected, which is a model organism with ground truth sets introduced as a result of 1001 Genomes Project [8]. In the case of human, there were also available confident call regions file, which was utilized in the experiments.

The following reads sets were used: SRR1945754 of sequencing depth ca. 180× for *A. thaliana*, and ERR174324, ERR174325, ERR174326 for human, each of the depth ca. 15×. To parametrize the sequencing depth, the data was prepared as follows:

- for *A. thaliana* pairs of reads were randomly shuffled, and the subset of the pairs was extracted to achieve depths of 30×, 60×, 90×,
- for *H. sapiens* three sets of reads pairs were used: ERR174324, concatenation of ERR174324 and ERR174325 and concatenation of all of three ones; such an approach was possible due to performing sequencing on the same sample, with the same machine etc.; it allowed to obtain sets of depths ca. 15×, 30×, 45×.

### 8.3.2. Error correction algorithms

Due to a plenty of existing algorithms, the limited set of them was selected, treating as criteria of choice being in the group of newest, most popular, or characterising of best quality noticed by other authors. The highest popularity of (i) algorithm type legitimizes its overrepresentation, whereas (iv) is represented only by one algorithm (PREMIER [9]) and as it is not publicly available, it was not analysed in the experiments. Fiona [10], initially appointed to experiments, representing the hybrid solution of groups (ii) and (iii), was also omitted, as its resulting reads had quality indicators decreased to the level, that caused VC returning no results. Table 8.1 presents correction algorithms compared in the experiments.

Table 8.1

Correction algorithms			
Algorithm	Type	Version	Describing paper
RECKONER	(i)	1.2	[11]
Musket	(i)	1.1	[12]
RACER	(i)	–	[13]
BLESS	(i)	1.02	[6]
Blue	(i)	1.1.3	[14]
Lighter	(i)	1.1.2	[15]
BFC	(i)	BFC-ht, version r181	[2]
Karect	(ii)	1.0	[16]
SAMDUDE	others	Uploaded 2 May, 2018	[1]

The majority of the algorithms need parametrization. The mostly required parameter is the oligomer ( $k$ -mer) length  $k$ . It was determined by performing a sequence of corrections with different odd  $k$  values and, if the correction succeeded, followed by VC. The value of  $k$  resulting in the best value in terms of F1-score was chosen. Actually, some of the algorithms have more sophisticated methods of the parameter determination, however, they are rather rules-of-thumb (e.g. BLESS needs to get  $k$  maximising the number of correcting changes in reads and such that the number of  $k$ -mers in data, speculated to represent correct sequences, be in some range, depending on a genome length). Choosing the best  $k$  gives insight into the potential of the algorithms. As  $k$ -mer length determining is an interesting problem itself, some of its results were observed.

The other parameters were genome length, sequencing depth (which ones were determined with information from a database [17]), number of reads  $k$ -mers (which was

determined by a tool for  $k$ -mers counting KMC [18]), ploidy for Karect (haploid for *A. thaliana* and diploid for *H. sapiens*). For Lighter probability  $\alpha$ , accordingly with authors guidelines, value  $3.5/(\text{sequencing depth})$  was chosen. Musket and Blue required so-called cutoff threshold and it was determined in a way, as RECKONER does.

All the input reads were paired. For correctors not supporting paired reads, the paired files were concatenated (by attaching a file of the latter reads to the end of a file of the first reads), then corrected, and finally split in a site of the concatenation.

### 8.3.3. Variant calling pipeline and its evaluation

To perform VC the reads were mapped with BWA[19] and variants were called with Strelka [20]. To evaluate the VC quality tool hap.py [21] was used. It returns statistics of variants set: TP, FP, FN, meaning as follows: number of detected true positive, false positive, and false negative (missing) variants. To compare results, it is convenient to define sensitivity (as  $TP/(TP+FN)$ ), precision (as  $TP/(TP+FP)$ ), and F1-score as their harmonic mean. All the values are independently defined for SNVs and indels.

## 8.4. Results

The experiments were performed on a server equipped with 256 GB of RAM and two Intel Xeon E5-2670 v3 processors, 12 cores (24 threads) each. The timeout limit of correction was set to 24 hours for every run.

### 8.4.1. Variant calling results

Fig. 8.1 shows the quality of VC for *A. thaliana*, separately for SNVs and short indels. To give a deeper view into the results, adequate sensitivity and precision graphs were shown. The “(raw)” designation denotes reads with no correction, acting as control cases. Figure 8.2 shows analogical results for *H. sapiens*.

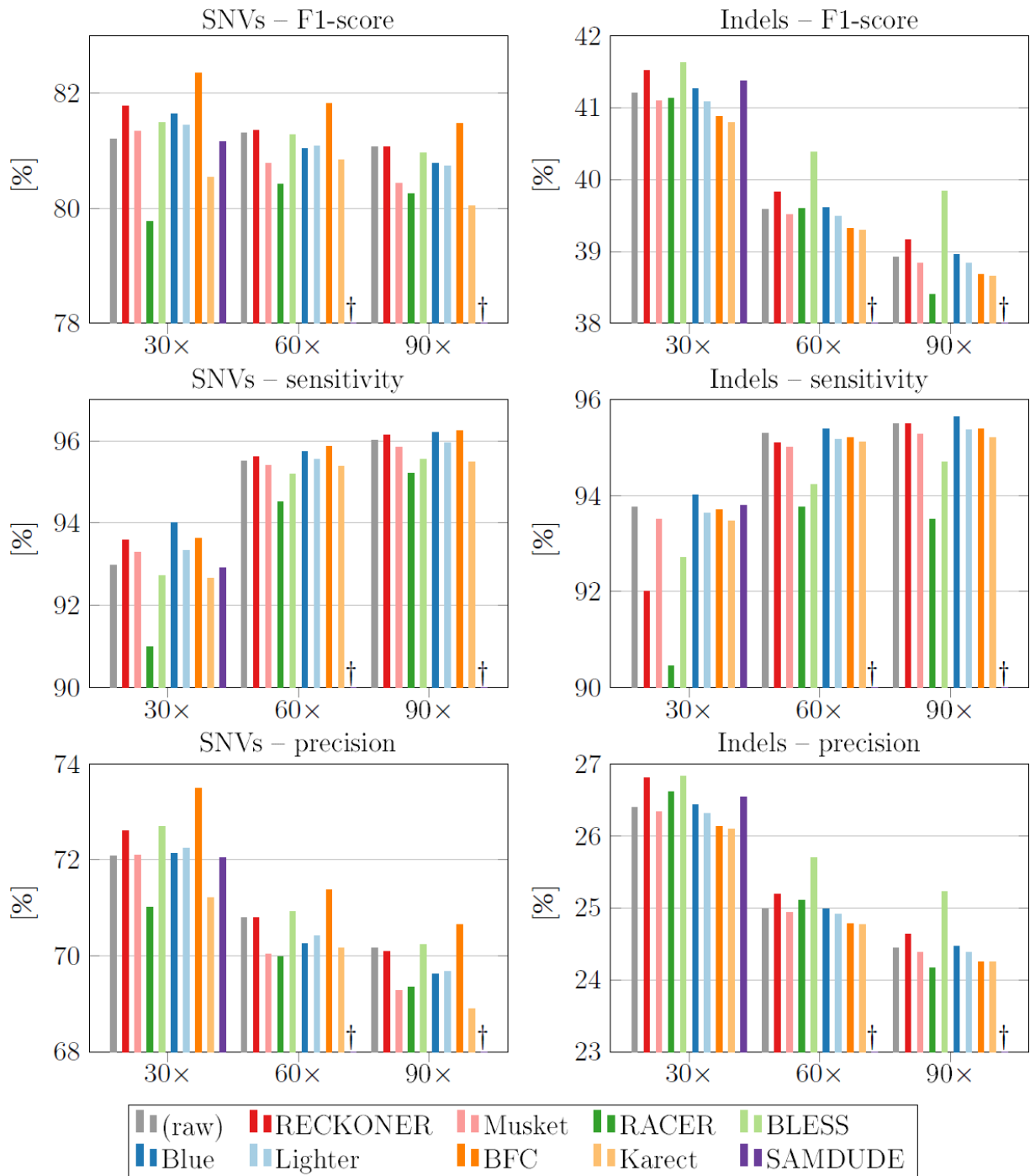


Fig. 8.1. VC results for *A. thaliana*; † – timeout.

Rys. 8.1. Wyniki detekcji wariantów dla *A. thaliana*.

Definitely better results of human VC are caused by the confident call regions utilization. It was observed, then after resignation of that, results were weaker, but the comparison of different correctors was analogical (results not shown).

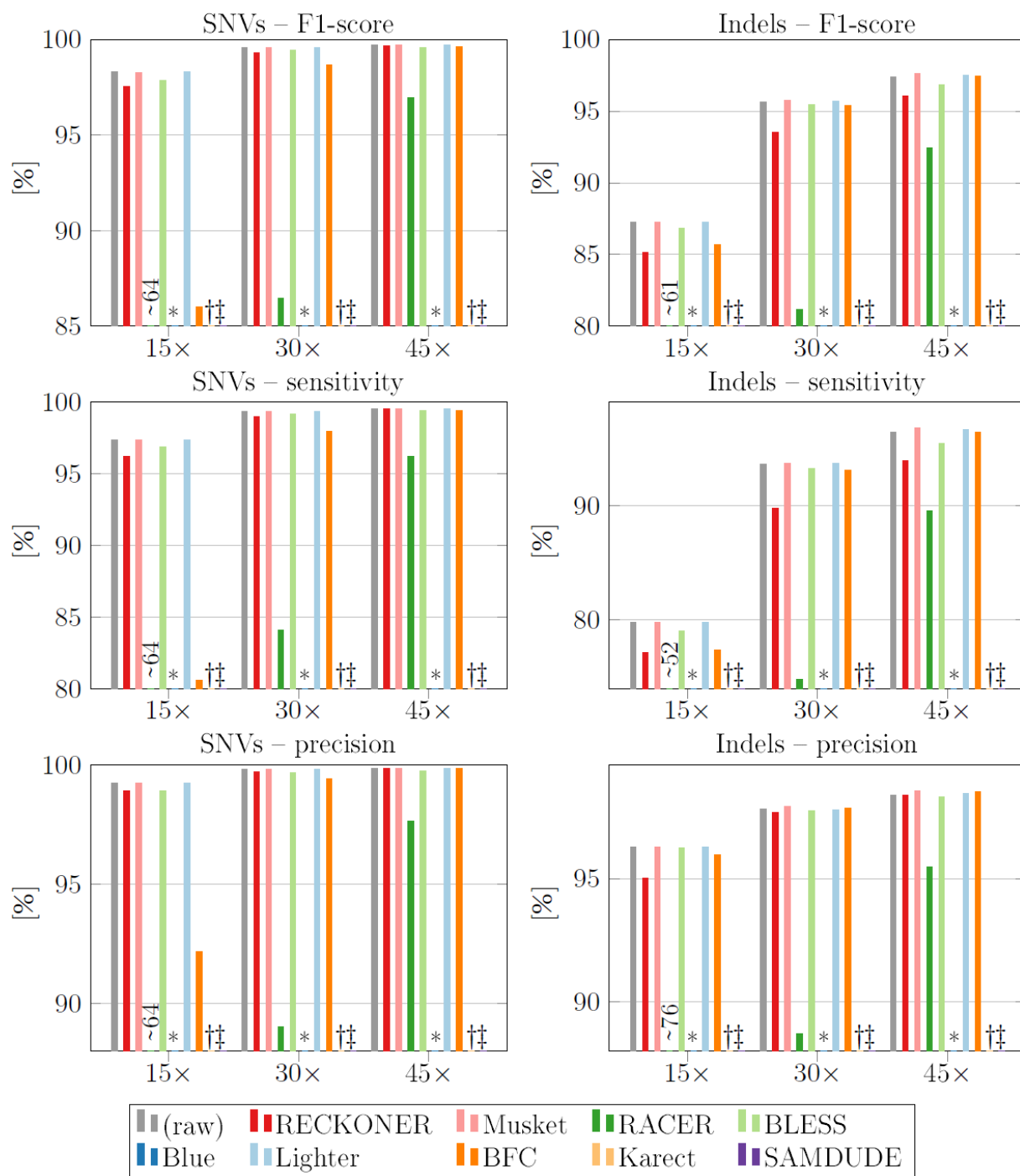


Fig. 8.2. VC results for *H. sapiens*; for selected RACER results numbers are given instead of the bars; \* – lack of memory; † – timeout; ‡ – algorithm crashes

Rys. 8.2. Wyniki detekcji wariantów dla *H. sapiens*; dla wybranych wyników algorytmu RACER zamieszczono liczby zamiast słupków

For all the *A. thaliana* experiments a low precision was observed. In many cases the correction caused increase of the quality, however, some of the algorithms caused its decline. The best algorithms was BFC (for SNVs) and Musket (for indels). Interesting is, that increasing the sequencing depth caused significant precision decline.



In the case of *H. sapiens*, Musket and Lighter return results of the same quality as the uncorrected data, what suggests, they actually do not correct the reads. They were run with a small value of  $k=13$ , as bigger values resulted in even weaker quality. Unfortunately, in most of the other cases the results were worse than before the correction. It means, that the correction destroyed the reads. Especially, the decrease of quality is visible for sensitivity, what means, that less number of variants is detected; as in most of the cases precision did not changed significantly, correction did not caused appearing a non-existent variants. For this organism increasing sequencing depth typically caused quality improvement in terms of all the measures.

It is noticeable, that RACER worked poorly for low sequencing depth reads. SAMDUDE finally was able to correct only the smallest set of the reads. As Blue crashed in all the human reads sets, its results are available only for *A. thaliana*.

#### 8.4.2. Oligomer length impact

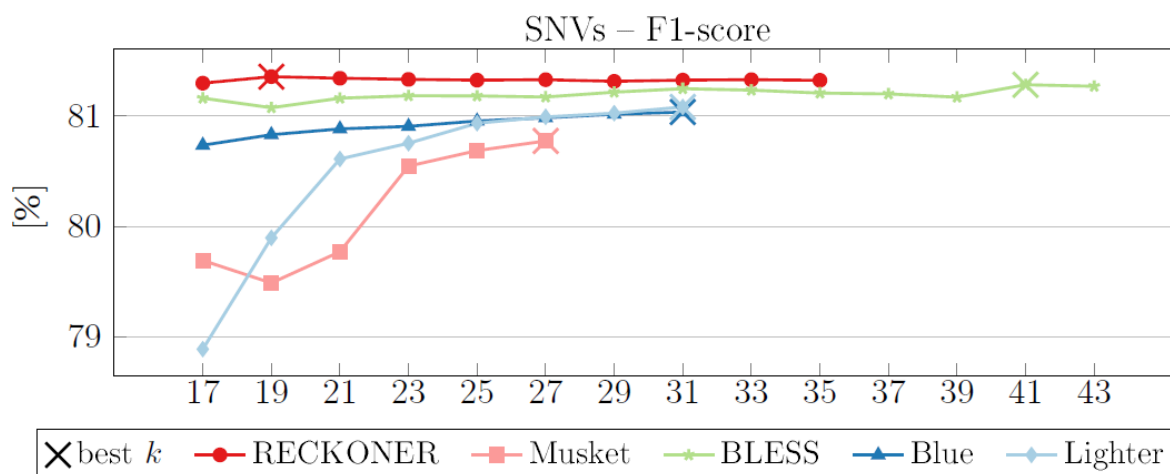


Fig. 8.3. Oligomer length impact on *A. thaliana* VC; sequencing depth 60×

Rys. 8.3. Wpływ długości oligomeru na detekcję wariantów *A. thaliana*; głębokość sekwencjonowania 60×

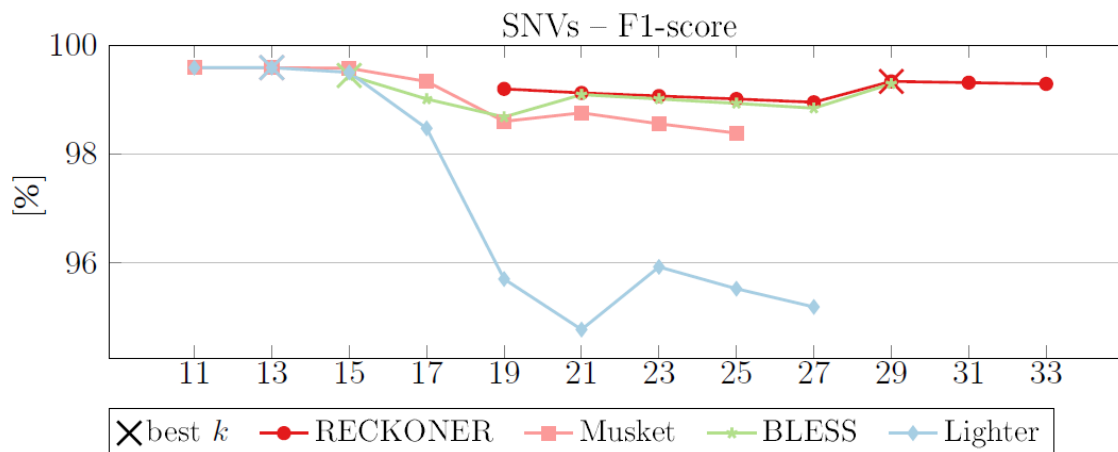


Fig. 8.4. Oligomer length impact on *H. sapiens* VC; sequencing depth 30×

Rys. 8.4. Wpływ długości oligomeru na detekcję wariantów *H. sapiens*; głębokość sekwencjonowania 30×

Fig. 8.3 show the  $k$ -mer length impact on F1-score for *A. thaliana* and *H. sapiens*, respectively. In some cases, the best value was the bound of the tested  $k$  values sequence. It means, that the following values caused some problems with its execution. Lighter undergoes the highest impact of  $k$ -mer length. In the case of Lighter and Musket the aforementioned observation, that they achieve the best results for small  $k$  values is visible (but they rather do not perform any correction).

## 8.5. Summary

The results show, that in the case of *A. thaliana* performing error correction is reasoned, as it allows slightly better results to be obtained. However, despite a significant number of correction algorithms and thorough analysis of the  $k$ -mer length, the differences are not huge, therefore utilizing them has not to be treated as a crucial part of variant calling. Unfortunately, in the case of long, mostly repeated human genome, the correction even causes the results quality decline.

In some cases correction  $k$ -mer length impact is not significant for variant calling, but in the others is crucial. It means, that it is necessary to put a big effort to determine this value properly.

It has to be in mind, that error correction is an additional stage of a data processing. As experiments prove, some of the algorithms are not able to correct reads in a day, which is rather a liberal limit. Requiring such a long time in practice disqualifies an algorithm.

## Bibliography

1. Fischer-Hwang, I. Ochoa, T. Weissman, M. Hernaez, Denoising of Aligned Genomic Data, *Scientific reports* (2019) **9**(1):1-11.
2. H. Li, BFC: correcting Illumina sequencing errors, *Bioinformatics* (2015) **31**(17):2885-2887.
3. S. Kosugi, *et al.*, Coval: improving alignment quality and variant calling accuracy for next-generation sequencing data, *PloS one* (2013) **8**(10):e75402.
4. D.C. Koboldt, Best practices for variant calling in clinical sequencing, *Genome Medicine* (2020) **12**(1):1-13.

5. X. Yang, S.P. Chockalingam, S. Aluru, A survey of error-correction methods for next-generation sequencing, *Briefings in bioinformatics* (2012) **14**(1):56-66.
6. Y. Heo, A. Ramachandran, W.-M. Hwu, J. Ma, D. Chen, BLESS 2: accurate, memory-efficient and fast error correction method, *Bioinformatics* (2016) **32**(15):2369-2371.
7. J. Zook *et al.*, Extensive sequencing of seven human genomes to characterize benchmark reference materials, *Scientific data* (2016) **3**(1):1-26.
8. C. Alonso-Blanco *et al.*, 1,135 genomes reveal the global pattern of polymorphism in *Arabidopsis thaliana*, *Cell* (2016) **166**(2):481-491.
9. X. Yin, Z. Song, K. Dorman, A. Ramamoorthy, *PREMIER-PRObabilistic error-correction using Markov inference in errored reads*, 2013 IEEE International Symposium on Information Theory, 7-12 July 2013, Istanbul (2013).
10. M. Schulz *et al.*, Fiona: a parallel and automatic strategy for read error correction, *Bioinformatics* (2014) **30**(17):i356-i363.
11. M. Długosz, S. Deorowicz, M. Kokot, *Improvements in DNA Reads Correction*, International Conference on Man-Machine Interactions, 3-6 October 2017, Kraków (2017).
12. Y. Liu, J. Schröder, B. Schmidt, Musket: a multistage k-mer spectrum-based error corrector for Illumina sequence data, *Bioinformatics* (2012) **29**(3):308-315.
13. L. Ilie, M. Molnar, RACER: Rapid and accurate correction of errors in reads, *Bioinformatics* (2013) **29**(19):2490-2493.
14. P. Greenfield, K. Duesing, A. Papanicolaou, D.C. Bauer, Blue: correcting sequencing errors using consensus and context, *Bioinformatics* (2014) **30**(19):2723-2732.
15. L. Song, L. Florea, B. Langmead, Lighter: fast and memory-efficient sequencing error correction without counting, *Genome biology* (2014) **15**(11):509.
16. A. Allam, P. Kalnis, V. Solovyev, Karect: accurate correction of substitution, insertion and deletion errors for next-generation sequencing data, *Bioinformatics* (2015) **31**(21):3421-3428.
17. National Center for Biotechnology Information: <https://www.ncbi.nlm.nih.gov>, accessed: 20 March, 2021.
18. M. Kokot, M. Długosz, S. Deorowicz, KMC 3: counting and manipulating k-mer statistics, *Bioinformatics* (2017) **33**(17):2759-2761
19. H. Li, R. Durbin, Fast and accurate short read alignment with Burrows-Wheeler transform, *Bioinformatics* (2009) **25**(14):1754-1760.
20. S. Kim *et al.*, Strelka2: fast and accurate calling of germline and somatic variants, *Nature methods* (2018) **15**(8):591-594.
21. GitHub - Illumina/hap.py: Haplotype VCF comparison tools: <https://github.com/Illumina/hap.py>, accessed: 20 March, 2021.

## GENOME VARIANT CALLING IN CONTEXT OF SEQUENCING READS CORRECTION

### Abstract

One of the most widely used tool in genomics is DNA sequencing, especially of Illumina technology. Its multiple applications include variant calling, which aims at determining variants present in a proband genome. However, presence of sequencing errors could impact quality of calling results. There has not been performed thorough analysis of error correction efficacy in terms of variant calling. This paper addresses that problem, for different state-of-the-art correction algorithms and two different-sized genomes. Moreover, the impact of oligomer length – main parameter of many of correction algorithms – on results quality is shown.

**Keywords:** DNA sequencing, variant calling, read error correction.

Marek SOCHA<sup>1</sup>, Aleksandra SUWALSKA<sup>1</sup>, Wojciech PRAZUCH<sup>1</sup>,  
Michał MARCZYK<sup>1</sup>, Joanna POLANSKA<sup>1</sup>, POLCOVID Study Group

## **Chapter 9. UMAP-BASED GRAPHIC REPRESENTATION OF POLCOVID CHEST X-RAY DATA SET HETEROGENEITY**

### **9.1. Introduction**

When analysing real problems, on real data, the researchers want to have a great understanding of underlying structures and existing patterns, which usually requires use of sophisticated and accurate visualisation techniques. In many fields, real datasets often have high dimensionality, which makes the computations complicated and time-consuming. Visualisations of high-dimensional data is difficult or even impossible in some cases. One way to overcome this issues is dimensionality reduction by projection of a data into low-dimensional space. However, most of the techniques are mainly dedicated to tabular data, making the projections of images less reliable.

Uniform Manifold Approximation and Projection (UMAP) is an embedding technique that projects high-dimensional data points into low-dimensional space [1]. It is a useful tool for data visualisation and pre-processing, with the potential to be used as a clustering method. Despite being mainly used for tabular data, some attempts have been made to apply UMAP to image data analysis.

The first usage of the UMAP embedding in the scope of image data analysis was described in the original paper [1]. Images was firstly vectorized and then passed to UMAP procedure. The experiments were made using the Pen digits [2], COIL 20 [3] and COIL 100 [4] datasets. This method was also used in other articles [5–7] which operated on MNIST [8], Fashion-MNIST [5], USPS [9] and Afro-MNIST [10] datasets.

---

<sup>1</sup> Department of Data Science and Engineering, Faculty of Automatic Control, Electronics and Computer Science, Silesian University of Technology, Gliwice, Poland. Corresponding author: [aleksandra.suwalska@polsl.pl](mailto:aleksandra.suwalska@polsl.pl).

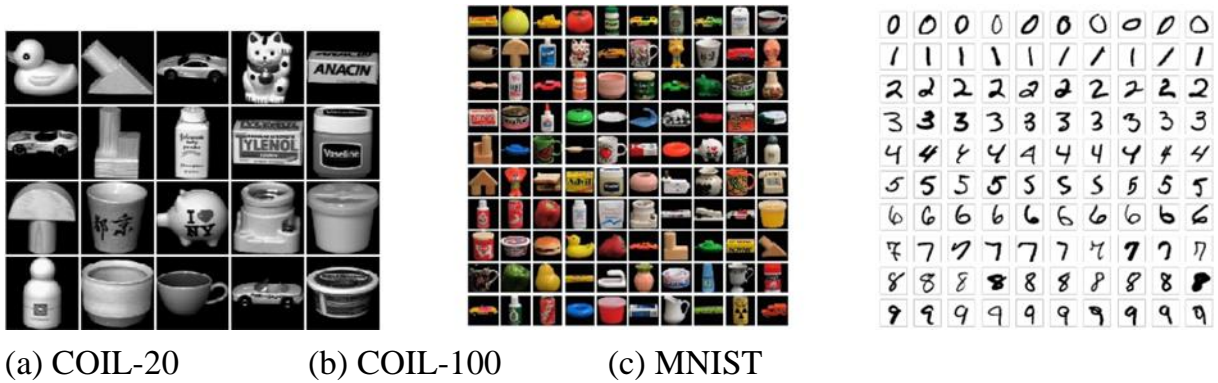


Fig. 9.1. Example images from commonly used benchmark datasets (a) COIL-20, (b) COIL-100, (c) MNIST

Rys. 9.1. Przykładowe obrazy z powszechnie używanych zestawów danych porównawczych (a) COIL-20, (b) COIL-100, (c) zbiór MNIST

These datasets consist of clearly defined, low-resolution images with a neutral background, either black or white. Image shapes are adjusted so the Region Of Interest (ROI) is dominant. However, these properties are not commonly seen in all real world image data sets, where the object of interest could be present in different locations across set of images, could have varying sizes and could be displayed with diverse backgrounds.

The ability to generate embeddings that will separate different categories of images in the 2D plane could be very helpful in medical image analysis to reveal differences and similarities between the analysed groups. There are examples of UMAP usage in this context in articles [11–13]. Each of them, aimed to describe structures of a Tumours and Nodules in Computed Tomography scan (CT), Positron Emission Tomography (PET) or Magnetic Resonance imaging (MRI) images. In those cases, ROI is located exactly on the area of interest. It is different in analysis of chest X-Ray (CXR) images, where we observe different shapes, alignment, intensities, background values, artefacts but more importantly, ROI placement. The place in which a disease that define lung change occurs is heterogeneous in shape and placement. Thus, it is very hard to precisely indicate it in the CXR image. Forcing the use of whole or a part of CXR image region, where in such a case the UMAP procedure could potentially capture information that is not related to the biological differences observed in a lung region.

The goal of the study was to obtain visual separability of analysed disease entities on UMAP plots in order to make this information useful for further analysis. This study proposes a novel method of semi-supervised UMAP embedding creation, suitable for the CXR image analyses. The method is robust to the ROI placement, image size, image alignment and type of background.

## 9.2. Materials and Methods

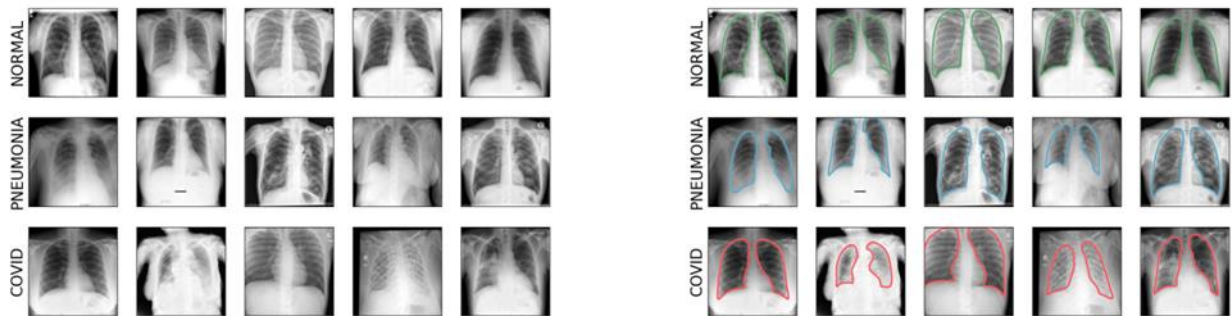


Fig. 9.2. POLCOVID database example images. (a) Example images from POLCOVID database, (b) Example images from POLCOVID database with segmentations

Rys. 9.2. (a) Przykładowe dane z bazy POLCOVID, (b) Przykładowe dane z bazy POLCOVID wraz z segmentacjami

In the study, images from the POLCOVID database were used. POLCOVID is an original and unique COVID-19 database containing X-Ray images. A data incorporated within the database were collected from Polish hospitals in the CIRCA project (COVID-19 RTG/CT-Based Diagnosis). The considered subset of POLCOVID database data consisted of 4956 CXR images, 2578 of which were normal (healthy), 1174 were non-COVID pneumonia and 1204 were COVID-19 (with positive RT-PCR test result). The images were collected from 24 different clinical hospitals in Poland, so they were acquired with different RTG devices and with different parameters of image scanning. Therefore, the dataset is heterogeneous in terms of pixel intensity and image resolution.

### 9.2.1. Image pre-processing

The images had to be properly standardised, in order to minimise the batch effect of obtaining data from various sources. The presence of white artefacts, like text on image, has a significant impact on the pixel intensity distribution of an image. To overcome this problem, 0.25% of extreme pixel intensity values were removed from images before the standardisation to the range of  $[0, 1]$ . This step made the image distributions closely related. All images were resized to 512x512 pixels.

### **9.2.2. Radiomic Features**

Radiomic Features [14–17] are a large set of numerical values aimed towards describing medical image fragment indicated by a given ROI. The usage of radiomic features was proven to be effective in task of cancer detection and evaluation [11–13] both in terms of UMAP visualisation and diagnostic potential. The extraction of the radiomic features was made using python package pyradiomics [18].

### **9.2.3. Features preprocessing**

In the method's pipeline, in the first step, from the set of whole features those with variance equal to zero were filtered out. Remaining features were scaled to the range of [0,1]. For the initial dimension reduction, the PCA technique [19] were used from which the features which explained from 85% to 95% variance were taken. This percentage value was adjusted depending on the final amount of PCA components.

### **9.2.4. U-Net segmentation**

U-Net [20] is a neural network architecture for image semantic segmentation. For the purpose of lung region segmentation some hyper-parameters and features of the model were adjusted. On the course of experiments, the final U-Net based model consisted of 4 encoding and decoding layers with SELU activation function [21], Batch Normalisation and Dropout with drop out coefficient of 0.5. The number of filters for each convolutional layer ranged from 32 to 512 depending on depth of the convolutional layer. The input images were resized and padded to the shape of 512x512. Neural network were trained using over 5200 train images with hand crafted lung masks.

### **9.2.5. Effect size**

Effect size is a quantitative measure of the strength, of a phenomenon calculated on the basis of data [22], in contrast to p-value which indicates whether an effect exists, not how great it is.



### 9.2.6. Features selection

Features selection process was based on the effect size. The non-parametric Kruskal-Wallis test [23] was performed on the features calculated for each group of patients and for each feature an effect size was computed. Then, the features were ordered according to the effect size (Figure 9.7) as a measure of feature importance in the task of distinguishing the patient categories. Final number of selected features were decided on the course of experiments described in the Results in subsection 3.4.

## 9.3. Results

### 9.3.1. UMAP on whole images

The most common approach for applying UMAP on images is flattening the images into vectors and storing them in a tabular manner. This method was successful while dealing with the distinction between classes on datasets like Fashion-MNIST [5] or COIL-100 [1, 4]. The result of the standard UMAP approach applied to the POLCOVID CXR dataset is shown on the scatter plot in Figure 9.3. The hyperparameters used for UMAP are as follows: metric=euclidean, n\_neighbors=500 and min\_dist=0.8.

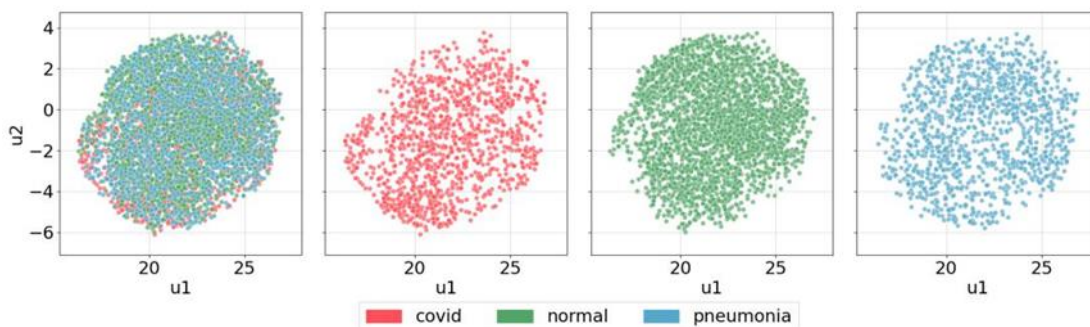


Fig. 9.3. Result of the UMAP procedure on the vectorized images

Rys. 9.3. Rezultat techniki UMAP wyliczonej na obrazach zwektoryzowanych

The scatter plot, in this case, does not provide any useful information. In the data, there is a lot of points, which makes it hard to properly presents them on the scatter plot. Another approach is to use kernel density estimate (kde) plots, also called density plots. Figure 9.4 presents the same UMAP embedding visualisation on kde plot.

But still a proper distinction between classes is not provided. While part of COVID images is slightly repulsed from the clump of clusters, clusters representing pneumonia

and normal images overlap almost entirely. This is also not coherent with medical expert knowledge. Images from normal class should be driven further away from both COVID and pneumonia. Clusters shown in Figure 9.4 result from UMAP based on probably inappropriate features.

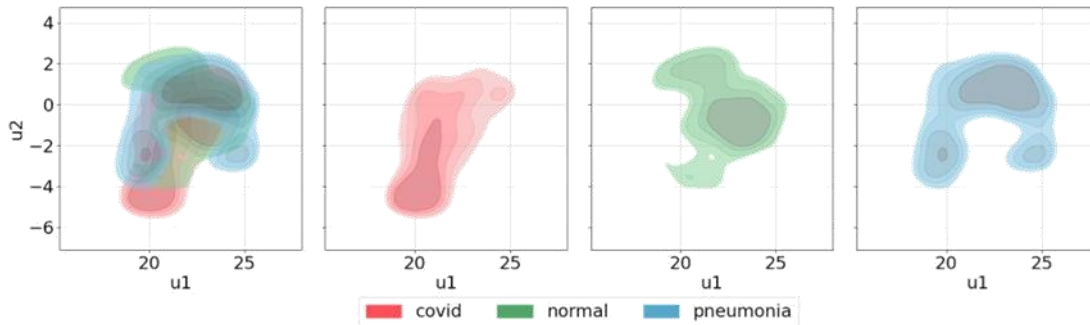


Fig. 9.4. Result of the UMAP procedure on the vectorized images

Rys. 9.4. Rezultat techniki UMAP wyliczonej na obrazach zwektoryzowanych – izolinie

### 9.3.2. UMAP on radiomics from whole images

To address issues occurring while calculating UMAP on vectorized images, we propose moving from the vectorized space into the feature space. Feature space is defined on the basis of radiomic features 2.2.

Initially, the whole image is considered as the ROI for radiomics calculations. Before the application of the UMAP procedure, features were pre-processed using pipeline described in subsection 2.3. The resulting embedding is presented in Figure 9.5.

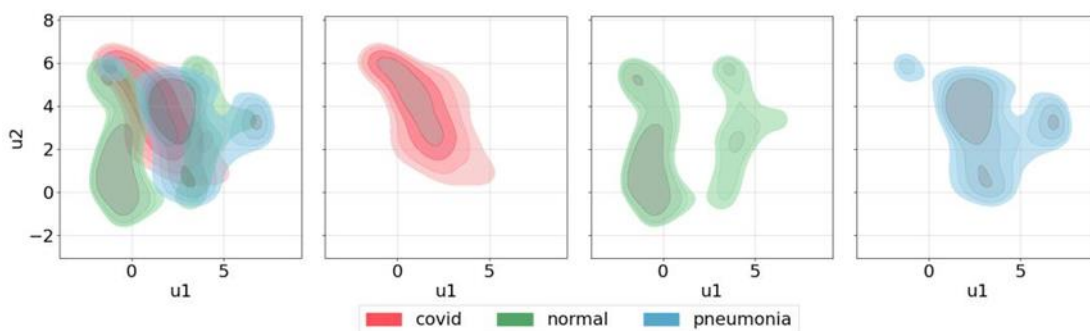


Fig. 9.5. Result of UMAP on radiomic features calculated from whole images

Rys. 9.5. Rezultat techniki UMAP wyliczonej na podstawie cech radiomicznych całych obrazów

As seen in Figure 9.5, there is a difference in the distribution of subsequent classes. While COVID images are forming one cluster, pneumonia and normal have multiple, scattered clusters.

### 9.3.3. UMAP on all radiomics from the lung regions

As the results are still not satisfying we propose to narrow down the ROI in order to gain access to the information more relevant to the problem.

According to [24–26] the most relevant information about the state of the patient are present within the lungs. Therefore, lung regions were extracted from the images and treated as a new ROI. The segmentation was done with the use of U-Net neural network architecture described in subsection 2.4. The results of the segmentation are shown in Figure 9.2b. The chosen radiomic features were calculated on the extracted lung regions and the UMAP procedure was conducted as before, with a change to the UMAP metric from 'euclidean' to 'seuclidean'. Results are presented in Figure 9.6.

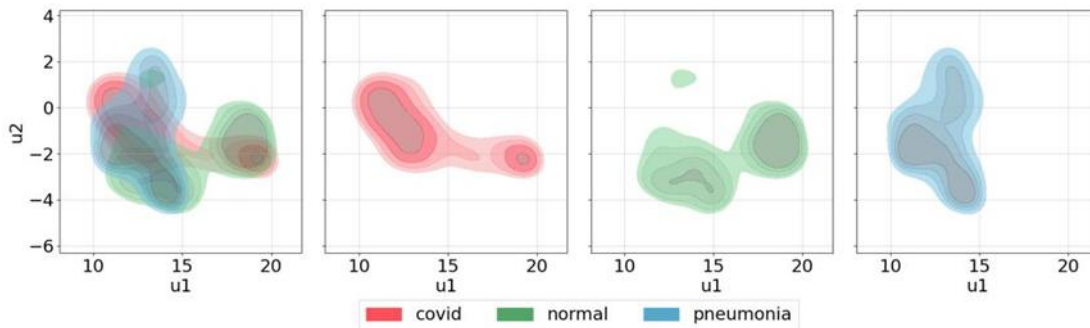


Fig. 9.6. Result of the UMAP procedure on lung radiomic features

Rys. 9.6. Rezultat techniki UMAP wyliczonej na podstawie cech radiomicznych wysegmentowanych płuc

The separation between classes is more visible but the number of clusters is overestimated. Also, a major part of normal class images overlaps with the smaller COVID cluster. Those results indicate that there still could be features that attract unrelated clusters towards each other.

### 9.3.4. UMAP on selected radiomics from the lung region

In contrast to [11–13] we are looking for information enveloped, hidden within the ROI and not directly indicated by it. In order to create UMAP embeddings more suited towards considered problem of normal, pneumonia and COVID distinction, we propose a semi-supervised embedding method with feature selection. The feature selection is based on effect size, 2.5 and described in subsection 2.6.

Three subsets of the features were considered based on the created ranking. Firstly, features with at least a small effect size ( $\eta^2 > 0.01$ ) were taken into consideration. This

resulted in 71 radiomic features that were fed into UMAP. However, the results were not satisfactory, the number of features was too high. In the second attempt, a line connecting the highest and the lowest effect size values on the bar plot (Figure 9.7) was drawn. Euclidean distance from each bar to the line was calculated and two shortest distances were chosen and marked on the plot that pointed to the threshold cut-offs for the feature selection. With the first cut-off point ( $\eta^2 > 0.04$ ), a set of 13 features was included and with the second cut-off point ( $\eta^2 > 0.03$ ), a set of 30 features was included. For both feature sets the UMAP procedure was conducted.

While both, 13 and 30 features UMAP were created, the one with 30 features was selected. The parameters were the same as in the previous section's UMAP.

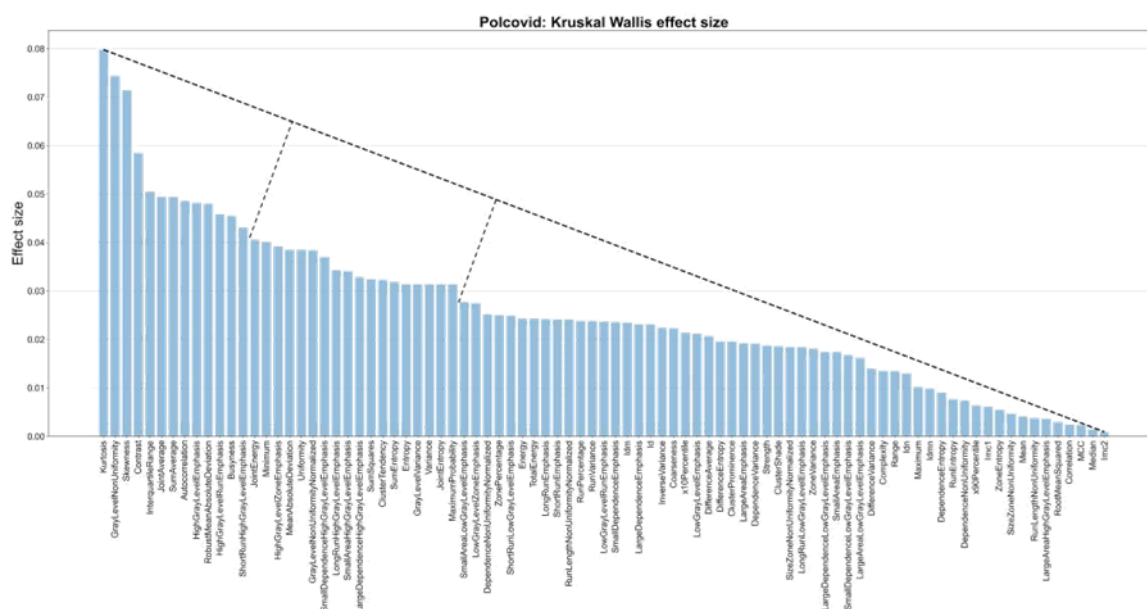


Fig. 9.7. Feature importance ranking based on calculated effect sizes

Rys. 9.7. Ranking ważności cech na podstawie obliczonych wielkości efektów

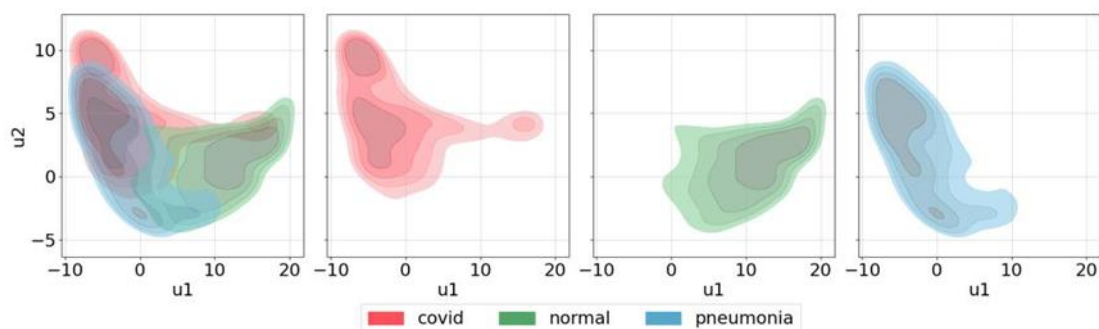


Fig. 9.8. Result of the UMAP procedure on lungs features

Rys. 9.8. Rezultat techniki UMAP wyliczonej na podstawie wybranych cech radiomicznych wysegmentowanych płuc

As shown in Figure 9.8, healthy (normal class) patients are clearly separated from the pneumonia and COVID patients. While COVID and pneumonia cluster overlaps, pneumonia has disjointed parts from the COVID cluster. COVID cluster concentration point lays partially beyond the pneumonia cluster and its edges have some independent parts.

## 9.4. Discussion

All figures shown up to this point, represented image embeddings created in order to differentiate disease entities. While the embeddings were shown in a form of density clusters, each cluster consisted of some points and each point indicated image form the POLCOVID data base. In order to compare proposed approach with a pure image vectorization, 12 example images from each class are shown on Figures 9.9 and 9.10. Images are taken from a vicinity of the most representative class density estimates.

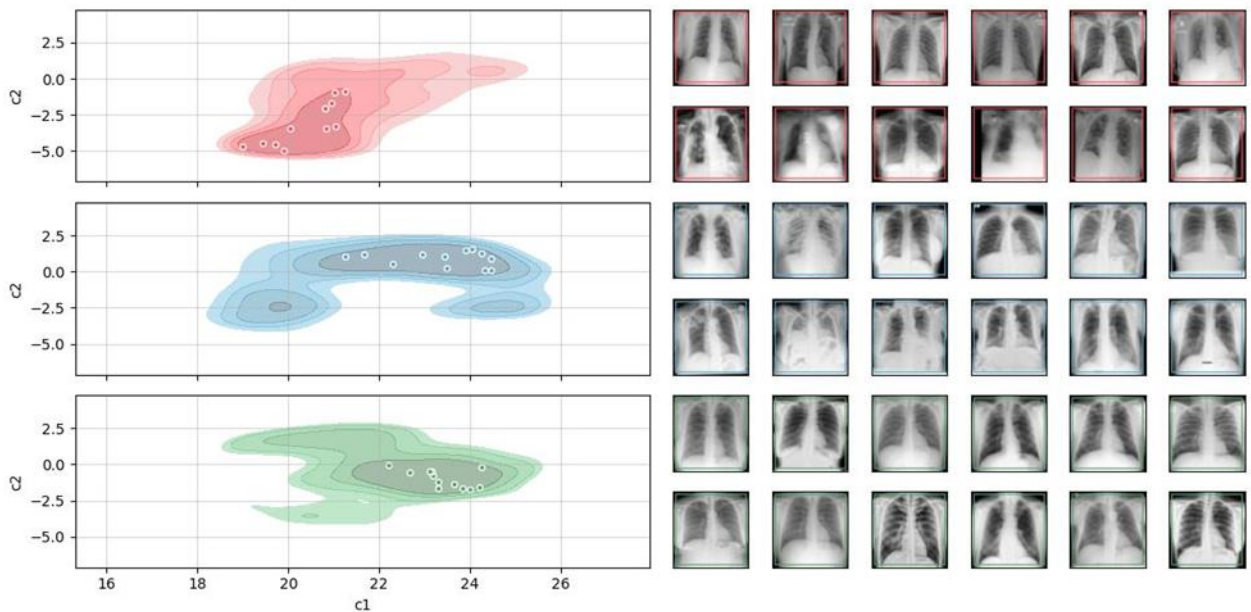


Fig. 9.9. Example images of each class from most prominent clusters of UMAP on vectorized images (4)  
Rys. 9.9. Przykładowe obrazy dla każdej klasy z najbardziej widocznych klastrów UMAP na zwektorowanych obrazach

At a first glance it is difficult to infer on what basis the images are distributed. Due to its high cluster overlap (Figure 9.4) the prominence of the features characteristic for patient state is not obvious. According to UMAP original paper [1], a UMAP embedding is also meant to distribute clusters preserving their inter-cluster differences. Most representative COVID cluster seems to consist of some studies with relatively low pathological lung involvement mixed together with those showing relatively high patholo-

gies. Cluster of pneumonia disease with quite significant lung changes seems to be close to the cluster of normal studies. On the Figure 9.10 the distribution of the clusters is much easier to interpret. COVID cluster with prominent pathological lung involvement is driven further away from the normal cluster, which does not contains aggressive changes. Pneumonia cluster has its points distributed close to the COVID cluster indicating similarities in lung abnormality. Normal cluster distributes itself between two most prominent clump of points, both laying quite far from pneumonia and COVID clusters. All around, the final shape creates structure similar to letter "U". It seems to indicate a shift from the changes with most prominent pathological lung involvement (upper left corner,) to the one with the lowest pathological lung involvement (upper right corner).

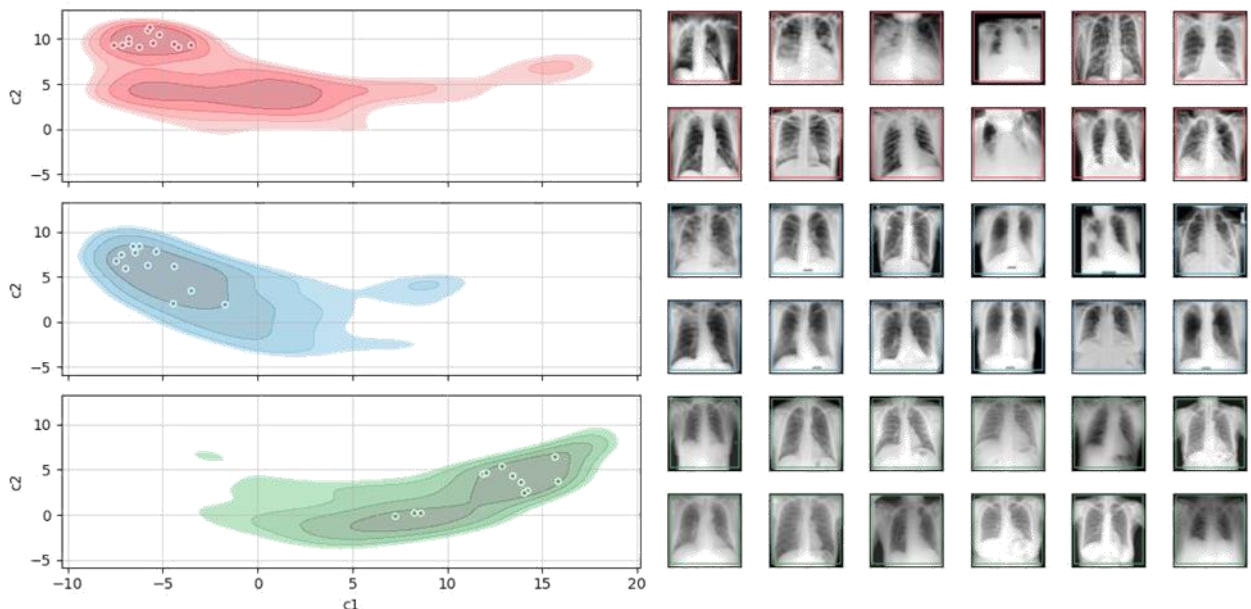


Fig. 9.10. Example images of each class from most prominent clusters of UMAP on lungs radiomic features (8)

Rys. 9.10. Przykładowe obrazy każdej klasy z najbardziej wyróżniających się skupień UMAP na wybranych cechach radiometrycznych płuc.

## 9.5. Conclusion

Obtained clusters in UMAP embedding are more readable and interpretative visualisation of disease distribution across the embedding, leading to much more meaningful conclusions.

**POLCOVID study group**

Department of Infectious Diseases and Hepatology, as coordinator: Jerzy Jaroszewicz (Medical University of Silesia in Katowice, Infectious Diseases Hospital No. 1 in Bytom), Jan Baron, Katarzyna Gruszczynska (Department of Nuclear Medicine and Image Diagnostics, Medical University of Silesia in Katowice), Magdalena Sliwinska, Mateusz Rataj, Przemyslaw Chmielarz (Voivodship Specialist Hospital in Wroclaw), Edyta Szurowska (II Department of Radiology, Medical University of Gdańsk), Jerzy Walecki, Samuel Mazur, Piotr Wasilewski (Central Clinical Hospital of the Ministry of Internal Affairs and Administration in Warsaw), Tadeusz Popiela, Justyna Kozub (Collegium Medicum of the Jagiellonian University in Kraków), Grzegorz Przybylski, Anna Kozanecka (Kujawsko-Pomorskie Pulmonology Center in Bydgoszcz), Andrzej Cieszanowski, Agnieszka Oronowicz-Jaskowiak, Bogumil Golebiewski (National Institute of Oncology in Warsaw, Department of Imaging Diagnostics), Complex of Health Care Centres, Mateusz Nowak (Silesian Hospital in Cieszyn), Barbara Gizycka (Single Infectious Diseases Hospital Megrez Ltd. in Tychy: Department of Imaging Diagnostics), Piotr Blewaska (District Hospital in Raciborz), Department of Infectious Diseases and Hepatology, University of M. Kopernika w Toruniu, Malgorzata Pawlowska, Piotr Rabiko, Pawel Rajewski (Collegium Medicum in Bydgoszcz), Department of Radiological and Imaging Diagnostics, Jerzy Walecki (Medical Center for Postgraduate Education, Warsaw), Clinical Department of Imaging Diagnostics, Katarzyna Sznajder (University Clinical Hospital in Opole), Department of Infectious Diseases University of Rzeszow, Robert Plesniak (Medical Center in Lancut), Department of Allergology and Internal Medicine, Marcin Moniuszko (Medical University of Bialystok), Department of Infectious Diseases and Hepatology, Robert Flisiak (Medical University of Bialystok), Andrzej Cieszanowski (Medical University of Warsaw: II Department of Clinical Radiology), Przemyslaw Bombinski (Department of Pediatric Radiology), Agata Majos (Medical University of Lodz: Department of Radiological and Isotopic Diagnostics and Therapy), Michal Mik (Department of General and Colorectal Surgery), Medical University of Wroclaw, Krzysztof Simon (Department of Infectious Diseases and Hepatology), Bartosz Markiewicz (Voivodship Comprehensive Hospital in Kielce: Department of Imaging Diagnostics), Gabriela Zapolska, Krzysztof Klaude, Katarzyna Rataj (Czerniakowski Hospital in Warsaw), Sebastian Hildebrandt, Katarzyna Krutul-Walenciej (Central Clinical Hospital of the Medical University of Gdansk), Adrianna Tur, Grzegorz Drabik (Prognostic Specialist Clinic in Knurów), Damian Piotrowski (Specialist Hospital No. 1 in Bytom).

## Acknowledgement

The research leading to these results was partially funded from the National Science Centre, Poland, grant MNiSW/2/WFSN/2020 project name CIRCA – COVID-19 online image diagnostic support service. Calculations were carried out using GeCONiI infrastructure funded by NCBiR project no. POIG.02.03.01-24-099/13. Additionally, AS and WP are a holders of European Union scholarship through the European Social Fund, grant POWR.03.05.00-00-Z305.

## Bibliography

1. Leland McInnes, John Healy, James Melville. Umap: Uniform manifold approximation and projection for dimension reduction, 2020.
2. Ethem Alpaydin, Fevzi Alimoglu. Pen-based recognition of handwritten digits data set. 1996.
3. A. Sameer Nene, K. Shree Nayar, Hiroshi Murase. Columbia object image library (coil-20). Technical report, 1996.
4. Sameer A. Nene, Shree K. Nayar, Hiroshi Murase. Columbia object image library (coil-100). 1996.
5. Han Xiao, Kashif Rasul, Roland Vollgraf. Fashion-mnist: a novel image dataset for benchmarking machine learning algorithms, 2017.
6. Yingfan Wang, Haiyang Huang, Cynthia Rudin, Yaron Shaposhnik. Understanding how dimension reduction tools work: An empirical approach to deciphering t-sne, umap, trimap, and pacmap for data visualization, 2020.
7. Abdelhakim Cheriet Mebarka Allaoui, Mohammed Lamine Kherfi. Considerably improving clustering algorithms using umap dimensionality reduction technique: A comparative study. In *Image and Signal Processing*, pages 317–325, Cham, 2020. Springer International Publishing.
8. Yann LeCun, Corinna Cortes. Mnist handwritten digit database. 2010.
9. Jonathan J. Hull. A database for handwritten text recognition research. *IEEE Transactions on Pattern Analysis and Machine Intelligence*, 16(5):550–554, 1994.
10. Andrew C. Yang, Daniel J. Wu, Vinay U Prabhu. Afro-mnist: Synthetic generation of mnist-style datasets for low-resource languages, 2020.



11. Jeong Hoon Lee, Eun Ju Ha, Jin Roh, Su Jin Lee, Jeon Yeob Jang. Technical feasibility of radiomics signature analyses for improving detection of occult tonsillar cancer. *Scientific Reports*, 11(1):192, Jan 2021.
12. Mohammadhadi Khorrami, Kaustav Bera, Rajat Thawani, Prabhakar Rajiah, Amit Gupta, Pingfu Fu, Philip Linden, Nathan Pennell, Frank Jacono, Robert C. Gilkeson, Vamsidhar Velcheti, Anant Mad-abhushi. Distinguishing granulomas from adenocarcinomas by integrating stable and discriminating radiomic features on non-contrast computed tomography scans. 03 2021.
13. Andrea Bizzego, Nicole Bussola, Damiana Salvalai, Marco Chierici, Valerio Maggio, Giuseppe Jurman, and Cesare Furlanello. Integrating deep and radiomics features in cancer bioimaging. 03 2019.
14. Virendra Kumar, Yuhua Gu, Satrajit Basu, Anders Berglund, Steven A. Eschrich, Matthew B. Scha-bath, Kenneth Forster, Hugo J.W.L. Aerts, Andre Dekker, David Fenstermacher, Dmitry B. Goldgof, Lawrence O. Hall, Philippe Lambin, Yoganand Balagurunathan, Robert A. Gatenby, and Robert J. Gillies. Radiomics: the process and the challenges. *Magnetic Resonance Imaging*, 30(9):1234–1248, 2012. Quantitative Imaging in Cancer.
15. Robert J. Gillies, Paul E. Kinahan, Hedvig Hricak. Radiomics: Images are more than pictures, they are data. *Radiology*, 278(2):563–577, 2016. PMID: 26579733.
16. Vishwa Parekh, Michael A. Jacobs. Radiomics: a new application from established techniques. *Expert Review of Precision Medicine and Drug Development*, 1(2):207-226, 2016. PMID: 28042608.
17. Stephen Yip and Hugo Aerts. Applications and limitations of radiomics. *Physics in Medicine and Biology*, 61(13):R150–R166, jun 2016.
18. Joost J.M. van Griethuysen, Andriy Fedorov, Chintan Parmar, Ahmed Hosny, Nicole Aucoin, Vivek Narayan, Regina G.H. Beets-Tan, Jean-Christophe Fillion-Robin, Steve Pieper, Hugo J.W.L. Aerts. Computational radiomics system to decode the radiographic phenotype. *Cancer Research*, 77(21):e104–e107, 2017.
19. Karl Pearson F.R.S. Liii. on lines and planes of closest fit to systems of points in space. *The London, Edinburgh, and Dublin Philosophical Magazine and Journal of Science*, 2(11):559–572, 1901.
20. Olaf Ronneberger, Philipp Fischer, Thomas Brox. U-net: Convolutional networks for biomedical image segmentation, 2015.

21. Günter Klambauer, Thomas Unterthiner, Andreas Mayr, and Sepp Hochreiter. Self-normalizing neural networks, 2017.
22. Jacob Cohen. Statistical power analysis for the behavioural sciences. hillsdale, nj: Laurence erlbaum associates, 1988.
23. *Kruskal-Wallis Test*, pages 288–290. Springer New York, New York, NY, 2008.
24. Wei Zhao, Zheng Zhong, Xingzhi Xie, Qizhi Yu, Jun Liu. Relation between chest ct findings and clinical conditions of coronavirus disease (covid-19) pneumonia: A multicenter study. *American Journal of Roentgenology*, 214(5):1072–1077, May 2020.
25. Adam Bernheim, Xueyan Mei, Mingqian Huang, Yang Yang, Zahi A. Fayad, Ning Zhang, Kaiyue Diao, Bin Lin, Xiqi Zhu, Kunwei Li, Shaolin Li, Hong Shan, Adam Jacobi, and Michael Chung. Chest ct findings in coronavirus disease-19 (covid-19): Relationship to duration of infection. *Radiology*, 295(3):200463, 2020. PMID: 32077789.
26. Shohei Inui, Akira Fujikawa, Motoyuki Jitsu, Naoaki Kunishima, Sadahiro Watanabe, Yuhi Suzuki, Satoshi Umeda, Yasuhide Uwabe. Chest ct findings in cases from the cruise ship diamond princess with coronavirus disease (covid-19). *Radiology: Cardiothoracic Imaging*, 2(2):e200110, 2020.

## **UMAP-BASED GRAPHIC REPRESENTATION OF POLCOVID CHEST X-RAY DATA SET HETEROGENEITY**

### **Abstract**

Visualisation is an essential step in the process of understanding the data. Characterisation of underlying structures is often difficult, especially when dealing with large number of dimensions. Uniform Manifold Approximation and Projection (UMAP) technique can solve this problem by transforming high-dimensional data to low-dimensional embedding. In image analysis, the dominant approach to define input of the UMAP procedure is to transform image into a single-column vector. This is justified for images where the key information is included in the dominant structures clearly visible on the image. In the case of chest X-ray imaging, in COVID-19 patients, the biological changes are subtle and hard to indicate in a single region of interest (ROI), but play a key role in medical diagnosis. We have analysed the data from POLCOVID database, which contains 4956 lung radiographs collected from 24 Polish hospitals. The dataset

includes radiographs of healthy subjects (n=2578), COVID-19 patients (n=1204) and pneumonia patients (n=1174). We propose a novel method of determining and selecting radiomic features to visualise significant differentiation of radiographs between patient groups in UMAP space. Our approach achieves significantly more interpretative UMAP embedding of the disease distribution.

**Keywords:** UMAP, chest X-Rays, COVID-19, radiomics, images.

Tomasz STRZODA<sup>1</sup>, Seweryn KALISZ<sup>1</sup>, Piotr JÓŹWIK-WABIK<sup>1</sup>,  
Dawid MACHA<sup>1</sup>, Marek HERMANSA<sup>1</sup>, Bartłomiej GŁADYS<sup>1</sup>,  
Adam POPOWICZ<sup>2</sup>, Paweł FOSZNER<sup>3</sup>, Michał MARCZYK<sup>4</sup>

## **Chapter 10. TUMOR DETECTION ON HE-STAINED HISTOPATHOLOGICAL IMAGES USING DEEP LEARNING METHODS: CHALLENGES AND SOLUTIONS**

### **10.1. Introduction**

Each year millions of people are diagnosed with cancer around the world. Therefore, research in many disciplines is constantly being done to understand the disease and ultimately increase the survival. One of the areas that provides research opportunities is digital pathology, which is the presentation of pathological images on a computer screen instead of a microscope and glass slides [1]. This opens up further possibilities for analyses based on processing these high-resolution images and using them, e.g. for tumor area detection tasks [2]. In the classical approach, the pathologist looks at the whole-slide image (WSI), analyses it carefully and marks the tumor region with a marker. This solution has one major drawback, namely the long time needed to carry out the assessment. Then, there is the human factor, where fatigue occurs after looking at images for a long time, directly affecting the expert's judgement. One possible solution is to use deep learning methods that can handle such task by operating on a scanned slide image [3]. In supervised deep learning, where data training samples are associated with class labels, we identify three major tasks in digital pathology: classification, regression and segmentation, and the main purpose is to train a model which is able to work on unknown test image based on optimizing loss function [3].

---

<sup>1</sup> Faculty of Automatic Control, Electronics and Computer Science, Silesian University of Technology.

<sup>2</sup> Department of Electronics, Electrical Engineering and Microelectronics, Silesian University of Technology.

<sup>3</sup> Department of Graphics, Computer Vision and Digital Systems, Silesian University of Technology.

<sup>4</sup> Department of Data Science and Engineering, Silesian University of Technology.

This manuscript presents the difficulties that must be taken into account when starting the task of detecting tumor regions in hematoxylin and eosin (HE) stained histopathological images. In section 2, we described the data that were used and the deep learning model created for detection task. In section 3, we presented issues devoted to usage of deep learning methods in HE stained images analysis that we found during our research, such as differences in tissue staining between the slides, magnification used during slide scanning, image patching to prepare data for model building, and different type of prediction methods.

## **10.2. Materials and methods**

### **10.2.1. Data**

Four breast cancer datasets were used in this study. The IDC\_regular\_ps50\_idx5 dataset [2] consist 162 whole slides prepared in magnification 40x. From it, 277 524 patches in size 50 x 50 were extracted and downsampled to the 2.5x magnification (198,738 images without cancer, and 78 786 images containing cancer). The file name consists of the patient identifier and the X and Y coordinates from which the patch was extracted. A 0 indicates no cancer and a 1 indicates the presence of cancer. BreastPathQ dataset [4] contains 96 images scanned at 20x magnification where 64 images contain tumour tissue. 2 579 patches in size 512 x 512 were extracted from the entire WSI images and each include expert opinion about cancer cellularity, i.e. proportion of cancer region to tissue region (from 0 to 1). Another dataset used in the research is TCGA-BRCA [5], which includes WSI for 1098 patients. Images have been prepared at 20x or 40x magnification. All images have been lossy compressed using JPEG with values between 30 and 70. Data contained in TCGA were collected from many sites all over the world in order to reach their accrual targets. The last collection used is BreCaHAD [6] which consist of 162 histopathological images of breast tissue from cancer patients. Each image has size 1360 x 1024 and was prepared in 40x magnification. The dataset contains various cases of tumor malignancy obtained from archived surgical pathology cases. All datasets used in this work were derived from publicly available sources. Example image from each dataset is shown in Figure 10.1.

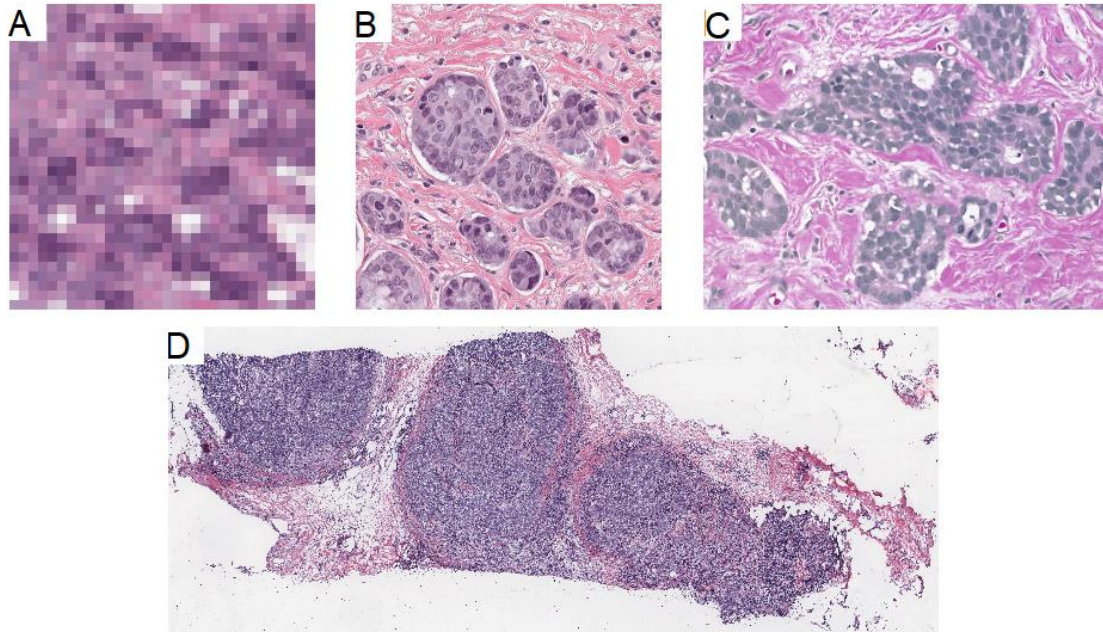


Fig. 10.1. Sample image from each dataset: (A) IDC\_regular\_ps50\_idx5, (B) BreastPathQ, (C) BreCaHAD, (D) TCGA-BRCA

Rys. 10.1. Przykładowy obraz z każdego zbioru danych: (A) IDC\_regular\_ps50\_idx5, (B) BreastPathQ, (C) BreCaHAD, (D) TCGA-BRCA

### 10.2.2. Models

The results presented in this manuscript were obtained using AlexNet deep convolutional neural network architecture, which is commonly used in image classification task [7]. AlexNet is composed of 3 convolutional layers, one max pooling layer, two average pooling layers, and 3 fully connected layers. The last layer uses softmax as an activation function. As deep learning framework, we selected open source framework Caffe, which was initially developed for deep learning vision solutions and allows rapid prototyping [8]. The models were trained on the datasets IDC\_reguls\_ps50\_idx5 and BreastPathQ due to the class labels held by the experienced pathologists and tested on the two other datasets. We note that the training time for each model is about 30 h on a NVIDIA Tesla C2075 graphic card using CUDA 9.0.

## 10.3. Results and discussion

### 10.3.1. Magnification of scanning

When looking at WSI from different sources, it can be noticed that such images often differ in resolution. This is due to hardware aspects such as the magnification of the microscope used by the scanner, the numerical aperture of the objective and the sensor used (size and number of individual pixels) [9, 10]. A model trained on a WSI dataset of a certain magnification will not perform well with images scanned on a different magnification, because the desired regions will have other sizes and properties sought by the neural network. To overcome this problem, the apparent magnification difference (factor  $K$ ) can be calculated and downsampling could be applied. There are several ways, but here we decided to calculate the average values for each  $K \times K$  window and insert them instead of the pixel squares. However, this approach also has its drawbacks. While there is no problem when the height and width of the WSI are multiples of the number representing the apparent magnification, it arises in the opposite situation. If  $K$  is an integer, it is possible to crop the image by removing excessive pixels, but when doing so we lose a part of the WSI that may be valuable. If  $K$  is a floating point number, such a solution may not suffice (if accuracy is to be achieved) because the WSI size divisible by a factor of  $K$  will never be reached.

Regardless of the method, the use of downsampling itself involves a significant loss of information. It is especially visible when the factor  $K$  has a large value (Figure 10.2). The larger the  $K$ , the more distant and less detailed the image is.

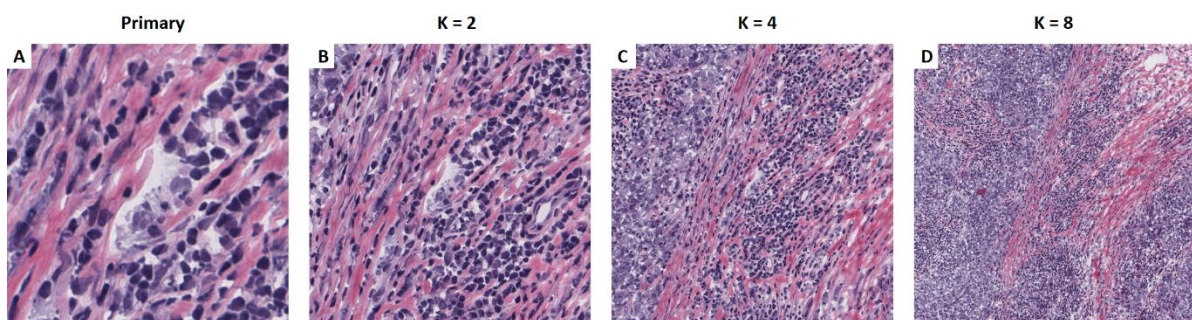


Fig. 10.2. WSI fragment (500 x 500 px) showing the effect of downsampling on the primary image. From left, magnification: (A) 40x, (B) 20x, (C) 10x, (D) 5x

Rys. 10.2. Fragment WSI (500 x 500 px) pokazujący efekt próbkowania w dół na obrazie bazowym. Od lewej, powiększenia: (A) 40x, (B) 20x, (C) 10x, (D) 5x

The effect of different magnification is also seen in a tissue region detection task (Figure 10.3). All elements from the 20x magnification dataset were downsampled ( $K = 8$ ) to obtain 2.5x. The neural network model was then trained and the 2.5x (64 x 64) and 20x (512 x 512) image predictions were made (Figure 10.3 B, C). As can be seen, the prediction of the image before downsampling (Figure 10.3 C), although it appears more detailed (consisting of more patches), contains much more noise, indicating a large number of false positives.

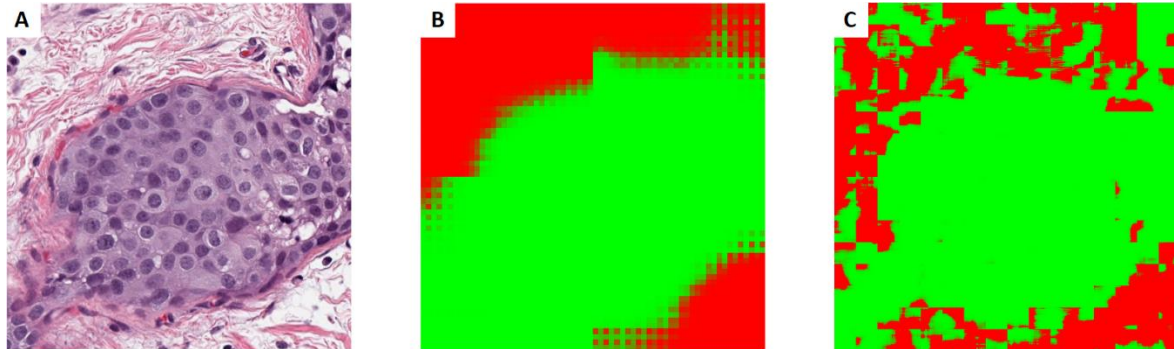


Fig. 10.3. From left: (A) input image, (B) model prediction, (C) model prediction for the image with inappropriate magnification. The green color indicates that the network has classified the region as a cancer, while the red color indicates no cancer

Rys. 10.3. Od lewej: (A) obraz wejściowy, (B) predykcja modelu, (C) predykcja modelu dla obrazu z nieodpowiednim powiększeniem. Kolor zielony oznacza, że sieć sklasyfikowała region jako nowotwór, natomiast kolor czerwony oznacza brak nowotworu

### 10.3.2. Variation in tissue staining

The next problem concerns the colors observed on the slides (Figure 10.4). The visible variations in the tissue staining stage are due to several factors. One of them is the lab protocols applied by individual laboratories. Also, parameters such as tissue thickness, staining concentration and staining time affect the final color. The second aspect is the variety of whole slide scanners that are on the market. The production of digital slides consists of several stages that largely depend on certain hardware or software properties. Unfortunately, manufacturers do not have commonly used standards, so there are visible differences in the final color of each structure [11].



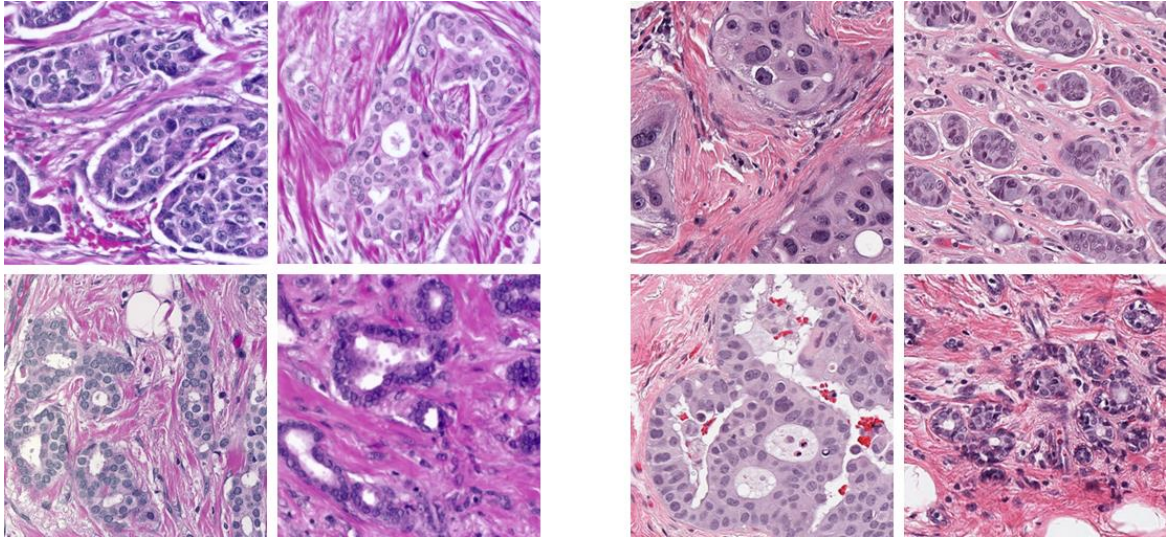


Fig. 10.4. Comparison of the WSI staining between slides  
Rys. 10.4. Porównanie barwienia WSI pomiędzy szkiełkami

A trained neural network may interpret staining variation as analysing images from a different cohort. It is enough for the input slides to have more intense coloring to cause improper prediction of the well-trained deep learning model (Figure 10.5).

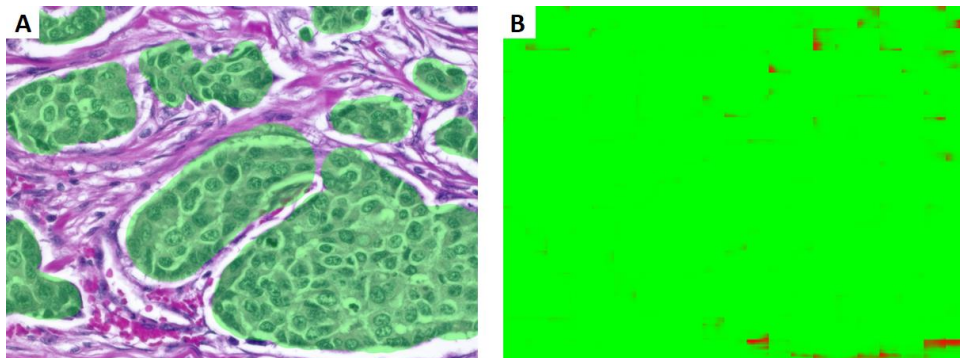


Fig. 10.5. Output image of the deep network, when given a part of the slide with more intense staining.  
From left: (A) expert opinion (in green), (B) prediction  
Rys. 10.5. Obraz wyjściowy sieci głębokiej, po podaniu fragmentu szkiełka z bardziej intensywnym barwieniem. Od lewej: (A) opinia eksperta (na zielono), (B) predykcja

One solution to this problem is tissue stain normalization. There are several algorithms available, but in our experiments we used the method introduced by Azevedo, et al. [12]. The effects of tissue stain normalization are shown in Figure 10.6.

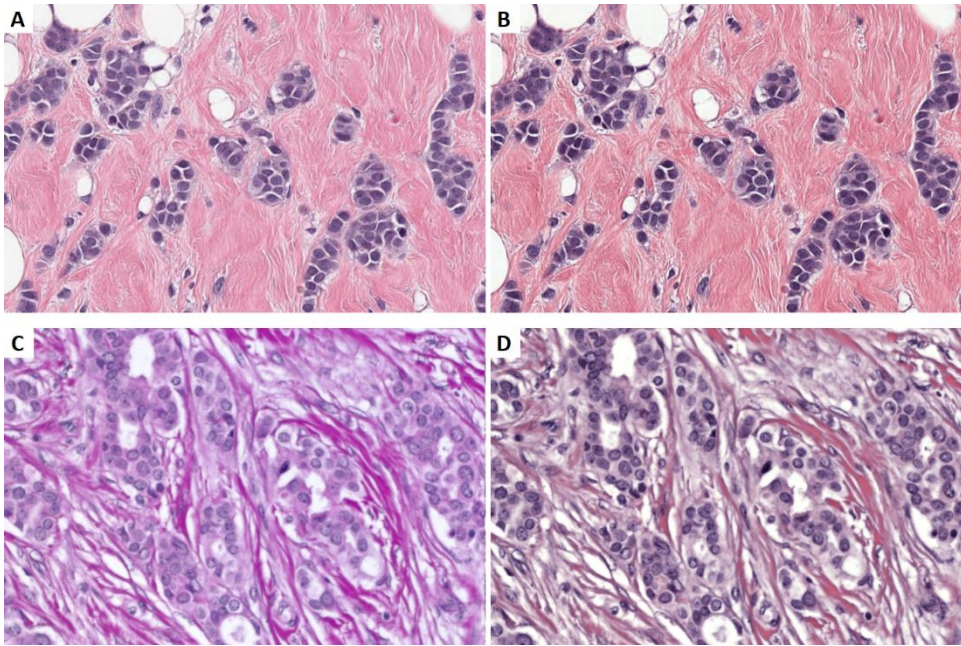


Fig. 10.6. Example of tissue stain normalisation. Left: original images (A, C), right: normalised images (B, D)  
 Rys. 10.6. Przykład normalizacji barwienia tkanek. Po lewej: obrazy oryginalne (A, C), po prawej: obrazy znormalizowane (B, D)

### 10.3.3. Selection of image patch size

When preparing a deep learning model, selection of hyperparameters or patch size might have much greater impact on the outcome than selection of network architecture itself [2, 3]. Choosing proper window size is a task-specific, time-consuming and problematic process. The small patch size is a frequently used in H&E image analysis, since it is not hardware limited and can be a good solution for the small number of images available for network training. Unfortunately, the disadvantage of this solution is the lack of information about the environment outside the patch, which generates opposite information at the edges of the two patches. Two tumor detection models trained on the same dataset with different patch window sizes can give much different prediction results (Figure 10.7). For the smaller window size (Figure 10.7C) prediction is much better on the borders of each structure, however smaller tissue components, like individual lymphocytes, are also predicted as cancer. On the other hand, when patch size is too big (Figure 10.7B), the detected cancer region is much more imprecise.

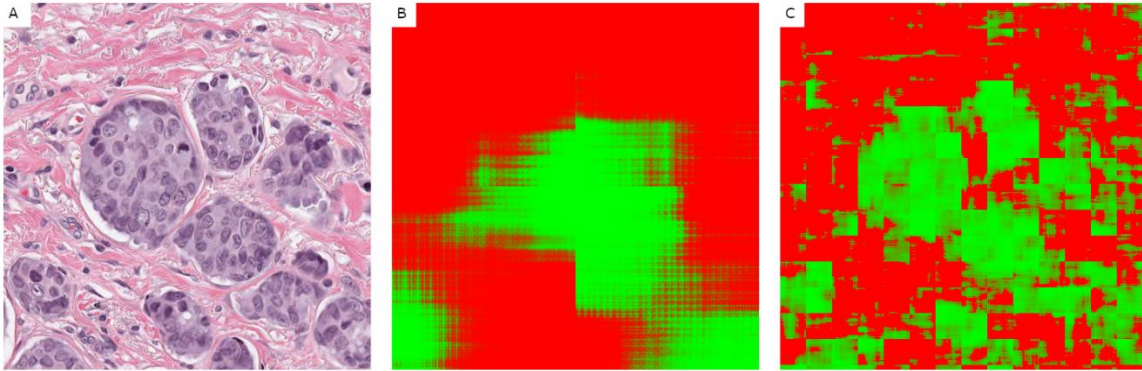


Fig. 10.7. Prediction results for models with different windows size: (A) input image, BreastPathQ dataset (B) window size 227 x 227 and (C) window size 32 x 32

Rys. 10.7. Wyniki predykcji dla modeli z różnymi rozmiarami okien: (A) obraz wejściowy (zbiór danych BreastPathQ), (B) rozmiar okna 227 x 227 oraz (C) rozmiar okna 32 x 32

The observed effect of sharp edges resulting from the merging of adjacent patches can be removed using a method of overlapping windows. To do this, a prediction must be made for the windows located at the boundaries of neighbours patches. When generating the output image for more values at a single point, an average score, min or max value can be determined (Figure 10.8).

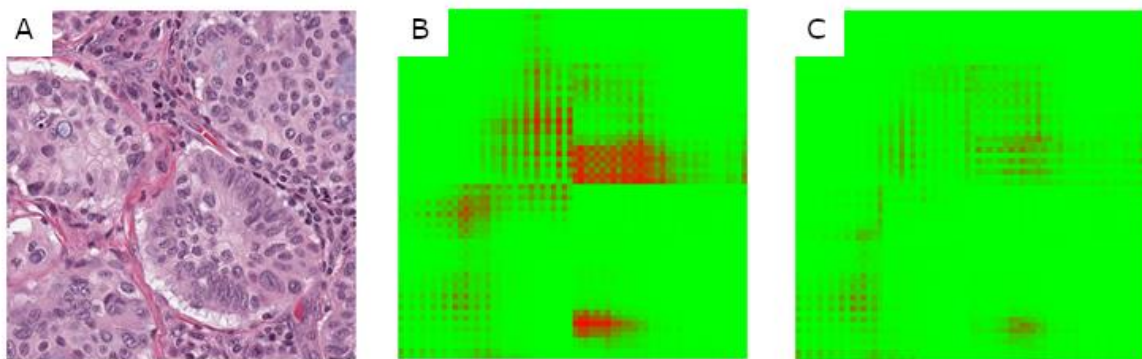


Fig. 10.8. Removal of sharp edges artifacts: (A) input image (BreastPathQ), (B) output image without overlapping, (C) output image after overlapping with max value per pixel

Rys. 10.8. Usuwanie artefaktów ostrych krawędzi: (A) obraz wejściowy (BreastPathQ), (B) obraz wyjściowy bez nakładania, (C) obraz wyjściowy po nałożeniu z wartością maksymalną na piksel

#### 10.3.4. Prediction methods

Image classification with deep neural network is done to assign a class for the entire patch or each individual pixel. In order to achieve higher accuracy, a pixel-level classification method can be used, but it results in a significant increase in computation time. For example, tissue presented on Figure 10.9 consists of 978 patches with size

32 x 32. The time required to perform the prediction for each pixel and generate the output image was 130 minutes. Remember that WSI images can be very large, which translates into tens of thousands of small patches. If the goal is to identify the tumor region for further analysis, e.g. to count cells in this region, image classification at the patch level will allow faster computations and could lead to obtain satisfactory results (Figure 10.9D).

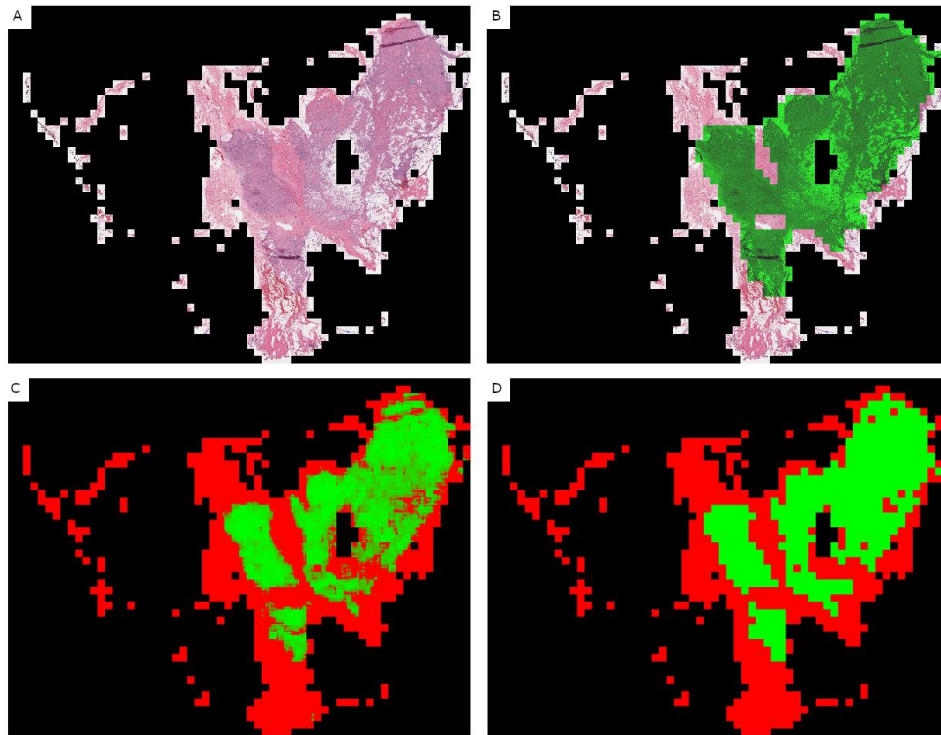


Fig. 10.9. Classification per pixel and patch results (A) input image (IDC\_regular\_ps50\_idx5), (B) expert opinion (C) output image, prediction per pixel, (D) output image, prediction per patch

Rys. 10.9. Wyniki klasyfikacji na piksel i wycinek: (A) obraz wejściowy (IDC\_regular\_ps50\_idx5), (B) opinia eksperta, (C) obraz wyjściowy predykcja na piksel, (D) obraz wyjściowy predykcja na wycinek

## 10.4. Conclusions

In this paper we presented how deep learning models can be used to analyze HE-stained histopathological images and discussed what problems can be encountered during process of model development, training and prediction. Breast cancer region detection task was used here as an example. Due to the use of different WSI scanners for data acquisition and different stain preparations the input data may vary greatly and thus they require more complex pre-processing algorithms. Also, the hardware limitations

resulting in long computation time, make it necessary to choose compromise solutions of varying accuracy. Obtaining a universal solution for histopathological image analysis is a lengthy process. We hope that the issues presented in our work, together with the proposed solutions, will contribute to the development of the field of digital histopathology.

### Acknowledgements

The research reported in this paper was co-financed by the European Union from the European Social Fund in the framework of the project "Silesian University of Technology as a Center of Modern Education based on research and innovation" POWR.03.05.00-00-Z098/17.

### Bibliography

1. S. Nam *et al.*, Introduction to digital pathology and computer-aided pathology. *J Pathol Transl Med* **54**, 125-134 (2020).
2. A. Janowczyk, A. Madabhushi, Deep learning for digital pathology image analysis: A comprehensive tutorial with selected use cases. *Journal of Pathology Informatics* **7**, 29-29 (2016).
3. C.L. Srinidhi, O. Ciga, A.L. Martel, Deep neural network models for computational histopathology: A survey. *Medical Image Analysis* **67**, 101813 (2021).
4. M. Peikari, S. Salama, S. Nofech-Mozes, A.L. Martel, Automatic cellularity assessment from post-treated breast surgical specimens. *Cytometry A* **91**, 1078-1087 (2017).
5. K. Clark *et al.*, The Cancer Imaging Archive (TCIA): Maintaining and Operating a Public Information Repository. *Journal of Digital Imaging* **26**, 1045-1057 (2013).
6. A. Aksac, D.J. Demetrick, T. Ozyer, R. Alhadj, BreCaHAD: a dataset for breast cancer histopathological annotation and diagnosis. *BMC Research Notes* **12**, 82 (2019).
7. A. Krizhevsky, I. Sutskever, G.E. Hinton, ImageNet classification with deep convolutional neural networks. *Commun. ACM* **60**, 84-90 (2017).
8. Y. Jia *et al.*, paper presented at the Proceedings of the 22nd ACM international conference on Multimedia, Orlando, Florida, USA, 2014.
9. N. Farahani, A.V. Parwani, L. Pantanowitz, Whole slide imaging in pathology: advantages, limitations, and emerging perspectives. *Pathology and Laboratory Medicine International* **7**, 23-33 (2015).

10. T.L. Sellaro *et al.*, Relationship between magnification and resolution in digital pathology systems. *Journal of pathology informatics* **4**, (2013).
11. P.A. Bautista, N. Hashimoto, Y. Yagi, Color standardization in whole slide imaging using a color calibration slide. *Journal of pathology informatics* **5**, (2014).
12. T.A. Azevedo Tosta, L.A. Neves, M.Z. do Nascimento, Segmentation methods of H&E-stained histological images of lymphoma: A review. *Informatics in Medicine Unlocked* **9**, 35-43 (2017).

## **TUMOR DETECTION ON HE-STAINED HISTOPATHOLOGICAL IMAGES USING DEEP LEARNING METHODS: CHALLENGES AND SOLUTIONS**

### **Abstract**

The advent of digital histopathology has opened up new possibilities for the processing and analysis of high-resolution tissue images using deep learning methods. While working to develop a model to detect region of breast cancer on HE-stained tissue slide, we encountered several major complications. The aim of this work is to describe these challenges and propose several solutions. We address the following issues and showed their impact on the performance of the deep learning model: (i) variation in tissue staining, (ii) different magnification of scanning, (iii) selection of size of the image patch, (iv) usage of patch-based or pixel-based model prediction method. The analysis were done using deep learning model consisting of convolutional layers that was constructed on several independent datasets. We believe that this publication is a good starting point for image analysis practitioners who want to construct deep learning models on histopathological images.

**Keywords:** digital pathology, histopathological images, HE-staining, deep learning, tumor detection.

Paweł PENDZIAŁEK\*<sup>1</sup>, Joanna POLAŃSKA<sup>1</sup>

## **Chapter 11. MALDI-MSI MOLECULAR IMAGING DATA CLASSIFICATION SYSTEM**

### **11.1. Introduction**

The aim of the research was to create an intelligent system that finds the signature of head and neck cancer based on the protein profile of mass spectrometry. It is currently the sixth most common cancer worldwide [1]. Despite the work of many teams, there is still no marker for use in biopsy and blood testing for this type of cancer. To find that marker, one of the stages are machine learning tools. In this stage, preparations properties are compared with their description from a specialist. The system was created through the fusion of histopathological information and molecular imaging data. Using both information, a mathematical model can be created that allows to distinguish diseased tissue from a healthy tissue. That model can be a part of the system used for diagnostic purposes. Mass spectrometry data from samples taken from patients can be loaded into the system. Then, using the previously created model, the system could assess whether the patient has a suspicion of head and neck cancer.

### **11.2. Materials & Methods**

The data used to find head and neck cancer signature comes from research carried out at the Maria Skłodowska-Curie Institute – Oncology Centre (MSCI), in Gliwice (Poland). These are 5 preparations taken from patients with diagnosed head and neck cancer. Each of the samples contains diseased and healthy parts. Preparation is

---

\* Corresponding author: pawel.pendzialek@polsl.pl, Łanowa 10/25, 41-800 Zabrze, PL.

<sup>1</sup> Department of Engineering and Data Exploratory Analysis, Silesian University of Technology.

a fragment of tissue with a very small thickness, therefore it is analyzed only in two-dimensional space. The pathologist places a grid over the sample (the grid consists of vertical and horizontal equidistant parallel lines). Then the pathologist examines the sample cell by cell, using a microscope. For each cell, the pathologist determines whether this fragment looks more like diseased or healthy tissue. These cells will be called mass spectra. Each of the preparations was also examined in the spectrometer using MALDI-MSI technique. This machine measured values of all 40 160 mass spectra for 109 000 mass channels with high accuracy. Gaussian Mixture Model technique was applied to reduce the number of mass channels to 3714. Mass channels are peptides (proteins) and they differ by the  $mz$  value. They will be called features. The feature values are numbers in the range from  $1.814e-32$  to  $2.254e8$ . Table 11.1 shows statistics of the preparations. The number of diseased and healthy tissue spectra is calculated on the basis of the pathologist's description. In parentheses there is information what part of the preparation is the given type of tissue. In the Figure 11.1 there are shown mentioned preparations.

Table 11.1

Preparations statistics

	Prep. 1	Prep. 2	Prep. 3	Prep. 4	Prep. 5
Number of spectra	8005	11869	11823	4505	3958
Number of diseased tissue spectra	844 (10.54%)	4885 (41.16%)	5631 (47.63%)	1962 (43.55%)	1963 (49.60%)
Number of healthy tissue spectra	7161 (89.46%)	6984 (58.84%)	6192 (52.37%)	2543 (56.45%)	1995 (50.40%)

prep. 1    prep. 2    prep. 3    prep. 4    prep. 5

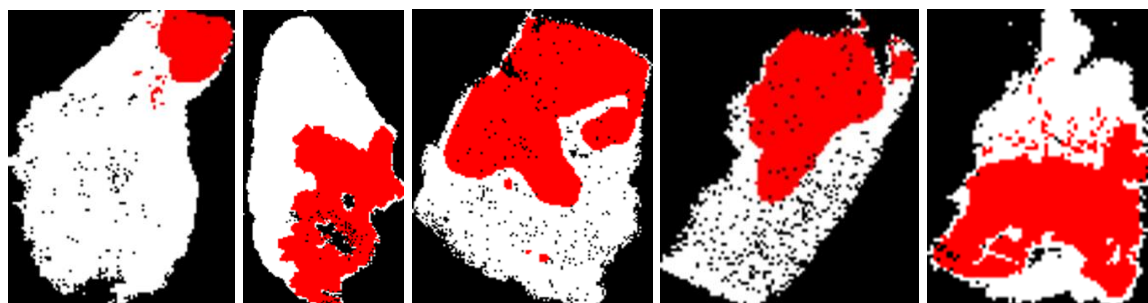


Fig. 11.1. 5 preparations used to create the system. Colors: healthy tissue spectra – white, diseased tissue spectra – red, background – black

Rys. 11.1. 5 preparatów użytych do utworzenia systemu. Kolory: widma zdrowe – biały, widma chore – czerwony, tło – czarny



The aim of the study was to create a system that classifies the data which was not "seen" before. Therefore, the data was split into three sets:

- training set (80% healthy and diseased tissue spectra from each of the preparations 1,2,3,4)
- test set (20% healthy and diseased tissue spectra from each of the preparations 1,2,3,4)
- validation set (all spectra from the preparation 5)

The training set was used to select the most important features and create a model. Next, the test set was used to find an optimal threshold value for classification task. This way the final model was obtained, and its quality was checked using the validation set. In the Figure 11.2 there is a block diagram which presents a scheme of classifier construction and validation. The system was implemented entirely in Python language.

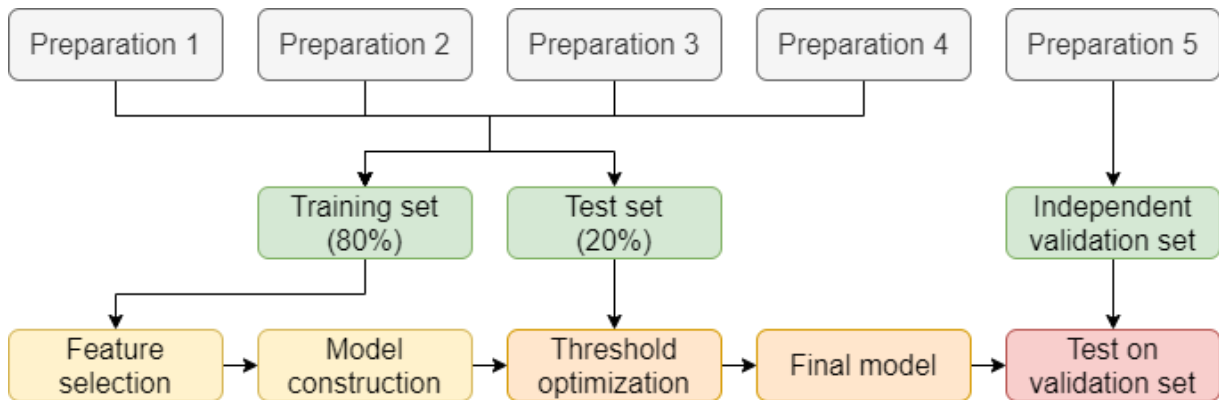


Fig. 11.2. Block diagram illustrating a classifier construction and validation scheme  
Rys. 11.2. Schemat blokowy ilustrujący sposób konstrukcji i walidacji klasyfikatora

The feature values differ by up to 40 orders of magnitude (range from  $1.814e-32$  to  $2.254e8$ ). If such data is loaded to the classifier, it extends the computation time, and secondly, the classifier builds a model using a small number of features with the highest values. To solve this problem, the data was logarithmic. Every  $x$  in the data was converted to  $\ln(1+x)$ . The number 1 was added so that the data in the range (0,1) after logarithm is positive and has small values. This method reduced the data range from  $1.814e-32$  to  $1.923e1$ .

The number of features is really big (there is 3714 of them). Reduction of feature number can speed up calculations and help to find only features which are related to the head and neck cancer signature. Probably there exist features which values are very small. Also there may be a group of features that have high values, but their variety is small. In each preparation there is healthy and diseased tissue so it can be assumed that both of

mentioned groups of features do not affect whether tissue part is diseased or not. The goal is to select features which values are large and highly variable.

To evaluate features importance, the variance was calculated for each of them (all spectra from the training set were used to calculate it). Variance is an arithmetic mean of the squares of deviations of numbers from their arithmetic mean. Looking at this definition, both features with low values and features with low variety have relatively small variance values. The question is, how many features with the highest variance should be taken to the classifier. The threshold variance value was selected using the GMM (Gaussian Mixture Model) method. This method is to present a data distribution as a sum of a finite number of Gaussian distributions with unknown parameters [2]. For distribution of feature variances, 3 Gaussian distributions were fit (Figure 11.3). The points of intersection of “neighboring” distributions divide the features into 3 groups. The group with highest variance values was selected – only features with variance higher than 0.364 were taken from the data. This way 217 features (less than 6%) remained.

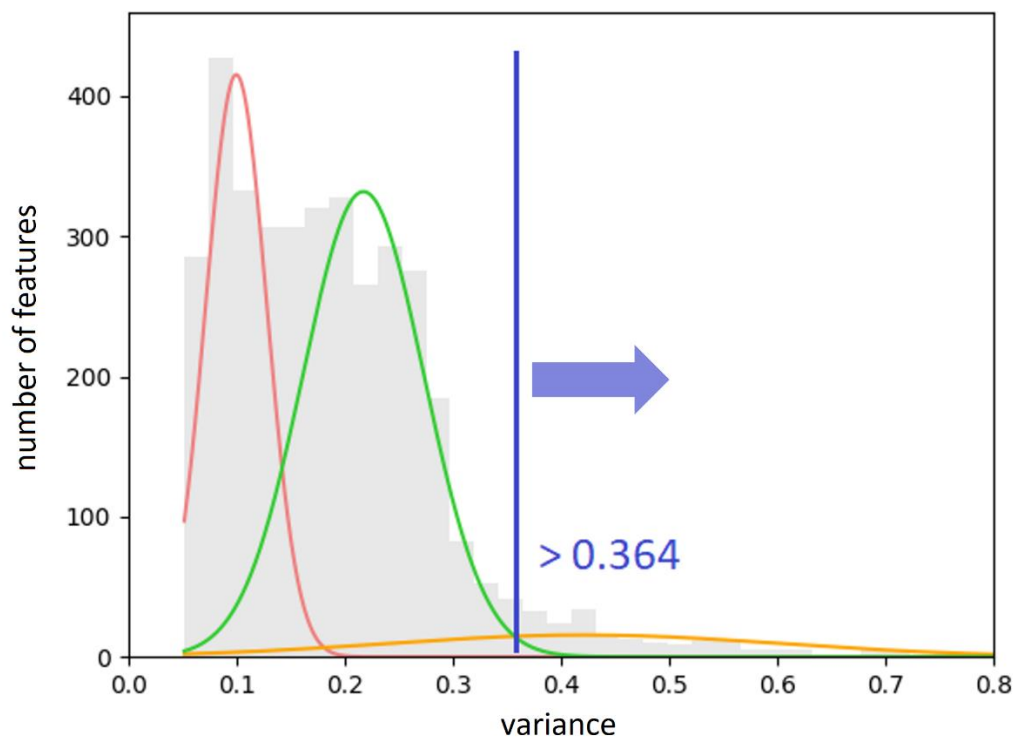


Fig. 11.3. Distribution of feature variances approximated by GMM

Rys. 11.3. Dystrybucja wariancji cech przybliżona przez GMM

The next step was the model building. The tool used for classification was SVM (Support Vector Machine) classifier with the RBF (Radial Basis Function) kernel. This is an algorithm which uses support vectors to construct the hyperplane that divides

classes. In analyzed data there are two classes: the "healthy" class and the "cancer" class. The model was built on the test set.

To evaluate the model's quality, it is necessary to know the following numbers:

- TP (true positive) – the number of data correctly classified to a positive class
- TN (true negative) – the number of data correctly classified to a negative class
- FP (false positive) – the number of data incorrectly classified to a positive class
- FN (false negative) – the number of data incorrectly classified to a negative class.

In analyzed data, "cancer" is the positive class, and "healthy" is the negative class. After counting above values, the classifier quality indicators can be calculated:

- Sensitivity (percentage of correctly classified positive data points)
- Specificity (percentage of correctly classified negative data points)
- PPV (percentage of correct "positive" assignments)
- NPV (percentage of correct "negative" assignments)
- Accuracy (percentage of correctly classified data points)
- Balanced accuracy (arithmetic mean of sensitivity and specificity)
- F1 score (harmonic mean of sensitivity and PPV).

To calculate the probability of spectra belonging to the cancer class, an algorithm that uses decision function was implemented. The classifier creates a decision function that returns a value for each of the data point in the test set. In case of 2 classes, on the one side of the hyperplane there are data points with negative values, and on the other side there are data points with positive values. The further from the hyperplane, the higher the absolute value of the data point is and the more it fits to the class it is inside (according to the classifier). A method for calculating probabilities is to scale all of the returned values linearly to values in the range [0,1]. Probabilities were calculated to find the threshold value for which classification results are the best. To find optimal threshold the Youden's  $J$  statistic was used, which is the sum of sensitivity and specificity minus 1. The best threshold value was calculated on the test set. For this threshold value, a test was performed on the independent validation set.

To check the quality of the system, all steps were repeated for the remaining splits into 4 training preparations and one preparation for independent validation. Training and test sets were created in the same way as before.

### 11.3. Results

In the Table 11.2 there are presented results for all 5 data splits. In the Figure 11.4 there are presented bitmaps showing classification results for independent validation preparations. Balanced accuracy for test sets is 90-92% (91%±1% on average). This results are very good. For validation preparations, a great result (almost 93%) is for preparation 1. In other cases, the result for the independent validation set is clearly worse than for the test set. The biggest difference is for preparation 5 (probably it contains a different cancer subtype) and for preparation 2 (the pathologist incorrectly assigned the lymphatic infiltration to the cancer class). However, balanced accuracy of 69-93% (81%±9% on average) obtained for validation sets is satisfactory.

Table 11.2

Results summary

		Independent validation preparation:				
		1	2	3	4	5
Number of features		204	201	206	202	217
Model building time [s]		63.01	43.94	43.22	63.54	68.43
Test set	PPV [%]	86.60	80.72	81.62	84.16	85.26
	NPV [%]	93.24	95.73	97.28	95.81	96.39
	Balanced accuracy [%]	90.26	90.18	92.05	91.47	92.35
Validation set	PPV [%]	46.58	77.34	82.69	76.27	63.22
	NPV [%]	99.89	76.29	87.49	90.21	79.38
	Balanced accuracy [%]	<b>92.88</b>	<b>74.30</b>	<b>85.17</b>	<b>83.79</b>	<b>68.54</b>

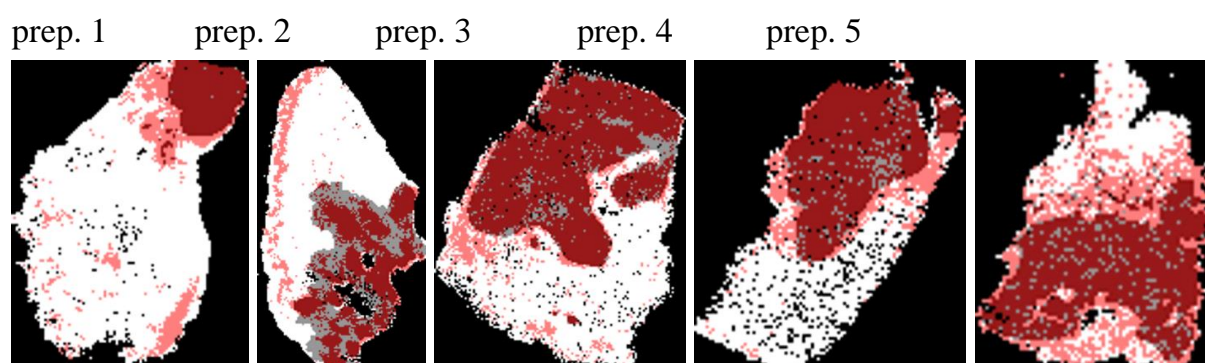


Fig. 11.4. Classification results for validation sets. Colors: TN – white, FP – light red, FN – gray, TP – dark red, background – black

Rys. 11.4. Wyniki klasyfikacji dla zbiorów walidacyjnych. Kolory: TN – biały, FP – jasny czerwony, FN – szary, TP – ciemny czerwony, tło – czarny

## 11.4. Discussion

### 11.4.1. Interpretation of the results

The goal was to find the signature of head and neck cancer. There were done 5 different splits, and from 3714 features only 277 were selected at least once to the classifier. In the Figure 11.5 there is a Venn diagram that shows how many features were common only for specific classifiers. For example, 15 features were selected only in the case when preparation 2 was the validation set (blue color on the very top). 44.4% of these 277 features were always selected, so the selection was quite repetitive and these 123 features are a representative part of this set.

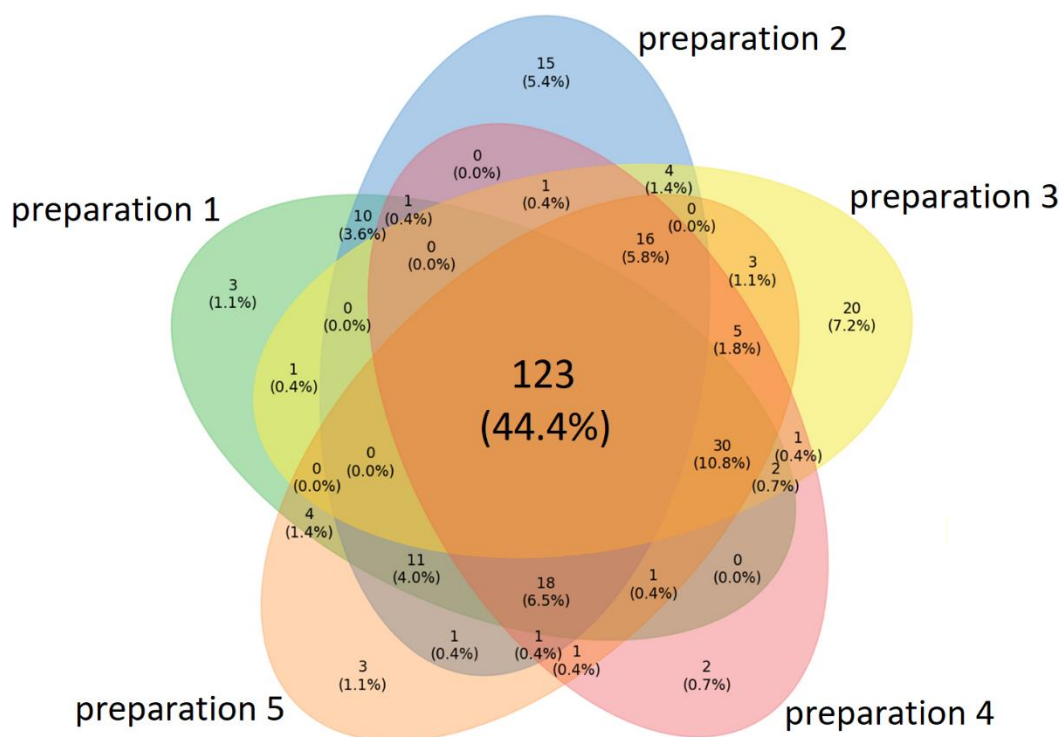


Fig. 11.5. A Venn diagram illustrating how many features were common only for specific classifiers  
Rys. 11.5. Diagram Venna ilustrujący ile cech było wspólnych tylko dla konkretnych klasyfikatorów

In the Figure 11.6 there is an axis with marked  $m/z$  values for 277 selected features. Most of them have small  $m/z$  values. Probably mass channels with low  $m/z$  values have bigger impact on healthy and diseased spectra distinction.



Fig. 11.6.  $m/z$  values of 277 selected features  
Rys. 11.6. Wartości  $m/z$  dla 277 wybranych cech

In the left part of Figure 11.7 there is a correlation matrix between all features. The features can be divided into 2 main groups (the border is about feature number 2000) which have stronger correlation than with features from another group. In the right part of Figure 11.7 there is a correlation matrix between 277 features which are in at least one classifier. Most of them are from the group with smaller m/z values. Selected features does not have much stronger correlation. Despite this, the classification results are satisfactory. If the number of preparations was greater, and if all of them were certainly the same cancer subtype, the results would probably be better.

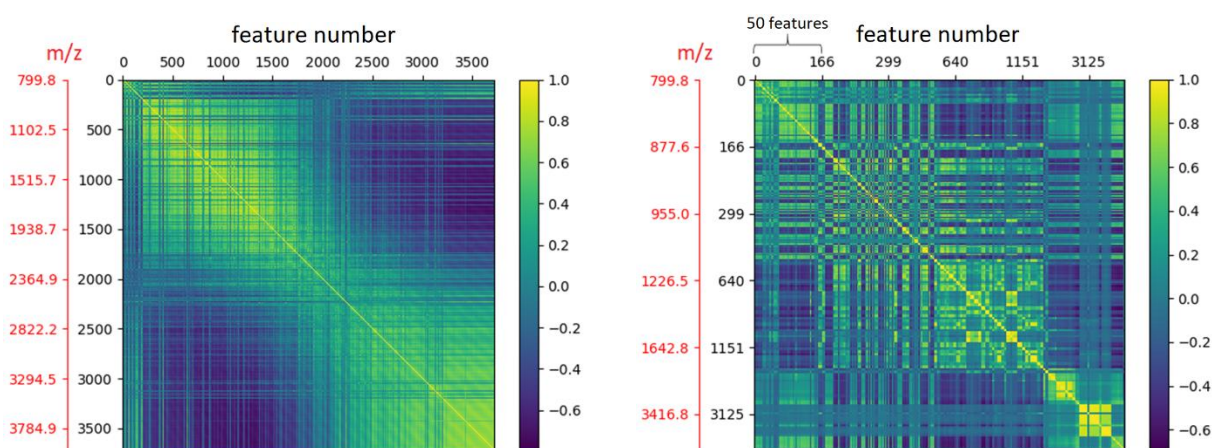


Fig. 11.7. Correlation matrices: between all 3714 features (left) and between 277 selected features (right)

Rys. 11.7. Macierze korelacji: pomiędzy wszystkimi 3714 cechami (z lewej) i pomiędzy 277 wybranymi cechami (z prawej)

#### 11.4.2. Comparison with standard approaches

At the beginning, the data was logarithmic to decrease its numerical range. The second advantage of this solution is that the natural logarithm is an increasing monotone function. It means that the features that had very small values before logarithm, still have smaller values comparing to the other features. Another popular solution for data processing is normalization, for example Z standardization. It is subtracting the arithmetic mean of the data from each variable and dividing this difference by the standard deviation. This can be performed separately for each feature and then they become more "comparable" with each other. Normalization is a good method if the features are independent of each other, but in analyzed data features are protein values. If the feature has very small values, probably this protein is not essential to distinguish classes in the preparation. If normalization is used, unfortunately such features can have a huge impact on the model. Moreover, the numbers can still have big numerical range.

The reduction of feature number was big (more than 94% of them were rejected). Without feature selection, 5 hours after starting the system the model was still not obtained. This operation was necessary not only to speed up calculations, but also to find only the features that create the signature of head and neck cancer.

In the standard approach, the classifier does not calculate probabilities of data points belonging to each class – it only creates a hyperplane and assignments to the classes are made according to it. In used classifier there is implemented a default method for calculating probabilities. This method internally uses 5-fold cross-validation to calculate them [3]. For this method the best Youden's index was obtained for the threshold of 30% for validation preparation 5. The optimal threshold for the implemented method (probabilities calculated using the values returned by decision function) is 54%. In the Figure 11.8 there are heatmaps of cancer probabilities for both default and implemented method.

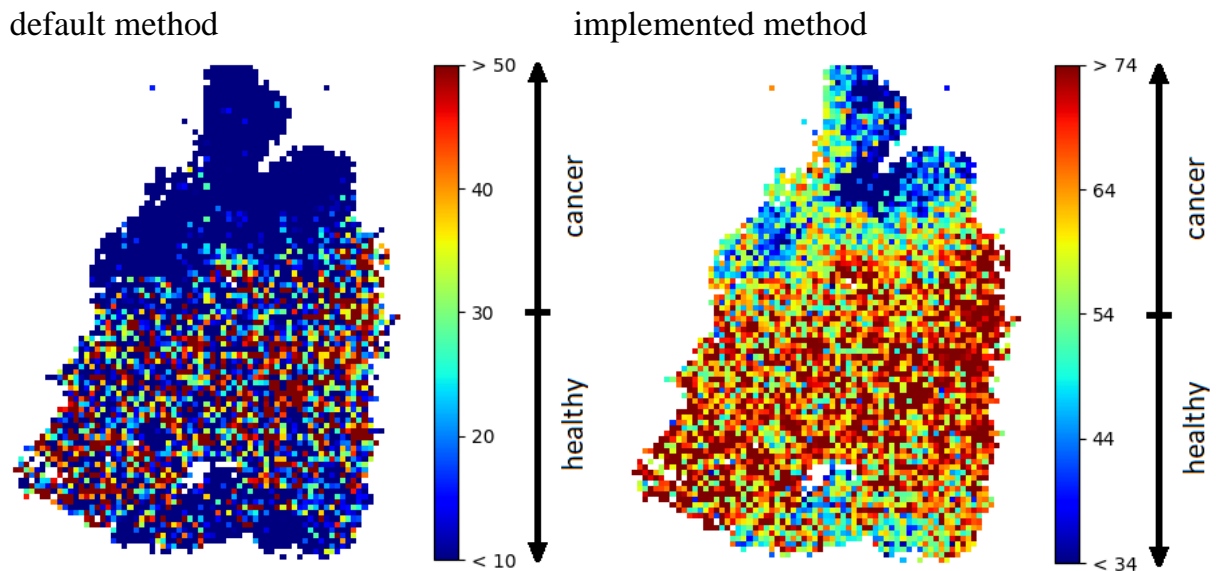


Fig. 11.8. Heatmaps of cancer probability [%] for validation preparation 5

Rys. 11.8. Heatmapy prawdopodobieństwa nowotworu [%] dla preparatu walidacyjnego 5

Comparison of the results for validation preparation 5 for 3 mentioned methods is shown in the Table 11.3 and in the Figure 11.9. The results without threshold detection are the worst and for method based on decision function they are the best. Without detection, the system tended to assign too many spectra to the healthy class (low sensitivity). For implemented method, balanced accuracy is more than 4 p.p. (percentage points) better than for the default method and more than 8 p.p. better than without calculating probabilities. Sensitivity is over 86% and F1 score is much higher than in other cases.

Model building time is much lower than in the default method because this method uses additional cross-validation.

Table 11.3

## Results for validation preparation 5

	Without detection	Default method	Implemented method
Sensitivity [%]	25.73	38.61	86.70
Specificity [%]	94.34	90.03	50.38
Accuracy [%]	60.31	64.53	68.39
Balanced accuracy [%]	60.03	64.32	68.54
F1 score [%]	39.13	51.92	73.13
PPV [%]	81.72	79.21	63.22
NPV [%]	56.35	59.85	79.38
Model building time [s]	68.34	440.5	68.34

without detection    default method    ...implemented method

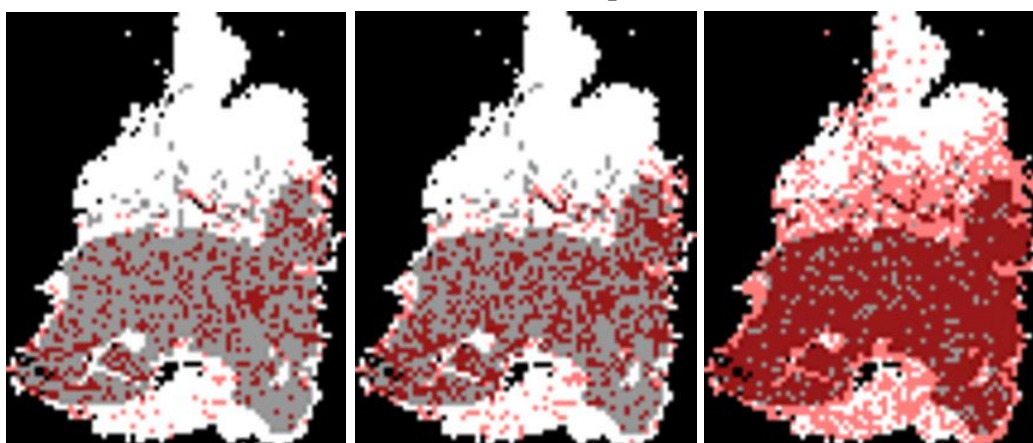


Fig. 11.9. Classification results for validation preparation 5. Colors: TN – white, FP – light red, FN – gray, TP – dark red, background – black

Rys. 11.9. Wyniki klasyfikacji dla preparatu walidacyjnego 5. Kolory: TN – biały, FP – jasny czerwony, FN – szary, TP – ciemny czerwony, tło – czarny

### Acknowledgements

Work was partially financially supported by the Polish National Science Centre, project BiTIMS grant 2015/19/B/ST6/01736.



## Bibliography

1. F. Bray, et al, Global cancer statistics 2018: GLOBOCAN estimates of incidence and mortality worldwide for 36 cancers in 185 countries, *CA Cancer J. Clin.* (2018) **68**:394-424.
2. Description of GMM method: <https://scikit-learn.org/stable/modules/mixture.html>, accessed: 16 March, 2021.
3. Description of the default method used by classifier to calculate probabilities: <https://scikit-learn.org/stable/modules/generated/sklearn.svm.SVC.html>, accessed: 21 March, 2021.

## MALDI-MSI MOLECULAR IMAGING DATA CLASSIFICATION SYSTEM

### Abstract

The aim of the research was to create an intelligent classification system for head and neck cancer biopsy results based on the mass spectrometry protein profile. The material was molecular imaging data and information about the tissue type of samples taken from 5 patients (40 160 mass spectra in total, measured for 109 000 mass channels). Gaussian Mixture Model technique was applied to reduce the number of mass channels to 3714. Further reduction was obtained by selection of most variable features based on the variance distribution of peptides abundance in preparation. The SVM classifier was used and the optimal threshold detection method was implemented. The learning was performed in the process of cross-validation per patient, and the proportion of training and test set was 80:20. Results of the classification are satisfactory. Balanced accuracy for test set was 90-92% (91%±1% on average), for validation set was 69-93% (81%±9% on average).

**Keywords:** oncology, mass spectrometry, machine learning, classification.

Paweł KUŚ<sup>\*1</sup>, Roman JAKSIK<sup>1</sup>, Marek KIMMEL<sup>2</sup>

## **Chapter 12. TUMOR SUBCLONAL RECONSTRUCTION PIPELINES – COMPARISON OF RESULTS**

### **12.1. Introduction**

Tumors arise from mutated single cells in the multistep evolutionary process, driven by two phenomenons: 1) the occurrence of new mutations, which can drive the tumor progression, and 2) the process of selection, which eliminates weak populations of cells and promotes the growth of the strongest ones. The resultant population is usually highly heterogeneous - even if the resulting evolutionary process has a branching, rather than a linear structure, old populations might not be entirely replaced by the new ones. This polyclonal nature of cancer carries a serious clinical impact: disease relapses and evolution of therapy-resistance [1], clonal cooperation [2] and, in general, poor prognosis. The knowledge of tumor subclonal structure might be the key to the development of effective, personalized cancer therapies and the improvement of patients' survival.

However, despite the recent advances in Next Generation Sequencing (NGS), the recognition of clonal structure of the tumor is still not a trivial task. Since the sequencing of single cells is still an expensive technology, struggling with the issue of accurate and uniform amplification of the whole genome, bulk sequencing remains the main method of tumor genotyping. Information provided by bulk sequencing is however averaged over the millions of cells and the distinction of subclonal populations, especially if they are small and share similar cellular prevalences, is therefore hard or even impossible.

Over the last decade, numerous algorithms aiming to resolve tumor heterogeneity from the bulk sequencing data have been created. Most of them define subclones by clustering together the detected single-nucleotide variants (SNVs) with similar allelic fre-

---

\* Corresponding author: pawel.kus@polsl.pl, Akademicka 2A, 44-100 Gliwice, PL.

<sup>1</sup> Department of Systems Biology and Engineering, Silesian University of Technology.

<sup>2</sup> Department of Statistics, Rice University, Houston, USA.

quencies, usually correcting them according to the detected copy number variation (CNV) of the mutation loci. Next, they estimate the cellular frequencies of detected subclones, which might be followed by the inference of phylogenetic relationships between them. Unfortunately, until now no golden standard of tumor clonality analysis has been established [13]. Lack of independent and wide assessment of the existing approaches makes the methodology selection a hard process. In this work, we apply and compare the results of few pipelines, consisting of two different methods of copy-number changes detection and two most common algorithms for the reconstruction of tumor subclonal structure.

### **12.1.1. Overview of the chosen algorithms**

Tests of the selected algorithms were performed on two datasets, for which multiple samples per patient were available. The first one included 4 female patients with HER2 positive breast cancer (BRCA), for which we performed Whole Exome Sequencing (WES) of two tumor samples (primary tumor and lymph node metastasis) along with the one normal sample. The second dataset, consisting of control-diagnosis-relapse triplets of samples from 11 patients with acute myeloid leukemia (AML) was retrieved from European Genome-phenome Archive (EGA) [4]. From both datasets we extracted 2 BRCA and 8 AML patients for which the number of detected high-quality non synonymous/intron/intergenic mutations did not exceed 3,000 to decrease the required computing time.

Two popular algorithms for the clonal reconstruction were tested: PhyloWGS [5] and PyClone [6], both supporting simultaneous analysis of multiple samples per patient and using SNVs as well as CNVs associate mutations into clones. In addition, PhyloWGS performs the evolutionary analysis of detected clones, generating and evaluating thousands of possible phylogenetic trees, which is not done by PyClone and might be performed using additional software like ClonEvol [7]. Two more algorithms were considered but were finally discarded for different reasons: SciClone [8]- which only clusters the mutations on the copy-number (CN) neutral regions, whereas CNVs were found common in our samples and CliP [9] - due to the lack of the multi-sample mode. Two methods of CNVs detection were used: FACETS [10] and TitanCNA [11]. They were chosen since both support the latest version of the reference genome (hg38), providing integer allele-specific copy numbers and easy integration with the

PhyloWGS, through the available CNV parser. We did not apply the popular GATK workflow for somatic CNV detection as it does not calculate integer CN. SNV and Indel mutations were called using Mutect2 [16].

Application of the two selected algorithms of clonal reconstruction to the mutation calls from two methods of CNV detection and one of SNV/Indel detection resulted in 4 pipelines being tested in this work (Fig. 12.1). In addition, as the NGS-based tumor purity estimates may significantly differ from the pathologist's assessments [3], to investigate the impact of purity estimations on the reconstruction results, all 4 pipelines were run twice: 1) with the purity estimates delivered by CNV callers and using default 100% purity only if the estimate was missing or below 0.1, and 2) assuming the perfect purity of all samples.

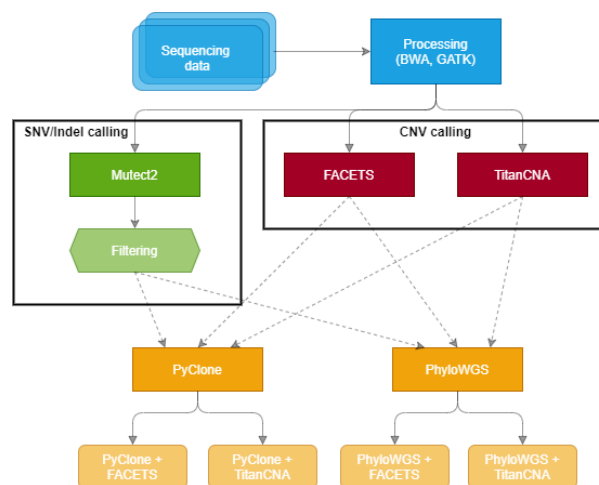


Fig. 12.1. Graph representing the 4 pipelines run in the study

Rys. 12.1. Graficzne przedstawienie 4 kombinacji metod zastosowanych w pracy

## 12.2. Results

### 12.2.1. CNV callers – comparison of FACETS and Titan calls

Both FACETS and Titan were run to call changes in total and minor allele copy numbers (Fig. 12.2). FACETS returned a single solution for each sample, Titan generated four different solutions across a set of given ploidies (2, 3) and numbers of clusters (1, 2) and successfully chose the optimal solution in all samples except those from the patient AMLRO-9, which except for some small regions was CN-neutral among non-sex

chromosomes according to FACETS. The computational time required by both methods was significantly shorter for FACETS than for Titan (data not shown).

For one patient (AMLRO-6) FACETS and Titan consistently showed different main ploidy (Titan: 3, FACETS: 2) and for 4 patients in both datasets (AMLRO-2 and 3, G30 and G31) Titan showed significantly different results for paired tumor samples, whereas all FACETS results for these patients were concordant.

Both algorithms were found prone to the detection of numerous, short CN calls, equally distributed along the genome, which after manual inspection should be classified as noise. The occurrence of these artifacts was more common in the FACETS results and among samples with limited or no true large-scale CN changes.

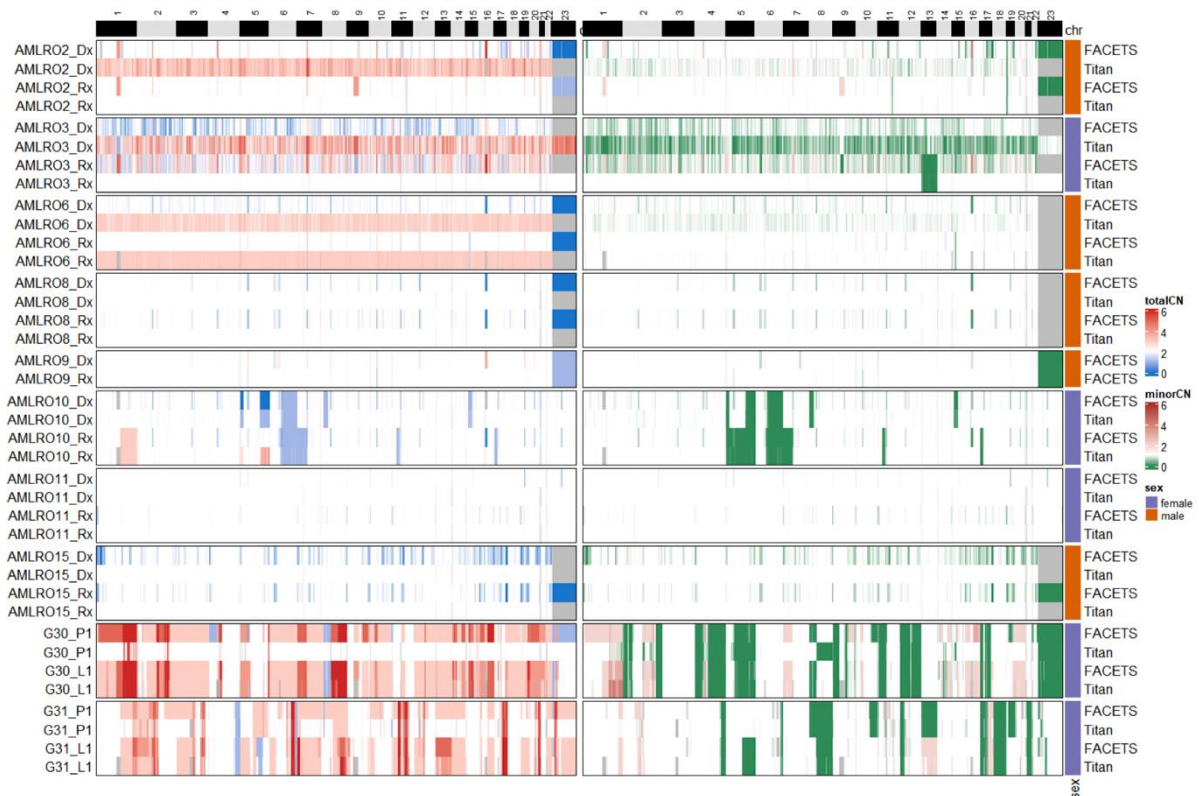


Fig. 12.2. Comparison of CNV calls obtained from FACETS and Titan. The left heatmap presents total CN changes, the right one changes in the minor allele CN. Gray – regions not reported by a caller. CNV callers are annotated on the right. Sample namings for AML: Dx – diagnosis, Rx – relapse; for BRCA: P1 – primary tumor, L1 – lymph node metastasis. Titan results for AMLRO-9 are missing, as it could not choose the optimal solution. Values above 6 were trimmed

Rys. 12.2. Porównanie wyników detekcji mutacji CNV otrzymanych za pomocą algorytmów FACETS i Titan

### 12.2.2. CNV callers - comparison of purity estimates

FACETS and Titan estimations of sample purities (Fig. 12.3) were significantly discordant and often incomplete or misleading. FACETS estimated purity of 14 out of 20 samples with values within the range from 0.16 to 0.81. In turn, Titan returned purity estimations of 18/20 samples, from which 8 were equal or almost equal to 0. These misleading values were associated with the nearly diploid state of samples and may impact the further analysis if propagated through the fully automated pipelines.

### 12.2.3. Clonal reconstruction - comparison number of clones

We found only the PhyloWGS to give a stable number of clusters, regardless of the dataset, CNV caller used, and the usage of estimated purity values or assuming them to be perfectly pure. In contrast, the number of clones returned by PyClone depended on all of these factors and in some cases differed by up to two orders of magnitude: starting from the few for AML dataset with FACETS calls and purity estimations, through dozens for the same dataset with other methods' combinations, up to the hundreds for BRCA dataset. Interestingly, when all purities were set to 1 the number of clones grew for the AML and decreased for the BRCA dataset. Therefore, we found only the PhyloWGS to be detecting a reasonable and predictable number of clones irrespective of the other methods used.

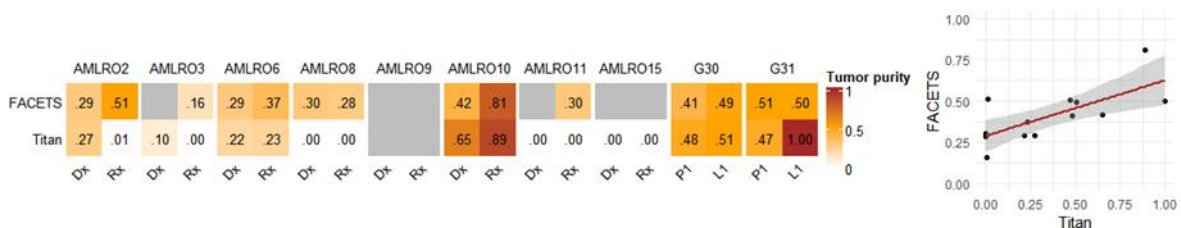


Fig. 12.3. Comparison of purity estimations from FACETS and Titan. Gray - missing estimation. Sample namings as in fig. 12.2. Pearson correlation coef. = 0.72,  $p = 0.0039$

Rys. 12.3. Porównanie czystości próbek estymowanych za pomocą algorytmów FACETS i Titan

### 12.2.4. Clonal reconstruction - comparison of mutation to clone assignments

Pairwise similarities of the results of selected pipelines were measured using two different similarity measures: Adjusted Rand Index (ARI) and Adjusted Mutual Information (AMI), both returning negative or close to 0 values for independent classifications and equal to 1 for the perfect match (Fig. 12.4). The range of obtained

values varied among the patients, lower among such cases like G30, G31, and AMLRO2, and significantly visibly higher for others, e.g. AMLRO15 (Fig. 12.4a). Therefore, average index values might correspond to the clonal distinguishability or detectability feature of given tumors.

Pipelines were more convergent when the purity estimates from CNV callers were not used but all samples were assumed to be 100% pure (Fig. 12.4a vs 12.4b). In association with the differences in the number of detected clones (Sec. 2.3) it shows that both algorithms significantly differ in how they deal with impure samples. Interestingly, under the assumption of the perfect purities, PyClone results were less affected by the choice of the CNV caller than the results of PhyloWGS.

Direct comparison of the results of the same pipelines obtained with and without the purity estimates from CNV callers showed significant differences between PhyloWGS and PyClone (Fig. 12.4c). The former showed a moderate agreement of both runs, even for those cases where purity estimates were missing or faulty and were assumed equal to 1 in both runs. The results returned by the latter matched nearly perfectly in such cases but were almost independent for some other cases. Again, a potential explanation for that might be related to the different number of detected clones which we cannot explain.

Table 12.1

The numbers of clones detected by sets of algorithms. FAC - FACETS, NA – pipeline did not completed within 4 days or was not run due to missing CNV calls, \* – Only the purities above 0.1 were used in the analysis. Purities below this threshold, as well as the missing values, were replaced with 1

with purity estimation*					all tumor purities set 1			
PyClone			PhyloWGS		PyClone		PhyloWGS	
patient	FAC.	Titan	FAC.	Titan	FAC.	Titan	FAC.	Titan
AMLRO2	3	3	7	6	33	21	6	6
AMLRO3	2	13	NA	NA	14	16	8	6
AMLRO6	2	2	6	4	7	6	7	7
AMLRO8	2	16	7	7	18	16	5	5
AMLRO9	4	NA	7	NA	4	NA	5	NA
AMLRO10	2	5	NA	7	17	21	6	6
AMLRO11	3	16	5	5	25	17	8	5
AMLRO15	14	15	9	6	13	15	9	6
G30	217	109	13	9	66	83	8	8
G31	91	122	17	10	66	66	13	10

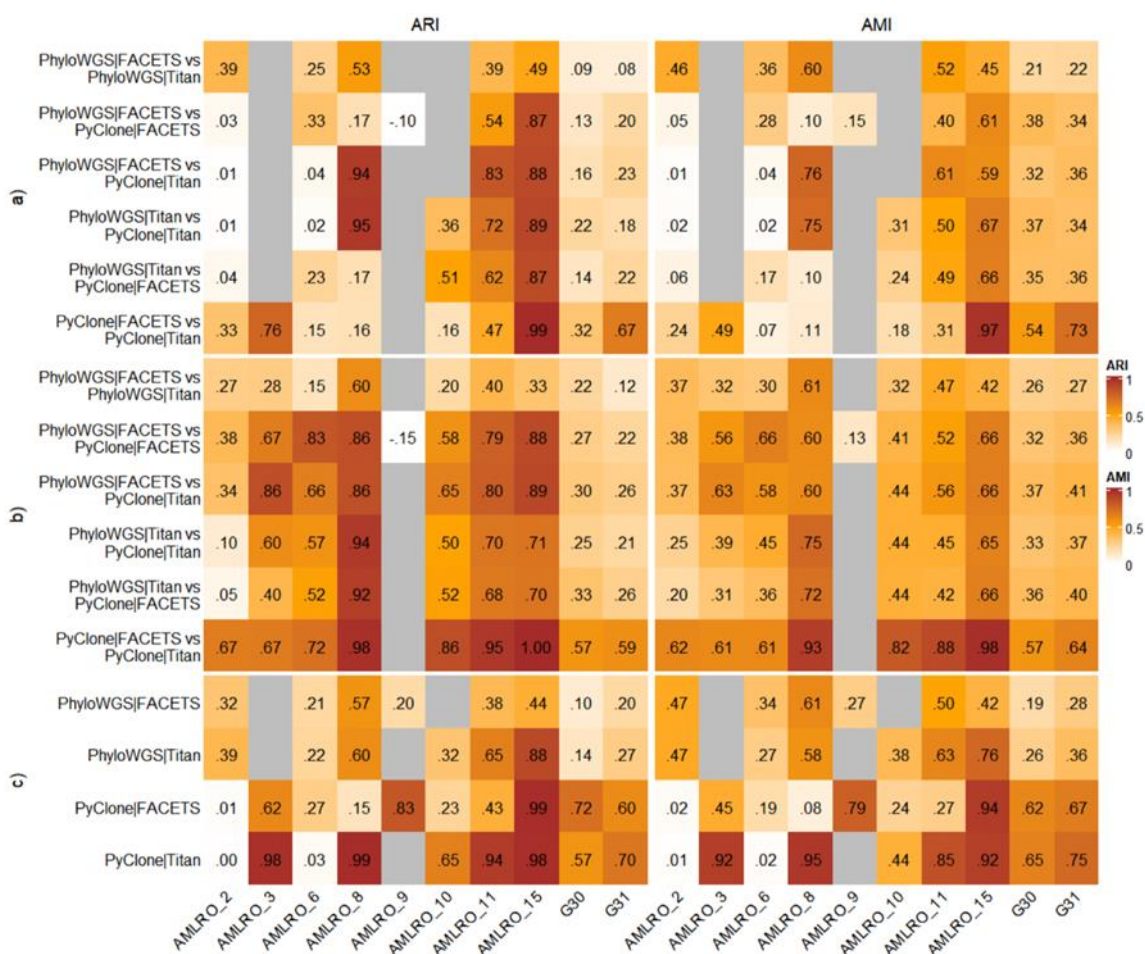


Fig. 12.4. The similarity of mutation-to-clone assignments by pipelines. Similarity measured by Adjusted Rand Index (ARI) and Adjusted Mutual Information (AMI). Panel a) presents results obtained with purity estimations from CNV corresponding, where only the values missing or below 0.1 were replaced with 1 (run 1). Results on panel b) were obtained with all required purity values set to 1 (run 2). Panel c) compares the results from both runs of the same combination of methods. Pearson coefficient of correlation of ARI and AMI = 0.92,  $p < 2.2e-16$

Rys. 12.4. Heatmapa zgodności przypisań mutacji do klonów uzyskanych przez różne kombinacje metod

### 12.3. Discussion

In this study, we established and compared the results of 4 different pipelines consisting of Mutect2 for SNV/Indel calling, two CNV callers: FACETS and Titan, and two methods of clonal reconstruction: PhyloWGS and PyClone. In addition, all pipelines were tested with and without the use of purity estimations derived from CNV callers. We found that change at any step of the analysis causes significant changes in the clonal reconstruction results. The level of similarity of different pipelines' results depended



more on the patient being analyzed than the pair of pipelines being compared. We found that pipelines using the same clonal reconstruction algorithm but different CNV caller were the most similar ones when PyClone was used and the most divergent in the case of PhyloWGS. This tendency was more visible when all samples were assumed to be perfectly pure than when we used the purity estimations from CNV callers.

Interestingly, we identified the significant effect of the purity estimation values used in the analysis, which we did not find reported in the previous studies. Especially in the pipelines involving PyClone change in the purity value had an unpredictable effect on the results, leading to nearly independent clusterization among some patients and only slightly affecting the results for the others. The number of clones detected by PyClone significantly differed if the purity estimations changed, in contrast to PhyloWGS which identified a similar and reasonable number of clones regardless of the used purity values. Limitations of this study involve the limited number of methods used and the lack of alternative SNV/Indel callers, which have been reported to be an additional source of variation [12, 13]. Another limitation of our work is the automatization of the workflow running the selected pipelines. The obtained results possibly could be improved by the manual inspection of eg. CNV calls, which could reduce the number of the noise and false CN calls. Unfortunately, the evaluation of accuracy provided by the wide spectra of available methods still needs to be done. To perform such evaluation the knowledge of the ground truth is needed, which requires the simulation of the synthetic data or usage of the real bulk sequencing data supported by single-cell sequencing.

## 12.4. Materials and methods

**Materials.** Whole Genome Sequencing results for 7 men and 4 women with AML were downloaded as hg19-aligned BAM files from the EGA (ID: EGAD00001003234). One normal and two tumor samples (diagnosis/relapse) were sequenced from each patient. BRCA cohort consisted of 4 female patients diagnosed with HER2+ breast cancer, from whom one normal and two tumor samples (primary tumor and lymph node metastasis) were obtained. Libraries for in cohort were prepared using the Agilent SureSelect v6 kit and subjected to the Whole Exome Sequencing.

**Processing and SNV/Indel calling for AML data.** Aligned BAM files were processed using MarkDuplicates/BaseRecalibrator from GATK toolkit (v4.1.1.0) [17]. Somatic mutations were identified with MuTect2 and annotated using VEP [18]. Variants from both tumor samples were combined using GATK's CombineVariants tool. Finally, we removed the variants that failed to pass at least one of the filters in both samples.

**Processing and SNV/Indel calling for BRCA data.** Raw reads were aligned against human genome hg38 using BWA-MEM (v0.7.17) [15] and processed using MarkDuplicates/BaseRecalibrator from GATK (v4.1.4.0) [17]. Somatic mutations were called with Mutect2, filtered using FilterMutectCalls, and annotated using VEP.

**Detection of CNV changes.** Integer, allele-specific copy numbers were detected using FACETS [10] and Titan [11]. FACETS input files were prepared with the command `snppileup -g -q10 -Q10 -P100 -r25,0 -d10000 snp.vcf.gz pileup.csv.gz normal.bam tumor.bam`, where SNP file for hg38 was downloaded from [ftp.ncbi.nlm.nih.gov/snp/organisms/human\\_9606/VCF/00-common\\_all.vcf.gz](ftp.ncbi.nlm.nih.gov/snp/organisms/human_9606/VCF/00-common_all.vcf.gz) and for hg19 from [ftp.ncbi.nlm.nih.gov/snp/organisms/human\\_9606\\_b151\\_GRCh37p13/VCF/00-common\\_all.vcf.gz](ftp.ncbi.nlm.nih.gov/snp/organisms/human_9606_b151_GRCh37p13/VCF/00-common_all.vcf.gz). Then FACETS was run using run\_facets.R script from aleighbrown/facets\_snakemake GitHub repository [19] with nhet = 15. Titan was run using the snakemake workflow for Standard WGS/WES analysis available through the Titan GitHub repository.

**SNVs/Indels and cases filtering.** bcftools were used to remove the synonymous/intron/intergenic variants, variants with MMQ below 50 or average coverage in tumor samples below 10. Then only the patients with less than 3000 mutations were kept to shorten the computational time (<4 days for PhyloWGS).

**Analysis of tumor structure.** CNV calls and filtered SNVs/Indels were parsed to the PyClone input format using custom scripts. For PhyloWGS, snakemake workflow created by A.L Brown [14, 20] was used to prepare input files and run the algorithm with 20 MCMC chains. PhyloWGS write\_results.py script was run with `--include-multiprimary --max-multiprimary 1` options to prevent it from throwing an error when only multiprimary trees were created. The best tree was extracted using an approach of the default browser of PhyloWGS results (selection of the tree with the highest density).

**Results analysis and visualization.** All results were analyzed and visualized using R (v4.0.3) and RStudio. Adjusted Rand Index and Adjusted Mutual Information for pairs

of results were calculated using ARI and AMI functions from the aricode package (v1.0.0). Visualizations were prepared using ggplot2 and ComplexHeatmap packages.

### **Acknowledgements**

This work was co-financed by the European Union through the European Social Fund (grant POWR.03.02.00-00-I029) and by Polish National Science Centre grant 2018/29/B/ST7/02550. Calculations were carried out using the computer cluster Ziemowit (<https://www.ziemowit.hpc.polsl.pl>) funded by the Silesian BIO-FARMA project No. POIG.02.01.00-00-166/08.

### **Bibliography**

1. Ch. Kim, R. Gao, E. Sei, N. Navin et al., Chemoresistance Evolution in Triple-Negative Breast Cancer Delineated by Single-Cell Sequencing, *Cell* (2018).
2. K. Polyak, A. Marusyk, Cancer: Clonal cooperation, *Nature* (2014).
3. S. Haider, P.C. Boutros et al., Systematic Assessment of Tumor Purity and Its Clinical Implications, *JCO Precision Oncology* (2020).
4. L. Shlush, A. Mitchell, L. Heisler et al., Tracing the origins of relapse in acute myeloid leukaemia to stem cells *Nature* (2017) 547, 104–108.
5. A.G. Deshwar, C.K. Yung et al., PhyloWGS: Reconstructing subclonal composition and evolution from whole-genome sequencing of tumors, *Genome Biol* (2015).
6. A. Roth, J. Khattra, D. Yap et al., PyClone: statistical inference of clonal population structure in cancer, *Nat Methods* 11, 396–398 (2014).
7. H.X. Dang, C.A. Maher et al. ClonEvol: clonal ordering and visualization in cancer sequencing, *Annals of Oncology* (2017).
8. C.A. Miller et al., SciClone: Inferring Clonal Architecture and Tracking the Spatial and Temporal Patterns of Tumor Evolution, *PLoS Computational Biology* (2014).
9. K. Yu, S.J. Shin, H. Zhu, W. Wang et al., CliP: fast subclonal architecture reconstruction from whole-genome sequencing data (2018).

10. R. Shen, VE. Seshan, FACETS: allele-specific copy number and clonal heterogeneity analysis tool for high-throughput DNA sequencing, *Nucleic Acids Res.* (2016).
11. G. Ha, SP. Shah et al., TITAN: inference of copy number architectures in clonal cell populations from tumor whole-genome sequence data, *Genome Res.* (2014).
12. L.Y. Liu, V. Bhandari, A. Salcedo et al., Quantifying the influence of mutation detection on tumour subclonal reconstruction, *Nat Commun* (2020) 11, 6247.
13. A. Salcedo, S.M.G. Espiritu et al., A community effort to create standards for evaluating tumor subclonal reconstruction, *Nat Biotechnol* (2020).
14. N. Roper et al. Clonal Evolution and Heterogeneity of Osimertinib Acquired Resistance Mechanisms in EGFR Mutant Lung Cancer, *Cell Reports Medicine* (2020).
15. H. Li, Aligning sequence reads, clone sequences and assembly contigs with BWA-MEM. *arXiv.org*: p. arXiv:1303.3997 (2013).
16. K. Cibulskis, G. Getz. et al., Sensitive detection of somatic point mutations in impure and heterogeneous cancer samples, *Nature biotechnology* (2013).
17. MA. DePristo, KV Garimella et al., A framework for variation discovery and genotyping using next-generation DNA sequencing data, *Nature Genetics* (2011).
18. W. McLaren, L. Gil, SE. Hunt, HS Riat, GR. Ritchie, A. Thormann, P. Flicek, F. Cunningham, The Ensembl Variant Effect Predictor, *Genome biology* (2016).
19. GitHub, FACETS snakemake workflow: [github.com/aleighbrown/facets\\_snakemake](https://github.com/aleighbrown/facets_snakemake), accessed: 11 March, 2021.
20. GitHub, PhyloWGS snakemake workflow: [github.com/aleighbrown/pwgs\\_snakemake](https://github.com/aleighbrown/pwgs_snakemake), accessed: 11 March, 2021.

## **TUMOR SUBCLONAL RECONSTRUCTION PIPELINES – COMPARISON OF RESULTS**

### **Abstract**

Tumors arise in a complex evolutionary process, which leads to the development of a heterogeneous population of malignant cells, composed of distinct cell subpopulations called clones. This clonal heterogeneity has been associated with cancer relapse and

drug resistance, both leading to poor prognosis. Among the methods of clonal heterogeneity analysis important place belongs to the algorithms that use bulk DNA sequencing data to identify subclonal tumor populations. Unfortunately, although many such tools have been developed during the last decade, no gold standard of analysis has been yet established. Here we compare the results of 4 analysis pipelines consisting of two clonal reconstruction algorithms: PyClone and PhyloWGS, and two CNV callers: FACETS and Titan. We found, that aside from the known factors affecting results like the choice of the CNV detection method, inaccuracies of the sample purity estimations are another significant source of variation.

**Keywords:** clonal evolution, tumor heterogeneity, subclones, clonal reconstruction.

Karolina ŁOPATA<sup>1</sup>, Iga ZDANOWSKA<sup>1</sup>, Magdalena LATOS<sup>1</sup>,  
Tomasz JASTRZĄB<sup>\*1,2</sup>, Jagoda RÓŻYCKA<sup>1,3</sup>, Agnieszka GORZKOWSKA<sup>1,4</sup>

## **Chapter 13. PROJEKTNEURO – A STEP TOWARDS EFFECTIVE PERSONALIZED THERAPY OF NEUROLOGICAL PATIENTS**

### **13.1. Introduction**

Therapy of neurological disorders poses a serious challenge to doctors, scientists, and patients. The challenge, especially in terms of post-stroke therapy and rehabilitation, will become even bigger in the future due to the demographic changes in Poland and Europe. As discussed in [1], we are faced with an unprecedented situation in which the age structure starts to reflect an inverted pyramid, meaning that the number of elderly people dominates over the younger ones. Due to this fact, it is predicted that the morbidity rates for strokes will increase in the nearest future. According to [2], in 2016, patients in Poland aged 54 and more, constituted over 80% of all the stroke cases treated both in hospitals and in outpatient treatment regardless of the place of living. Furthermore, the mortality rate within the group of patients aged 65+ was at the level of 84%. Based on Fig. 13.1 it can be observed that the number of patients in neurological or rehabilitation wards in Poland was slowly increasing over the years 2009-2019. Based on the statistics for year 2017 included in [3], it can be predicted that about 17% of all neurological patients suffered from strokes, with the mortality rate of 11%. The same study shows that only 15% of survivors were contracted for neurorehabilitation.

---

<sup>1</sup> Technicenter Sp. z o.o.

\* Corresponding author: tomasz.jastrzab@polsl.pl, ul. Akademicka 16, 44-100 Gliwice, PL.

<sup>2</sup> Department of Algorithmics and Software, Silesian University of Technology.

<sup>3</sup> Institute of Psychology, Faculty of Social Science, University of Silesia.

<sup>4</sup> Department of Neurology, Medical University of Silesia.

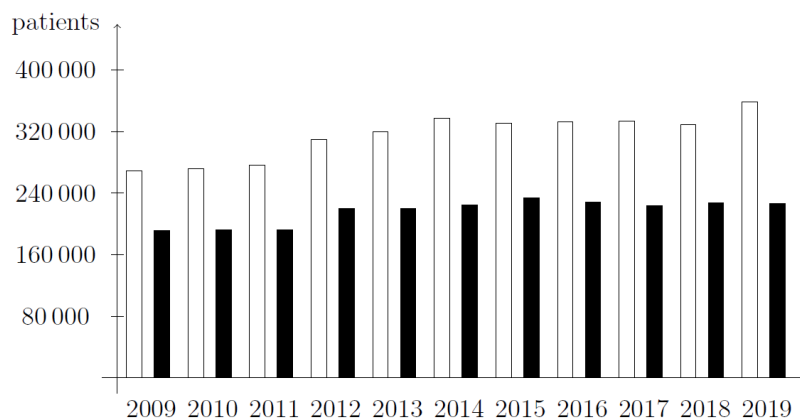


Fig. 13.1. The numbers of neurological (white) and rehabilitation ward patients in Poland in 2009-2019 (based on [4])

Rys. 13.1. Liczba pacjentów na oddziałach neurologicznych (biały) i rehabilitacyjnych w Polsce w latach 2009-2019 (opr. na podstawie [4])

Successful therapy of neurological disorders is essential for patient's health-related quality of life (HRQOL). HRQOL is a multi-dimensional concept that includes domains related to physical, mental, emotional, and social functioning [5]. These areas may be affected by the status of health. Thus, stroke has a short- and long-term impact on patients' life domains. Undergoing a stroke may have negative health, social, and economical effects [6]. In terms of health effects the stroke results in physical and/or mental disabilities, frequently affecting cognitive functions, speech or emotions. Disorders in these areas easily lead to social exclusion and deteriorated QOL, caused by the reduced ability to undertake professional and physical activities. These observations are also confirmed in [7], where patients report worse QOL after stroke than before the attack. This evaluation is positively correlated with the overall patient fitness, level of education (the higher the level, the better the self-assessed quality), marital status (married patients find their QOL better), and place of residence (patients living in urban areas perceive their QOL as better). The negative impact of craniocerebral injuries on the HRQOL is also pointed out in [8]. Although its assessment depends on the cause of the disorder, the overall QOL is considered worse.

Taking the above into account, it is clear that tools supporting effective therapy and rehabilitation of neurological patients are needed. It is also important that the tools not only help to reduce the deficits by regular brain training, they should also help to overcome the problems related to everyday activities [9]. Responding to this need, we present a tool that can be used for the therapy of neurological patients, especially suffering from post-stroke cognitive deficits. Let us note however, that the tool has a potential of being used for the therapy of, e.g., Alzheimer's disease or dementia.

Our contribution is the ProjektNeuro application aimed at the neuropsychological therapy of adults. The application aims to help in the rehabilitation of the following areas: executive functions, attention, visuospatial functions, and memory. In this paper, we present the assumptions made while developing the application and respective therapeutic tasks. We also point out the features which allow to personalize the therapy and adjust it to patient's needs. Since we also intend to scientifically confirm the efficiency of patient's therapy with the use of the designed application, we briefly describe the foundations of the clinical study being currently conducted in the University Clinical Center of the Medical University of Silesia in Katowice.

The paper is organized into 4 sections. In section 2, we briefly review the literature, focusing on the personalization aspects as well as the existing hardware and software-supported rehabilitation methods. In section 3, we describe the ProjektNeuro application the clinical study assumptions. Section 4 concludes the paper.

### **13.2. Related work**

Personalized (precision) medicine is typically related to the analysis of genes and biomarkers, e.g., in the treatment of cancer. Such an analysis is also applicable in the field of neurological disorders treatment [10]. However, here we look at the personalized medicine from a different perspective. Namely, we focus on the individual features of each patient, as pointed out in [11]. The authors underline the influence of patients on their rehabilitation process, which should take into account their individual features. A similar suggestion, related to social inclusion support of people with disabilities, is also discussed in [12]. The author considers personalized therapy in the context of individual educational, professional, or development path planning. EEG signals or eye-tracking mechanisms are the sources of data for personalization. Personalized neuropsychology of children is studied in [13]. The authors discuss the pre-appointment assessment of the patients based on the information provided by their parents. Based on the collected data, the time and approach taken during the first meeting is decided individually for each patient. In [8] it is stated that a personal approach to each patient's difficulties and injuries may help in their return to normal, daily life. The neurorehabilitation which is fitted to the cognitive disorders' configuration will benefit in better adjustment level. The positive impact of personalized therapy as compared to “one-size-fits-all” therapy is also confirmed in the clinical study by Peretz et al. [14].



The authors consider the therapy of cognitive functions by comparing the use of standard computer games with the approach in which the games adapt themselves to the patient's progress. The latter approach turns out to be more efficient.

Successful therapy, either personalized or general, is often supported by specialized hardware or software solutions. The work by Semprini et al. [11] points out a few major groups of such solutions. The authors discuss the positive effects of using robotic devices (motor rehabilitation), non-invasive brain stimulation (cognitive functions) or neural interfaces (both motor and cognitive functions rehabilitation). Successful therapy of neurological disorders can also be achieved by using the Virtual Reality (VR) or Augmented Reality (AR) based solutions. These solutions can help with motor and cognitive functions rehabilitation, including post-stroke neurorehabilitation [15, 16]. The big advantage of VR-based therapy, especially in its immersive version, is that the patient gets a realistic feeling of performing different activities of daily living. Additionally, the VR devices allow to track and objectively assess the patient's progress. Such an information helps to make the therapy more personalized [15].

Finally, there are also commercial solutions such as RehaCom [17], CogniPlus [18], and Dr Neuronowski<sup>®</sup> [19]. RehaCom software allows to train executive and cognitive functions including attention, visuospatial functions, and memory. It adjusts the level of difficulty to patient's progress and enables post-training evaluation [17]. The main drawback of the solution is that it is equipped with a relatively large steering panel, which lowers the ability of rehabilitation for patients with reduced mobility. The CogniPlus system is similar in nature to the RehaCom solution. It also supports the training of the same cognitive functions and allows for automatic level adjustment. It is also equipped with a steering panel. The main difference stems from the fact that it is closely related to the Vienna Test System tool which supports patient diagnostics [18]. Dr Neuronowski<sup>®</sup> differs from the previous solutions in that it is based on the idea of neural clock, and focuses on the time aspect of the exercises. It does not support visuospatial functions training, and focuses primarily on speech disorder treatment (although support for cognitive functions is also available). Since it is available on tablets without additional steering equipment except for headphones, it is better suited for patients with reduced mobility, especially children.

### 13.3. ProjektNeuro overview

Our application focuses on the therapy and rehabilitation of executive and cognitive functions such as attention, visuospatial functions, and memory. Executive functions are responsible for self-regulation processes and the cognitive flexibility. Attention is a basic neuropsychological ability to process the information from the environment. Visuospatial functions are necessary to identify visual and spatial relationships among objects. Memory refers to the processes of acquiring, storage, retaining, and retrieving of the information. The reason for choosing these particular functions is that they constitute the typical areas affected by strokes [20]. Moreover, it has been shown in numerous clinical studies and literature reviews that there is some positive evidence that the neuropsychological interventions in these areas are helpful [21].

#### 13.3.1. Application design

The ProjektNeuro application was developed with the aim of supporting adults with reduced mobility, therefore it is designed to run on 10-inch or larger tablets. The application is divided into four functional modules, corresponding to respective functions described before (cf. Fig. 13.2). Within each module one may find four varying tasks, each supporting different number and types of difficulty levels.

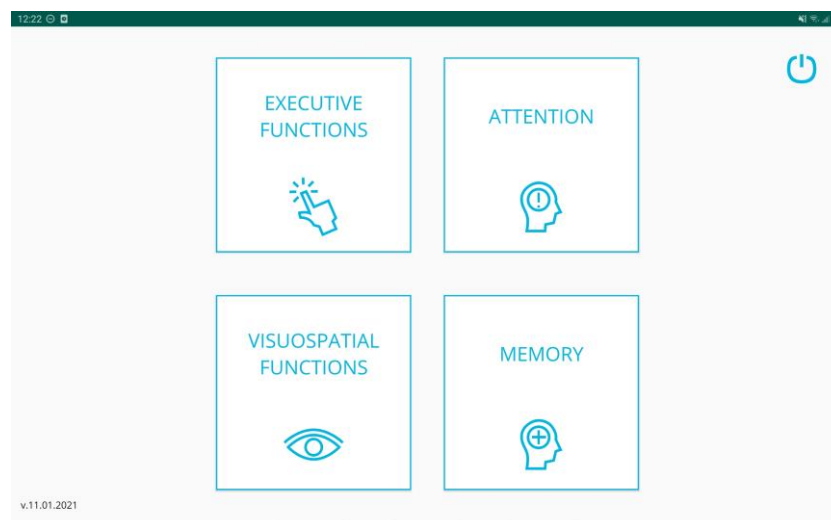


Fig. 13.2. ProjektNeuro modules

Rys. 13.2. Moduły aplikacji ProjektNeuro

Here we present a brief summary of the tasks in the respective modules:

1. Executive functions – the patient trains categorization and abstract thinking (by assigning products to proper baskets), real-life arithmetic (by paying appropriate amount of money, cf. Fig. 13.3), planning (by preparing meals according to given or self-designed recipes), and self-control (by repeatedly packing all products and later refraining from packing some of them).
2. Attention – the patient trains alertness, both visual and auditory (by reacting to different stimuli in the kitchen context, cf. Fig. 13.4, as well in the environment of, e.g. waiting room), selective attention (by admitting only chosen people through the door), and attention switching (by changing the focus from one stimulus to another).
3. Visuospatial functions – the patient trains visual synthesis and analysis capabilities (by combining small images into a single one, cf. Fig. 13.5, or doing the reverse), spatial orientation (by planning and following a route), and shape recognition (by finding a matching object by its shadow).
4. Memory – the patient trains operational (by remembering heard phone numbers) and direct memory, in an immediate and deferred setup, with different modalities of the stimuli (by remembering shown shopping list or heard story, or by identifying changes in a picture, cf. Fig. 13.6).

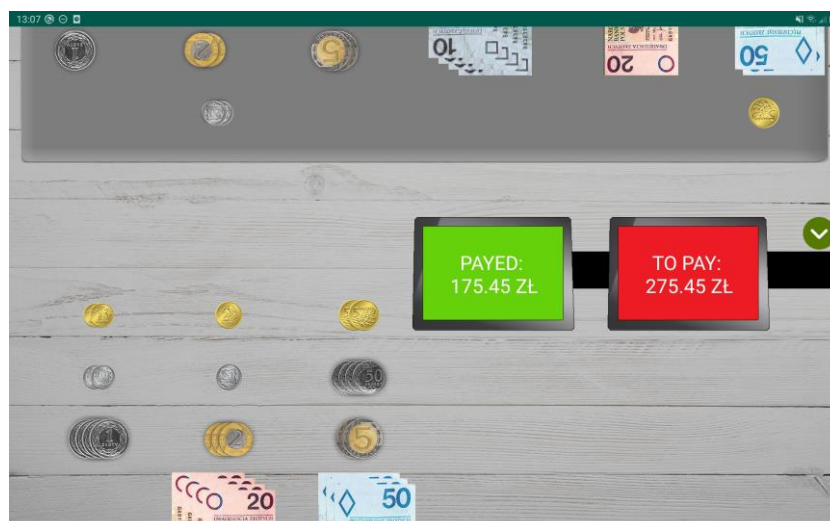


Fig. 13.3. Example Payment task setup (executive functions module). The patient is supposed to pay the given amount using available cash

Rys. 13.3. Przykład zadania pn. Płacenie (moduł funkcji wykonawczych). Pacjent ma za zadanie zapłacić określoną kwotę korzystając z dostępnych nominałów



Fig. 13.4. Example Cooking task setup (attention module). The patient is supposed to peel off the potato and react to cooking pot and kettle

Rys. 13.4. Przykład zadania pn. Gotowanie (moduł uwagi). Pacjent ma za zadanie obierać ziemniaka i reagować na gotujący się garnek i czajnik

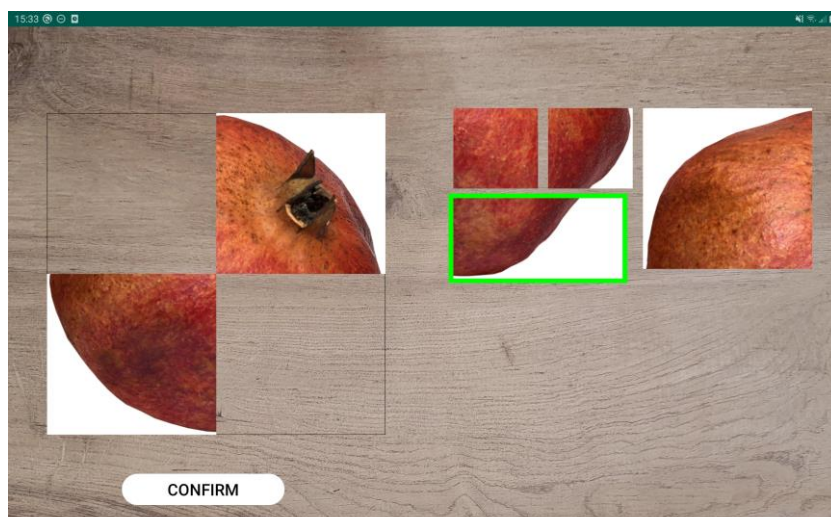


Fig. 13.5. Example Puzzle task setup (visuospatial functions module). The patient is supposed to combine smaller images into a single, larger one

Rys. 13.5. Przykład zadania pn. Układanka (moduł funkcji wzrokowo-przestrzennych). Pacjent ma za zadanie połączyć mniejsze obrazki w jeden, większy obraz



Fig. 13.6. Example Remember objects task setup (memory module). The patient is supposed to remember shown locations and then point the changed element

Rys. 13.6. Przykład zadania pn. Zapamiętaj elementy (moduł pamięci). Pacjent ma za zadanie zapamiętać pokazane lokalizacje, a następnie wskazać element, który uległ zmianie

In terms of therapy personalization, the application adapts itself to patient progress by automatically changing the difficulty level. Furthermore, it tracks various factors for each task, such as the number of correct/incorrect answers, reaction times, number of hints displayed, etc. The data is collected on the device and automatically uploaded to the server, where it can be analyzed by the person working with the patient. Since the therapists have the access to patient's data, they can effectively plan the next-day therapy, easily identifying the areas that require more intensive training.

### 13.3.2. Clinical study

In the clinical study, we focus on patients which suffered their first-ever stroke at most 3 months before the therapy and do not have the symptoms of aphasia, delirium, or depression, as well as at least one functional upper limb. Additionally, we require the patient to be present on the ward for at least 21 days.

We apply the pre-post methodology, meaning that the patient is tested using a battery of psychological tests (including MoCA attention subtest [22], selected RBANS subtests [23], CTT 1 & 2 [24], selected WAIS-R tests [25], and TUS subtest [26]) before and after the therapy. Based on pre-test results, the patients are assigned to work with a given module. Upon study completion, collected test results will be made subject to statistical

analysis, supported by the analysis of data gathered during therapy. The aim is to confirm statistically significant improvement of patients' cognitive functions.

To give the reader a hint on the efficacy of the proposed therapy, we analyzed the changes in difficulty levels recorded by the tool. The best daily change was equal to +7, while the largest drop amounted to -4 levels. We observed some drops in 7 out of 16 modules, however, they constituted at most 17% of observed changes for a given task. We found out that the Cooking and Queue tasks (attention module) as well as the Labyrinths task (visuospatial functions module) were the hardest (the greatest number of drops, or the fewest increases). Overall, for almost 85% patient-task pairs we recorded net progress in difficulty level, while the remaining 15% stayed at the same level after the therapy.

#### **13.4. Summary**

In the paper, we presented a tool, called ProjektNeuro, supporting the therapy of neurological patients. Currently, the tool aims at helping the patients suffering from cognitive and executive functions disorders resulting from stroke. We presented the main features of the application, mentioning the possible personalization elements. We have also briefly outlined the presently conducted clinical study in which the application is used and hinted at some results of this study. We believe that the tool can play a significant role in improving the quality of life of patients suffering from post-stroke disorders, not only during the therapy in the hospital but also afterwards.

#### **Acknowledgements**

The research has been supported by the European Union under the Regional Operational Program of the Śląskie Voivodeship 2014-2020 within the project *Opracowanie innowacyjnych metod terapii neuropsychologicznej osób dorosłych* (“Development of innovative methods for the neuropsychological therapy of adults”) awarded to Technicenter Sp. z o.o.

## Bibliography

1. J. Mazurek, A. Blaszkowska, J. Rymaszewska, Rehabilitacja po udarze mózgu – aktualne wytyczne, *Nowiny Lekarskie* (2013) **82(1)**:83-88.
2. Ministerstwo Zdrowia, Mapa potrzeb zdrowotnych w zakresie chorób układu nerwowego (neurologicznych wieku podeszłego) (2018).
3. Agencja Oceny Technologii Medycznych i Taryfikacji, Analiza organizacji udzielania świadczeń w zakresie rehabilitacji neurologicznej (2019).
4. Central Statistical Office of Poland, Local Data Bank: <https://bdl.stat.gov.pl/>, accessed 23 March, 2021.
5. G.H. Guyatt, D.H. Feeny, D.L. Patrick, Measuring Health-related quality of life, *Annals of Internal Medicine* (1993) **118(8)**:263-270.
- A. Kłak, Następstwa udaru mózgu, In: F. Raciborski, M. Gujski (eds.): *Udary mózgu – rosnący problem w starzejącym się społeczeństwie*, 47-63, Instytut Ochrony Zdrowia, Warszawa (2016).
6. D. Kulina, A. Chomicka, W. Fidecki, M. Wysokiński, P. Chruściel, T. Zdanowicz, Ocena jakości życia pacjentów po udarze mózgu, *Pielęgniarstwo Neurologiczne i Neurochirurgiczne* (2017) **6(4)**:163-169.
7. M. Pąchalska, *Rehabilitacja neuropsychologiczna*, UMCS, Lublin (2009).
8. Sarzyńska-Długosz, Rehabilitacja po udarze: <https://www.infozdrowie.org/download/101/28317/4sarzyńska.pdf>, accessed: 23 March, 2021.
9. L. Tan, T. Jiang, L. Tan, J.-T. Yu, Toward precision medicine in neurological diseases, *Annals of Translational Medicine* (2016) **4(6)**:104.
10. M. Semprini, M. Laffranchi, V. Sanguineti, L. Avanzino, R. De Icco, L. De Michieli, M. Chiappalone, Technological Approaches for Neurorehabilitation: From Robotic Devices to Brain Stimulation and Beyond, *Frontiers in Neurology* (2018) **9**:212.
11. J. Zielińska, Sprofilowana i spersonalizowana terapia pobudzana (sterowana) danymi, *Niepełnosprawność – zagadnienia, problemy, rozwiązania* (2017) **23**:132-148.
12. T.A. Zabel, L.A. Jacobson, A.E. Pritchard, E.M. Mahone, L. Kalb, Pre-appointment online assessment of patient complexity: Towards a personalized model of neuropsychological assessment, *Child Neuropsychology* (2021) **27(2)**:232-250.
13. C. Peretz, A.D. Korczyn, E. Shatil, V. Aharonson, S. Birnboim, N. Giladi, Computer-Based, Personalized Cognitive Training versus Classical Computer Games: A Randomized Double-Blind Prospective Trial of Cognitive Stimulation, *Neuroepidemiology* (2011) **36**:91-99.

14. A. Stasieńko, I. Sarzyńska-Długosz, Zastosowanie rzeczywistości wirtualnej w rehabilitacji neurologicznej, *Postępy Rehabilitacji* (2016) **4**:67-75.
15. G. Riva, V. Mancuso, S. Cavedoni, Ch. Stramba-Badiale, Virtual reality in neurorehabilitation: a review of its effects on multiple cognitive domains, *Expert Review of Medical Devices* (2020) **17(10)**:1035-1061.
16. RehaCom, [https://www.treningmozgu.pl/doc/metody/katalog\\_rehacom.pdf](https://www.treningmozgu.pl/doc/metody/katalog_rehacom.pdf), accessed: 23 March, 2021.
17. CogniPlus, <https://cognific.pl/produkt/cogniplus/>, accessed: 23 March, 2021.
18. Dr Neuronowski®, <https://neuronowski.com/>, accessed: 23 March, 2021.
19. K. Kot-Bryćko, F. Pietraszkiewicz, Psychologia w medycynie. Część 2 – rehabilitacja neuropsychologiczna po udarze mózgu, *Medycyna Ogólna i Nauki o Zdrowiu* (2012) **12(4)**:344-347.
20. X.-D. Xu, H.-Y. Ren, R. Prakash, Vijayadas, R. Kumar, Outcomes of neuropsychological interventions of stroke, *Annals of Indian Academy of Neurology* (2013) **16(3)**:319-328.
21. Z.S. Nasreddine, N.A. Phillips, V. Bedirian, S. Charbonneau, V. Whitehead, I. Collin, J.L. Cummings, H. Chertkow, The Montreal Cognitive Assessment, MoCA: a brief screening tool for mild cognitive impairment, *Journal of the American Geriatrics Society* (2005) **53(4)**:695–699.
22. C. Randolph, M.C. Tierney, E. Mohr, T.N. Chase, The Repeatable Battery for the Assessment of Neuropsychological Status (RBANS): preliminary clinical validity, *Journal of Clinical and Experimental Neuropsychology* (1998) **20(3)**:310–319.
23. L.F. D'Elia, P. Satz, C.L. Uchiyama, T. White, *Color Trails Test. Professional manual*, Psychological Assessment Resources, Odessa, FL (1996).
24. J. Brzeziński, M. Gaul, E. Hornowska, A. Jaworowska, A. Machowski, M. Zakrzewska, *WAIS-R (PL) – Skala Inteligencji Wechslera dla Dorosłych – Wersja Zrewidowana. Renormalizacja 2004*, Pracownia Testów Psychologicznych Polskiego Towarzystwa Psychologicznego, Warszawa (2004).
25. A. Ciechanowicz, J. Stańczak, *TUS – Testy Uwagi i Spostrzegawczości*, Pracownia Testów Psychologicznych Polskiego Towarzystwa Psychologicznego, Warszawa (2006).



## **PROJEKTNEURO – A STEP TOWARDS EFFECTIVE PERSONALIZED THERAPY OF NEUROLOGICAL PATIENTS**

### **Abstract**

Personalized therapy and rehabilitation of post-stroke deficits is an important factor influencing patient's quality of life. The process can be greatly aided by using the advancements of information technology. In the paper, we present a novel tool supporting the therapy of adults, suffering from deficits in the areas of executive and visuospatial functions, attention, and memory. We describe selected elements of the application, mentioning the aspects of therapy personalization. We also outline the assumptions of the clinical study being conducted using this application.

**Keywords:** neuropsychology, neurorehabilitation, stroke, personalized therapy.

Michał KRĘCICHWOST\*<sup>1</sup>, Natalia MOĆKO<sup>2</sup>, Agata SAGE<sup>1</sup>

## **Chapter 14. MEASUREMENT STATION FOR APD DIAGNOSTICS AND THERAPY CREATED AS PART OF THE "ASSIST MED SPORT SILESIA" PROJECT**

### **14.1. Introduction**

#### **14.1.1. State of the Art**

Auditory Processing Disorder (APD) is a group of symptoms defined as problems with the correct understanding of auditory information, despite the lack of damage to peripheral hearing [1]. Usually, these types of disorders occur among school-age children. Their diagnosis criterion is related to symptomatic characteristics, i.e., school failure [2, 3].

The process of diagnosis and therapy of APD among Polish children consists of several steps. The first step is to diagnose APD in medical facilities (an audiologist diagnoses APD). The second step is to conduct therapy by an educational institution. The basis for starting the therapy is the opinion issued by the Psychological and Pedagogical Counseling Center. This opinion concerns the need for psychological and pedagogical help at school [4, 5]. Such a procedure significantly impedes the flow of information. Often, the parent constitutes the only person transmitting data between the healthcare facility and the educational institution.

The audiological diagnosis that confirms the presence of APD-is time-consuming. The process requires the assessment of physiological hearing, the psychological examination of the patient's intelligence quotient, and the qualification to test higher auditory functions. The listed procedures require several visits to different medical facilities.

---

\* Corresponding author: [michal.krecichwost@polsl.pl](mailto:michal.krecichwost@polsl.pl).

<sup>1</sup> Department of Biomedical Engineering, Silesian University of Technology.

<sup>2</sup> Faculty of Humanities, Institute of Linguistics, Silesian University.

Institutions must be equipped with a battery of electrophysiological tests (to assess the physiological hearing) and psychoacoustic tests (to check the level of higher auditory functions) [6]. However, the equipment is not always available in a single facility.

Among the tools for diagnosing APD (after excluding physiological hearing loss), clinical diagnostics methods prevail, i.e., psychoacoustic tests [7]. These use mainly the perception of acoustic sound parameters. Special devices enable performing considered tests. Due to the nature of sound perception, tests are divided into several categories, including temporal, dichotic, and assessing the understanding of signals with reduced redundancy. The translation of the percentage results into work with the children in school conditions is ambiguous for the teacher. Some tools allow for the presentation of the symptomatic criterion. Still, they are mainly based on English-language prototypes, often outdated, or based on determinants of a high degree of generality [8].

Specialized diagnostic tools for assessing physiological hearing require adapted rooms with specific acoustic parameters [9]. Psychoacoustic tests should be performed on children in the same facility because any change in the environment can affect the test result. Similarly, the change of a person performing the test impacts its outcomes, e.g., an inappropriate approach of the specialist to a child might distort results. However, few institutions have a set of all devices - testing the physiological hearing and higher hearing functions. The reason is due to the high cost of devices necessary for the diagnostic process. Assuming that the therapy takes place in the same location, it is essential to equip it with the required auditory stimulation tools adapted to a particular disorder profile of a patient. It increases the comfort of examined person and speeds up the diagnostic process. By linking the patient to one specific diagnostic and therapeutic unit, it will also be possible to use the results to expand the scientific knowledge about APD.

Registration of speech signals is essential for the study of the quality of the patient's speech. The parameterization of the speech signal also allows for voice diagnostics [10]. Adjusting the room to professional speech signal recording needs is necessary to include this criterion in the diagnostic process of the patient. The compilation of the recorded signal connected with all the parameters of specialist tests obtained by the child in medical tests should be performed in one location.

### **14.1.2. Aims and Scope**

The main objective of this study is a detailed description of the measuring stand developed under the project: Silesian Engineering Support for Medicine and Sports "Assist Med Sport Silesia" in Zabrze, designed to improve the process of diagnosis and therapy of auditory processing disorders. The data obtained as part of the diagnostic process will constitute a fuzzy expert system's knowledge base. The purpose of the system will be to define the disorder profile of a patient and indicate development areas that require improvement during the therapy of auditory functions.

### **14.1.3. Paper Structure**

The section 'Measuring station' contains a description of the proposed measuring station: the characterization of individual diagnostic-therapy devices and the set of premises. Furthermore, the section covers information about the possible employment of the equipment in diagnosing and therapy of auditory processing disorders. The section 'Conclusion' ends the article.

## **14.2. Measuring station**

The proposed measuring stand is divided into two parts. The first part includes the purchased specialist diagnostic and therapeutic equipment. The second part is a set of visually and acoustically adjusted rooms. The set of premises will meet the requirements necessary for using the purchased equipment (e.g., the appropriate background noise level for audiometric tests). The description also contains information about the equipment dedicated to recording, processing, and evaluating the speech signal, an integral part of the rooms.

### **14.2.1. Devices**

The measuring station includes three audiometers, two auditory-voice training systems, and a set for electrostimulation. Additional equipment consists of a set of disposable diagnostic and therapeutic tools (including spatulas, gloves, or ear specula) and reusable tools (including speech therapy vibrators with replaceable tips).

### *Audiometers*

The **AD528** allows testing air and bone conduction and speech audiometry (Fig 14.1). It is also possible to test auditory attention, called audiolaterometric diagnosis. This test allows determining the child's ability to perceive auditory stimuli appropriately. During the examination, an auditory attention test is performed based on bone-conduction, air-conduction, auditory laterality, readiness for a sound stimulus, selectivity, and correct localization of sound. Also, the audiometer allows performing the Stenger test, the Hughson-Westlake test, and the SISI test [11]. Stenger test detects monaural deafness simulation. Hughson Westlake is an automatic pure-tone test procedure. SISI test determines the ability to perceive changes in sound intensity (loudness) and selects the nature of sensorineural hearing loss and the location of a damage. The audiometer also allows to connect active speakers to a free field, which gives ability to carry out audiometric tests in a free hearing field. This test determines the ability to understand speech at various levels. It employs loudspeakers connected to the audiometer, placed at a distance of about 1 m on both sides of the tested person - the test results in information about the degree of speech understanding of the respondent. In APD, the examination of auditory attention is essential. It allows for the determination of irregularities in the perception of sounds detected through the received air-conduction and bone-conduction. For the correct programming of therapy, it is necessary to obtain results for both types of conductivity [2].

**The PATH Medical system** allows performing tonal audiometry. The purpose of this test is to determine the threshold of hearing in the air-conduction and bone-conduction in the range of tested frequencies, i.e., the minimum sound intensity that the examined person can hear (Fig. 14.2). The examination is carried out in cooperation with the patient and allows for the initial determination of the nature and depth of hearing loss. The PATH Medical system will also enable the performance of MAGIC (Multiple-Choice Auditory Graphical Interactive Check) play audiometry. MAGIC is an image-based, self-monitoring test that offers a fun alternative to conventional tonal audiometry. The test is designed specifically for preschool and school children, but its usage is possible in other collaborative subjects. PATH Medical can prepare the patient before measuring physiological hearing and performing psychoacoustic tests. Due to its simple form, it reduces the effects of unprepared patients for testing. Performing tests is possible as long as the patient understands the instructions. This principle especially concerns tests of higher auditory function. Often, stress and the lack of precisely given

instructions have an impact on the results. The stage of familiarizing the patient with the examination and reducing the level of nervousness translates into credibility.



Fig. 14.1. Device visualization: Audiometer AD528 (source: <https://www.interacoustics.com>)  
Rys. 14.1. Wizualizacja urządzenia: audiometr AD528 (źródło: <https://www.interacoustics.com>)



Fig. 14.2. Device visualization: The PATH Medical system (source: <https://www.pathme.de>)  
Rys. 14.2. Wizualizacja urządzenia: system PATH Medical (źródło: <https://www.pathme.de>)

**The Senses Examination Platform (SEP)** is a mobile device for hearing, vision, speech screening (Fig. 14.3). SEP also allows hearing and speech rehabilitation in children (also with special educational needs), teenagers, and adults. The device provides early detection of hearing, sight, and speech defects, allowing assessing the physiological readiness of children to learn to read, write, and communicate at school. The device will enable to carry out: audiogram, DDT Test, GDT Test, FPT Test, DPT test, and Pure-tone test.

In addition to the hearing threshold and tonal audiometry, the described tests are considered tests of higher auditory functions necessary in the diagnosis of APD. Also, their performance is an essential element of programming therapy with auditory stimulation. Thus, the use of platform directly impacts the initial diagnosis and the initiation of the therapeutic process immediately after obtaining the results of individual tests.

#### *Systems for auditory and vocal training*

**Polimodal Sensory Perception Stimulation (SPPS)** is a therapeutic device that enables polysensory therapy for patients with abnormalities resulting from auditory processing disorders (Fig. 14.4). Therapy involves various human senses (hearing, sight, touch) and their integration and coordination. The basis of the therapy is primarily auditory training. It uses multiple types of filtration (including the so-called phonetic filtration), separation of the air-conduction and bone-conduction, and changes in the intensity and duration of a sound. The effect on the effectiveness of the therapy results from the division into stimulating auditory perception in terms of various auditory functions (as part of training

involuntary attention) and developing auditory attention, especially in voice and speech perception and expression. It is also crucial to stimulate auditory-visual-motor integration through active exercise. People with various disorders and difficulties resulting from limitations in auditory processing are the therapy target using SPSS. In students' case, the most common difficulties are i.a.: problems with understanding speech, difficulties in reading and writing, articulation disorders, speech disfluency, voice disorders, delayed speech development, auditory concentration, difficulties in learning foreign languages, etc. However, the therapy is prevalent among patients with APD as an alternative to other auditory stimulation types, especially those that only consider air-conduction improvement.



Fig. 14.3. Device visualization: The Senses Examination Platform (source: <https://csim.pl>)  
Rys. 14.3. Wizualizacja urządzenia: Platforma do Badań Zmysłów (źródło: <https://csim.pl>)



Fig. 14.4. Device visualization: Polimodal Sensory Perception Stimulation (source: <https://csim.pl>)  
Rys. 14.4. Wizualizacja urządzenia: Stymulator Polimodalnej Percepcji Sensorycznej (źródło: <https://csim.pl>)

**Forbrain** is used for auditory and voice training (Fig. 14.5). The primary purpose of the device is to train the brain, which improves auditory attention, pronunciation, and fluency of speech. Also, the employment of the device enhances short-term memory and the skills of correct reading and writing. The operation of the device uses auditory-voice feedback, as well as bone and air-conduction. Forbrain transmits the content in two paths: air via air earphones and bone through bone earphones (additionally reinforced by the device). Proper operation of the auditory-vocal feedback relates to auditory discrimination, phonological awareness, and rhythm perception. In the case of APD, this coupling is usually disturbed. It results in, among others, an inability to understand speech in noise, deterioration of phonological awareness, and rhythm perception. Using the device supports the improvement of auditory attention.

### *A set of electrostimulation devices*

The electrostimulation system supports muscle training (Fig. 14.6). The possibility of stimulating the orofacial areas enables the employment of this system in speech therapy. This type of stimulation is necessary for the event of difficulties resulting from the incorrect distribution of muscle tone. One of the APD profiles includes impaired visual-auditory-motor coordination. Usually, students with the predominant profile additionally have problems with oral apraxia and articulation kinetics. Thus, appropriate stimulation of the face muscles and the mouth interior significantly accelerates the therapeutic progress of process. The device enables electrostimulation. It consists of a set of electrodes, such as point labile electrodes (ball, cone, needle, mushroom shaped) and area electrodes. This type of equipment supports the therapy of impaired speech functions, often coexisting with auditory processing disorders. Correcting the abnormalities in the disturbed distribution of muscle tone is also advisable due to the possibility of translating these disorders into impaired sensorineural-visual integration of patients. The electrostimulation device can generate two types of currents: TENS (Transcutaneous Electrical Nerve Stimulation) and EMS (Electrical Muscle Stimulation). The currents help in orofacial disorders, e.g., hypersensitivity of the ear area and head area, preventing auditory stimulation with headphones in patients with APD.



Fig. 14.5. Device visualization: Forbrain (source: <https://pl.forbrain.com/>)

Rys. 14.5. Device visualization: Forbrain (source: <https://pl.forbrain.com/>)



Fig. 14.6. Electrostimulation devices with a various set of electrodes (source: <https://ecostim.pl/>)

Rys. 14.6. Wizualizacja urządzenia: urządzenia do elektrostymulacji z różnym zestawem elektrod (źródło: <https://ecostim.pl/>)



### 14.2.2. Rooms

The described measuring stand consists of two rooms (Fig. 14.7). The first one is an audiometric laboratory/acoustic measurement laboratory, and the second one is a control room. The audiometric/acoustic measurement laboratory will be used to carry out diagnostic and therapeutic processes (using the equipment described in the section 'Devices') and record acoustic signals. A local LAN computer network will integrate the devices included in the measurement stand. Furthermore, the Dante network will transmit the acoustic signal. The design of the laboratory equipment allows recording speech signals in the digital domain. The microphones set enables recording the acoustic signal both with a single microphone (SHURE SM 7B model) and with a set of five measuring microphones (Sonarworks XREF20). The primary role of the control room will include collecting, describing, evaluating, and analyzing the recorded data. The listening system installed in the control room will consist of a GENELEC 8020DPM loudspeaker set and Beyerdynamic DT770 M listening headphones.

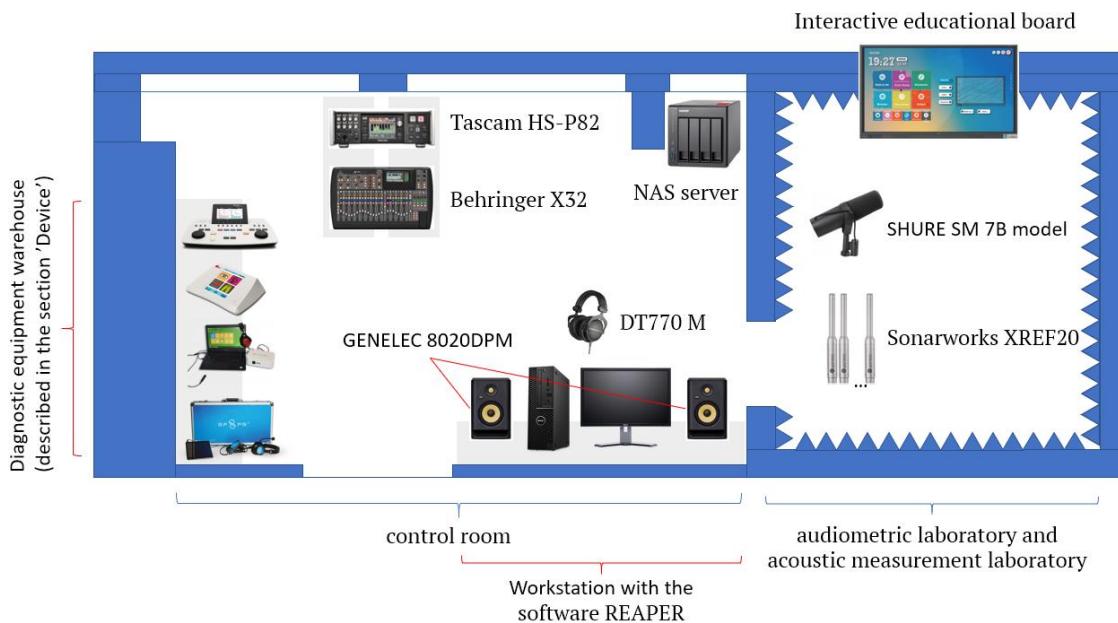


Fig. 14.7. Scheme of measuring stand consisting of two rooms: audiometric laboratory/acoustic measurement laboratory (right part) and control room (left part)

Rys. 14.7. Wizualizacja urządzenia: schemat stanowiska pomiarowego składającego się z dwóch pomieszczeń: laboratorium audiometrycznego/laboratorium pomiarów akustycznych (część prawa) i pokoju kontrolnego (część lewa)

Additionally, the project involves a high-class workstation, which connects a 32-channel DANTE expansion card and a Behringer X32 signal mixer with the Tascam HS-P82 audio recorder. The workstation has multitrack recording and audio processing software

called REAPER. Additional equipment is a NAS server, which enables storing and collecting of the material.

The rooms included in the considered measuring station will meet the permissible sound level requirements in rooms specified in the PNB 0215102:2018 standard. Regarding the rooms' specifications, the maximum acceptable A sound level should not exceed 30 dB. The standard PNB 021513:201510P determines the room's acoustic insulation requirements against airborne and impact sounds. For the described room, airborne noise insulation should be  $R'A1 \geq 55$  dB. In general communication (corridors, lobbies, staircases), the walls' airborne sound insulation should be  $R'A1 \geq 48$  dB. The applied standard PNB 021514:201506 defines the permissible reverberation time requirements for each of the discussed rooms individually. The reverberation time in the frequency domain (200-8000 Hz) should be uniform and should not exceed 0.3 seconds to ensure comfort when performing acoustic measurements and conducting diagnostic and therapeutic tests. The room design for therapy and diagnosis also includes visual adaptation for children in preschool and early school age. The use of light colors of upholstery in the room and the image of the photo wallpaper placed on the damping cover reduces the stress of the child during diagnostic and therapeutic activities. Additional equipment such as multimedia therapeutic programs, tablets, and an interactive educational board allows the use of an extra audiovisual layer to increase the attractiveness of activities.

### **14.3. Conclusion**

The APD diagnostic process requires specialized equipment and specialists from various fields [12]. The determination of whether a child has a problem with auditory processing requires audiological, otolaryngological, and speech therapy evaluation. Early diagnosis of the child is crucial, although many diagnostic tools/tests require the appropriate age of the examined person (7, 8 years). This situation translates directly into the number of undiagnosed children and the late start of the therapy. The stand for the diagnosis and treatment of APD discussed in this study allows for a comprehensive psychophysical assessment and diagnosis of problems with the patient's auditory processing. Also, it will enable the expansion of knowledge in the field of APD and the development of new tests to accelerate the diagnosis process.

## Acknowledgments

Publication supported under the Excellence Initiative - Research University program at the Silesian University of Technology, 2020/2021, No.: 07/010/SDU/10-22-02

PL: Publikacja wspierana w ramach programu Inicjatywa Doskonałości – Uczelnia Badawcza realizowanego na Politechnice Śląskiej, rok 2020/2021, nr: 07/010/SDU/10-22-02

## Bibliography

1. M. Sharma, S.C. Purdy, P. Humburg, Cluster Analyses Reveals Subgroups of Children With Suspected Auditory Processing Disorders, *Front Psychol.* (2019) 10:2481, doi: 10.3389/fpsyg.2019.02481.
2. V. Iliadou, GD. Chermak, DE Bamiou, FE. Musiek, Gold Standard, Evidence-Based Approach to Diagnosing APD, *The Hearing Journal* (2019) Vol. 72:42-46, doi: 10.1097/01.HJ.0000553582.69724.78.
3. R. Gokula, M. Sharma, L. Cupples, JT. Valderrama, Comorbidity of Auditory Processing, Attention, and Memory in Children With Word Reading Difficulties. *Front Psychol.* (2019) 10:2383, doi:10.3389/fpsyg.2019.02383.
4. TFG. Lynch, CM. Richburg, School Polices, Process, and Services for Children with CAPD. *Handbook of Central Auditory Processing Disorder: Comprehensive Intervention* (2014) Vol. 2.
5. D.S. Geffner, D. Ross-Swain, *Auditory processing disorders: assessment, management, and treatment*, Plural Publishing (2019) ISBN13: 978-1-94488-341-6.
6. LJ . Leibold, E. Buss, Masked Speech Recognition in School-Age Children. *Front Psychol* (2019) Vol. 10:1981, doi:10.3389/fpsyg.2019.01981.
7. O. Armero, A. Cerkoney, Auditory Processing Assessment Model for Older Patients, *The Hearing Journal* (2018) Vol. 71:38-43, doi :10.1097/01.HJ.0000530649.99256.25.
8. B. McPherson, A. Fuente, Central auditory processing: introduction and description of tests that can be used in Polish-speaking patients (PL: Ośrodkowe procesy przetwarzania słuchowego: wprowadzenie i opis testów możliwych do zastosowania u pacjentów polskojęzycznych), *Otolaryngologia* (2007) Vol. 6:66-76.
9. C. Portnuff, B. Bell, Effective Use of Speech-in-Noise Testing in the Clinic, *The Hearing Journal*, (2019) Vol. 72:40-43, doi: 10.1097/01.HJ.0000559502.51932.b1.
10. Y.A. Berg, A.V. Nenko, D.V. Borovikova, Analysis of Acoustic Parameters of the Speech Apparatus, W: 21st International Conference of Young Specialists on

Micro/Nanotechnologies and Electron Devices (2020) Vol. 1:450-453, doi: 10.1109/EDM49804.2020.9153533.

11. E. Hojan, Chosen methods of hearing testing (PL: Wybrane metody badania słuchu) chapter: Hearing healthcare profession (PL: Protetyka słuchu), Adam Mickiewicz University Press, (2017) Vol 19:863, ISBN 978-83-232-2748-9.

12. F.E. Musiek, G.D. Chermak, Handbook of central auditory processing disorder, Auditory neuroscience and diagnosis, Plural Publishing, (2014) Vol. 1.

## **MEASUREMENT STATION FOR APD DIAGNOSTICS AND THERAPY CREATED AS PART OF THE "ASSIST MED SPORT SILESIA" PROJECT**

### **Abstract**

A measuring station for auditory processing disorders (APD/CAPD) diagnosis and therapy is being built as a part of the project The Silesian Engineering Support Center for Medicine and Sports, "Assist Med Sport Silesia". The designed measuring station includes audiometers, electro-stimulators, auditory-voice training devices, and devices recording the speech signal. The measuring equipment will be installed in a set of premises visually adapted to preschool children and subjected to acoustic adaptation enabling audiological research. The measuring station will allow for comprehensive audiological and speech therapy diagnosis and patient therapy (mainly children in preschool and early school age). The usage of the proposed measuring station will broaden the knowledge of APD, especially the diagnosis of this disorder. The primary purpose of the article is to describe the proposed measurement station.

**Keywords:** measurement station, auditory processing disorders, hearing diagnosis, speech signal, Assist Med Sport Silesia.

Sławomir SIWEK<sup>\*1</sup>, Wojciech WIĘCŁAWEK<sup>2</sup>

## **Chapter 15. AUTOMATIC BLOOD VESSEL SEGMENTATION ALGORITHM IN ULTRAWIDE-FIELD FLUORESCENCE ANGIOGRAPHY**

### **15.1. Introduction**

Latest data from the IDF (International Diabetes Federation) published in November 2019 shows that already 463 million people in the world suffer from diabetes. With the current upward trend, the epidemic will increase to 700 million by 2045 [1]. Diabetes is an incurable disease, but its early detection allows extending the patient's life by an average of 5 years and prevent serious complications such as heart attack, stroke or diabetic retinopathy [2].

Diabetic retinopathy is the most frequent cause of blindness among adults aged 20-74 years. During the first two decades of disease, retinopathy occurs in nearly all patients with type 1 diabetes and 60% of patients with type 2 diabetes [3]. In the early stages of development, the disease is asymptomatic. It does not cause any deterioration in vision nor causing pain. The small retinal blood vessels thicken locally to form microaneurysms. The disease can be diagnosed only during a specialist ophthalmological examination with the use of funduscamera. In later stages of retinopathy, high levels of sugar damage the blood vessels in the retina of the eye. Weakened vessels crackle and their contents ooze into the vitreous. This causes a visual disturbance leading to complete blindness.

Given the benefits of rapid diagnosis, it is essential to develop screening tests that cover as much of the population as possible. Such tests, supported by computer programs,

---

\* Corresponding author: slawomir.s.iwek@gmail.com, G. Narutowicza 11/12, 80-233 Gdańsk, PL.

<sup>1</sup> Department of Biomedical Engineering, Gdańsk University of Technology.

<sup>2</sup> Department of Medical Informatics and Artificial Intelligence, Silesian University of Technology.

allow for quick reactions and treatment of the disease in its initial stage [4]. Automatic segmentation of blood vessels is one of the tools that helps diagnosing retinopathy [5].

## 15.2. Materials

Researchers have proposed many algorithms to address the problem of segmentation of blood vessels in the retina of the eye. Unfortunately, all methods were developed for images recorded with standard funduscameras with a range of  $45^\circ$  from the DRIVE [6] and STARE [7] databases. These databases contain original images, hand-segmented blood vessel masks and additional annotations made by experts. Fig. 15.1 presents difference between standard and ultrawide-field fluorescein angiography [8].

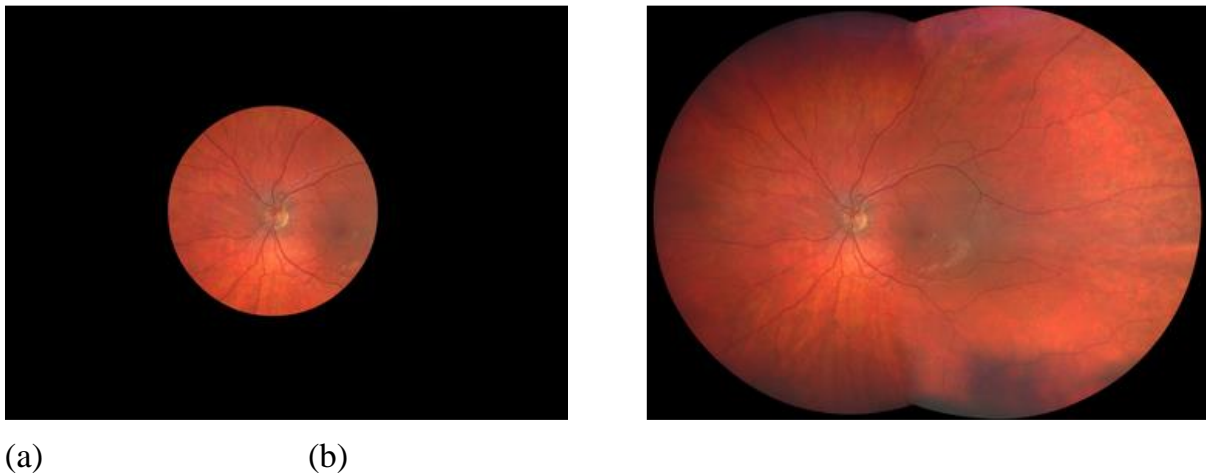


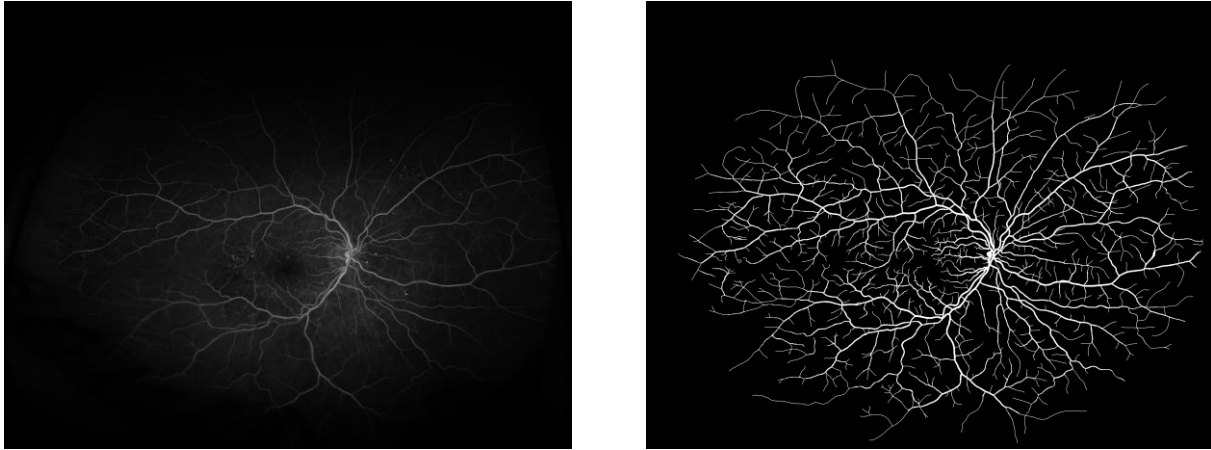
Fig. 15.1. Funduscamera field of view: (a)  $45^\circ$ , (b)  $200^\circ$  [8]

Rys. 15.1. Zakresy widoczności funduskamer: (a)  $45^\circ$ , (b)  $200^\circ$  [8]

Comparing to standard  $45^\circ$  field of view UWFA allows imaging at  $200^\circ$ . As microaneurysms, which are the most frequent symptoms of retinopathy, occur in the peripheral areas of the image, this technique shows a significant advantage over the standard one. In addition UWFA has high geometrical resolution. A single pixel is a representation of the area that can be approximated with a square with a side reaching several micrometers.

To develop the proposed segmentation algorithm 43 images recorded with ultrawidefield fluorscein angiography were used. All photos were previously anonymised so as not to infringe the privacy of patients. The images include both physiological and pathological images. Ophthalmologist classified pathologies as: leaks of blood vessels, occurrence of ischemic areas, occurrence of microaneurysms.

Additionally, 12 photos were outlined by a specialist. The obtained binary masks were used for the numerical evaluation of the quality of the developed algorithm. Fig. 15.2 shows the original image and an exemplary blood vessel mask prepared by an expert.



(a)

(b)

Fig. 15.2. Image from funduscamera: (a) original, (b) expert delineation

Rys. 15.2. Obraz dna oka pochodzący z funduskamery: (a) obraz oryginalny, (b) obrys naczyń krwionośnych wykonany przez eksperta

### 15.3. Method

The blood vessel segmentation algorithm proposed in the current paper is presented in Fig. 15.3.

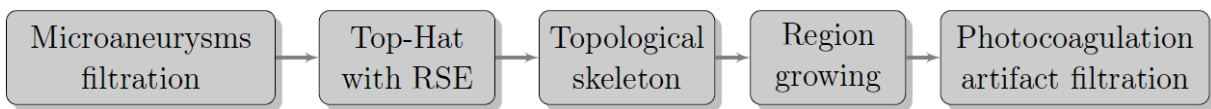


Fig. 15.3. Automatic blood vessel segmentation algorithm in UWFA images

Rys. 15.3. Schemat blokowy proponowanego algorytmu segmentacji

#### 15.3.1. Rotating Structuring Element

In the chapters that follow, the term “Rotating Structuring Element” (RES) appears twice, so we will cover this approach in detail here. It’s used in tandem with mathematical morphology in filtration and signal enhancement.

Best shape matching blood vessels is line. Vessel network is a complex structure and a single linear structuring element would pick out vessels oriented in only one direction,

so more than one structuring element must be utilized [9]. With a compromise in computational complexity and segmentation quality, the structural element is rotated at 18 different angles: from  $0^\circ$  to  $170^\circ$ , rotating  $10^\circ$  per iteration. Final result is a combination of maximum values from the obtained 18 images.

### 15.3.2. Microaneurysms filtration

Microaneurysms are the protrusions of the walls of the blood vessels of the retina, visible as white, spherical points in the image. They are the earliest symptom of diabetic retinopathy [10]. Filtering them out is crucial in the segmentation of the narrowest blood vessels, which give a much weaker image signal due to the lower blood content.

The proposed method allows segmentation of the mask of microaneurysms, which can be then removed from the original image. It is based on the isolation of contrasting structures which are obtained by subtracting median filter smoothed image from the original image. The effect of this strengthening are microaneurysms and thin fragments of blood vessels network. Morphological opening with linear RSE is then used to remove vascular fragments from the aneurysms mask. Finally, in the original image the places where the microaneurysms are found are then equated with the surrounding background. Fig. 15.4 shows fragment of original image before and after microaneurysms removal.

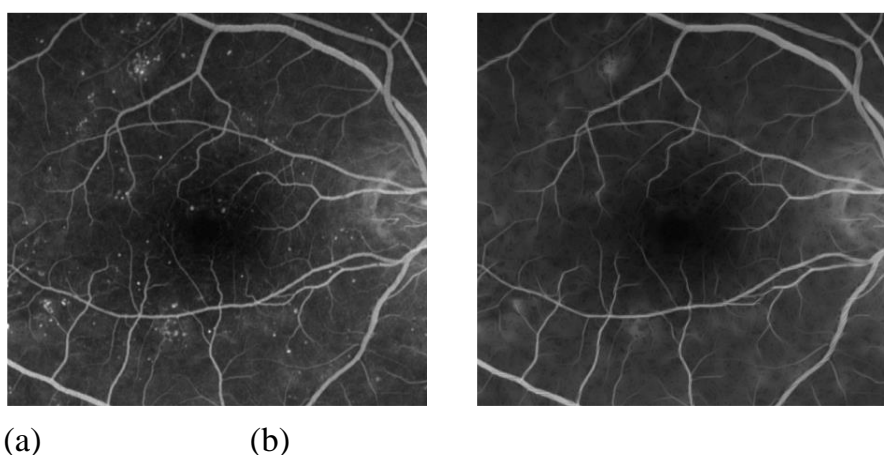


Fig. 15.4. Microaneurysms filtration: (a) original, (b) result

Rys. 15.4. Filtracja mikrotętniaków: (a) obraz oryginalny, (b) wynik filtracji



### 15.3.3. Enhancing blood vessel signal

The second step of the algorithm is to apply top-hat transform to image (Fig. 15.5a) obtained in previous step. This operation amplifies the signal coming from the blood vessels against the background (Fig. 15.5b).

Strong contrast between the blood vessels and the background allows binarization with Otsu method to be used. Binarized image is skeletonized (Fig. 15.5c) followed by removal of small elements.

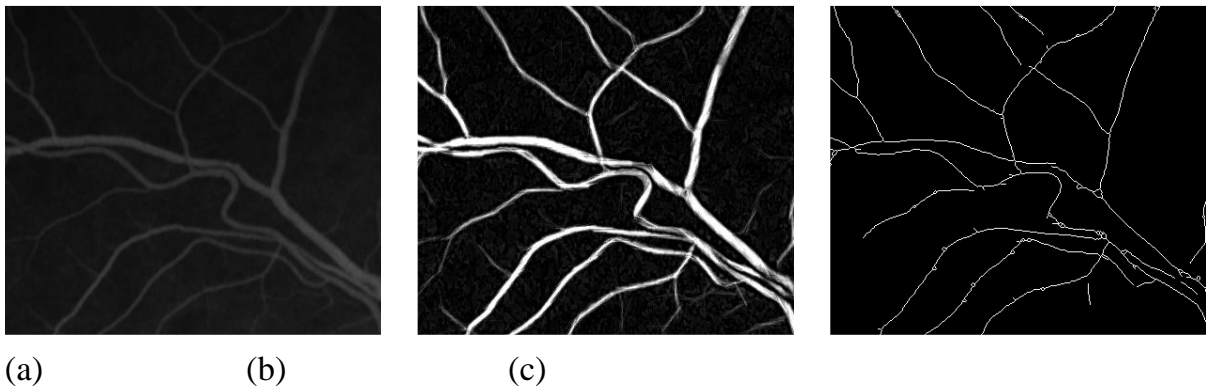


Fig. 15.5. Enhancing blood vessel signal: (a) original, (b) top-hat transform, (c) skeleton

Rys. 15.5. Wzmocnienie sygnału obrazowego z naczyń krwionośnych: (a) obraz oryginalny, (b) biała transformata cylindryczna, (c) szkieletyzacja

The resulting mask, which reflects the center of the blood vessels is passed as argument (seed points) for region growing function. With each iteration, the vessels widen until they reach their full volume. Region growing algorithm stops when the results of the current iteration do not differ from the previous one.

### 15.3.4. Filtering photocoagulation artifacts

Last step of proposed algorithm is post-processing filtration of photocoagulation artifacts. Photocoagulation of the retina is a minimally invasive procedure used to treat various diseases of the retina. Unfortunately, the eyes of patients after this procedure have specific changes that negatively affect segmentation. It can be observed as groups of small, white circles in close proximity to blood vessels.

Due to close proximity to blood vessels region growing algorithm often classifies them incorrectly. To decrease the number of false positive pixels in segmentation results post-process filtration is applied.

Photocoagulation filter is based on size and circularity of analysed objects. If an object is big enough and has a shape similar to a circle it is removed from the image (Fig. 15.6). Artifacts that have fused together and have lost their circularity are still challenging.

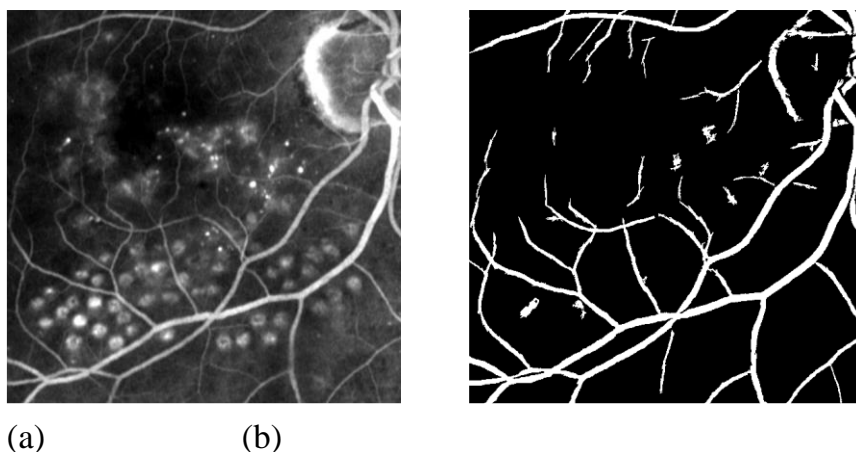


Fig. 15.6. Photocoagulation filtration: (a) original, (b) result

Rys. 15.6. Filtracja artefaktów fotokoagulacji: (a) obraz oryginalny, (b) wynik filtracji

## 15.4. Results

The effectiveness of the segmentation algorithm was assessed by comparing segmentation results with expert contours, expressed as 12 binary masks. Selected numeric indicators determining the degree of similarity of the compared images are summarized in Tab. 15.1. All of them were determined by the values from confusion matrix.

Table 15.1

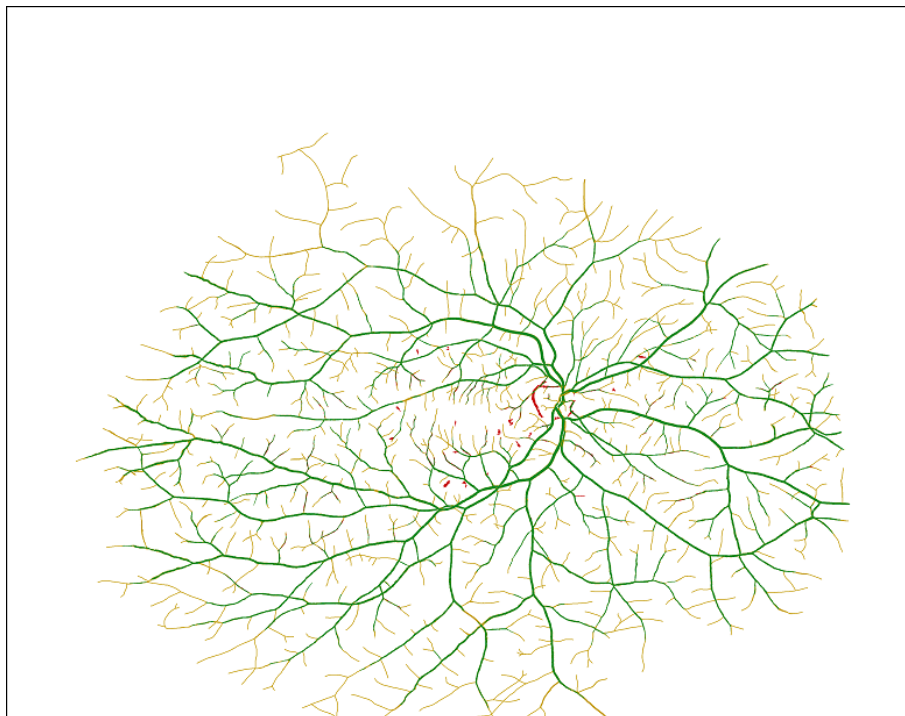
Parameterized evaluation of segmentation					
No.	TPR	TNR	PPV	ACC	Dice
1	0.690	0.999	0.981	0.983	0.811
2	0.730	0.999	0.986	0.985	0.839
3	0.823	0.999	0.971	0.989	0.891
4	0.603	0.999	0.955	0.981	0.740
5	0.611	1.000	0.994	0.976	0.757
6	0.661	1.000	0.985	0.986	0.791
7	0.665	1.000	0.994	0.978	0.797
8	0.884	0.998	0.954	0.992	0.918
9	0.777	0.999	0.979	0.984	0.866
10	0.648	1.000	0.997	0.985	0.786
11	0.717	1.000	0.994	0.983	0.833
12	0.698	1.000	0.997	0.984	0.821
avg.	0.709	0.999	0.982	0.984	0.820

Among results based on confusion matrices the largest number of pixels was classified as true negative. This is due to a relatively small number of blood vessel pixels compared to the background pixels. Value specifying a number of true positive pixels is also high. On average 98% of the all pixels have been correctly segmented.

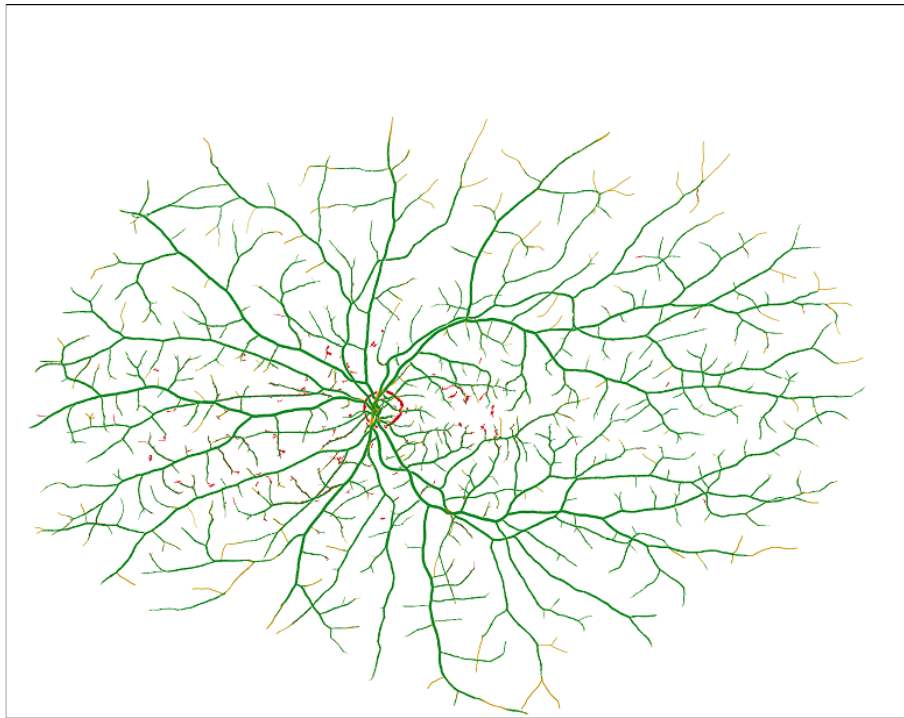
The average number of incorrectly classified pixels is less than 2%. Values of false positive and false negative pixels demonstrate that the developed algorithm is more prone to undersegmentation than oversegmentation. This problem is related to the relatively low contrast of the peripheral areas of the image.

The algorithm correctly segments large blood vessels, located in the central part of the image. On the contrary, thinnest blood vessels in the periphery are usually not detected due to uneven contrast. That causes increase of false negatives. False positive pixels are a result of clustering adjacent microaneurysms or merging bright optic nerve disc with blood vessels.

In addition to numerical results, segmentation results are also presented graphically. Fig. 15.7a shows the worst and Fig. 15.7b shows best result. The effectiveness of segmentation was assessed by comparing the values of the Dice coefficient. For the presented images, they were equal to 0.743 and 0.919, respectively. On both images, the same conventions were adopted: true negative marked as white, true positive as green, false negative as yellow, false positive as red.



(a)



(b)

Fig. 15.7. Graphical comparison of segmentation results with the expert delineations: (a) worst, (b) best case

Rys. 15.7. Graficzna reprezentacja tablicy pomyłek: (a) najgorszy rezultat segmentacji, (b) najlepszy rezultat segmentacji

## 15.5. Conclusions

Main purpose of the work was to develop and implement an algorithm for automatic segmentation of blood vessels in fundus images, which would be a useful tool for ophthalmologists in the diagnosis of diabetic retinopathy. The proposed approach is based on filtration of image structures that are not blood vessels, top-hat transform that strengthens the vessels, region growing and post-processing transformations reducing artifacts.

Segmentation results were verified on the basis of physiological and pathological images. The observed pathologies were classified by the ophthalmologist as: leaks of blood vessels, the presence of ischemic areas and microaneurysms. The database consists of 43 images, 12 of which have the expert contour of the blood vessel network. Medical annotations allow numerical determination of the quality level of segmentation. The obtained results allowed to state that on average 98% of segmented pixels are

consistent with the outlines prepared by a specialist. Moreover, the average value of Dice coefficient has relatively high value, equals to 0.82.

The proposed algorithm can be used by ophthalmologists to develop a screening strategy to minimize the incidence of diabetic retinopathy. However, the disease also manifests itself through the presence of microaneurysms or macular deformities. Therefore, the best solution would be to create a modular system that checks for more symptoms of the disease. The blood vessel segmentation algorithm would be an integral part of such a system. Information from other modules could be used to eliminate structures that negatively affect the result of segmentation of blood vessels. For example, a method of optic disc filtration would be useful, thus reducing the number of false positives.

The two-dimensional image obtained from wide-angle fluoerscein angiography is in fact a reflection of the spherical plane, therefore it is characterized by a strongly uneven distribution of brightness. The central part of the image is best lit, while the peripheral areas are less lit. The contrast is also deteriorating: the blood vessels differ only by a few levels of gray from the background. By using a transform that would enhance the brightness of the pixels located in the peripheral parts of the image without changing the central pixels, the algorithm would probably be able to segment the narrowest blood vessels as well.

### **Acknowledgements**

Authors would like to thank ophthalmologists from **SPZOZ Okręgowy Szpital Kolejowy in Katowice** for sharing anonymized fundus images that enabled development and tests of described algorithm.

The presented algorithm is a result of an engineering thesis in the field of Biomedical Engineering (specialization Informatics and Medical Equipment) defended at the Silesian University of Technology, Faculty of Biomedical Engineering during the academic year 2020/2021.

### **Bibliography**

1. International Diabetes Federation. IDF Diabetes Atlas, 9th edn. Brussels, Belgium: International Diabetes Federation, 2019.
2. Konstantinos Papatheodorou, Maciej Banach, Eleni Bekiari, Manfredi Rizzo, Michael Edmonds, Complications of Diabetes 2017, Journal of Diabetes Research, vol. 2018, Article ID 3086167, 4 pages, 2018. <https://doi.org/10.1155/2018/3086167>

3. D.S. Fong, L. Aiello, T. W. Gardner, G.L. King, G. Blankenship, J.D. Cavallerano, F.L. Ferris, R. Klei,. Retinopathy in diabetes. *Diabetes Care* 27, Supplement 1 (Dec. 2003), S84-S87.
4. P. Scanlon, The english national screening programme for diabetic retinopathy 2003-2016. *Acta diabetologica* 54 (02 2017).
5. H. Jelinek, M. Cree, J. Leandro, J. Soares, R. Cesar Junior, A. Luckie, Automated segmentation of retinal blood vessels and identification of proliferative diabetic retinopathy. *Journal of the Optical Society of America. A, Optics, image science, and vision* 24 (06 2007), 1448-56.
6. DRIVE, Digital Retinal Images for Vessel Extraction: <https://drive.grandchallenge.org>, accessed: 10 March, 2021.
7. STARE, STructured Analysis of the Retina: <https://cecas.clemson.edu/ahoover/stare>, accessed: 10 March, 2021.
8. Zeiss Clarus 500, product website: <https://www.zeiss.com/meditec/us/products/ophthalmology-optometry/retina/diagnostics/fundus-imaging/clarus-500.html>, accessed: 10 March, 2021.
9. B.D. Thackray, A.C. Nelson, (1993), Semi-automatic segmentation of vascular network images using a rotating structuring element (ROSE) with mathematical morphology and dual feature thresholding. *IEEE Transactions on Medical Imaging*, 12(3), 385-392. doi:10.1109/42.241865
10. T. Spencer, J. Olson, K. McHardy, P. Sharp, J. Forrester, An image-processing strategy for the segmentation and quantification of microaneurysms in fluorescein angiograms of the ocular fundus. *Computers and biomedical research, an international journal* 29, 4 (August 1996), 284-302.

## **AUTOMATIC BLOOD VESSEL SEGMENTATION ALGORITHM IN ULTRAWIDE-FIELD FLUORESCEIN ANGIOGRAPHY**

### **Abstract**

Extraction of blood vessels in retinal images is an important step for computer-aided diagnosis of ophthalmic pathologies such as diabetic retinopathy. So far, methods have been developed to work on narrow-angle images – the most popular DRIVE and STARE datasets. This paper presents a segmentation algorithm for ultrawide-field images based on mathematical morphology with the use of rotating structuring element. Along with the segmentation, filters have been developed to remove non-blood vessel structures

from the images. The proposed method successfully segments most of the blood vessel network. Experimental results on prepared dataset, show that the segmentation results reach an average Dice coefficient of 0.82%. Segmentation errors are mostly false negative pixels due to uneven contrast on peripheral image areas.

**Keywords:** ultrawide-field fluorescein angiography, rotating structuring element, blood vessels, segmentation.

Kornelia JANKOWSKA<sup>1</sup>, Marek J. ŁOS<sup>2</sup>,  
Andrzej HUDECKI<sup>\*3</sup>, Jolanta HYBIAK<sup>‡1</sup>

## **Chapter 16. IMPACT OF THE MULTI-WALL MWCNT CARBON NANOTUBES ON THE BIOCOMPATIBILITY OF MICRO AND NANOFIBERS OF COMPOSITE POLYCAPROLACTONE MATRIX**

### **16.1. Introduction**

Biomanufacturing is an indispensable part of regenerative medicine. It is a field of research that can use knowledge of cells and tissue together with biomaterial production techniques to manufacture cell and tissue scaffolds (Fig. 16.1) [1]. Biomaterial is a material intended for integration with biological systems in order to treat, augment or replace any tissue, organ or their function [2]. Biomaterials need to meet numerous of requirements to be qualified as a material for scaffolds production. First of all, it has to be biocompatible which means it needs to be acceptable by human body without any immunity response or allergic reaction. Biocompatibility as the basic requirement that each biomaterial must meet is much more difficult to achieve than it seems, because it is a complicated process depending on various factors, such as surface or structural biocompatibility, function, period of the implant application and most important its interaction with the surroundings [3]. Furthermore, biodegradable biomaterials must be able to degrade to non-toxic products within required time. It should also support cell growth and proliferation, which is necessary to heal a tissue defect. Moreover, good biomaterial should be easy to form into specific shapes with required porosity and meet appropriate mechanical requirements. The low cost of production is an additional advantage [4].

---

<sup>1</sup> Pomeranian Medical University, Dept. of Pathology.

<sup>2</sup> Biotechnology Center, Silesian University of Technology.

\* Corresponding authors: andrzej.hudecki@gmail.com; Łukasiewicz Research Network – Institute of Non-Ferrous Metals.

<sup>3</sup> Łukasiewicz Research Network – Institute of Non-Ferrous Metals.

<sup>‡</sup> Corresponding authors: Jhybiak@pum.edu.pl; Pomeranian Medical University, Dept. of Pathology, Szczecin.



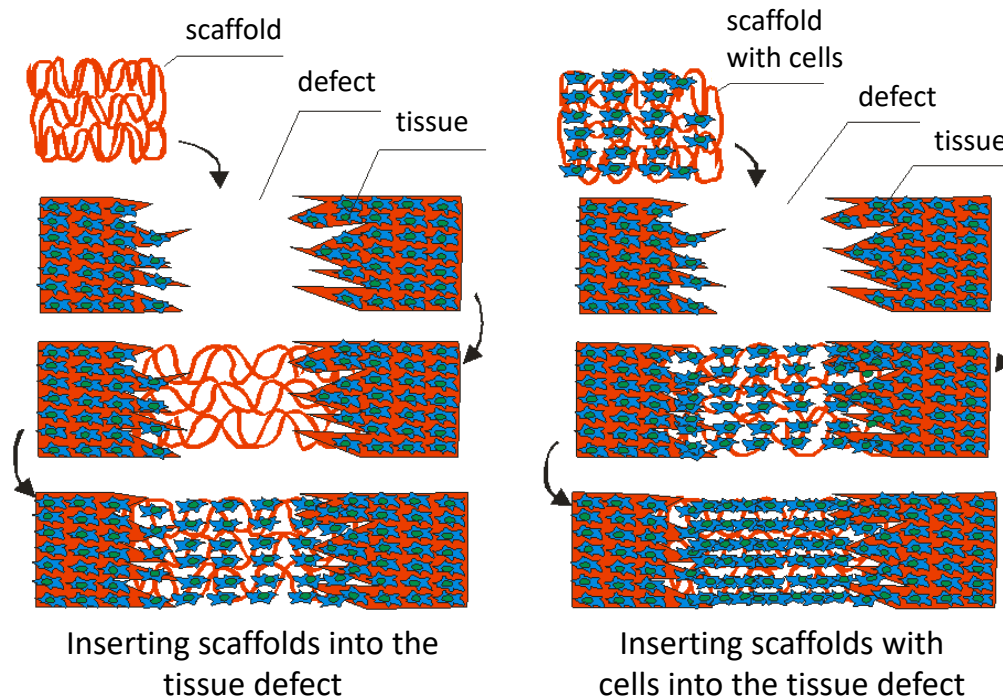


Fig. 16.1. Cell scaffolds in regenerative medicine

Rys. 16.1. Rusztowania komórkowe w medycynie regeneracyjnej

One group of materials that meet these requirements are synthetic polymers. Apart from meeting the basic biomaterial requirements, such as biocompatibility and good mechanical properties, their advantages include being cost efficacy and uniformly in large quantity production. In addition, their tensile strength, elasticity and degradation rate are similar to the bones, so they are readily used as scaffolds for bone regeneration. The group of these polymers among others includes polycaprolactone (PCL), which stands out from other polymers in this group by slower rate of degradation- up to two years, which made it attract the attention of many researchers in recent years [5].

PCL was firstly synthesized in 1930s by F. J. Van Natta and co-researchers [6]. It is hydrophobic, linear, aliphatic, semi-crystalline material with melting point at 59°C-64°C which is relatively low. PCL surface properties can be easily modified by addition of appropriate functional groups, such as hydroxyapatite or calcium carbonate. Sufficient additions can render its hydrophilic, adhesive or biocompatible. Thereat researchers found a variety of application for this biomaterial [7]. One of the first uses was in drug delivery systems to extend the time of drug delivery in the controlled manner [8]. Another example can be a scaffold manufacturing for various of tissue type, such as skin, bone or periodontal tissues [9-11]. Taking into account the emerging new

applications for the biomaterial, after discovering its properties in combination with new additives, research in that field carry a potential for discoveries important in field of regenerative medicine.

## **16.2. Material and methods**

### **16.2.1. Biomaterial production**

To obtain polycaprolactone in a form of micro and nanofibers firstly polymer material (Sigma Aldrich) in form of granules with or without addition of carbon nanotubes (Ssnano) has been converted into a solution with a solvent. Used solvent was a mixture of dimethyl sulfoxide, dimethylformamide and tetrahydrofuran (Chemland). Next, obtained solution was transformed into micro or nanofibers with an electrostatic field. The size of obtained fibers was depended on the viscosity of the polymer solution.

### **16.2.2. Cell culture**

Biocompatibility tests of PCL and PCL/C 3% were carried out using human dermal fibroblasts adult (HDFa). Cells were cultured in Dulbecco's Modified Eagle Medium (Gibco, 2007787) with addition of 10% fetal bovine serum (Corning, 35079002), 2mM L-Glutamine (Corning, 34717007) and 1% Anti-Anti (Gibco, 1989506) and incubated at 37°C, 5% CO<sub>2</sub>.

### **16.2.3. Biomaterial sterilization**

Appropriate amount of biomaterial was placed in multiwell plate. Next, wells with biomaterials were filled to the brim with 70% ethanol and incubated for 1h. After incubation time, biomaterials were washed twice with Phosphate Buffered Saline (Lonza, 0000708833) and left to dry.

#### **16.2.4. Biomaterial extract preparation**

To obtain 100% biomaterial extract, 6 cm<sup>2</sup> of sterilized biomaterial was placed in 1 ml of DMEM with addition of 10% FBS, 2 mM L-Glutamine and 1% Anti-Anti and has been incubated for 24 h at 37°C, 5% CO<sub>2</sub> in 6-well plate. After incubation time obtained extract was portioned and diluted with cell medium to get following concentration: 75%, 50% and 25%.

#### **16.2.5. MTT Assay**

HDFa were seeded into 96-well plate at density 10 000 cells/well. After 24 h cell medium from 96-well plate was replaced with 100 µl of fresh medium, biomaterial extract at appropriate concentration or 5% DMSO (Corning, 25-950-CQC) as control. Cells were incubated for another 24 h at 37°C, 5% CO<sub>2</sub>. After incubation time, MTT solution has been prepared by dilution of 3 mg Thiazoyl Blue Tetrazolium Bromide (Sigma, MKCK7253) in 3 ml DMEM without phenol red (Gibco, 2036286). Thereafter cell medium and biomaterial extracts were replaced with 50 µl MTT solution. After 2 h of incubation, MTT solution was replaced with 100 µl isopropanol which was used to dissolve formazan crystals. The absorbance was determined spectrophotometrically at 570 nm.

### **16.3. Results**

#### **16.3.1. PCL micro and nanofibers**

The study of structure of the micro and nano fibers obtained in electrostatic field that was performed with use of SEM Scanning Electron Microscope showed differences between obtained fibers (Fig. 16.2-16.3). The following fibers and their characteristics are obtained in PCL samples: (i) fiber's diameter of less than 1000 nm (30% of all studied fibers), (ii) fiber's diameter between 1001 and 1500 nm (15% of all studied fibers), (iii) fiber's diameter above 1501 nm (55% of all studied fibers).

Adding 3% share of carbon nanotubes to the solution changes the diameter of the obtained fibers. In a PCL sample containing 3% share of carbon nanotubes, the

following fibers were found: (i) of diameter below 1000 nm (25% of the sample), (ii) of diameter between 1001 and 1500 nm (40% of the sample), (iii) of diameter above 1501 nm (35% of the fibers).

The total number of fibers below 1500 nm in diameter stands for 45% of the total share while 1500 nm in diameter stands for 55% share in the tested PCL sample. In the sample containing 3% addition of carbon nanotubes fibers with a diameter below 1500 nm constitute 65% and those above 1500 nm only 35% of all fibers.

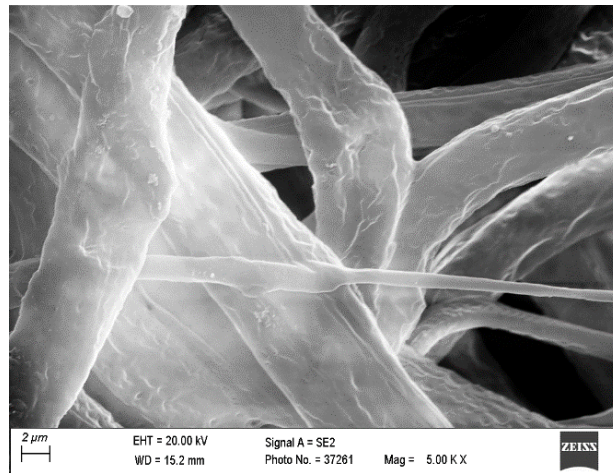


Fig. 16.2. The structure of the polycaprolactone fibers. Images taken using a scanning electron microscope (SEM)

Rys. 16.2. Struktura włókien polikaprolaktonu. Zdjęcia wykonane z zastosowaniem skaningowego mikroskopu elektronowego (SEM)

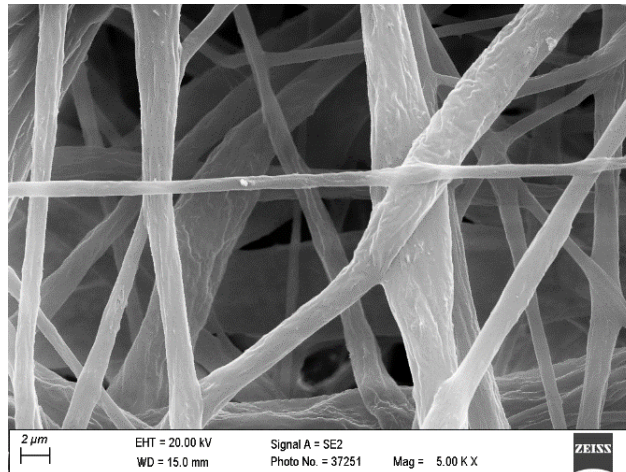


Fig. 16.3. The structure of the polycaprolactone fibers with carbon nanotubes. Images taken using a scanning electron microscope (SEM)

Rys. 16.3. Struktura włókien polikaprolaktonu z nanorurkami węglowymi. Zdjęcia wykonane z zastosowaniem skaningowego mikroskopu elektronowego (SEM)

### 16.3.2. Biocompatibility of PCL extract

The experiment was carried out once with three replications for each extract and six replications for controls. No toxic effect of the PCL extract on HDFa was found (Fig. 16.4). The lowest cell viability was observed in 75% PCL extract, where it was decreased by 23.1% and the highest in 50% extract, where it was decreased by 9%.

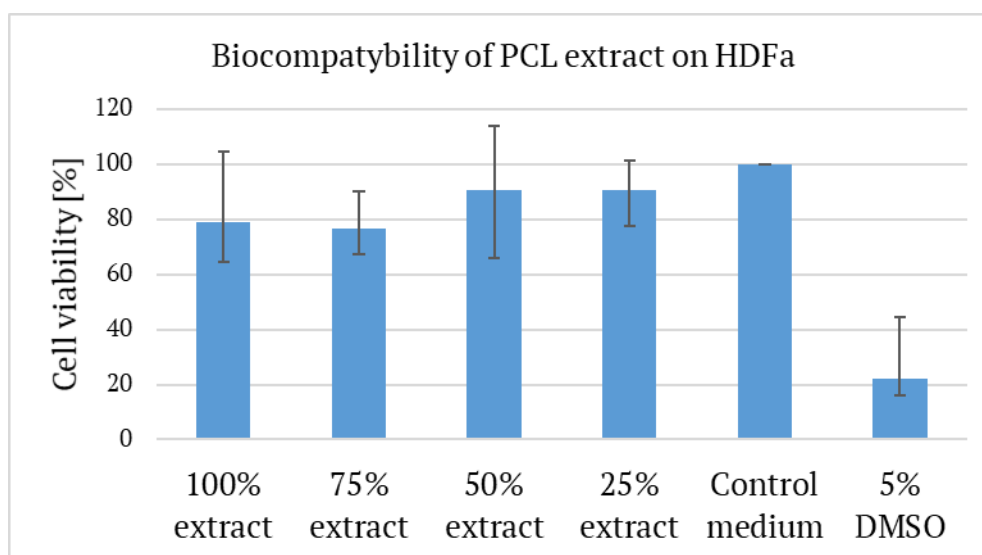


Fig. 16.4. Biocompatibility of PCL extract on HDFa

Rys. 16.4. Biokompatybilność ekstraktu z PCL testowana na komórkach HDFa

### 16.3.3. Biocompatibility of PCL/C 3% extract

The experiment was carried out once with three replications for each extract and six replications for controls. No toxic effect of the PCL/C 3% extract on HDFa was found (Fig. 16.5). The lowest cell viability was observed in 50% extract and it was decreased to 77.3%. Furthermore in 75% extract HDFa viability was increased to the value of 108.3%.

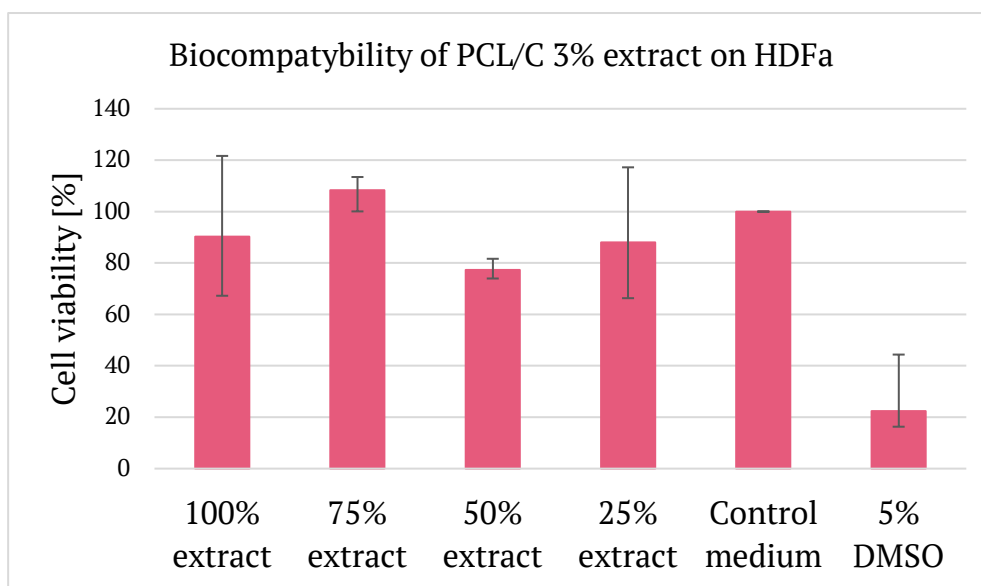


Fig. 16.5. Biocompatibility of PCL/C 3% extract on HDFa

Rys. 16.5. Biokompatybilność ekstraktu z PCL/C 3% testowana na komórkach HDFa

## 16.4. Discussion and Conclusion

PCL is well known biomaterial with well-known properties. Thanks to the possibility of combining, it with various additives and a relatively low production cost, it has found wide range of application in regenerative medicine. Its biocompatibility was repetitively confirmed in its basic form. However, taking in consideration a complexity of cell viability and proliferation processes, any modification in structure of PCL has to be tested for its biocompatibility.

The conducted research has shown that electrically conductive additives such as carbon nanotubes are conducive to the production of fibers with a smaller diameter. Furthermore, based on the performed analysis, it can be concluded that produced PCL extracts and PCL with 3% carbon nanotubes have no toxic effect on cells. According to UNE-EN ISO guidelines cell viability must be reduced to <70% in comparison to cells in control medium to state a cytotoxic potential of tested material [12]. In the performed analysis, cell viability was not reduced below 70% in any of the tested extracts. The lowest cell viability for PCL were observed in 100% extract and 75% extract, where it was 79.02% and 76.91% respectively. As the concentration decreased, the viability was less reduced and amounted to 99.9% in 50% extract and to 90.72% in 25% extract. The result suggests that PCL extract can exert an effect on cell viability, but it is not intense enough to be determined as a toxic biomaterial. Similarly, induced modification of

biomaterial in the form of carbon nanotubes also did not show toxic effect. Cell viability was decreased the most in 50% extract to 77.25% and in 25% extract to 87.98%. In 100% extract cell viability was less reduced to the level of 90.29%. Furthermore, in 75% extract cell viability was increased by 8,25% compare to cells in control medium. In contrast to PCL extracts, in the case of PCL/C 3% extracts, a lower cell viability is observed in extracts with lower concentrations. Moreover, observed cell viability increase in 75% extract suggest potential viability stimulating effect of tested biomaterial on HDFa. However, it should be taken into account that the results may have been affected by differences in cell density, so the number of test repetitions should be increased. Additionally, considering that the biomaterials are produced to be used as cells scaffolds, direct contact tests are planned, which will provide more information on the impact of the addition of carbon nanotubes to PCL on the viability of HDFa.

### **Acknowledgements**

MJŁ, JH and KJ were supported by the National Science Centre, Poland grant #: 2016/21/B/NZ1/02812.

### **Bibliography**

1. W. Wang, B. Huang, J.J. Byun, P. Bártolo, Assessment of PCL/carbon material scaffolds for bone regeneration, *Journal of the Mechanical Behavior of Biomedical Materials*, vol. 93, pp. 52-60, May 2019, doi: 10.1016/j.jmbbm.2019.01.020.
2. P. Tranquilli Leali, A. Merolli, Fundamentals of biomaterials, in *Biomaterials in Hand Surgery*, Springer Milan, 2009, pp. 1-11.
3. L. Cvrček, M. Horáková, Plasma Modified Polymeric Materials for Implant Applications, in *Non-Thermal Plasma Technology for Polymeric Materials*, Elsevier, 2019, pp. 367-407.
4. P.A. Gunatillake, R. Adhikari, N. Gadegaard, Biodegradable synthetic polymers for tissue engineering, *European Cells and Materials*, vol. 5. AO Research Institute Davos, pp. 1-16, 2003, doi: 10.22203/eCM.v005a01.
5. R. Dwivedi *et al.*, Polycaprolactone as biomaterial for bone scaffolds: Review of literature, *Journal of Oral Biology and Craniofacial Research*, vol. 10, no. 1. Elsevier B.V., pp. 381-388, Jan. 01, 2020, doi: 10.1016/j.jobcr.2019.10.003.

6. F.J. van Natta, J.W. Hill, W.H. Carothers, Studies of Polymerization and Ring Formation. XXIII.  $\epsilon$ -Caprolactone and its Polymers, *Journal of the American Chemical Society*, vol. 56, no. 2, pp. 455–457, Feb. 1934, doi: 10.1021/ja01317a053.
7. M.A. Woodruff, D.W. Hutmacher, The return of a forgotten polymer – Polycaprolactone in the 21st century, *Progress in Polymer Science (Oxford)*, vol. 35, no. 10. Elsevier Ltd, pp. 1217-1256, Oct. 01, 2010, doi: 10.1016/j.progpolymsci.2010.04.002.
8. A. Merkli, C. Tabatabay, R. Gurny, J. Heller, Biodegradable polymers for the controlled release of ocular drugs, *Progress in Polymer Science (Oxford)*, vol. 23, no. 3. Elsevier Ltd, pp. 563-580, Jan. 01, 1998, doi: 10.1016/S0079-6700(97)00048-8.
9. M.-O. Christen and F. Vercesi, Polycaprolactone: How a Well-Known and Futuristic Polymer Has Become an Innovative Collagen-Stimulator in Esthetics, 2020, doi: 10.2147/CCID.S229054.
10. Z. Pedram Rad, J. Mokhtari, and M. Abbasi, Fabrication and characterization of PCL/zein/gum arabic electrospun nanocomposite scaffold for skin tissue engineering, *Materials Science and Engineering C*, vol. 93, pp. 356-366, Dec. 2018, doi: 10.1016/j.msec.2018.08.010.
11. C.H. Park, Biomaterial-based approaches for regeneration of periodontal ligament and cementum using 3D platforms, *International Journal of Molecular Sciences*, vol. 20, no. 18. MDPI AG, Sep. 01, 2019, doi: 10.3390/ijms20184364.
12. G.K. Srivastava *et al.*, Comparison between direct contact and extract exposure methods for PFO cytotoxicity evaluation, *Scientific Reports 2018 8:1*, vol. 8, no. 1, pp. 1-9, Jan. 2018, doi: 10.1038/s41598-018-19428-5.

**IMPACT OF THE MULTI-WALL MWCNT CARBON NANOTUBES  
ON THE BIOCOMPATIBILITY OF MICRO AND NANOFIBERS OF  
COMPOSITE POLYCAPROLACTONE MATRIX**

**Abstract**

Regenerative medicine uses tissue scaffolds made of various polymeric materials to rebuild tissue. One of the biomaterials that scientists pay a lot of attention to is polycaprolactone (PCL), which is widely studied for its use as a base for an electrically conductive biomaterial. This study focused on the preparation of fibrous tissue scaffolds obtained in an electrostatic field with the addition of MWCNT carbon nanotubes and



the assessment of their biocompatibility. The viability of cells incubated with extracts from the assessed biomaterials was not less than 76.9% for fibroblast cells. The extracts of the tested biomaterials showed no toxic effect on the tested cell line.

**Keywords:** biocompatibility, polycaprolactone, carbon nanotubes.

# **POSTĘPY W ONKOLOGII OBLICZENIOWEJ I SPERSONALIZOWANEJ MEDYCYNIE**

**Tom 1**

**TU I TERAZ!**

## **Streszczenie**

Analizując rozwój medycyny jako nauki osiągającej coraz lepsze efekty w walce o zdrowie i życie człowieka, z pełnym przekonaniem można stwierdzić, że ochrona zdrowia jest priorytetowym zadaniem w wielu krajach. Postęp medycyny sprzyja biomedycznemu spojrzeniu na zdrowie oraz dominacji nowego podejścia zwanego medycyną precyzyjną (spersonalizowaną), która uwzględnia indywidualne różnice w genach, środowisku i stylu życia pacjentów.

Niniejsza wieloautorska monografia doskonale wpisuje się w najnowsze trendy inżynierii biomedycznej, w szczególności związane z onkologią obliczeniową i medycyną spersonalizowaną. Praca zawiera 16 rozdziałów, w których Autorzy dzielą się z Czytelnikiem swoim doświadczeniem i wiedzą w odniesieniu do następujących zagadnień:

- przetwarzanie obrazów medycznych (usuwanie artefaktów, wykrywanie zmian nowotworowych w badaniach histopatologicznych),
- zagadnienia segmentacji na przykładzie angiografii, segmentacji naczyń krwionośnych, zmian chondromalacyjnych głowy kości udowej,
- zagadnienia bioinformatyki, w tym sekwencjonowanie genomu i analiza struktury klonalnej nowotworów, modelowanie w biomedycynie, m.in. problematyka transmisji ciepła w hipertermii onkologicznej czy w kriokonserwacji tkanek oraz modelowanie reakcji dyfuzja – strącanie,
- systemy klasyfikacji (np. w biopsji raka głowy i szyi) i wizualizacja dużych zbiorów danych (w badaniach klatki piersiowej),
- klasyfikacja obrazów rentgenowskich pacjentów z podejrzeniem COVID-19, która pozwala na różnicowanie chorych,

- skuteczna spersonalizowana terapia u pacjentów neurologicznych i nowatorskie oprogramowanie stosowane w rehabilitacji różnych zaburzeń,
- zagadnienia biomateriałów, w tym materiały polimerowe w regeneracji.

W prezentowanych rozdziałach Autorzy łączą rozważania teoretyczne, projektowe oraz prace eksperymentalne, co w konsekwencji prowadzi do zaprezentowania oryginalnych rozwiązań metodycznych zwiększających efektywność procesów diagnozowania i terapii chorób społecznych, takich jak choroby nowotworowe, terapie neurologiczne czy choroby wirusowe przez infekcję wirusem COVID-19.

Publikacja monografii jest jednym z działań realizowanych przez Politechnikę Śląską. Wydawana jest m.in. w ramach programu Inicjatywa Doskonałości – Uczelnia Badawcza, a jej tematyka doskonale wpisuje się w temat Priorytetowego Obszaru Badawczego 1 (POB1; Onkologia Obliczeniowa i Spersonalizowana Medycyna) Politechniki Śląskiej.



**WYDAWNICTWO POLITECHNIKI ŚLĄSKIEJ**  
**ul. Akademicka 5, 44-100 Gliwice**  
**tel. (32) 237-13-81, faks (32) 237-15-02**  
**www.wydawnictwopolitechniki.pl**

**UIW 48600**

**Sprzedaż i Marketing**  
**tel. (32) 237-18-48**  
**wydawnictwo\_mark@polsl.pl**

**Sprawy wydawnicze**  
**tel. (32) 237-13-81**  
**wydawnictwo@polsl.pl**

The book covers the recent research and applied solutions in the area of computational oncology and personalized medicine, being the topic of the Priority Research Area #1 (POB1) of the Silesian University of Technology. The chapters are the result of the research conducted by the staff of the Silesian University of Technology and cooperating partners of the socio-economic environment. The idea behind this monograph is to promote the paradigm change from delayed reactive medical services to evidence-based Predictive, Preventive & Personalised Medicine (3PM / PPPM). The presented research is the response of the scientific community to the needs raised by clinical partners including up-to-date and critical research on medical image processing and segmentation, bioinformatics, modelling in biomedicine, classification systems and visualization of the large datasets, personalized medicine, novel software and biomaterials research.

ISBN 978-83-7880-800-8  
Wydawnictwo Politechniki Śląskiej

**Series:** Excellence Initiative - Research University

